A STUDY OF DISPERSION AND COMBUSTION OF PARTICLE CLOUDS IN POST-DETONATION FLOWS

A Thesis
Presented to
The Academic Faculty

by

Kalyana Chakravarthi Gottiparthi

In Partial Fulfillment
of the Requirements for the Degree
Doctor of Philosophy in Aerospace Engineering in the
School of Aerospace Engineering

Georgia Institute of Technology
August 2015

A STUDY OF DISPERSION AND COMBUSTION OF PARTICLE CLOUDS IN POST-DETONATION FLOWS

Approved by:

Professor Suresh Menon
School of Aerospace Engineering
Georgia Institute of Technology
School of Aerospace Engineering
Georgia Institute of Technology

Professor Jechiel Jagoda
School of Aerospace Engineering
Georgia Institute of Technology
School of Aerospace Engineering
Georgia Institute of Technology

Professor Stephen Ruffin
School of Aerospace Engineering
Georgia Institute of Technology
School of Aerospace Engineering
Georgia Institute of Technology

Dr. Julian Rimoli
School of Aerospace Engineering
Georgia Institute of Technology
School of Aerospace Engineering
Georgia Institute of Technology

Dr. Devesh Ranjan
School of Mechanical Engineering
Georgia Institute of Technology
School of Aerospace Engineering
Georgia Institute of Technology

Date Approved: August 2015

guruḍē yaṭa padmabhavuḍu

guruḍē ī jagamu gācu gōvindunḍun

guruḍē ā paramaśivuḍu

guruḍē sarvamu gurutuga guri gurudāsā

Dedicated to the Guru who imparted the required knowledge and made this thesis possible

ACKNOWLEDGEMENTS

Soon after arriving from India to pursue my doctoral studies, I was fortunate to be introduced to the captivating field of detonation and explosion research. The exciting aspects of the physics and the challenges involved in computational modeling have kept me motivated and developed a desire to delve for unexplored areas. Without this thirst for knowledge, staying focused and committed to research would have been very difficult and I am very grateful to my thesis advisor, Prof. Suresh Menon, for introducing me to this fascinating field. I am also thankful for his support and advice during this period. I would like to thank Defense Threat Reduction Agency (DTRA, Program Manager - Dr. Suhithi Peiris) for funding this research. This thesis would not have been possible without the continued support from DTRA and the computational resources provided by the DoD High Performance Computing Modernization Program (HPCMP). I sincerely thank the thesis committee members, Prof. Suresh Menon, Prof. Jechiel Jagoda, Prof. Stephen Ruffin, Dr. Julian Rimoli and Dr. Devesh Ranjan for taking time to read this thesis and provide their valuable assessment and suggestions. I further thank Prof. Jechiel Jagoda for the kind help on several occasions during my stay at Georgia Tech.

At Computational Combustion Laboratory (CCL), I have been given a chance to work with friendly and industrious students and research staff. I am thankful to Dr. Srikant Srinivasan, Dr. Jung Choi, Dr. Reetesh Ranjan and Dr. Michel Akiki for their support, encouragement and helpful discussions. I would like to thank Dr. Franklin Génin, Dr. Matthieu Masquelet, Dr. Martin Sanchez-Rocha, Dr. Kenji Miki, Dr. Satish Undapalli and Dr. Kaushik Balakrishnan for explaining to me several aspects of computational combustion and helping me on multiple occasions. I am very grateful for the support provided by my friend and colleague, Joseph Schulz, whose company has made the long hours in the lab fruitful and multiple cups of tea/coffee palatable. I also thank my co-workers at CCL, Andrew Smith, Timothy Gallagher, Balaji Muralidharan, Yusuke Nagaoka, Sayop Kim and

Umesh Unnikrishnan. I acknowledge the help and support provided by the past and the present Georgia Tech students, Matthew Clay, Orcun Kozaka, Burak Korkut and Amrita Basak.

I have been fortunate to have friends, Sreekar, Imon, Salil, Gauri, Prabuddha, Vrishank and Debesh, who made my long stay away from my family possible. I am grateful for their kind moral support and being there for me in times of need. Many thanks to my relatives Pavan, Haritha and Deepika for their help and advice. Finally, I would like to thank the people dear to me. To my parents, Padma and Yadagiri Rao, who have been very patient all these years and have always been there to support my personal and career paths, I am forever indebted. My thanks to my sister and brother-in-law, Kiranmayi and Shravan Kumar, for their affection and unwavering confidence in me. Above all, to the *Guru*, who in several forms has guided me, I am always a *Dasa*.

TABLE OF CONTENTS

LIST OF TABLES

LIST OF FIGURES

SUMMARY

Reactive gas-particle flows formed after detonation of explosive charges are investigated using a robust combination of Eulerian-Eulerian (EE) and Eulerian-Lagrangian (EL) methods. The focus of the investigations is to explore the physics of dispersal of particles, both within the charge and in the surroundings, by explosives. A wide range of total mass of particles in the domain of interest is considered to study and quantify dispersal and mixing. The hydrodynamic instabilities induced in the post-detonation flow are examined to understand their effect on the particle trajectories. The challenging task of solving for dense clouds of micron and sub-micron particles in complex flows is successfully addressed in this thesis.

Post-detonation flows with dense particle clouds, i.e., clouds with dispersed phase volume fraction greater than 0.01, comprise of large number of particles i.e. $\mathcal{O}(10^6 - 10^9)$. Further, the variation in the particle volume fraction transitions the flow from a very dense regime to very dilute regime. In order to account for all the particles in the flow and accurately describe the flow properties in both dense and dilute flows, a robust massively parallel Lagrangian solver has been developed, verified and validated. The solver is capable of accounting for a wide range of dispersed phase volume fractions and adjusts the gas-phase fluxes based on the volume occupied by the dispersed phase. The gas and the dispersed phases are two-way coupled and the transfer of mass, momentum and energy between the two phases is computed based on empirical laws. This EL strategy has been successfully employed to study the post-detonation flow of homogeneous and heterogeneous charges. However, in some cases, the post-detonation flow comprises of localized dense clusters of particles. These local clusters render tracking of the particles computationally infeasible. To overcome this difficulty, a robust EE solver has been developed. The EE implementation is based on the kinetic theory for granular flows and is comparable to the EL approach. While EL method is accurate even when the particles are rarefied, it is expensive compared to EE

approach. Thus, the localized dense particle clusters are solved employing EE method and as the flow becomes dilute the method transitions from EE to EL. This combined approach brings together the advantages of both EE and EL methods. Thus, investigation of dense clusters of small particles in post-detonation flow is made feasible by the combined EE-EL approach.

Before dealing with the dense micron/sub-micron particle clusters in the initial charge using EE-EL method, EE method is evaluated to determine the range of the dispersed volume fraction and the particle size which provides good performance. The accuracy of results from EE solver are dependent on the dispersed phase volume fraction in the flow and number of particles in a given computational cell. The analysis of EE and EL methods has suggested that the EE is better suited in cases with marginally dense to dense flow. Further, EE provides good and comparable accuracy as the number of particles per computational cell is increased. Thus, for combined EE-EL approach it is valid to use EE for dense regions of small particles and transition to EL as the particles disperse. Based on the evaluation of EE and EL methods, a criteria for transition between solvers for the combined EE-EL solver is developed and tested. The transition from EE to EL is dependent on the dispersed phase volume fraction and the number of particle resulting from the transition. The transfer volume fraction is adjusted based on the desired number of particles which render the simulation feasible.

With the leverage of the EL and the EE-EL solvers, the interaction of particle clouds with a homogeneous explosion and the dispersal of metal particles from heterogeneous explosions are investigated. First, studies focused on aerosol cloud interaction with homogeneous nitromethane (NM) explosion aimed at quantifying the neutralization of bacterial spores embedded in the aerosol droplets are performed. The percentage of intact spores after impact by the explosion is determined by the initial distance from the charge. The ideal distance for optimal neutralization is determined by the spore dispersal by the initial blast wave and the droplet residence time in the post-detonation mixing zone. These studies provide the criteria for optimal droplet evaporation in post-detonation flows and demonstrate the importance of residence time in the mixing zone to achieve desired effects.

Followed by the analysis of the interaction of dilute particle clouds with explosions, the dispersal of micron size particles in post-detonation flow is investigated. Steel and aluminum particles emanating from heterogeneous NM charges are considered. The combustion of the aluminum particles in the flow is determined by the combined kinetic and diffusive mass transfer. The reaction rate of aluminum is influenced by the particle size and the volume fraction of the dispersed phase. The reduction in the particle size allowed for higher particle temperatures and diffusive limited mass transfer. These studies have indicated that the particle combustion and thereby the afterburn can be enhanced by packing the explosive charge with micron sized particles that result in a dense post-detonation flow.

The simulation strategy has been successful in addressing the problem of large number of particles encountered in post-detonation flow modeling. The studies have shown robustness of the method and its applicability to problems where flow transitions from dense regime to dilute regime. Thus, the influence of the current studies is not limited to post-detonation flows and the simulation methodology is useful to develop strategies for complex multiphase flows such as spray combustion and soot modeling. Also, the efficacy of the method allows for the investigation of phenomena yet to be explored in detail like the particle jet formation in the post-detonation flow.

CHAPTER I

INTRODUCTION AND MOTIVATION

Control of fire and channeling the energy generated by combustion has been important for the development of human civilization. Historical records show several inventions and innovations to achieve optimal control of combustion. For centuries, different reactive materials have been tailored to produce desired effects and satisfy specific requirements. Certain materials, however, are known to react very rapidly, rendering the prediction and the control of combustion very difficult. The explosive energy of these materials has been employed to manufacture fireworks used as a part of rituals, ceremonies or entertainment. The earliest use of an explosive material for military purpose was documented in China [22]. Later the methods of manufacture and usage of explosive materials spread to other regions and have now become an irreplaceable component of many industries. Mainly, the advent of high explosives revolutionized the construction and the mining operations essential for industrial revolution. The high explosives, unlike low explosives such as gun powder or black powder, detonate when ignited. In these explosives, the confinement necessary for rapid pressure and temperature raise leading to a very rapid reaction, is provided by the explosive itself. Most modern explosives are high explosives and when ignited produce a detonation which leads to a strong blast wave and a post-detonation zone comprising of hot gases. The detonation product gases interact with the ambient gases and generate complex hydrodynamic structures which influence the energy release associated with afterburn [18]. The total impact of the explosive is determined by the afterburn processes and it is vital to understand the underlying physics to predict the effect of a given explosive on the environment.

Modern high explosives have applications in multiple areas such as mining, construction, defense and threat reduction. In many scenarios, explosives are designed to impact target structures. Penetration or destruction of target structures is not trivial and is determined by the focus of the energy and the total impact of the explosive. The major impulse on

the structures in the vicinity of an explosion is produced by the blast wave. However, the interaction of the blast wave with the surrounding structures is momentary and may not always produce the desired effect. Based on the proximity, targets can interact with the post-detonation gases. The post-detonation mixing and combustion occur at relatively larger time scales, and in many cases help in effective destruction of the targets [51]. In some threat reduction scenarios, explosives are employed to neutralize chemical or biological (CB) agents. Effective neutralization of some CB agents can be achieved by the high temperature zone generated by the explosion [107, 121]. However, interaction with specific neutralizing agents is required for certain CB agents [107]. In these cases, explosives can be manufactured to contain neutralizing agents. These explosives eject neutralizing agents which react in the post-detonation flow and achieve the required neutralization. For effective neutralization, CB agents must be in the mixing and the combustion zone for $\mathcal{O}(10^{-3})$ to $\mathcal{O}(1.0)$ s [53]. The time of interaction can be reduced by enhancing the mixing and the energy release due to the afterburn [106]. Thus, for a given application, the mixing and the afterburn in the post-detonation flow play a key role in determining the range and the relevance of the explosive.

To augment the impact and their applicability, explosives are often packed with metal particles. When these explosives are detonated, the particles in the explosive charge eject with high velocity and impact any target structure in their path. The momentum and the energy carried by the particles enable them to penetrate targets and enhance the destructive nature of the explosion. Since the particle inertia is dependent on the density of the particle, typically, iron or tungsten particles are packed in the explosive [129]. However, certain metal particles react in the post-detonation flow and provide relatively higher temperatures desired in some applications. Also, the energy release due to particle combustion is known to add to the impact of the explosion. Thus, aluminum or zirconium particles are also used to tailor explosives [41]. The fraction of the volume of metal particles in the explosive charge is typically greater than 0.1. In case of inert particles, this provides sufficient number of projectiles to target the environment. If particles are reactive, the fuel content for the afterburn is increased with increase in the volume of the particles in the explosive. Thus, in

most cases, the flow after the detonation is dense and it is important to consider the effect of the particle volume and inter-particle interactions in the flow. Here, we define dense flow as a flow with the volume fraction of the particles greater than 0.01 [52, 127].

Apart from uniformly distributing particles in the explosive charge, explosives are also made with a core of pure energetic material encased by a shell of particles. These explosives when ignited, detonate in the pure explosive material with no loss of momentum or energy to the particles. The strong detonation or blast wave interacts with the particle shell and ejects the particles away from the charge [40]. The complex post-detonation flow followed by the blast wave comprises of high velocity particles. The initial interaction of the blast with the particle shell determines the combustion or the dispersion of the particles. In all cases, either with particles in the charge or enveloping the charge, the hydrodynamic instabilities play a crucial role in the post-detonation processes [15, 16, 17]. It is vital to understand the particle dispersal and mixing with the surrounding gases in dense flows to characterize a given explosive, and investigations into the underlying physics will enable production of efficient novel weapon systems. Also, increased predictive capabilities will ensure safe and effective use of explosives and in certain cases help prevent naturally occurring undesired detonations and explosions.

1.1 On detonations and explosions in gas-particle mixtures

When a reactant mixture is ignited, a combustion wave propagates through the mixture converting the energy stored in the chemical bonds of the reactants into internal energy and kinetic energy of the products. The energy release causes large changes in thermodynamic and gas dynamic states across the combustion wave, which result in physical and chemical processes that allow self-sustained propagation of the wave. Generally, there are two types of self-propagating combustion waves: deflagration and detonation [69]. A deflagration is a combustion wave which propagates at sub-sonic velocities with respect to the reactants ahead of it whereas a detonation propagates at supersonic velocities and comprises of a strong shock wave, which is sustained by the energy release of the shock induced reaction. Both deflagrations and detonations can result in explosions if the reaction processes result in

sudden increase in volume accompanied by extreme energy release. Low explosives produce subsonic explosions through deflagrations whereas high explosives detonate to generate supersonic explosions [133].

Detonations and explosions are ubiquitous in nature. Some of the largest known detonations occur in the universe when a star explodes in an event called supernova [42]. Explosions occur on sun during solar flare events and are also reported when asteroids impact other objects such as a planet or a moon. Many of the earth bound natural explosion events are related to volcanic activity or earthquakes [47]. In this thesis, only chemical explosions are considered. Chemical explosions occur in reactive mixtures and are initiated by an ignition source. In man made structures such as mines and industrial storage units, detonations and explosions can occur when triggered by a natural or an accidental spark. These pose a severe threat to the safety of the workers and it is desired to prevent or control these unwanted events. In mines, the methane gas and the suspended coal particles can ignite developing into uncontrolled deflagrations [90]. If constrictions are present in the path of the propagating deflagration, it can transition to a detonation and cause a violent explosion [49, 89]. There are several reported incidents of detonations in storage units due to the suspended corn starch particles [59]. In order to control and prevent unwanted damage to life and property, several investigations have focused on detonation and explosion quenching [52]. However, prediction and appropriate counter measures are still lacking and incidents of safety being compromised are reported frequently.

1.1.1 Physics of detonations and explosions

An explosion in a high explosive starts with the initiation of a detonation. There are several mechanisms for formation of a detonation and typically the initiation occurs through shock-to-detonation transition (SDT) [4]. When a heat source is provided, the combustion of the energetic material with naturally occurring voids can lead to the formation of hot spots and strong shock waves. These hot spots and the reaction zone interact with the shock wave to produce a detonation. Detonations are self-sustained by the coupled propagation of the reaction zone and the detonation front. Previous studies, both experimental and numerical,

Figure 1: Cellular structures recorded on the ground by a gasoline spray detonation [132]. Reprinted with kind permission from Springer Science and Business Media (Figure 7 from Zhang et al., Shock Waves, 25, 239-254, 2014; Copyright 2014, Springer)

showed that the leading shock at the detonation front is wrinkled and comprises of alternate strong Mach stems and weak incident shocks [48, 52, 109]. These strong and weak shocks are connected at triple points by transverse waves which extend back into the reaction zone. As the detonation propagates, the triple points move back and forth along the detonation front. This movement of triple point is traced to form a soot foil as shown in Fig. 1. The size and the pattern of the cellular structures and any alteration in the generally observed cellular structures are useful in predicting the detonation quenching [52, 91]

Once the detonation reaches the surface of the explosive charge, a blast wave is formed. The propagation of the blast wave and the flow behind it can be described in four stages [18, 61, 65] (i) *Primary blast wave*: the outward propagating blast wave heats up the air while a rarefaction wave propagates inwards. The interface between the detonation product gases and the ambient air is accelerated. This acceleration combined with the large density gradients across the contact surface induces Rayleigh–Taylor instabilities (RTI) [111]. The inward propagating rarefaction over-expands, after a short time, and results in the formation of a second shock wave, also called secondary shock. The secondary shock initially moves outwards due to the expanding detonation products from the center of the charge. A thin mixing zone is developed between the primary blast wave and the secondary shock. The mixing zone, the primary blast wave and the secondary shock formed at this stage are shown in Figs. 2 and 3 (a). In this stage, the mixing layer grows primarily due to

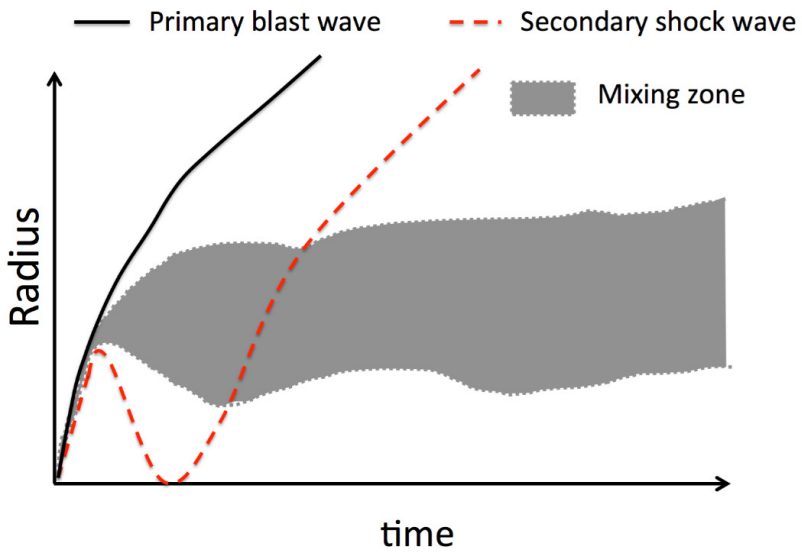

Figure 2: Schematic of the radial location of the blast wave, the secondary shock and the mixing zone with time in the post-detonation flow of spherical homogeneous charge. Sketch is not to scale.

RTI. (ii) *Implosion*: The accelerating detonation product gases (generating a low pressure region at the origin) strengthen the secondary shock to the point of implosion (See Fig. 3). The implosion entrains the ambient gases into the mixing zone. This enhances the post-detonation combustion, i.e., afterburn. (iii) *Reshock*: The secondary shock, after the implosion, is reflected outwards from the origin. The reflected shock interacts with the mixing zone formed by RTI (as shown in Fig. 4 (a)) and the impulsive acceleration by the shock induces Richtmyer-Meshkov instabilities (RMI) [99]. RMI enhances the mixing and the afterburn. (iv) *Asymptotic mixing*: The mixing of the hot detonation product gases and the air continues after reshock. The hydrodynamic structures developed in the flow acquire features independent of the initial perturbations at the contact. This behavior is due to RMI and is also observed in other similar flows with RMI induced mixing. The mixing continues as the reminder of the unreacted gases are consumed.

If the explosive charge is packed with particles, the particles interact with the flow in each of the phases described above. The dispersion of the particles is dependent on their location in the post-detonation flow relative to the blast wave and the mixing zone [16, 129]. When homogeneous explosives, i.e., explosives without particles, are detonated,

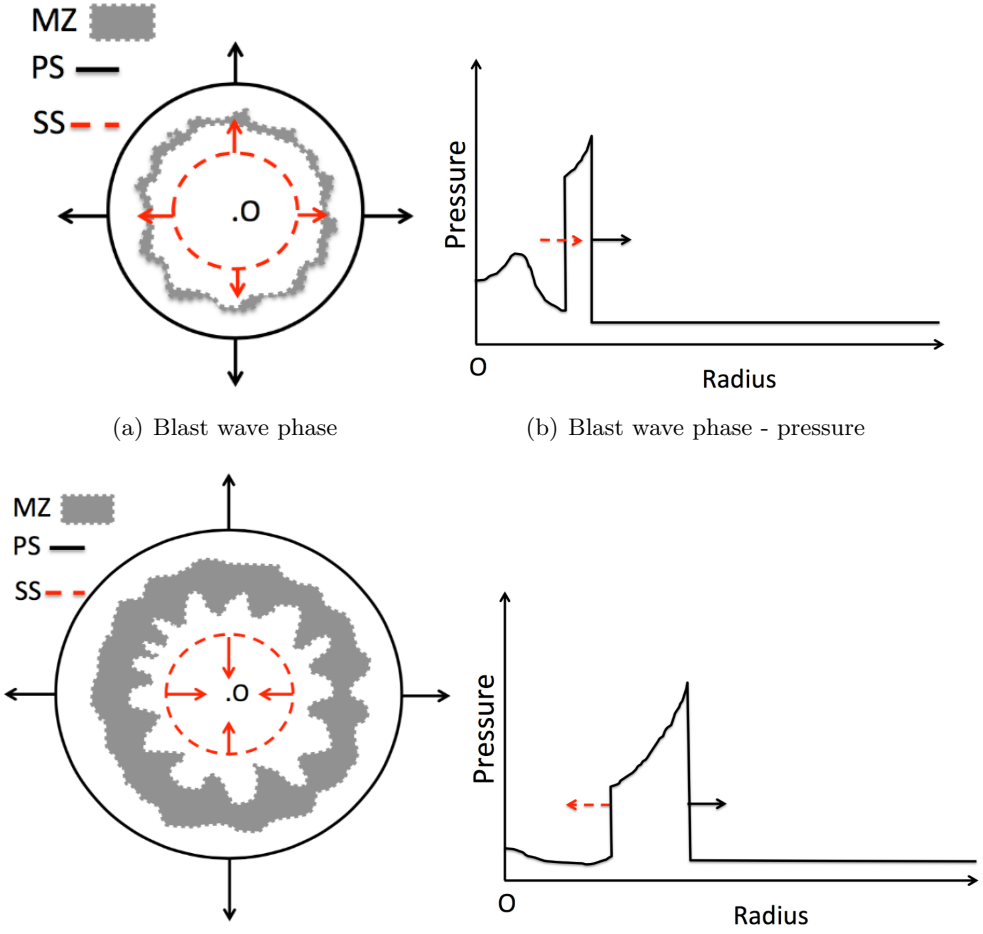

(a) Blast wave phase

(b) Blast wave phase - pressure

(c) Implosion phase

(d) Implosion phase - pressure

Figure 3: Schematic ((a) and (c)) of primary shock/blast wave (PS) (black, solid line), secondary shock (SS) (red, dashed line) and mixing zone (MZ) (gray, dotted line) evolution during the blast wave and the implosion phases. The cross section of the domain after detonation of a spherical homogeneous explosive (Origin - O) is shown in the sketch. (b) and (d): The pressure plots corresponding to each phase along with the direction of the waves are shown. Note that the sketches are not to scale.

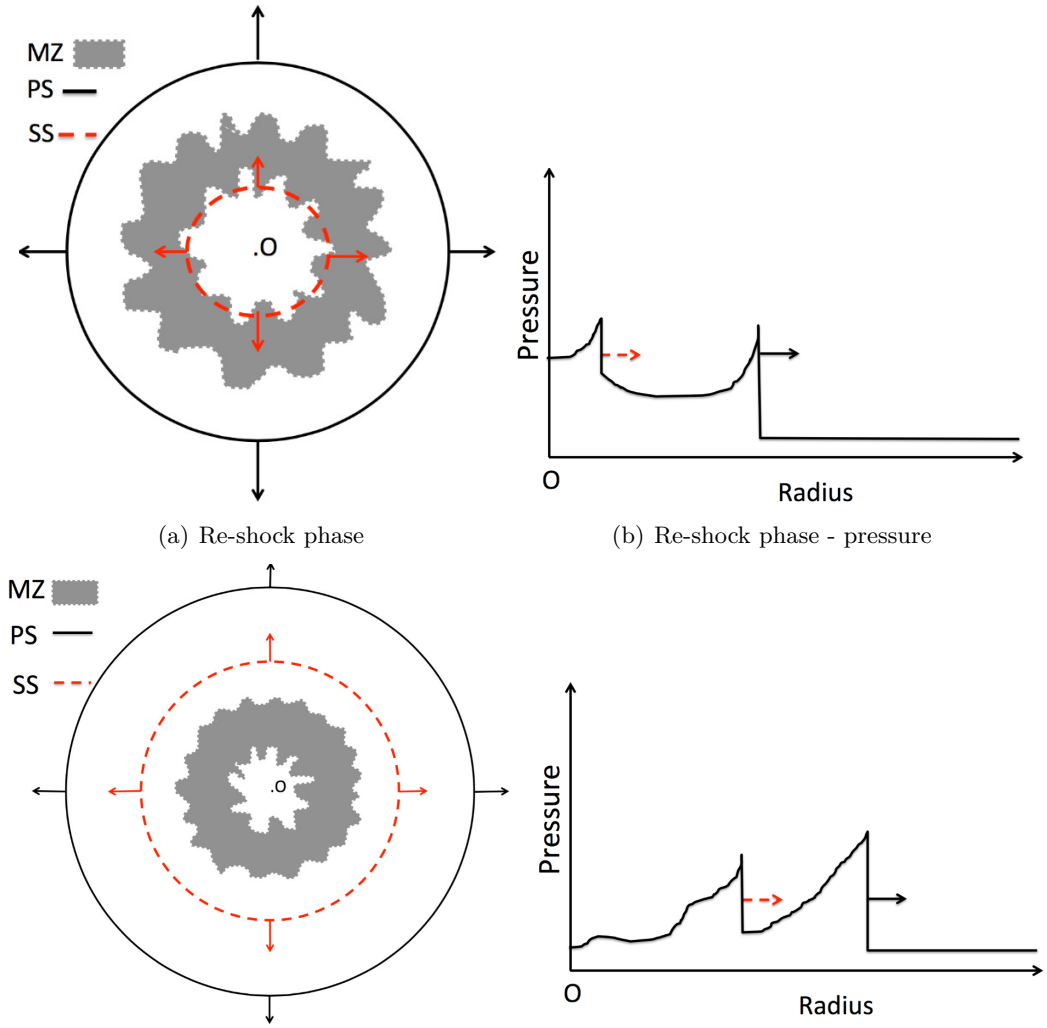

(a) Re-shock phase

(b) Re-shock phase - pressure

(c) Asymptotic phase

(d) Asymptotic phase - pressure

Figure 4: Schematic ((a) and (c)) of primary shock/blast wave (PS) (black, solid line), secondary shock (SS) (red, dashed line) and mixing zone (MZ) (gray, dotted line) evolution during the re-shock and the asymptotic phases. The cross section of the domain after detonation of a spherical homogeneous explosive (Origin - O) is shown in the sketch. (b) and (d): The pressure plot corresponding to each phase along with the direction of the waves are shown. Note that the sketches are not to scale.

the initial contact perturbations are generated by the variations in the charge surface, either at macro or molecular scales. These perturbations later help in inducing RTI and RMI. For heterogeneous explosives, i.e., explosives with particles, the initial perturbations can be induced in three ways: (i) as observed in the case of homogeneous explosives, the imperfections on the charge surface can develop the perturbations. (ii) The particles perturb the flow and the flow in turn perturbs the contact surface. (iii) The particles overtake the contact surface due to the initial momentum and perturb the contact surface [17, 20, 53]. Thus, particles apart from imparting required impulse also help in afterburn processes. Accurate description of the underlying phenomena is important to understand and produce explosives suited for a given purpose. However, investigation of the post-detonation flow is very challenging and involves resolution of several coupled problems.

1.1.2 Challenges in investigation

Detonation and evolution of the post-detonation flow has been investigated for several years, both experimentally and numerically [18, 41, 53, 63, 129, 132]. Because of the destructive nature of the flow, experimental investigation of explosions is not trivial. The apparatus must be set to withstand the blast wave, the fireball and the ejecta emanating from the explosion. In most cases, the data is collected to trace the motion of the blast front, to measure the particle dispersion, and to estimate the extent of the fireball. These parameters can be recorded either by high speed imaging or by sensors which measure variation in the flow pressure. Figures 5 and 6 show the blast wave, the fire ball and the particle clouds obtained from experimental investigations [132]. However, it is difficult to characterize and quantify mixing from such data. Further, the underlying phenomena, which lead to the formation of the complex flow structures and particle dispersion patterns, is obscured by the fireball, soot and other fragments emanating from the explosion. Thus, to develop insights into the physics of explosions, numerical investigations have become indispensable. Simulations have been successfully employed to study and explain the detonation and the post-detonation physics [18, 52, 53, 63]. However, performing numerical simulations is also challenging, especially, when the post-detonation flow comprises of dense particle clouds.

Figure 5: Blast wave and fireball formed after detonation of gasoline spray cloud [132]. Reprinted with kind permission from Springer Science and Business Media (Figure 3 from Zhang et al., Shock Waves, 25, 239-254, 2014; Copyright 2014, Springer)

One of the basic requirements to be satisfied by any numerical method chosen to investigate the post-detonation flow is to model the high pressure and the high temperature zone in the post-blast region. Typically, the pressure, before attenuation, at the blast wave is $\mathcal{O}(10^9 - 10^{11})$ Pa whereas the pressure before the blast wave is nearly 10^5 Pa. The temperatures also vary from 300 K to more than 10000 K based on the explosive material. Further, the post-blast pressure and temperature can be below the ambient conditions because of the flow expansion. The size of an ordinary chemical explosive charge is typically $\mathcal{O}(1.0 - 100)$ cm. When detonated, the blast wave and the fireball from the explosion can spread to a region with a length scale $\mathcal{O}(1.0 - 100)$ m. The particles present in the flow are of radius $\mathcal{O}(0.1 - 100)$ μm. Thus, a wide range of length scales are encountered. Also, the explosion events, starting from the detonation to the asymptotic mixing, occur over a wide range of time scales. To accurately describe the post-detonation flow, all the relevant time and length scales must be resolved.

In most heterogeneous explosive charges, the particle are packed to form a dense cluster. This dense cluster of particles disperses, and as the particles spread, the flow becomes dilute. In dense flows, the particles block the flow of the gases and the role of the inter-particle interactions on particle dispersal cannot be ignored [15, 52]. Thus, both dense and dilute

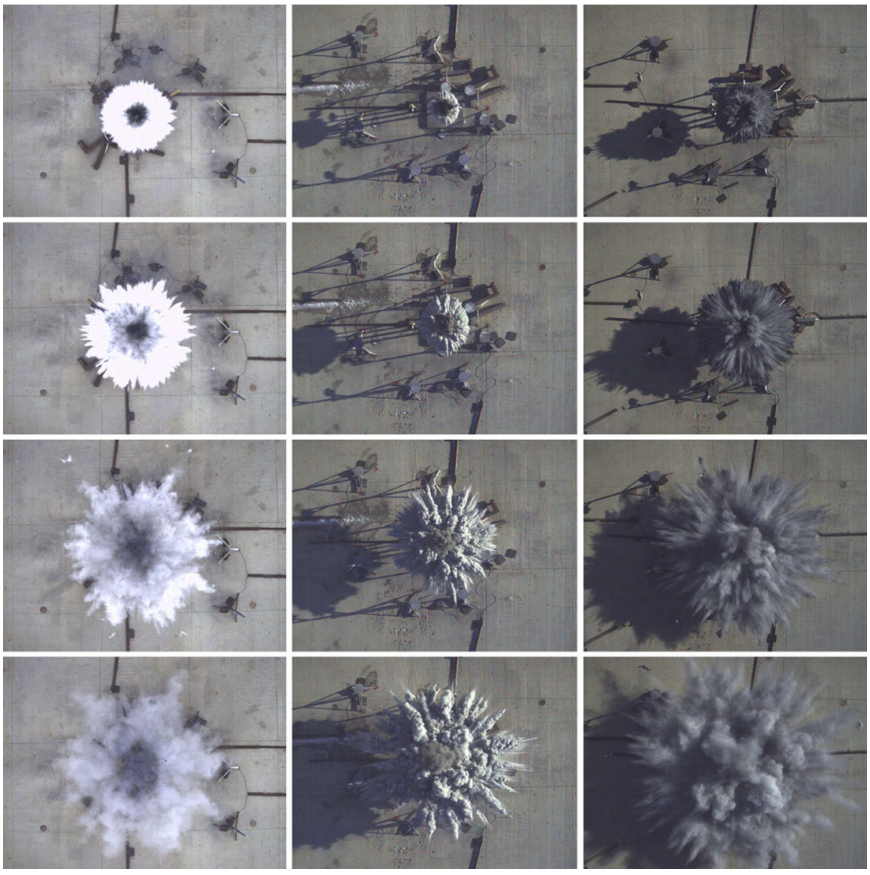

Figure 6: Dispersion of annular payload by a 114 mm diameter cylindrical explosive. The payload consists of pure liquid (left), Al particles (middle), and a hybrid mixture of Al particles and liquid (right). The frames are taken at 5, 10, 25, and 50 ms (top to bottom) [132]. Reprinted with kind permission from Springer Science and Business Media (Figure 1 from Zhang et al., Shock Waves, 25, 239-254, 2014; Copyright 2014, Springer)

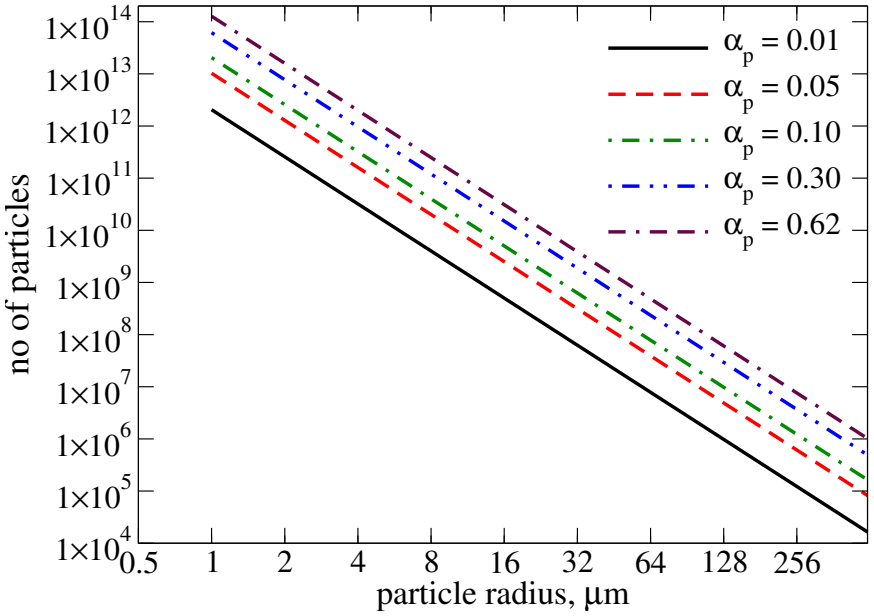

Figure 7: Number of particles in an explosive charge of radius 5.9 cm for different initial particle volume fraction (α_p).

effects must be modeled simultaneously to simulate the post-detonation flow. Also, the number of particles present in the flow increases with increase in the initial volume fraction of the particles in the explosive charge. In some cases, when the particle size is $\mathcal{O}(1.0-100.0)$ μm, for a typical initial explosive charge diameter, the number of particles is $\mathcal{O}(10^6 - 10^{14})$ (see Fig. 7). Tracking or solving for all of these particles is currently not feasible even with a massively parallel solver, especially when the particles form small dense clusters. Thus, there is a requirement for strategies which go beyond the conventional Lagrangian or Eulerian multi-phase methods.

1.2 Literature review

The flow ensuing an explosion or a detonation has been the focus of several past investigations. These investigations resulted in some important insights into the underlying physics of the post-detonation flow. Researchers employed both experimental and numerical techniques to explore chemical explosions. Experiments investigated the blast wave, the fireball and the particle dispersion characteristics using pressure sensors and high speed photography whereas numerical studies focused on the combustion, the mixing and various modeling

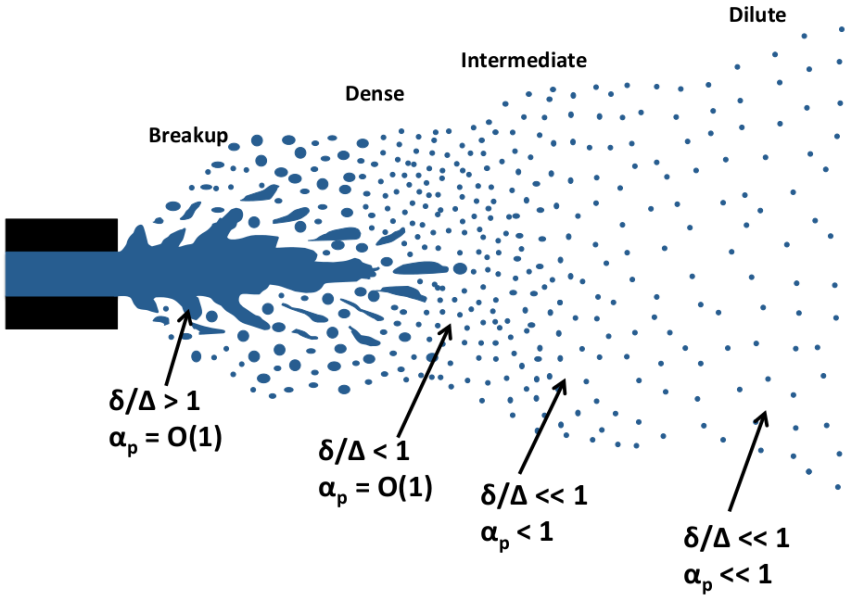

Figure 8: Evolution of liquid spray from injection to dispersion in dilute regime [6]. The volume fraction of the liquid phase, the characteristic length scale of the liquid film and the grid resolution are is denoted by α_p, δ and Δ, respectively.

aspects. In this section, the existing literature leading to the current thesis is reviewed with focus on past work on modeling dense flows, explosives, hydrodynamic instabilities and particle combustion.

1.2.1 Dilute and dense two-phase flows

1.2.1.1 Modeling and simulation methods

Multi-phase flow modeling has wide range of applications. Dispersion of aerosols, atomization and combustion of liquid fuel, and burning of coal/soot particles are few example scenarios where simulations of flows with droplets and/or solid particles provide vital insights and aid in engineering new or better devices. To improve performance in different engines, several investigations focused on simulations of fuel sprays [83, 88, 103] . The modeling challenges encountered in spray combustion research are similar to the ones in the post-detonation flow research. In both cases, the flow starts with a dense droplet/particle core and transforms into a dilute flow field. Figure 8 shows this transformation for a typical

liquid spray [6]. As the particles or droplets move away from the dense core region, the role of inter-particle interaction is diminished and the influence of particles on the gaseous flow decreases. Modeling these variations in flow features is important to capture the particle dispersion and combustion accurately.

Multi-phase flows have been modeled, in general, using two approaches: Eulerian-Eulerian (EE) and Eulerian-Lagrangian (EL). EL method employs Lagrangian tracking to solve for the dispersed phase and Eulerian approach to solve for the gas-phase. In EE, Eulerian approach is used to solve for both the gas and the dispersed phases. Both methods can be used to investigate the post-detonation flow with certain limitations. The features of each these methods are summarized in Table 1. Multi-phase flows with detonations or blast waves have been investigated employing EE approach by several researchers [38, 62, 129]. The seminal work of Baer and Nunziato [8] provides a robust multi-phase model for reactive granular mixtures. In particular, for dense multi-phase flows, i.e., flows where the volume occupied by the dispersed phase is at least 1.0%, this model includes the effect of the non-equilibrium between the phases along with the compressibility of all the phases. The primary concern while solving for dense multi-phase flows is the treatment of the non-conservative terms. These terms appear due to the variations in the volume fraction of the particles, i.e., the fraction of volume occupied by the particles in a given volume, and are expressed in terms of the gradient of the volume fraction in the conservation equations for the momentum and the energy. An efficient way to account for the non-conservative terms is developed by considering the volume fraction to be a piece-wise continuous variable. Using this approach, an interpretation of the Baer-Nunziato model [8] with appropriate closures for interfacial velocities and pressures has been developed [104]. Here, the inter-cell interfaces are solved using distinct Riemann problems on the either side of the interface in pure materials [1]. This method, called Discrete Equations Method (DEM) using an Eulerian-Eulerian formulation (EE-DEM), has been further developed to investigate detonations in heterogeneous energetic materials [27]. DEM allows unique equations of state for each pure material rendering it robust for multiple applications involving shocks, detonations and blast waves. In these studies with EE-DEM, authors employed a Godunov

scheme [113] with HLLC (Harten-Lax-Van Leer with contact) Riemann solver [45]. HLLC Riemann solver has been specifically chosen as it facilitates the determination of different inter-cell interface configurations necessary to compute the direction and the amount of flux at each interface.

With an aim to compute precise particle trajectories in the post-detonation flows, the DEM has been adapted to an Eulerian-Lagrangian formulation (EL-DEM) [15]. EL-DEM allows for the correction of the gas phase fluxes based on the volume fraction of the dispersed phase computed using Lagrangian tracking. The volume fraction is still treated as a piece-wise continuous quantity and the interface terms are evaluated based on the techniques developed for EE-DEM. However, particles are treated as incompressible and the relaxation at the internal interfaces is based on the momentum and the heat transfer between the phases. This is well suited to investigate accurate explosive particle dispersal and we use this method for studies employing EL. Although, EL-DEM is robust and provides high fidelity results, two constraints of this approach are note worthy. The first constraint is that the dispersed phase cannot occupy the entire volume at a given location as it violates the continuum assumption for gas phase flux computation. The number of particles required to solve for the dense dispersed phase places the second constraint. In most cases of interest, the number of particles to be tracked, based on the volume fraction of the particles, exceeds the computational resources available. Thus, an assessment is required on the limits of EL-DEM which will clearly demarcate the limits of the volume fraction of the particles and the number of particles handled. Here, this assessment is performed using a robust EE approach for granular flows. The EE approach is chosen to mirror the EL approach for accurate comparison.

Kinetic theory based granular flow models are one of the most popular models for granular flows [33]. These models provide ways to solve for the granular random kinetic energy, Θ, along with the usual flow variables. The granular random kinetic energy is related to the granular pressure, the granular stress and the granular frictional pressure, all of which are important for extremely dense gas-particle flows, i.e., near the packing limit. In most multi-phase post-detonation flow analysis using EE or EL methods, the effects of Θ

Table 1: Features, merits and limitations of EE, EL and EE-EL methods

Aspect	EE	EL	EE-EL
Dispersed phase	Eulerian	Lagrangian	Eulerian and Lagrangian
Dilute flows	Valid for particle number densities satisfying continuum	Valid for all particle number densities	Valid for all particle number densities
Dense flows	Valid with corrections for gas-phase flux and continuum assumption	Valid with corrections for gas-phase flux	Valid with corrections for gas-phase flux
Memory requirement	Special accommodation not required	Depends on the number of particles	Depends on the number of particles and the transition criteria
Computational cost	Cheap and almost same as that for gas-phase	Expensive and varies based on number of particles per processor	Varies based on number of particles per processor
Poly-disperse flow	Special modeling required	Built into the method	Need modeling based on the transition criteria and initial distributions
Pure condensed phase or liquid core	Modeled using an interface tracking approach with different equations of state for each individual phase	Particles are discrete and sub-grid Does not represent continuous material	Can be modeled using the approach employed for EE

are ignored [15]. Since most heterogeneous explosives are densely packed with the particles, there is a necessity to investigate the relevance of Θ in the post-detonation flow. Although, inclusion of the granular energy effects help in accurate analysis of the particle dispersal, the solution of the governing equations would require the computation of the wave speed in the dispersed phase. Further, in the regions with very low or no particle concentration, the wave speed tends to zero and any solver must be able to handle this. Recently, a method which solves this problem has been developed and resolves the wave speed in granular mixtures accurately [57, 75]. Also, the non-conservative terms are treated appropriately in this method. Since this EE method, along with being robust, is comparable to the EL-DEM approach, it is chosen to investigate dense multi-phase flows in this thesis. It should be noted that, Houim and Oran [57] used AUSM$^+$-up scheme for dispersed phase along with HLLC Riemann solver for gas-phase. This choice is dependent on the fact that the AUSM$^+$-up scheme (Advection Upstream Splitting Method) [74] converges to the pressure-less Riemann solver developed by Collins et al. [29], which is used by many researchers [14, 63] to accurately model the dispersed phase flow with zero wave speed in the granular material.

EE methods, for a given volume fraction of dispersed phase, in general, provide results at a relatively lower computational cost in comparison to EL methods. Also, the ability of the EE methods to span over a wider range of volume fractions made them a good choice for several past investigations. However, EE methods need special treatment for polydispersed flow, i.e., for flows with non-uniform particle sizes, as encountered in most afterburn problems [35, 77, 81]. Also, for EE methods, interface tracking or special dissipation control techniques are needed to get reasonable particle dispersion characteristics [55]. EL methods, although expensive, are inherently polydisperse and compute the particle dispersion with great accuracy. In this thesis, two robust methods, one EE and another EL, for dense post-detonation flows, are considered with an aim to demarcate the limits and merits of each method under different flow conditions. The results define regimes of volume fraction and particle sizes under which either EE or EL is appropriate. Further, the simulations are conducted using the EE method to check the relevance of Θ in post-detonation flows.

As illustrated in Fig. 8, the particle dispersion transitions from dense to dilute regime, and it is vital to account for this transition. Although, EL-DEM can achieve this, in some cases, the number of particles and the volume fraction of the dispersed phase renders it unfeasible. In some cases, the resolution of the interface between the phases is not possible, and methods which transition from EE to EL are used to accurately model the dispersion while preserving the mass, the momentum and the energy of both the phases [55, 134]. Combined EE and EL solvers have been used to simulate primary and secondary atomization of sprays [55, 134]. Herrmann [55] used a refined level set grid to resolve the interface for the Eulerian solver and the small unresolved liquid droplets are transferred to a Lagrangian solver. Using this description, atomization of a turbulent liquid jet was simulated from injection to dilute spray dispersion. In the work by Zuzio and coworkers [134], the primary atomization is simulated using an Eulerian approach and the secondary atomization is modeled employing Lagrangian models. So far the combined EE-EL approaches have not been used with dense Lagrangian methods [19] required to resolve the dense and the intermediate regimes shown in Fig. 8. Also, there have been no development of methods for dense flows with solid particles which are of interest in the current work.

1.2.1.2 Investigations of shock-particle interactions

One of the key problems of interest related to explosive dispersal of particles is shock-particle interaction. Shock-particle interaction studies help in understanding the different physical parameters that play a key role in the dispersion of the particles. Mainly, the influence of different particle acceleration terms and the significance of modeling the dense regime have been explored by several researchers. The shock-particle interaction studies enable verification and validation of the complex numerical models employed to investigate the post-detonation flows. Here, key experimental and numerical studies relevant to the current research are discussed.

Experimental investigation of particle dispersion has been, in general, investigated to estimate the drag on the particles. As a consequence several drag laws have been proposed, which assist in computing or modeling particle trajectories in different flows [30]. A vast

collection of correlations for the particle drag as a function of Mach number and Reynolds number is also available [9, 31, 102]. However, when particles are clustered, the drag on the individual particle is affected by the local particle concentration. Thus, experiments focused on dilute and dense particle cloud dispersion have been conducted. Marginally dense and dilute acrylic particle cloud dispersion by shock waves has been studied by Boiko et al. [23] and a drag correlation has been developed. Experiments using very dense glass particle clouds, with particle volume fraction in the cloud nearly 65.0%, have also been reported [101]. In these experiments, the particles were supported by a plastic membrane. Since such supports affect the shock-particle interaction, recently, studies have been performed with particles clouds placed in the shock tube without any support. In one such setups, particles continuously fall through a slit at the top section of the shock tube and exit through a slit at the bottom of the shock tube [73]. This gravity-fed particle curtain interacts with a shock wave without any obstruction. However, in this setup, the shock-particle interaction is still influenced by the shock tube boundaries. Experiments employing free-standing particle wafers have been recently reported to eliminate the boundary effects [60].

Numerical simulations of shock-particle interaction have reported the dynamics of the shock transmission and reflection through dense particle clouds [19]. The volume occupied by the particles is accounted by employing appropriate flux corrections. The relevance of the unsteady particle acceleration terms on the particle dispersion has also been explored [71, 73, 98]. Recently, role of particle deformation on particle dispersal has also been investigated [72]. Employing kinetic theory for granular flows, dense particle cloud dispersion by shock waves has also been studied [57, 75]. The current state-of-the art simulations use dense flow modeling with correlations for particle acceleration due to quasi-steady forces, unsteady forces and inter-particle interaction.

1.2.2 Homogeneous and heterogeneous explosions

Explosions have been focus of research for past several decades. A detailed review of numerical and experimental investigations of explosives can be found elsewhere [86, 133]. Here, only the literature relevant to this thesis is reviewed with an aim to provide an

overview of the current understanding and challenges discussed above.

1.2.2.1 Experimental investigations

Investigation of the blast wave from explosions has been the focus of many studies to assess the performance of a given explosive. Afterburn has been reported to affect the velocities behind the shock wave emanating from TNT explosions by Dewey [32]. Explosions have been investigated in a small-scale apparatus to record the afterburn phenomena [122]. Pronounced reactions in oxygen enriched air have been noticed in these experiments. Large-scale experiments have also been reported with focus on afterburn in the post-detonation flow of high explosives [66, 128]. Experiments in confined chambers have been conducted to analyze the effect of afterburn on the blast wave pressure and the temperature in the post-detonation flow [34]. These experiments, with the assistance of numerical simulations, show the importance of the equation of state employed to model the afterburning processes. Experiments aimed at exploring the role of combustion of condensed phase detonation products on the energy release due to afterburn have also been reported [68]. These experiments suggest that the reaction processes in the post-detonation flow can be considered to occur at infinite rate but the assumption that the condensed phase products follow the gases without any inertial effects is incorrect.

When heterogeneous explosives are detonated, the particle clouds generated in the post-detonation flow are complex and have been investigated with an aim to characterize the dispersion pattern [41, 129]. Experiments have been conducted with explosives uniformly packed with steel particles to study the effects of particle penetration and interaction with the blast wave [129]. These experiments show that the particles cross the shock front based on the particle material density, the particle size, the charge geometry and the size of the charge. When particles are packed to envelop the explosive charge, the dispersion in the post-detonation flow involved formation of particle jets [40] as shown in Fig. 6. The particle jets are formed at the early stages of the blast wave propagation and can be characterized by the standard fragmentation models [124]. Particle jet formation has been investigated in small scale and large scale experiments to determine the number of jets formed and the

variation in the structure of the jets with time [100, 132]. These experiments suggest that the number of jets formed is dependent on the particle size, the particle material density and the volume fraction of the particles in the initial charge. In spite of these investigations, the phenomena influencing the particle jets and combustion in these jets are largely unexplored.

1.2.2.2 Numerical investigations

Explosive events are destructive, and cause damage to personnel and equipment involved in experimental investigations. Thus, the exploration of the underlying physics using experiments is difficult and has been limited. Where experimental investigations have been insufficient, numerical studies have been successful and a considerable insight into the explosion phenomena has been achieved because of multiple modeling and simulation efforts [18, 34, 65]. High fidelity simulations have been employed to explore in detail the chronology of the blast wave and the mixing zone evolution in confined and unconfined environments [18, 65, 112]. In these studies, the role of RMI and RTI in post-detonation mixing has been analyzed. The analysis emphasizes the role of hydrodynamic instabilities in developing the asymptotic mixing regime. Simulations have also been performed to show the need for equations of state which are tailored to capture the blast wave, the shocked air and the mixing zone [18, 34].

Combustion of reactive particles in the post-detonation flow has been investigated to focus on the enhancement of energy release due to afterburn [14, 63]. These simulations show preferential particle clustering and combustion based on the particle size and interaction with the post-detonation flow structures [20]. The dispersion of particles, initially uniformly packed in the explosive or packed to envelop the charge, by the explosion has also been simulated [17, 129]. In particular, the dispersion pattern of the particle jets formed by explosives has been investigated [132]. In these studies, two-dimensional simulations have been performed that qualitatively agree with the experimental results. The particles have been solved for using Lagrangian tracking, and formation of jets and the number of jets formed has been investigated.

1.2.2.3 RTI and RMI in two-phase flows

The formation of hydrodynamic instabilities is vital for mixing in the post-detonation flow. The density gradient across the contact surface generates *bubbles* of hot gases based on the initial perturbations. The competition between these bubbles allow for merger and development of asymptotic regime with structures independent of initial perturbations [70, 84, 85]. To understand RTI and RMI in context of explosions, several investigations have been performed to characterize instabilities induced by shock waves [56, 97, 108, 118, 116]. Experimental investigations have provided the mixing layer growth rates for different configurations with and without reshock. Based on these experimental investigations, numerical simulations have been performed to explore the evolution of flow structures at late times [54, 114]. These investigations suggest that the flow acquires turbulent-like characteristics with multiple length scales. These range of length scales are also observed in explosion events [132].

In case of heterogeneous explosions, RTI and RMI are influenced by the presence of particles. To investigate the effect of the particles on the mixing layer growth RTI and RMI have been investigated in gas-particle flows [13, 76, 105, 119]. These investigations suggest that the particles act as a source/sink of momentum and energy and effect the vorticity in the flow based on the particle size and the particle volume fraction [105]. Numerical investigations have shown that the particle can provide a density interface similar to the contact surface and disperse based on the perturbations at the interface [119, 115]. The *bubbles* and *spikes* of particles based on different initial contact configurations can play a key role in the development of jet structures at later stages of mixing. Hence, these observations from the past research are vital to understand the interaction of the blast wave with particles and the particle jet formation.

1.2.3 Combustion modeling

Afterburn process in the post-detonation flow is vital mainly because of the energy release bolstering the blast wave and the high temperatures due to reactions desired in some applications. Thermobaric explosives exploit these advantages provided by afterburn process

to generate explosions of high intensity. Small reactive particles have a potential to ignite and react at later stages of the explosion event and are desired in multiple applications. To throughly characterize explosives with reactive particles, experimental and numerical investigations have been performed by several researchers [15, 65, 63, 130]. For numerical investigations, the combustion of gases has been generally modeled assuming the reactions to occur at infinite rate [16, 53, 65, 63]. Some investigations have also been reported with finite rate kinetics [36, 37]. However, all these investigations assumed all the reactions to occur in gases and even the condensed phase detonation products, such as carbon or soot, have also been modeled as gases. Recent experiments suggest that modeling using the infinite rate kinetics is valid [68] but the combustion of the condensed phase products must be modeled considering the multi-phase effects.

Most explosives packed with reactive particles use aluminum particles. The availability and the rapid combustion releasing large quantities of heat has made aluminum popular choice for explosive applications. Thus, modeling combustion of aluminum particles is necessary to simulate explosive dispersion and combustion of aluminum particles. Early models of aluminum particle combustion have assumed the particle combustion to be governed by the diffusive mass transfer [14, 21]. This is similar to the case of fuel droplet combustion (d^2-law) where the mass transfer rate is dependent on the square of particle diameter (d_p^2). However, investigations have shown that the combustion of aluminum particles of diameter $\mathcal{O}(0.1 - 10.0)\ \mu m$ does not follow the d^2-law and varies as d_p [126, 131]. This is due to the mass transfer being limited by the reaction kinetics rather than the diffusion processes. Thus, a hybrid combustion model for aluminum particles has been developed and used to model detonations and explosions in aluminum-air mixtures [12, 24, 130]. This model accommodates different particle sizes and considers the mass transfer due to reaction kinetics on the particle surface and the diffusion of gases.

1.3 Objectives of the research

The main focus of this thesis is to investigate dense post-detonation flows formed after detonation of explosive charges. Post-detonation flows comprise of complex interplay of fluid

instabilities and gas-particle interactions. Further, the variation in the concentration of the particles results in very dilute to very dense, i.e., near packing limit, flow. The hydrodynamic instabilities and the particle dispersion determine the mixing and the combustion and are important to characterize the impact of the explosive on the environment. With an aim to accurately describe the post-detonation combustion processes numerical simulations are performed. However, numerical investigation of post-detonation flows poses certain unique challenges. These challenges must be systematically addressed to study and quantify mixing and combustion in these flows. The following essential features must be contained in the methodology chosen to investigate dense multi-phase post-detonation flows

(a) The primary blast wave and the ensuing flow must be captured and well resolved.

(b) The gas-particle interaction and the inter-particle interaction should be accounted.

(c) The gas-phase flux computation must include the effect of presence of particles in the flow.

(d) The method must be suited to solve for a wide range of particle volume fractions and particle sizes encountered in the post-detonation flow.

(e) The particle combustion modeling must include the kinetic and the diffusive burning regimes.

These features are implemented, verified and validated in this thesis using a combination of EE and EL methods. Due to its accuracy EL method has been preferred over EE method in many simulations involving complex gas-particle flows. However, in many scenarios, simulations using EL are unfeasible due to the number of particles in the flow. This is true even with a massively parallel EL solver as the particles initially form a localized dense cluster. To preserve accuracy and enable computation, a combined EE-EL approach is developed and employed to investigate post-detonation flows. In the novel combined approach, EE-DEM is coupled with EL-DEM and the particles transition from EE-DEM to EL-DEM based on the number of particles and the volume fraction of the particles in a given computational cell. The dispersed phase is thus computed efficiently in both dense

and dilute regions. Also, the overall strategy spans the dispersed phase volume fraction range from near packing limit to a rarefied flow. This methodology is established through extensive validation and is then used to investigate the post-detonation flow. The primary focus of the thesis is addressed by four objectives. The first and the second objectives form the verification and the validation part, and the last two objectives form the application part of this thesis. The objectives which describe the goals of this thesis are:

1. **Compare Eulerian-Eulerian and Eulerian-Lagrangian methods for dense granular flows**

   Merits and limitations of EE and EL methods for dense gas-particle flows are evaluated by implementing a massively parallel Lagrangian solver and an Eulerian dispersed phase solver for granular flows. Both the methods are verified and validated based on available theoretical and experimental data. The limits of EE and EL to study the post-detonation flow are also investigated by considering explosion of spherical nitromethane (NM) charges with steel particles. The particle volume fraction is varied from the dilute limit (≥ 0.01) to the dense limit (≤ 0.74). The flow features, in particular, the transmitted and the reflected shock waves, in each case where EE or EL is used, are analyzed and compared. Also, the particle dispersion is quantified and compared. These tests are performed with an aim to demarcate the particle volume fraction and particle size limits for EE and EL. Further, the best regimes, based on volume fraction and particle size, to use EE or EL are identified.

2. **Evaluate the combined EE-EL method for simulation of post-detonation flow with dense particle clouds**

   Dense post-detonation flow of a spherical explosive charge of initial radius $\mathcal{O}(1-10)$ cm comprising of particles of initial radius $\mathcal{O}(0.1-10)$ μm is challenging due the number of particles present in the flow. However, these size regimes are of practical interest and are investigated in this thesis using a combined EE and EL strategy (EE-EL). The combined approach is required to account for the number of particles in the flow and accurately transition from the dense limit to the dilute limit. EE-EL solver

is developed from the independent EE and EL solvers described in the first objective.

The combined solver is validated based on several post-detonation particle dispersal studies. The accuracy of particle dispersion is quantified as the solver transitions from pure EE approach to pure EL approach. The regimes of volume fraction valid for this transition are identified. For these validation cases, spherical heterogeneous NM charges with steel particles, initially uniformly distributed in the explosive, are considered.

3. **Investigate ambient particle dispersal in post-detonation flow**

   The impact of a given homogeneous explosive on ambient particle or droplet cloud dispersion is investigated. Here, the focus is on the role of hydrodynamic instabilities and their effect on the evaporation of the particles. Bacterial aerosol neutralization in post-detonation flows is also addressed. The droplet clouds are modeled to contain endospores embedded in them. The aerosol droplet model is validated based on experimental studies and extensive numerical studies. The initial distance of the droplet cloud from the initial charge is varied to obtain the optimal distance for effective neutralization. Apart from providing valuable threat reduction information, these studies are also aimed to show the efficacy of the EL solver under dilute conditions.

4. **Study and quantify the mixing and the combustion of reactive particles in dense post-detonation flows**

   With an aim to develop insights into the afterburn in the dense post-detonation flow with aluminum particles, combustion of aluminum particles in the post-detonation flow is studied by considering spherical nitromethane charges. The particles are initially arranged uniformly within the explosive. The aluminum particle combustion is simulated considering the hybrid kinetic-diffusive mass transfer model. The particle size is varied to span from the pure kinetic mass transfer limit to the pure diffusive limit. The volume fraction of the particles is also varied to span from the dilute to the dense limit. The role of hydrodynamic instabilities on particle combustion is addressed. Combustion in the post-detonation flow with aluminum particles is compared

with the afterburn in the flow with steel particles. Apart from aiding with the investigation of the post-detonation combustion, these studies also demonstrate the ability of the EE-EL approach to simulate explosive charges with micron size particles.

1.4 Thesis outline

This thesis is organized into 9 chapters. In Chapter 2, the governing equations for gas-phase, Lagrangian dispersed phase and the Eulerian dispersed phase are discussed. The equations of state, different closures and chemical kinetics are also discussed in Chapter 2. The numerical method employed to solve the governing equations is described in Chapter 3. Different test cases used to verify and validate the numerical strategy employed in this thesis are discussed in Chapter 4. EE and EL methods for dense post-detonation flows are compared in Chapter 5. In this chapter, explosive particle dispersal from charges packed with inert particles is also analyzed. The combined EE and EL solver is used to study the dense post-detonation flow in Chapter 6. The advantages of this method over pure EE and pure EL method are discussed here. In Chapter 7, dispersion of dilute particle clouds and evaporation of aerosol droplets in post-detonation flow are analyzed. In Chapter 8, combustion of aluminum particles in dense post-detonation flow is discussed. Also, in this chapter, afterburn in the post-detonation flows with aluminum particles is compared with the afterburn in the flow with steel particles. Finally, in Chapter 9, conclusions from the research conducted are discussed and possible future directions are suggested.

CHAPTER II

FORMULATION FOR NUMERICAL SIMULATION OF DENSE TWO-PHASE FLOWS

Numerical simulation of multi-phase systems is performed using a set of governing equations for each phase. While the gas-phase is modeled using an Eulerian approach, multiple complementary approaches are available to solve for the dispersed phase. The applicability of these approaches varies based on the relative particle size and the dispersed phase volume fraction as shown in Fig. 9. The approaches are broadly classified into 5 categories [10], based on the relative length and time scales of the dispersed phase, as described below:

1. **Dusty Gas Approach:** In this approach, the multi-phase mixture is considered as a single fluid whose density is dependent on the density of the local gases and the local mass of the particles. The advantage of this approach is that the solution can be obtained by solving for the mass of the particles along with the conservation of the mixture mass, the mixture momentum and the mixture energy. The single fluid approach assumes that the particles perfectly follow the local carrier phase and hence is applicable for very small particles or the particles with very small time constant.

2. **Equilibrium Eulerian Approach:** The simplicity of the dusty gas approach is retained in the equilibrium Eulerian approach but the particle velocity is allowed to be different from the surrounding gases. The particle velocity is obtained as a function of the local gas-phase velocity and Stokes number (St), i.e., the ratio of the particle time scale (τ_p) to the fluid time scale (τ_k) ($St = \tau_p/\tau_k$). Here, as in the dusty gas approach, the assumptions of the approach hold only for small particles whose motion is dependent only on the local flow. Since the particle motion is allowed to vary and does not follow the fluid perfectly, this approach allows preferential clustering of the particles and has been shown to provide accurate results for particles with $St \leq 0.2$ [10].

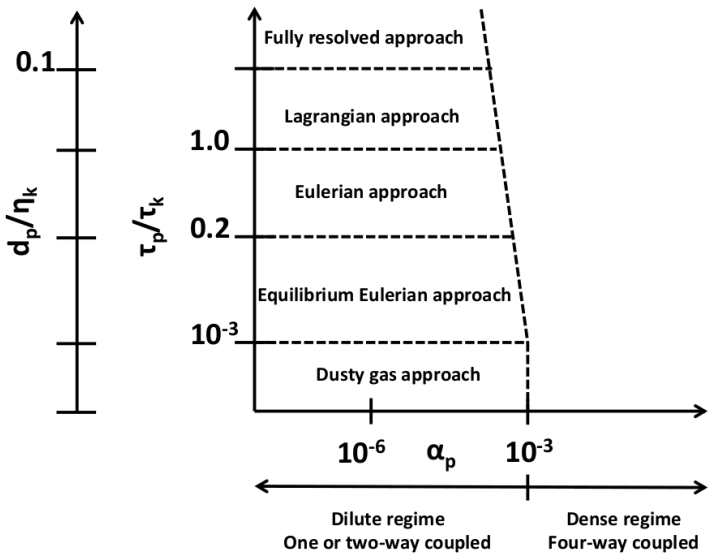

Figure 9: Different approaches for two-phase flows and thier applicability based on the length and the time scales [10]. d_p, η_k, τ_p and τ_k denote the particle diameter, the smallest resolved length scale, the particle time scale and the smallest resolved time scale, respectively.

3. **Eulerian Approach:** The Eulerian approach, also known as the two-fluid approach, considers the dispersed phase and the gas phase as inter-penetrating fluids and the solution is obtained by solving for the mass, the momentum and the energy of both the dispersed phase and the gas phase. The dispersed phase quantities are considered to be field variables and the interaction between the two phases is modeled using source or sink terms. The relaxation of the equilibrium assumption allows for this approach to be used in cases with relatively large particles or St as indicated in Fig. 9. Also, this approach is applicable in cases where the equilibrium assumption fails, such as shock-particle interaction. However, this method is relatively expensive than the equilibrium approaches. The method can be extended to dense flows by introducing appropriate corrections for the volume occupied by the particles and inter-particle collisional models [1], i.e., four-way coupling. In granular systems, i.e., in cases with the inter-particle collision and the inter-particle frictional forces are non-negligible, this approach has been a popular choice [33]. Although the two fluid approach is

relatively expensive for cases with a wide range of particle sizes, i.e., polydisperse systems, with an appropriate probability density function approach, the polydispersity can be modeled [77, 95].

4. **Lagrangian Approach:** Tracking of particles in the flow by solving for the position, the mass, the momentum and the energy of each particle is performed in the Lagrangian approach. Based on St and α_p, this approach has been used in one-, two- and four-way coupled systems. Since each particle is individually treated, this approach is very useful in polydisperse systems without any additional considerations. In the Eulerian approach, as the dispersed phase properties are field variables, the number of particles at a given location in the flow must be sufficient to form an ensemble average that represents the local dispersed phase properties. This imposes a limit of the minimum α_p, for the Eulerian approach. However, Lagrangian approach spans a wide range of α_p and is applicable to both the dilute and the dense flow regimes, simultaneously. It is important to note that the computational cost of the Lagrangian approach increases with increase in the number of particles in the flow, and the feasibility of the approach is limited by the available computational resources.

5. **Fully Resolved Approach:** When particle size (d_p) is comparable to the size of the smallest fully resolved scale (η_k) in the flow, the flow scales introduced by the particles are fully resolved. Unlike the Lagrangian and the Eulerian approaches, this approach does not assume the particles to be point-particles, i.e., the volume occupied by the particles is resolved. However, this is the most expensive of all the approaches and is only feasible to $\mathcal{O}(10^3)$ particles [10]. In foreseeable future, application of this method to solve four-way coupled systems with $\mathcal{O}(10^4)$ or more particles can be ruled out, especially for the cases considered in the current work. In these complex cases, finite size point-particle methods (with $d_p \lessapprox \eta_k$), both Eulerian and Lagrangian, are feasible and provide satisfactory results.

Given the assumptions and the applicability of the above approaches, primarily two approaches have been in use to model four-way coupled multiphase systems; Eulerian-Lagrangian (EL) [15, 52, 88] and Eulerian-Eulerian (EE) [1, 33, 57]. Different set of governing equations have been employed by past researchers for each method based on the assumptions and approximations considered. In this chapter, the governing equations employed in the current studies to solve for the gas-phase and the dispersed phase are described. The gas-phase properties are computed using an Eulerian approach by solving the three-dimensional Navier-Stokes equations for compressible, unsteady, reactive, multiphase flows. Equations of State (EOS) used for thermodynamic closure and the combustion model for the post-detonation afterburn are also discussed.

The dispersed phase is solved for using both Eulerian and Lagrangian approaches. The Eulerian dispersed phase employs the continuum assumption and the dispersed phase properties are obtained by solving the conservation equations for the mass, the momentum, the internal energy and the granular energy. When Lagrangian approach is used, each particle in the flow is tracked by solving for the position, the mass, the momentum and the energy of the particle. Here, both the Eulerian approach and the Lagrangian approach assume finite size point-particles. i.e., $d_p \lessapprox \eta_k$. Along with the governing equations for the Eulerian dispersed phase and the Lagrangian dispersed phase, the models employed to compute the dispersed phase mass transfer, the particle acceleration and the dispersed phase heat transfer are described in this chapter. The set of equations for the inter-phase mass, momentum and heat transfer are also outlined. Note that the EE-EL method, which combines the individual EE and EL methods, uses the governing equations for Lagrangian dispersed phase and Eulerian dispersed phase simultaneously.

The sections below are organized as follows. The gas-phase governing equations, the gas-phase thermodynamic closures and the combustion modeling are discussed first. This is followed by the description of the Eulerian dispersed phase governing equations and the dispersed phase thermodynamic closures. Finally, the Lagrangian dispersed phase equations are presented along with the inter-phase coupling terms.

2.1 Gas-phase

2.1.1 Governing equations

The gas-phase governing equations for the conservation of mass, momentum, energy and species, respectively, are [1, 15, 33, 57]:

$$\frac{\partial \alpha_g \, \rho_g}{\partial t} + \frac{\partial \alpha_g \, \rho_g u_{g,i}}{\partial x_i} = \dot{\rho}_D, \tag{1}$$

$$\frac{\partial \alpha_g \, \rho_g u_{g,i}}{\partial t} + \frac{\partial}{\partial x_j}[\alpha_g \, \rho_g u_{g,i} u_{g,j} + \alpha_g \, p_g \delta_{ij} - \alpha_g \, \tau_{g,ij}] = p_g \frac{\partial \alpha_g}{\partial x_j}\delta_{ij} + \dot{F}_{D,i}, \tag{2}$$

$$\begin{aligned}\frac{\partial \alpha_g \, \rho_g E_g}{\partial t} + \frac{\partial}{\partial x_j}[\alpha_g \, \rho_g u_{g,j} E_g + u_{g,j}\alpha_g \, p_g + \alpha_g \, q_{g,j} - u_{g,i}\alpha_g \, \tau_{g,ji}] \\ = -p_g \bar{u}_{d,j}\frac{\partial \alpha_d}{\partial x_j} - p_g \bar{u}_{p,j}\frac{\partial \alpha_p}{\partial x_j} + \dot{Q}_D + \dot{W}_D + \phi,\end{aligned} \tag{3}$$

$$\frac{\partial \alpha_g \, \rho_g Y_{g,k}}{\partial t} + \frac{\partial}{\partial x_i}[\alpha_g \, \rho_g (Y_{g,k} u_{g,i} + Y_{g,k} V_{g,i,k})] = \alpha_g \dot{\omega}_{g,k} + \dot{S}_{D,k}, \tag{4}$$

where ρ_g is the gas-phase density, p_g is the gas-phase pressure, $u_{g,i}$ is the $i-th$ component of gas-phase velocity, E_g is the total specific energy of the gas-phase obtained as the sum of internal (e_g) and kinetic energies ($\frac{1}{2}u_{g,i}u_{g,i}$), α_g is the volume fraction of the gas-phase, Y_k is the mass fraction of the $k-th$ species and δ_{ij} is the Kronecker delta. The internal energy is computed as the sum of contributions from all species and is expressed as:

$$e_g = \sum_{1}^{N_s} Y_{g,k} e_{g,k}, \tag{5}$$

where N_s is the total number of species in the flow and $e_{g,k}$ is the internal energy of $k-th$ species. Assuming Newtonian fluid, the gas-phase stress tensor, $\tau_{g,ij}$, is obtained as

$$\tau_{g,ij} = \mu_g \left(\frac{\partial u_{g,i}}{\partial x_j} + \frac{\partial u_{g,j}}{\partial x_i}\right) + \lambda_g \frac{\partial u_{g,k}}{\partial x_k} \delta_{ij}, \tag{6}$$

where μ_g is the viscosity coefficient of the gas, assumed to be a function of the gas temperature (T_g) only and is obtained from the Sutherland's law as:

$$\mu_g = \mu_0 \left(\frac{T_g}{T_0}\right)^{3/2} \frac{T_0 + S}{T_g + S}. \tag{7}$$

Here, S is the Sutherland's constant, μ_0 is the reference viscosity and T_0 are the reference temperature. The bulk viscosity, λ_g [120], following Stokes' hypothesis, is assumed to be related to μ_g as $\lambda_g = -2/3\,\mu_g$. Note that the viscous terms are dominant in the later stages of the post-detonation flow [18]. Since the temperature and the pressure at this later times are in 250 K - 3000 K and 1.0 KPa - 10 MPa range, the assumptions involved in computing the viscous terms are valid. The heat flux vector, $q_{g,j}$, obtained using Fourier's law of thermal conduction, is summarized as:

$$q_{g,j} = -\kappa_g \frac{\partial T_g}{\partial x_j} + \rho_g \sum_{1}^{N_s} Y_{g,k} h_{g,k} V_{g,j,k}, \tag{8}$$

where $h_{g,k}$ denotes the specific enthalpy of the k-th species and κ_g is the thermal conductivity of the gas. κ_g is assumed to be a function of T_g and is computed using the Prandtl number (Pr) as

$$\kappa_g = \frac{C_{p,g}\mu_g}{Pr}, \tag{9}$$

where $C_{p,g}$ is the specific heat at constant pressure for the gas-phase. Pr is assumed to be 0.72 in all the studies discussed here. The species diffusion velocities, $V_{g,j,k}$, are modeled assuming Fickian diffusion, and obtained as:

$$V_{g,j,k} = -\frac{D_{g,k}}{Y_{g,k}} \frac{W_k}{\overline{W}} \frac{\partial X_{g,k}}{\partial x_j}. \tag{10}$$

Here, $D_{g,k}$ is the diffusion coefficient, W_k is the molecular weight, and X_k is the mole fraction of the $k-th$ species. Also, $\overline{W}$ is the mean molecular weight. $D_{g,k}$ depends on species k, and is obtained from a constant Lewis number (Le) assumption.

2.1.2 Non-conservative terms

In Eqns. 2 and 3, the terms $p_g \frac{\partial \alpha_g}{\partial x_j}$, $p_g \bar{u}_{d,j} \frac{\partial \alpha_d}{\partial x_j}$, and $p_g \bar{u}_{p,j} \frac{\partial \alpha_p}{\partial x_j}$ are in non-conservative form and are generally termed as "non-conservative terms". These terms which comprise of the

gradient of the volume fraction are important for dense multi-phase flows and are dominant at the multiphase interface where the gradient effect is dominant. Further, these terms are analogous to the equations that govern the flow in a variable area nozzle and are thus also referred to as "nozzling terms" [1, 19].

Baer and Nunziato [8] have first identified these terms and later many researchers have noted their relevance for granular flows [19, 33]. These terms can be obtained by combining the gas-phase pressure gradient ($\frac{\partial p_g}{\partial x_j}$) with the effect of pressure gradient on the dispersed phase ($(\alpha_d + \alpha_p)\frac{\partial p_g}{\partial x_j}$) as follows:

$$\begin{aligned} -\frac{\partial p_g}{\partial x_j} + (\alpha_d + \alpha_p)\frac{\partial p_g}{\partial x_j} &= -(1 - \alpha_d - \alpha_p)\frac{\partial p_g}{\partial x_j}, \\ &= -\alpha_g \frac{\partial p_g}{\partial x_j}, \\ &= -\frac{\partial \alpha_g p_g}{\partial x_j} + p_g \frac{\partial \alpha_g}{\partial x_j}. \end{aligned} \tag{11}$$

Similarly, the terms in the energy equation (Eq. 3) are obtained by combining the pressure gradient effect ($\frac{\partial u_{g,j} p_g}{\partial x_j}$) and the work done by the pressure gradient on the dispersed phase ($\alpha_d u_{d,j}\frac{\partial p_g}{\partial x_j} + \alpha_p u_{p,j}\frac{\partial p_g}{\partial x_j}$) as

$$\begin{aligned} -\frac{\partial p_g u_{g,j}}{\partial x_j} + (\alpha_d u_{d,j} + \alpha_p u_{p,j})\frac{\partial p_g}{\partial x_j} &= -\frac{\partial}{\partial x_j}\left[(\alpha_g + \alpha_d + \alpha_p) u_{g,j} p_g\right] + (\alpha_d u_{d,j} + \alpha_p u_{p,j})\frac{\partial p_g}{\partial x_j}, \\ &= -\frac{\partial(\alpha_g u_{g,j} p_g)}{\partial x_j} - \frac{\partial(\alpha_d u_{g,j} p_g)}{\partial x_j} - \frac{\partial(\alpha_p u_{g,j} p_g)}{\partial x_j} \\ &\quad + \alpha_d u_{d,j}\frac{\partial p_g}{\partial x_j} + \alpha_p u_{p,j}\frac{\partial p_g}{\partial x_j}, \\ &\approx -\frac{\partial(\alpha_g u_{g,j} p_g)}{\partial x_j} - \bar{u}_{d,j}\frac{\partial(\alpha_d p_g)}{\partial x_j} - \bar{u}_{p,j}\frac{\partial(\alpha_p p_g)}{\partial x_j} \\ &\quad + \alpha_d \bar{u}_{d,j}\frac{\partial p_g}{\partial x_j} + \alpha_p \bar{u}_{p,j}\frac{\partial p_g}{\partial x_j}, \\ &= -\frac{\partial(\alpha_g u_{g,j} p_g)}{\partial x_j} - p_g \bar{u}_{d,j}\frac{\partial \alpha_d}{\partial x_j} - p_g \bar{u}_{p,j}\frac{\partial \alpha_p}{\partial x_j}. \end{aligned} \tag{12}$$

In the above equation, the value of the gas-phase velocity at the material interfaces are assumed to be the mean dispersed phase velocities at the interface ($\bar{u}_{d,j}$ and $\bar{u}_{p,j}$) [19]. Equations (11) and (12) can also be derived by multiplying the momentum and the energy

equations with α_g and combining with the continuity equation [1, 19]. Note that, if a common interface velocity ($\bar{u}_i$) is assumed, the final form of Eqn. (12) can be written as $-\frac{\partial(\alpha_g u_{g,j} p_g)}{\partial x_j} + p_g \bar{u}_j \frac{\partial \alpha_g}{\partial x_j}$, which is consistent with the term derived by earlier researchers for pure EL [19] or pure EE formulations [1]. However, the second approach to the derivation does not clearly indicate the inclusion of the source terms due to pressure gradient effect to obtain the non-conservative terms. Note that, since the source terms due to the pressure gradient are already added in the gas-phase governing equations, they are not included in the inter-phase coupling terms discussed later. The non-conservative terms in Eqns. 2 and 3 need closure and are determined by the velocities ($\bar{u}_{d,i}$ and $\bar{u}_{p,i}$) and pressures at the material interface. The solution procedure for the gas-phase equations that includes these terms is discussed in detail in the next chapter.

2.1.3 Equations of state

The relation between the thermodynamic variables, p_g, ρ_g, e_g and T_g, for the gas phase is expressed using an equation of state appropriate for the flow conditions. Several EOS have been used by past researchers and the choice is based on the range of the thermodynamic variables considered. The choice of the equation of state determines the speed of sound in the gas (c_g). With chemical composition of the gas phase frozen at a given instant, the gas phase pressure can be represented as a function of ρ_g and e_g, i.e., $p_g = p_g(\rho_g, e_g)$ and hence c_g can be obtained as:

$$c_g^2 = \left(\frac{\partial p_g}{\partial \rho_g}\right)_{e_g} + \frac{p_g}{\rho_g^2}\left(\frac{\partial p_g}{\partial e_g}\right)_{\rho_g}. \tag{13}$$

Since a wide of pressures, temperatures and densities are encountered in different flow configurations under consideration in the current investigations, different EOS are used, each suited to a particular flow. In rest of this section, EOS employed are summarized along with the respective speeds of sound and the relations for specific heats.

2.1.3.1 Perfect gas equation of state

The perfect gas equation of state is expressed as

$$p_g = \rho_g R_g T_g, \tag{14}$$

where R_g is the gas constant and for a mixture of gases is obtained as

$$R_g = R_u \sum_{k=1}^{N_s} \frac{Y_{g,k}}{W_k}. \tag{15}$$

Here, R_u is the universal gas constant. In case of a perfect gas, the internal energy is a function of only T_g. Thus, the specific heat at constant volume $C_{v,g}$ is also a function of only T_g. The specific heat of the gas at constant pressure is given as

$$C_{p,g}(T_g) = C_{v,g}(T_g) + R_g. \tag{16}$$

From this, the ratio of specific heats, $\gamma = C_{p,g}/C_{v,g}$, can be expressed as a function of T_g. Further, based on the specific heats at constant volume ($C_{v,g,k}$) and constant pressure ($C_{p,g,k}$) for a given $k-th$ species, the sensible energy and the sensible enthalpy of $k-th$ species, respectively, are

$$e_{g,k} = e^0_{g,k} + \int_{T_0}^{T_g} C_{v,g,k}(T^\dagger) dT^\dagger, \tag{17}$$

$$h_{g,k} = h^0_{g,k} + \int_{T_0}^{T_g} C_{p,g,k}(T^\dagger) dT^\dagger, \tag{18}$$

where $e^0_{g,k}$ and $h^0_{g,k}$ are the reference energy and the reference enthalpy for $k-th$ species evaluated at a reference temperature. $C_{p,g}$ and $C_{v,g}$ are related to $C_{p,g,k}$ and $C_{v,g,k}$ as

$$C_{p,g} = \sum_{k=1}^{N_s} Y_{g,k} C_{p,g,k} \tag{19}$$

$$C_{v,g} = \sum_{k=1}^{N_s} Y_{g,k} C_{v,g,k} \tag{20}$$

For a perfect gas, since e_g is a function of only T_g, the speed of sound is expressed as

$$c_g = \left(\frac{\gamma p_g}{\rho_g} \right)^{1/2}. \tag{21}$$

When the temperature or the variation in temperature is low such that the degrees of freedom of the molecules of the gas do not change, the specific heat ratio, γ, is a constant, and the gas is calorically perfect. However, if the temperature variations are higher, the specific heats are computed as a function of temperature and can be obtained from polynomial curve-fits for various species [79]. The temperature of the gas is obtained from the internal energy or the enthalpy using iterative methods in cases with polynomial curve-fits for specific heats (thermally perfect gas). Note that the thermally perfect gas assumption is applicable to the post-detonation flow at later times, i.e., after the blast wave attenuates and results in a mixing/combustion dominated flow. Also, during the initial stages, perfect gas assumption is valid in regions behind the blast where the expansion processes dominate.

2.1.3.2 JWL equation of state

The perfect gas equation of state is not ideal to predict the flow behavior in the post-detonation flow in the vicinity of the blast wave and the secondary shock. Due to the high pressures and densities in these regions of the post-detonation flow, the internal energy is dependent on both the pressure and the density, and this is modeled by employing a real gas equation of state. One such equation of state routinely used for explosive modeling is Jones-Wilkins-Lee (JWL) equation of state and is expressed as [133]

$$p_g = A\left(1 - \frac{\omega\rho_g}{R_1\rho_0}\right)\exp\left(\frac{-R_1\rho_0}{\rho_g}\right) + B\left(1 - \frac{\omega\rho_g}{R_2\rho_0}\right)\exp\left(\frac{-R_2\rho_0}{\rho_g}\right) + \omega\rho_g(e_g - e_0), \quad (22)$$

where the constants ω, ρ_0, A, B, R_1, R_2 and e_0 are dependent on the explosive used. These constants for several explosives are listed elsewhere [133]. With the assumption that $C_{v,g}$ is constant, JWL equation of state can be further simplified and expressed as

$$p_g = A\exp\left(\frac{-R_1\rho_0}{\rho_g}\right) + B\exp\left(\frac{-R_2\rho_0}{\rho_g}\right) + \omega\rho_g C_{v,g}T_g. \quad (23)$$

This format of JWL equation of state with constant $C_{v,g}$ is routinely used for explosive modeling. Note that the different terms in the JWL equation of state are important to model different density regimes in the flow and at low densities the equation asymptotes to

the perfect gas equation of state. Evaluating the pressure derivatives, the speed of sound in the flow for JWL equation of state is

$$c_g = \Bigg[A \left(-\frac{\omega}{R_1\rho_0} + \frac{R_1\rho_0}{\rho_g^2} - \frac{\omega^2}{R_1\rho_0} \right) \exp\left(-\frac{R_1\rho_0}{\rho_g} \right) \tag{24}$$

$$+ B \left(-\frac{\omega}{R_2\rho_0} + \frac{R_2\rho_0}{\rho_g^2} - \frac{\omega^2}{R_2\rho_0} \right) \exp\left(-\frac{R_2\rho_0}{\rho_g} \right) \tag{25}$$

$$+ \omega(1+\omega)e_g \Bigg]^{1/2} \tag{26}$$

2.1.3.3 Noble-Abel equation of state

Apart from the JWL equation of state, Noble-Abel equation of state is also a popular choice to simulate explosions [16, 133] and is given as

$$p_g = \frac{\rho_g R_g T_g}{1 - A_{AN}\rho_g}, \tag{27}$$

where A_{NA} is a constant and is set such that $1 - A_{NA}\rho_g$ is always positive. Further, specific value of A_{NA} for a given explosive is determined based on the blast overpressure values available from the literature. When Noble-Abel equation of state is used the specific heats can be varied as a function of temperature (T_g). The values of specific heats, obtained from the polynomial cure-fits, are available for a wider range of species in comparision to equation of states (such as JWL) designed to a specific explosive. The speed of sound for Noble-Abel equation of state is

$$c_g = \frac{\sqrt{\gamma R_g T_g}}{1 - A_{NA}\rho_g}. \tag{28}$$

2.1.4 Combustion modeling

Based on the past studies [18, 53, 68], the combustion processes in the post-detonation flow are assumed to be mixing-controlled rather than chemically-controlled. Thus, the chemical source term, $\dot{\omega}_{g,k}$, is computed based on the concentrations of the fuel and the oxidizer in the flow. At each time step, the concentration of the fuel is compared within a computational cell to determine if the mixture is fuel lean or fuel rich. All the fuel is instantaneously

consumed, if the mixture is fuel lean, and the amount of the oxidizer required is determined based on the following chemical reactions described below. If the mixture is fuel rich, the oxidizer is completely consumed and the amount of fuel needed is determined based on the stoichiometry.

For simulations with homogeneous NM charges, a two step mechanism is used and the chemical equations are:

$$\begin{aligned} &(1) \quad CO + \tfrac{1}{2}O_2 \rightarrow CO_2, \\ &(2) \quad H_2 + \tfrac{1}{2}O_2 \rightarrow H_2O. \end{aligned} \tag{29}$$

For simulations with aluminum particles, the chemical equations for aluminum combustion are added to the above reactions and a 6 step mechanism [15, 50] is used. The mechanism has 'aerobic' and 'anaerobic' reactions which are based on the choice of the oxidizer used, i.e., O_2 (for aerobic) or H_2O and CO_2 (for anaerobic). The mechanism is given as

$$\begin{aligned} &(1) \quad CO + \tfrac{1}{2}O_2 \rightarrow CO_2, \\ &(2) \quad H_2 + \tfrac{1}{2}O_2 \rightarrow H_2O, \\ &(3) \quad Al + \tfrac{1}{2}O_2 \rightarrow AlO \qquad if\ T_g > 3500K, \\ &(4) \quad Al + \tfrac{3}{4}O_2 \rightarrow \tfrac{1}{2}Al_2O_3(L) \qquad if\ T_g \leq 3500K, \\ &(5) \quad Al + H_2O \rightarrow AlO + H_2, \\ &(6) \quad Al + CO_2 \rightarrow AlO + CO. \end{aligned} \tag{30}$$

Note that, here, reactions (3) and (4) are the 'aerobic' reactions, and reactions (5) and (6) are the 'anaerobic' reactions.

2.2 Eulerian dispersed phase

2.2.1 Governing equations

In post-detonation flows, both the dense and the dilute regimes are present. In dense flows, apart from the inter-phase interactions (two-way coupling), particles are affected by the collisions/contact with the neighboring particles (four-way coupling). Gas-particle flows

dominated by inter-particle forces (collisional force, friction and inter-particle stress) are termed as *granular* flows. In the problems of current interest, the flow is granular in the initial stages and transitions to a dilute flow at later times. Assuming that the particles are finite-sized point-particles, the governing equations for the conservation of the volume fraction, the mass, the momentum, the internal energy, the granular energy and the particle number density, respectively, for the Eulerian dispersed phase are [33]:

$$\frac{\partial \alpha_d}{\partial t} + \bar{u}_{d,i}\frac{\partial \alpha_d}{\partial x_i} = 0, \tag{31}$$

$$\frac{\partial \alpha_d\, \rho_d}{\partial t} + \frac{\partial \alpha_d\, \rho_d u_{d,i}}{\partial x_i} = -\dot{\rho}_d, \tag{32}$$

$$\frac{\partial \alpha_d\, \rho_d u_{d,i}}{\partial t} + \frac{\partial}{\partial x_j}[\alpha_d\, \rho_d u_{d,i} u_{d,j} - \alpha_d\, \tau_{d,ij}] = -\alpha_d \frac{\partial p_g}{\partial x_j}\delta_{ij} - \frac{\partial p_d}{\partial x_j}\delta_{ij} - \frac{\partial p_f}{\partial x_j}\delta_{ij} - \dot{F}_{d,i}, \tag{33}$$

$$\frac{\partial \alpha_d\, \rho_d e_d}{\partial t} + \frac{\partial}{\partial x_j}[\alpha_d\, \rho_d u_{d,j} e_d] = -\dot{Q}_d - \bar{e}_d\dot{\rho}_d + \dot{\gamma}, \tag{34}$$

$$\frac{\partial \alpha_d\, \rho_d E_s}{\partial t} + \frac{\partial}{\partial x_j}[\alpha_d\, \rho_d u_{d,j} E_s] = -p_d\frac{\partial u_{d,j}}{\partial x_j} + \alpha_d \tau_{d,ij}\frac{\partial u_{d,i}}{\partial x_j} + \frac{\partial}{\partial x_j}\alpha_d\lambda_d\frac{\partial \Theta}{\partial x_j} - \phi - \dot{\gamma} - \bar{E}_s\dot{\rho}_d, \tag{35}$$

$$\frac{\partial N_d}{\partial t} + \frac{\partial N_d u_{d,i}}{\partial x_i} = -\dot{N}_d. \tag{36}$$

In the above equations, ρ_d is the dispersed phase density, p_d is the granular pressure, $u_{d,i}$ is the $i-th$ component of the dispersed phase velocity, e_d is the internal energy of the dispersed phase, α_d is the volume fraction of the dispersed phase, and N_d is the Eulerian dispersed phase particle number density. E_s is the granular energy and is related to the granular random kinetic energy (Θ) as $E_s = 1.5\Theta$. $\bar{E}_s$ and $\bar{e}_d$ are the granular energy and the internal energy associated with the mass transfer, respectively. $\bar{u}_i$ is the interface velocity

computed as the average of the velocity of the dispersed phase in the computational cell. p_f is the inter-granular frictional pressure and is given by empirical expressions based on the close packing fraction, α_{cs}, and the maximum packing fraction α_{ms}. The expression for p_f used in each case is dependent on the nature of the flow being considered [8, 15, 17, 52, 57].

The granular stress, $\tau_{ij,d}$ is given as

$$\tau_{d,ij} = \mu_d \left(\frac{\partial u_{d,i}}{\partial x_j} + \frac{\partial u_{d,j}}{\partial x_i} \right) - \left(\xi_d + \frac{2}{3}\mu_d \right) \frac{\partial u_{d,k}}{\partial x_k} \delta_{ij}, \tag{37}$$

where μ_d is the granular shear viscosity and ξ_d is the granular bulk viscosity and are given as

$$\mu_d = \rho_d d_p \left(\frac{\Theta}{\pi} \right)^{1/2} [f_{coll}(\alpha_d) + f_{kin}(\alpha_d)] + \frac{p_f}{\alpha_d + \zeta} sin\psi, \tag{38}$$

$$\xi_d = \frac{4}{3}\rho_d d_p \left(\frac{\Theta}{\pi} \right)^{1/2} g_0(1+\epsilon), \tag{39}$$

where d_p is the diameter of the particle, ζ is a small number to avoid division by zero, ψ is the angle of internal friction set as $\pi/6$ [57], ϵ is the coefficient of restitution and g_0 is the radial distribution function given as [46]

$$\frac{1}{g_0} = 1 - \left(\frac{\alpha_d}{\alpha_{ms}} \right)^{\frac{1}{3}}. \tag{40}$$

The diameter of the particle is determined using N_d and α_d as

$$d_p = \left(\frac{6\alpha_d}{\pi N_d} \right)^{1/3}. \tag{41}$$

In the current Eulerian dispersed phase formulation, the particles are mono-disperse within each computational cell and the particle size changes based on the dispersed phase volume fraction and the number density. Note that the dispersed phase viscosity for granular material (in Eqn. (38)) is given as a summation of the collisional ($f_{coll}(\alpha_d)$), the kinetic ($f_{kin}(\alpha_d)$) and the frictional components. $f_{coll}(\alpha_d)$ and $f_{kin}(\alpha_d)$ are given as [57]

$$f_{coll}(\alpha_d) = \frac{4}{5}\alpha_d g_0(1+\epsilon), \tag{42}$$

$$f_{kin}(\alpha_d) = \frac{\pi}{6(3-\epsilon)}\left[1 + \frac{2}{5}(3\epsilon - 1)(1+\epsilon)\alpha_d g_0\right]. \tag{43}$$

The thermal conductivity of the dispersed phase (granular material) is expressed as [33, 57]

$$\lambda_d = \rho_d d_p \left(\frac{\Theta}{\pi}\right)^{1/2} f_\lambda, \tag{44}$$

where f_λ is given as [57]

$$f_\lambda(\alpha_d) = \frac{15\pi}{4(41-33\eta)}\left[1 + \frac{12}{5}(4\eta - 3)\eta^2\alpha_d g_0 + \frac{16}{15\pi}(41 - 33\eta)\eta\alpha_d g_0\right], \tag{45}$$

where $\eta = (1+\epsilon)/2$. The dissipation of the granular energy due to particle collisions, $\dot{\gamma}$, and the dissipation due to viscous damping, ϕ, are expressed as [57]

$$\dot{\gamma} = 6(1-\epsilon^2)g_0\alpha_d^2\rho_d\frac{\Theta}{r_d}\sqrt{\frac{\Theta}{\pi}}, \tag{46}$$

$$\phi = \frac{9\alpha_d C_D \rho_g ||u_{g,i} - u_{d,i}|\Theta}{8r_d} + \frac{81\alpha_d\mu_g^2}{8g_0 r_d^3\rho_d\sqrt{\pi\Theta}}|u_{g,i} - u_{d,i}|^2. \tag{47}$$

Note that the dissipated granular energy due to collisions ($\dot{\gamma}$) acts as a sink/source to the internal energy of the dispersed phase where as the dissipation due to the viscous damping (ϕ) provides an energy sink/source to the gas-phase.

2.2.2 Equation of state

The thermodynamic variables for the dispersed phase are related by expressing the dispersed phase pressure as a function of ρ_d and e_d. In many cases, the equation of state has a form similar to the one discussed for the gas-phase. The equation of state widely used to model the Eulerian dispersed phase is stiffened gas equation of state and is given as

$$p_d = (\gamma_d - 1)\rho_d e_d - \gamma_d\pi_d, \tag{48}$$

where γ_d and π_d are constants based on the dispersed phase material. Note that, the stiffened gas equation of state is used only when Eqns. (34) and (36) are replaced with

the conservation equation for total energy of the dispersed phase [1]. For granular flows, considered in the current studies, however, the solid pressure, p_d, is related to the granular temperature, the solid density and the solid phase volume fraction and is given as is given as [46]

$$p_d = \rho_d \Theta \alpha_d [1 + 2(1+\epsilon)\alpha_d g_0]. \tag{49}$$

The internal energy of the dispersed phase is related to the dispersed phase temperature with a constant specific heat assumption. Due to the dense packing of the solid particles, the collisions and the contact between the particles result in frictional pressure (p_f). The frictional pressure is computed based on the packing fraction of the particles in the flow, and for $\alpha_d > \alpha_{cr}$, p_f (in Pa) is given as [57]

$$p_f = 0.1\alpha_d \frac{(\alpha_d - \alpha_{cr})^2}{(\alpha_{max} - \alpha_d)^5}, \tag{50}$$

where $\alpha_{max} = 0.74$ is the maximum packing limit and α_{cr} is set to 0.5. Another expression for p_f is also widely used [52] and is given as

$$p_f = \frac{P_s \alpha_d^{\beta}}{\alpha_{cs} - \alpha_d}. \tag{51}$$

Here, P_s and β are model constants and α_{cs} for close packing is set to 0.9 [19]. The total dispersed phase pressure, p_{tot}, is computed as the sum of p_d and p_f. The wave speed in the granular dispersed phase, also called as the granular compaction wave speed, is non-zero in regions with non-zero p_d and p_f. This wave speed is computed as [57]

$$c_d^2 = \frac{1}{\rho_d}\left[\left.\frac{\partial p_d}{\partial \alpha_d}\right|_{\Theta} + \frac{2\Theta}{3\rho_d \alpha_d^2}\left(\left.\frac{\partial p_d}{\partial \Theta}\right|_{\alpha_d}\right)^2 + \left.\frac{\partial p_f}{\partial \alpha_d}\right|_{\Theta}\right]. \tag{52}$$

2.3 Lagrangian dispersed phase

2.3.1 Governing equations

The equations to solve for the position, the mass, the momentum and the energy of a given particle (assumed to be finite-sized point particle with upper limit of $d_p \approx \eta_k$), respectively,

using Lagrangian approach are [53, 78]:

$$\frac{dx_{p,i}}{dt} = u_{p,i}, \tag{53}$$

$$\frac{dm_p}{dt} = -\dot{m}_p = -\frac{d}{dt}\left(\frac{4}{3}\pi r_p^3\right), \tag{54}$$

$$\begin{aligned} m_p\frac{du_{p,i}}{dt} &= \frac{\pi}{2}{r_p}^2 C_D \rho_g |u_{g,i} - u_{p,i}| \left(u_{g,i} - u_{p,i}\right) - \frac{4}{3}\pi {r_p}^3 \frac{\partial p_g}{\partial x_i} \\ &+ \frac{4}{3}\pi r_p^3 C_A \left(\frac{D(\rho_g u_{g,i})}{Dt} - \frac{d(\rho_g u_{p,i})}{dt}\right) + m_p A_{c,i}, \end{aligned} \tag{55}$$

$$m_p C_p \frac{dT_p}{dt} = 2\pi r_p \kappa_g Nu \left(T_g - T_p\right) - \dot{m}_p L_v + 4\pi {r_p}^2 \epsilon\sigma \left({T_g}^4 - {T_p}^4\right). \tag{56}$$

Here, $x_{p,i}$ is the particle position vector, $u_{p,i}$ is the particle velocity vector, m_p is the mass of the particle, r_p is the radius of the particle and T_p is the temperature of the particle. L_v is the latent heat of vaporization, C_p is the specific heat of the particle, ϵ is the emissivity, and σ is the Stefan-Boltzman constant. The force acting on each particle is computed as sum of forces due to quasi-steady drag, added mass effect, pressure gradient, and inter-particle collision and contact [78]. The acceleration due inter-particle interactions, $A_{c,i}$, is computed as [93]

$$A_{c,i} = -\frac{1}{\alpha_p \rho_p}\frac{\partial p_f}{\partial x_i}. \tag{57}$$

Note that the inter-particle acceleration is dependent on the collisions/contact between the particles and is determined by the friction/stress (p_f) between the particles.

To determine the variation of the internal temperature of a given particle, the ratio of the convective heat transfer to the particle and the thermal conduction within the particle is considered. This ratio, called the particle Biot number, Bi, is defined as

$$Bi = \frac{h d_p}{\kappa_p}, \tag{58}$$

where h is the convective heat transfer coefficient, d_p is the particle diameter and κ_p is the material thermal conductivity. If Bi is small, i.e., < 0.1, it is valid to assume that the temperature is uniform within the particle. This limit on Bi and the uniform temperature assumption is valid for small particles and when material thermal conductivity is infinitely large. Since the particle size is in the order of micron and the thermal conductivity of the materials considered is large in comparison to the h, the particle temperature is assumed to be uniform.

The temperature of each particle is computed based on the heat transfer between the gas and the particle via convection. In current studies, the convection is considered to be the dominant effect determining the particle temperature and the effect of the radiation is neglected [14]. The Nusselt number, Nu, the drag coefficient, C_D, and the coefficient for the added-mass effect, C_A, are expressed as empirical functions of Reynolds number (Re), Prandtl number (Pr), Mach number(M) and α_g [15, 30, 52]. The expressions for Nu, C_D, and C_A used in each case is provided for each case in the following chapters. Also, the detailed expressions for C_D, Nu and C_A are provided in Appendix A. Note that in some cases, tracking all the particles in the flow is not feasible and the particles are tracked in a group, called parcel [52]. A parcel is a group of particles and all the particles in the group are considered to have same properties. The solution for one representative particle from the group is obtained and all particles in the group (or parcel) are updated to have same properties. The number of particles in each parcel is set based on the total number of particles in the domain and the computational resources available.

The relation between the volume fractions of the gas-phase, the Eulerian dispersed phase and the Lagrangian dispersed phase is

$$\alpha_g = 1.0 - \alpha_p - \alpha_d, \tag{59}$$

where α_p, the volume fraction of the Lagrangian dispersed phase, is computed as

$$\alpha_p = \frac{1}{Vol} \sum_{n=1}^{N} n_{p,n} \left[\frac{4}{3} \pi {r^3}_{p,n} \right], \tag{60}$$

where Vol is the volume of the computational cell, n_p number of particles in each particle group (referred to as a parcel) and N is the total number of parcels in the computational cell. α_d can be obtained from Eqn. (31). However, for granular flows, the particle density is nearly constant and α_d is obtained from Eqn. (32) and Eqn. (31) is neglected.

2.3.2 Mass transfer

The heat transfer to the particles, based on the properties of the material, results in the evaporation, melting and/or pyrolysis of the particles. Thus, mass is transferred from the dispersed phase to the gas-phase. The rate of mass transfer is governed by Eqn. (54). For liquid droplets, the rate of mass transfer is given as [2]

$$\dot{m_p} = 2\pi\rho_g D_g r_p Sh \ln(1 + B_M), \tag{61}$$

where D_g is the diffusivity of the gas, Sh is the Sherwood number and B_M is the Spalding mass transfer number [2, 30].

In the current studies, along with the evaporation of water droplets, combustion of aluminum particles in the post-detonation flow is also considered. The mass transfer for aluminum particles, based on the flow and the particle properties, is limited by the reaction kinetics or diffusion of species. The diffusion-limited mass transfer is dependent on the concentration of the oxidizer where as the kinetic-limited mass transfer is dependent on the rate of reactions at the particle surface [130]. The net mass transfer for aluminum particles is thus defined as [130]

$$\frac{1}{\dot{m_p}} = \frac{1}{\dot{m_D}} + \frac{1}{\dot{m_K}}, \tag{62}$$

where $\dot{m_D}$ and $\dot{m_K}$ are the diffusion-limited mass transfer and the kinetic-limited mass transfer, respectively, and are obtained as [12, 130]

$$\dot{m_D} = \frac{4\pi\rho_p r_p^3}{\tau_b}(1 + 0.276 Re^{1/2} Pr^{1/3}), \tag{63}$$

$$\dot{m_K} = 4\pi r_p^2 Z \exp\left(\frac{-Ea_p}{T_p}\right), \tag{64}$$

where Z is the pre-exponential factor, and Ea_p is the activation energy for mass transfer and are set based on experimental observations [24, 130]. Here, the kinetic-limited rate for mass transfer is based on the reaction rates observed for detonations in aluminum-oxidizer mixtures and in the post-detonation flows with aluminum-oxidizer mixtures [24]. The particle burn time τ_b is determined by the oxidizer concentration and the particle size. Several correlations to determine τ_b based on the ratio of the particle surface area and the oxidizer concentration exist [24, 130]. In the current studies, the relation obtained for detonation in aluminum-oxidizer mixtures is used and is given as [24]

$$\tau_b = \frac{K d_{p_0}^2}{X_O^{0.9}}, \tag{65}$$

where X_O is the mole fraction of the oxidizer, d_{p_0} is the initial diameter of the particle, and K is a constant set based on the aluminum combustion characteristics observed in experiments [24, 130].

2.4 Inter-phase coupling terms

The inter-phase interaction terms that couple the dispersed phase and the gas-phase are denoted as $\dot{\rho_D}$, $\dot{F_D}$, $\dot{Q_D}$, $\dot{W_D}$ and $\dot{S_{D,k}}$ in Eqns. (1)-(4). These terms represent the mass transfer ($\dot{\rho_D}$), the momentum transfer ($\dot{F_D}$), the heat transfer ($\dot{Q_D}$), the work transfer ($\dot{W_D}$) and the production of the $K-th$ species ($\dot{S_D}$) and are closed as

$$\dot{\mathcal{F}_D} = \dot{\mathcal{F}}_p + \dot{\mathcal{F}}_d, \tag{66}$$

where $\dot{\rho}$, $\dot{F}$, $\dot{Q}$, $\dot{W}$ and $\dot{S}_k$ are represented by $\dot{\mathcal{F}}$. The source terms from Lagrangian dispersed phase and Eulerian dispersed phase are computed as:

$$\dot{\rho}_p = \frac{1}{Vol} \sum_{n=1}^{N} n_{p,n} \dot{m}_{p,n}, \tag{67}$$

$$\dot{F}_{p,i} = \frac{1}{Vol} \sum_{n=1}^{N} n_{p,n} \left[\dot{m}_{p,n} u_{p,i,n} + \frac{\pi}{2} r^2{}_{p,n} C_{D,n} \rho_{g,n} |u_{p,i,n} - u_{g,i,n}| \left(u_{p,i,n} - u_{g,i,n}\right) \right.$$
$$\left. - \frac{4}{3} \pi r_{p,n}^3 C_A \left(\frac{D(\rho_{g,n} u_{g,i,n})}{Dt} - \frac{d(\rho_{g,n} u_{p,i,n})}{dt} \right) \right], \tag{68}$$

$$\dot{Q}_p = \frac{1}{Vol}\sum_{n=1}^{N} n_{p,n}\left[\dot{m}_{p,n}h_{v,n} + 2\pi r_{p,n}\kappa_g Nu_n\left(T_{p,n}-T_{g,n}\right) + 4\pi {r_{p,n}}^2\epsilon\sigma\left(T_{p,n}^4 - T_{g,n}^4\right)\right], \tag{69}$$

$$\dot{W}_p = \frac{1}{Vol}\sum_{n=1}^{N} n_{p,n}\left[\dot{m}_{p,n}u_{p,i,n}u_{p,i,n} + \frac{\pi}{2}{r^2}_{p,n}C_{D,n}\rho_{g,n}|u_{p,i,n}-u_{g,i,n}|\left(u_{p,i,n}-u_{g,i,n}\right)u_{p,i,n}\right.$$
$$\left. -\frac{4}{3}\pi r_{p,n}^3 C_A u_{p,i,n}\left(\frac{D(\rho_{g,n}u_{g,i,n})}{Dt} - \frac{d(\rho_{g,n}u_{p,i,n})}{dt}\right)\right], \tag{70}$$

$$\dot{\rho}_d = N_d\dot{m}_d = N_d\frac{d}{dt}\left(\frac{4}{3}\pi r_d^3\rho_d\right), \tag{71}$$

$$\begin{aligned}\dot{F}_{d,i} &= N_d\left[\dot{m}_d u_{d,i} + \frac{\pi}{2}{r^2}_d C_D\rho_g|u_{d,i}-u_{g,i}|\left(u_{d,i}-u_{g,i}\right)\right. \\ &- \left.\frac{4}{3}\pi r_d^3 C_A\left(\frac{D(\rho_g u_{g,i})}{Dt} - \frac{D(\rho_g u_{d,i})}{Dt}\right)\right],\end{aligned} \tag{72}$$

$$\dot{Q}_d = N_d\left[\dot{m}_d h_v + 2\pi r_d\kappa_g Nu\left(T_d - T_g\right) + 4\pi {r_d}^2\epsilon\sigma\left({T_d}^4 - {T_g}^4\right)\right], \tag{73}$$

$$\dot{W}_d = N_d\left[\dot{m}_d u_{d,i}u_{d,i} + \frac{\pi}{2}{r^2}_d C_D\rho_g|u_{d,i}-u_{g,i}|\left(u_{d,i}-u_{g,i}\right)u_{d,i}\right.$$
$$\left. -\frac{4}{3}\pi r_d^3 C_A u_{d,i}\left(\frac{D(\rho_g u_{g,i})}{Dt} - \frac{D(\rho_g u_{d,i})}{Dt}\right)\right], \tag{74}$$

where h_v is the enthalpy change associated with the mass transfer. Note that for mass transfer of single species $\dot{S}_D = \dot{\rho}_D$. The source term for the particle number density $\dot{N}_d$ is modeled based on the fragmentation or agglomeration of the particles in the flow. However, in the current studies, droplet or particle fragmentation and agglomeration are not considered and hence $\dot{N}_d$ is set to zero. The summation of the source terms in Eqns. (30) - (35) and the source terms from the Lagrangian dispersed phase equals the summation of the source terms in Eqns. (1) - (4). Thus, the summation of the gas-phase and the dispersed phase governing equations result in mixture governing equation without inter-phase

coupling terms. However, the contributions of granular pressure, the granular stress and the inter-particle collision force to the momentum and the energy of the dispersed phase do not effect the gas-phase source terms as they are inter-particle effects and are present in the mixture governing equations.

CHAPTER III

NUMERICAL METHOD

A robust numerical strategy capable of capturing shock waves or blast waves along with the mixing/combustion zones is required to investigate the post-detonation flow. The solver should account for the variation in the dispersed phase and the gas phase fluxes due to the volume occupied by the particles. Further, an efficient way to track individual particles is necessary as the number of particles in the dense two-phase flows under investigation can be $\mathcal{O}(10^8)$. In this chapter, the scheme which satisfies these constraints is described. Numerical methods to solve for the gas phase, the Eulerian dispersed phase and the Lagrangian dispersed phase are discussed.

3.1 Finite volume scheme

The conservative form of the equations for the gas-phase and the dispersed phase can be expressed as:

$$\frac{\partial Q}{\partial t} + \frac{\partial F_x}{\partial x} + \frac{\partial F_y}{\partial y} + \frac{\partial F_z}{\partial z} = S, \tag{75}$$

where the assumptions that the conditions are dilute, i.e., $\alpha_g = 1.0$, to obtain the gas-phase equations and $\alpha_d = 1.0$ to obtain the dispersed phase equations have been made. S in Eqn. (75) denotes the source term. When Eqn. (75) is considered for the gas-phase, Q = (ρ_g, $\rho_g u_g$, $\rho_g v_g$, $\rho_g w_g$, $\rho_g E_g$, $\rho_g Y_{g,k}$)^T is the matrix of the conserved state variables, and F_x, F_y and F_z represent the fluxes in the x-, y- and z- directions, respectively, given as

$$F_x = (\rho_g u_g, \rho_g u_g u_g + p_g, \rho_g u_g v_g, \rho_g u_g w_g, \rho_g u_g (E_g + p_g), \rho_g u_g Y_{g,k})^T, \tag{76}$$

$$F_y = (\rho_g v_g, \rho_g u_g v_g, \rho_g v_g v_g + p_g, \rho_g v_g w_g, \rho_g v_g (E_g + p_g), \rho_g v_g Y_{g,k})^T, \tag{77}$$

$$F_z = (\rho_g w_g, \rho_g u_g w_g, \rho_g w_g v_g, \rho_g w_g w_g + p_g, \rho_g w_g (E_g + p_g), \rho_g w_g Y_{g,k})^T. \tag{78}$$

Here, u_g, v_g and w_g are gas-phase velocities in x-, y- and z- directions, respectively. For the Eulerian dispersed phase governing equations, Q can be expressed as Q = (ρ_d, $\rho_d u_d$, $\rho_d v_d$, $\rho_d w_d$, $\rho_d e_d$, $\rho_d E_s$, $N_d)^T$, and the fluxes are given as

$$F_x = (\rho_d u_d, \rho_d u_d u_d, \rho_d u_d v_d, \rho_d u_d w_d, \rho_d u_d e_d, \rho_d u_d E_s, N_d u_d)^T, \quad (79)$$

$$F_y = (\rho_d v_d, \rho_d u_d v_d, \rho_d v_d v_d, \rho_d v_d w_d, \rho_d v_d e_d, \rho_d v_d E_s, N_d v_d)^T, \quad (80)$$

$$F_z = (\rho_d w_d, \rho_d u_d w_d, \rho_d w_d v_d, \rho_d w_d w_d, \rho_d w_d e_d, \rho_d w_d E_s, N_d w_d)^T. \quad (81)$$

Again, u_d, v_d and w_d are dispersed phase velocities in x-, y- and z- directions, respectively. Using a finite volume approach, the governing equations are integrated over a control volume, Vol, as follows:

$$\int\int\int_{Vol} \frac{\partial Q}{\partial t} dV + \int\int\int_{Vol} \left(\frac{\partial F_x}{\partial x} + \frac{\partial F_y}{\partial y} + \frac{\partial F_z}{\partial z} \right) dV = \int\int\int_{Vol} S dV, \quad (82)$$

where the volume, Vol, is bounded by a surface A. Equation (82), using Green's theorem, can be represented as

$$\frac{\partial Q}{\partial t} + \frac{1}{Vol} \oint_A (F_x n_x + F_y n_y + F_z n_z) dA = S. \quad (83)$$

Here, (n_x, n_y, n_z) denote the normalized Cartesian components of the elemental surface normal vector, and Q and S are volume averaged. In the current studies, computational cells are considered to be hexahedral with coordinates (i, j, k). Each cell is bounded by 6 interfaces (A_m, m = 1 to 6) which are located at (i $\pm$ 1/2, j, k), (i, j $\pm$ 1/2, k) and (i, j, k $\pm$ 1/2). The increment in the cell-centered Q is evaluated as:

$$dQ = -\frac{dt}{Vol} \sum_{m=1}^{6} (F_m A_m) + S dt, \quad (84)$$

where $F_m = F_x n_x + F_y n_y + F_z n_z$. Thus, by computing the fluxes at the cell boundaries, the conservative variable Q can be updated. The evaluation of the fluxes at cell boundaries for the gas-phase and the dispersed phase are discussed in detail in this chapter. Note that while converting the dispersed phase equation into the form given in Eqn. (75), pressure

terms have been ignored. The equation for Q with these terms included is also discussed in the following sections.

3.2 MacCormack time integration

The computation can be advanced in time by integrating the governing equations using an explicit or an implicit approach. When the flow variables at time t are used to directly compute the flow variables at time $t + \Delta t$ the scheme is called an explicit scheme. In an implicit scheme, both the variables at t and $t + \Delta t$ are used to compute the variables at $t + \Delta t$. While the explicit approach is straightforward, the implicit scheme is non-trivial and requires iterative procedures or matrix inversion. Without dealing with the computational expense involved in an implicit scheme, an explicit scheme is used in the present study. Although, implicit schemes provide stability and favorable time step for computation, an explicit approach is adopted here mainly due to easy of implementation and mathematical simplicity.

A two-stage MacCormack time integration scheme is used here and the steps involved in the integration, called *predictor* and *corrector* steps, are given as

$$Q^* = Q^n + dQ^n \qquad (Predictor); \tag{85}$$

$$Q^{n+1} = \frac{1}{2}\left[Q^n + Q^* + dQ^*\right] \qquad (Corrector). \tag{86}$$

The superscript n and $n+1$ in the above equations denote quantities at t and $t+\Delta t$. Also, the quantities with superscript * are intermediate quantities evaluated at the *predictor* step. The $\frac{1}{2}$ in Eqn (86) allows Q^{n+1} to be evaluated at $t + \Delta t$ while the *predictor* and the *corrector* steps use Δt as the time step. The increments in the state variables, dQ^n and dQ^* are obtained using the fluxes and are given as

$$dQ^n = -\Delta t \left[\frac{1}{Vol}\sum_m (F^n_m A_m) - S^n\right], \tag{87}$$

$$dQ^* = -\Delta t \left[\frac{1}{Vol}\sum_m (F^*_m A_m) - S^*\right]. \tag{88}$$

Note that the above equations are based on Eqn. (84).

Explicit schemes, although straightforward, suffer due to the restrictions imposed on the time step, Δt. For numerical stability and accuracy, Δt is determined by using the *Courant-Friefrichs-Levy* number (CFL number). The maximum allowable time step for the gas-phase is determined as

$$\Delta t_{gas} = CFL \left(\frac{Vol}{|dA|\omega_{gas}} \right), \tag{89}$$

and the maximum time step allowed for the Eulerian dispersed phase is evaluated as

$$\Delta t_{dispersed} = CFL \left(\frac{Vol}{|dA|\omega_{dispersed}} \right), \tag{90}$$

where dA is the surface area of the hexahedral computational cell, ω_{gas} is the wave speed in the gas-phase, $\omega_{disperesed}$ is the wave speed in the dispersed phase. CFL is generally less than 1.0. The time step for computation based on the time step for the gas-phase and the Eulerian dispersed phase is determined as

$$\Delta t = \min(\Delta t_{gas}, \Delta t_{dispersed}). \tag{91}$$

The CFL criteria restricts the propagation of information to a distance no farther than the volume-to-area ratio of the computational cell. This aids in the stability of the scheme [5]. The time integration procedure discussed here provides a second order accurate method in time.

3.3 Discrete Equations Method - Gas phase

In dense multi-phase mixtures, finite volume is occupied by both the dispersed phase and the gas-phase. A robust multi-phase model is required to account for the volume occupied by the particles and adjust the flux of the gas-phase based on the volume fraction and the distribution of the particles. The Discrete Equations Method (DEM), originally proposed by Abgrall and Saurel [1] for Eulerian dispersed phase and extended by Balakrishnan et al. [19] for Lagrangian dispersed phase, is used here since it provides an efficient way to account for the volume fraction of the individual phases. The volume fraction of each phase

is treated as a piece-wise continuous quantity and is represented at the computational cell interface using Monotone Upstream-centered Schemes for Conservation Laws (MUSCL) reconstruction. When EE method is used, the value of volume fraction of the dispersed phase in each cell is computed by solving the governing equations for the Eulerian dispersed phase. However, if EL method is employed, the volume fraction of the dispersed phase is obtained as the average volume of all the particles in each computational cell.

In order to integrate in space and time, the gas-phase governing equations without the viscous terms and the multi-phase source terms in three-dimensions can be written as

$$\frac{(\partial \lambda W)}{\partial t} + \frac{(\partial \lambda F)}{\partial x} + \frac{(\partial \lambda G)}{\partial y} + \frac{(\partial \lambda H)}{\partial z} = F_I \frac{\partial \lambda}{\partial x} + G_I \frac{\partial \lambda}{\partial y} + H_I \frac{\partial \lambda}{\partial z}, \tag{92}$$

where W, F, G, H, F_I, G_I and H_I are given as

$$W = (\rho_g, \rho_g u_g, \rho_g v_g, \rho_g w_g, \rho_g E_g, \rho_g Y_k)^T, \tag{93}$$

$$F = \left(\rho_g u_g, \rho_g u_g^2 + p_g, \rho_g u_g v_g, \rho_g u_g w_g, \rho_g E_g u_g, \rho_g u_g Y_k\right)^T, \tag{94}$$

$$G = \left(\rho_g v_g, \rho_g u_g v_g, \rho_g v_g^2 + p_g, \rho_g v_g w_g, \rho_g E_g v_g, \rho_g v_g Y_k\right)^T, \tag{95}$$

$$H = \left(\rho_g w_g, \rho_g u_g w_g, \rho_g v_g w_g, \rho_g w_g^2 + p_g, \rho_g E_g w_g, \rho_g w_g Y_k\right)^T, \tag{96}$$

$$F_I = (0, p_g, 0, 0, p_g u^*, 0)^T, \tag{97}$$

$$G_I = (0, 0, p_g, 0, p_g v^*, 0)^T, \tag{98}$$

$$H_I = (0, 0, 0, p_g, p_g w^*, 0)^T, \tag{99}$$

where u^*, v^* and w^* are the interface velocities. In two-phase flows, an interface or a material indicator function, λ, is used to distinguish between the phases [19]. The interface indicator function takes values 0 and 1 in the regions with pure dispersed-phase and pure gas-phase, respectively, and is governed by the following equation [1, 19]:

$$\frac{\partial \lambda}{\partial t} + u^* \frac{\partial \lambda}{\partial x} + v^* \frac{\partial \lambda}{\partial y} + w^* \frac{\partial \lambda}{\partial z} = 0. \tag{100}$$

Note that the above equation vanishes in the regions with pure phases and is only non-zero at the material interfaces. Equation (92) is split into three integrals, I_1, I_2 and I_3,

corresponding to the temporal derivative, conservative flux and the non-conservative flux, respectively, in each direction. These integrals for each computational cell, C_{ijk} are summarized as

$$\begin{aligned} I_1 &= \int_0^{\Delta t} \int_{C_{ijk}} \frac{\partial(\lambda W)}{\partial t} dV\ dt, \\ I_2 &= \int_0^{\Delta t} \int_{C_{ijk}} \frac{\partial(\lambda F)}{\partial x} dV\ dt, \\ I_3 &= \int_0^{\Delta t} \int_{C_{ijk}} F_I \frac{\partial \lambda}{\partial x} dV\ dt. \end{aligned} \tag{101}$$

Integrals I_1 and I_2 are approximated as [19]

$$I_1 = \int_{C_{ijk}} \left((\lambda W)^{n+1} - (\lambda W)^n \right) dV \tag{102}$$

$$= \left((\lambda W)_{ijk}^{n+1} - (\lambda W)_{ijk}^n \right) \Delta x\ \Delta y\ \Delta z, \tag{103}$$

$$I_2 = \int_0^{\Delta t} \int_{z_{k-1/2}}^{z_{k+1/2}} \int_{y_{j-1/2}}^{y_{j+1/2}} \int_{x_{i-1/2}}^{x_{i+1/2}} \frac{\partial(\lambda F)}{\partial x} dV\ dt \tag{104}$$

$$= \int_0^{\Delta t} \int_{z_{k-1/2}}^{z_{k+1/2}} \int_{y_{j-1/2}}^{y_{j+1/2}} \left((\lambda F)_{i+1/2} - (\lambda F)_{i-1/2} \right) dS\ dt, \tag{105}$$

where $dS = dy\ dz$. Computation of I_2 requires the computation of flux at surfaces $i + 1/2$ and $i - 1/2$. Since each surface can comprise of gas-gas (g-g), gas-solid (g-s), solid-gas (s-g) or solid-solid (s-s) interfaces, as shown in Fig. 10, the flux at each location can be split into four parts. Thus, the flux at $i + 1/2$ can be written as

$$\begin{aligned} \int_{z_{k-1/2}}^{z_{k+1/2}} \int_{y_{j-1/2}}^{y_{j+1/2}} (\lambda F)_{i+1/2} dS\ dt = {} & \lambda^*_{i+1/2} F^*_{i+1/2,g-g} S_{g-g} \\ & + \lambda^*_{i+1/2} F^*_{i+1/2,g-s} S_{g-s} \\ & + \lambda^*_{i+1/2} F^*_{i+1/2,s-g} S_{s-g} \\ & + \lambda^*_{i+1/2} F^*_{i+1/2,s-s} S_{s-s}. \end{aligned} \tag{106}$$

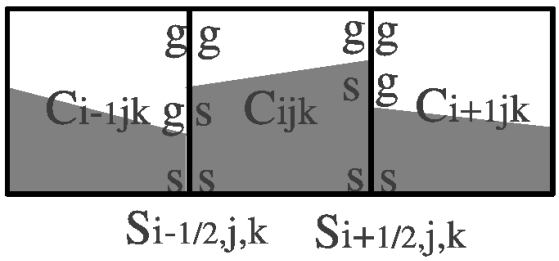

Figure 10: Computational cells showing the different types of interfaces. The region of the computational cell occupied by particles is shown in gray and the region occupied by the gas is shown in white.

Here, the terms with the * superscript are computed at the interface. The indicator function and the interface surface area for each type of interface depends on the interface velocity. The expression for the interface surface area and the value of the indicator function for each interface type are summarized in Table 2. Note that the gas-flux is zero when the interface is solid-solid, i.e., there is no gas flux when solid is present on both sides of the interface. The splitting of the conservative flux allows for the waves propagating through the gas-particle mixture to transmit and reflect according to the volume fraction of the particles. This is essential to compute the total flux at the cell interface and capture the difference in the compressibility of the gas phase and the dispersed phase.

Table 2: Conservative and non-conservative flux at cell interface $i + 1/2$

Contact type	Contact surface	Indicator function, λ^*
Conservative flux		
Gas-Gas	S min($\alpha_{g,i}$, $\alpha_{g,i+1}$)	1
Gas-Solid	S max($\alpha_{g,i}$ - $\alpha_{g,i+1}$, 0)	1 if $u^* \geq 0$; 0 otherwise
Solid-Gas	S max($\alpha_{g,i+1}$ - $\alpha_{g,i}$, 0)	1 if $u^* < 0$; 0 otherwise
Solid-Solid	S min($1 - \alpha_{g,i}$, 1 - $\alpha_{g,i+1}$)	0
Non-conservative flux		
Gas-Gas	S min($\alpha_{g,i}$, $\alpha_{g,i+1}$)	0
Gas-Solid	S max($\alpha_{g,i}$ - $\alpha_{g,i+1}$, 0)	-1 if $u^* \geq 0$; 0 otherwise
Solid-Gas	S max($\alpha_{g,i+1}$ - $\alpha_{g,i}$, 0)	1 if $u^* \geq 0$; 0 otherwise
Solid-Solid	S min($1 - \alpha_{g,i}$, 1 - $\alpha_{g,i+1}$)	0

The non-conservative flux, I_3, is computed by considering the flux at the cell boundaries ($i - 1/2$ and $i + 1/2$) and at the internal interfaces [19] and is expressed as

$$I_3 = \int_0^{\Delta t} \int_{z_{k-1/2}}^{z_{k+1/2}} \int_{y_{j-1/2}}^{y_{j+1/2}} \left[\Big((F_I)_{i-1/2}[\lambda]_{i-1/2} + (F_I)_{i+1/2}[\lambda]_{i+1/2} \Big) + \big((F_I)_i[\lambda]_i \big) \right] dS \; dt. \tag{107}$$

Here, we follow the procedure described by [19] and compute the flux at the internal interface (in I_3), which represent the coupling/relaxation terms, using empirical correlations and are obtained as a summation over all the particle in a cell. The non-conservative flux at the cell boundary, $i + 1/2$, is expressed as

$$\int_{z_{k-1/2}}^{z_{k+1/2}} \int_{y_{j-1/2}}^{y_{j+1/2}} \Big((F_I)_{i+1/2}[\lambda]_{i+1/2} \Big) \, dS = [\lambda^*]_{i+1/2} (F_I^*)_{i+1/2,s-g} S_{s-g} + [\lambda^*]_{i+1/2} (F_I^*)_{i+1/2,g-s} S_{g-s}. \tag{108}$$

The values of the indicator function and the interface contact surface for non-conservative flux at $i + 1/2$ are given in Table 2. Note that, in the above discussion, computation of fluxes in x-direction is elucidated and this procedure can be applied to compute fluxes in y- and z- directions.

The interface velocity in each direction is evaluated as the mass-weighted average velocity of all the solid particles in the cell. When dispersed phase is solved using Lagrangian tracking the interface velocity is expressed as

$$u_i^* = \frac{\sum_{n=1}^{N} m_{p,n} u_{p,i,n}}{\sum_{n=1}^{N} m_{p,n}}. \tag{109}$$

The dispersed phase velocity in the cell is used as the interface velocity when Eulerian dispersed phase equations are used to solve for the dispersed phase. When both Eulerian dispersed phase and Lagrangian tracking are used, the interface velocity is computed as a weighted average of the interface velocity from Lagrangian tracking ($u_{p,i}^*$) and the interface velocity from the Eulerian dispersed phase ($u_{d,i}^*$). Here, the weights used are α_p and α_d, and the expression for the combined interface velocity is

$$u_i^* = \frac{\alpha_d u_{d,i}^* + \alpha_p u_{p,i}^*}{\alpha_d + \alpha_p}. \tag{110}$$

Further details about different interface closures can be found elsewhere [1, 19].

Along with MUSCL reconstruction with Monotonized Central limiter [11], Harten-Lax-van Leer Riemann solver with contact (HLLC) is used to compute the fluxes at the cell interfaces. Specifically, HLLC is used here since this Riemann solver provides contact surface required to evaluate the interface velocity [11]. The scheme employed is second order accurate in space. The solution procedure described above (for gas-phase only) and the scheme employed for the gas phase have already been validated for post-detonation flows [15, 52].

3.4 Eulerian dispersed phase

One of the key restrictions in choosing an appropriate solver for Eulerian dispersed phase equations is posed by the compaction wave speed. At low α_d the compaction wave speed, the granular pressure and the granular temperature can be zero. Thus, the Riemann solver chosen must be able to handle the pressure-less Euler equations and AUSM$^+$-up solver (Advection Upstream Splitting Method) satisfies this condition [74]. The dispersed phase flux vector, F_d, (From Eqns. (31) - (36)) at $i+1/2$ using AUSM is expressed as [57]

$$F_{d,i+1/2} = \mathbf{p}_{i+1/2} + \dot{m}_{i+1/2} \begin{cases} \psi^L & if\ \dot{m}_{i+1/2} \geq 0 \\ \psi^R & if\ \dot{m}_{i+1/2} < 0, \end{cases}$$

where $\mathbf{p}_{i+1/2} = (0, p_{tot,i+1/2}, 0, 0, 0)^T$ is the pressure flux vector and $\psi = (1, u_d, e_d, E_s, N_d)^T$ is the passively advected scalar vector. The superscripts ^{L} and ^{R} denote the value at the left and the right cell interface, respectively. The values at the cell interface are evaluated using MUSCL reconstruction with monotonized central limiter. $\dot{m}_{i+1/2}$ is the mass flux at the cell interface and is expressed as

$$\dot{m}_{d,i+1/2} = (c_{d,i+1/2} + \zeta) M_{i+1/2} \begin{cases} \alpha_d^L \rho_d^L & if\ M_{i+1/2} \geq 0 \\ \alpha_d^R \rho_d^R & if\ M_{i+1/2} < 0. \end{cases}$$

Here, the compaction wave speed at the cell interface is given as

$$c^2_{i+1/2} = \frac{\alpha_d^L \rho_d^L (c_d^L)^2 + \alpha_d^R \rho_d^R (c_d^R)^2}{\alpha_d^L \rho_d^L + \alpha_d^R \rho_d^R + \zeta}, \tag{111}$$

where ζ is the a small number set to 10^{-15} to avoid division by zero. The Mach number at the left and the right interface are defined as

$$M^{L/R} = \frac{u_d^{L/R}}{c_{i+1/2} + \zeta} \tag{112}$$

and at the interface, $M_{i+1/2}$, is expressed as

$$M_{i+1/2} = M_4^+(M^L) + M_4^-(M^R) - \frac{1}{2}\max(1 - \frac{3}{4}\bar{M}^2, 0)\frac{p_{d,tot}^R - p_{d,tot}^L}{(\alpha_d^L \rho_d^L + \alpha_d^R \rho_d^R)c_{i+1/2}^2} \tag{113}$$

where $M_4^{\pm}$ and $\bar{M}^2$ are [26]

$$M_4^{\pm}(M_{i+1/2}) = \begin{cases} \frac{1}{2}(M_{i+1/2} \pm |M_{i+1/2}|) & if\ |M_{i+1/2}| \geq 1 \\ \pm\frac{1}{4}(M_{i+1/2} \pm 1)^2[1 \mp \frac{1}{2}\left(\mp(M_{i+1/2} \mp 1)^2\right)] & if\ |M_{i+1/2}| < 1, \end{cases}$$

$$\bar{M}^2 = \frac{(u_d^L)^2 + (u_d^R)^2}{2c_{i+1/2}^2}. \tag{114}$$

The total dispersed phase pressure at the interface are given as

$$p_{tot,i+1/2} = P_5^+(M^L)p_{tot}^L + P_5^-(M^R)p_{tot}^R - \frac{3}{4}c_{i+1/2}P_5^+(M^L)P_5^-(M^R)(\rho_d^L + \rho_d^R)(u_d^R - u_d^L), \tag{115}$$

where $P_5^{\pm}$ as a function of $M_{i+1/2}$ is

$$\begin{aligned} P_5^{\pm}(M_{i+1/2}) &= \frac{1}{2M_{i+1/2}}(M_{i+1/2} \pm |M_{i+1/2}|) \quad \text{if } |M_{i+1/2}| \geq 1 \\ &= \pm\frac{1}{4}(M_{i+1/2} \pm 1)^2[(\pm 2 - M_{i+1/2}) \\ &\quad \mp\frac{3}{4}M_{i+1/2}\left(\mp(M_{i+1/2} \mp 1)^2\right)] \quad \text{if } |M_{i+1/2}| < 1. \end{aligned} \tag{116}$$

α_d at the interface is set to be α_d^L if $\dot{m}_{i+1/2} \geq 0$ and α_d^R if $\dot{m}_{i+1/2} < 0$. Based on the scheme described, the Eulerian dispersed phase governing equations are discretized as

$$\int_{C_{ijk}} \left((\alpha_d \rho_d)^{n+1} - (\alpha_d \rho_d)^n\right) dV = -\int_{z_{k-1/2}}^{z_{k+1/2}} \int_{y_{j-1/2}}^{y_{j+1/2}} \left(\dot{m}_{i+1/2} - \dot{m}_{i-1/2}\right) dS\ dt, \quad (117)$$

$$\begin{aligned}\int_{C_{ijk}} \left((\alpha_d \rho_d u_d)^{n+1} - (\alpha_d \rho_d u_d)^n\right) dV &= -\int_{z_{k-1/2}}^{z_{k+1/2}} \int_{y_{j-1/2}}^{y_{j+1/2}} \Big[\dot{m}_{i+1/2} u_{d,i+1/2} \\ &\quad -\dot{m}_{i-1/2} u_{d,i-1/2} + (p_{tot,i+1/2} - p_{tot,i-1/2}) \\ &\quad -\alpha_{d,i}(p_{g,i+1/2} - p_{g,i-1/2})\Big]\, dS\ dt,\end{aligned} \quad (118)$$

$$\begin{aligned}\int_{C_{ijk}} \left((\alpha_d \rho_d e_d)^{n+1} - (\alpha_d \rho_d e_d)^n\right) dV = &- \int_{z_{k-1/2}}^{z_{k+1/2}} \int_{y_{j-1/2}}^{y_{j+1/2}} \Big(\dot{m}_{i+1/2} e_{d,i+1/2} \\ &- \dot{m}_{i-1/2} e_{d,i-1/2}\Big)\, dS\ dt,\end{aligned} \quad (119)$$

$$\begin{aligned}\int_{C_{ijk}} \left((\alpha_d \rho_d E_s)^{n+1} - (\alpha_d \rho_d E_s)^n\right) dV &= -\int_{z_{k-1/2}}^{z_{k+1/2}} \int_{y_{j-1/2}}^{y_{j+1/2}} \Big[\dot{m}_{i+1/2} E_{s,i+1/2} \\ &- \dot{m}_{i-1/2} E_{s,i-1/2} \\ &- p_{d,i+1/2}(u_{d,i+1/2} - u_{d,i-1/2})\Big]\, dS\ dt,\end{aligned} \quad (120)$$

$$\int_{C_{ijk}} \left((N_d)^{n+1} - (N_d)^n\right) dV = -\int_{z_{k-1/2}}^{z_{k+1/2}} \int_{y_{j-1/2}}^{y_{j+1/2}} \left(N_{d,i+1/2} u_{d,i+1/2} - N_{d,i-1/2} u_{d,i-1/2}\right) dS\, dt, \quad (121)$$

Note that in the above discussion, the fluxes are discussed in x-direction and can be written in y- and z- directions following the same procedure.

3.5 Lagrangian tracking

Compared to the strategy of treating dispersed phase using Eulerian approach, several researchers prefer Lagrangian particle tracking. Lagrangian approach, especially in complex flows ubiquitous in spray combustion, offers unique advantages such as the ability to model accurate particle dispersion, mixing, breakup and range of particle sizes. From an implementation perspective, Lagrangian particle tracking can be achieved mainly by two MPI

communication strategies, i.e., point-to-point and gather-scatter (shown in Fig. 11). In the gather-scatter strategy, the communication is based on a master-slave approach. The dispersed phase data is gathered in the master at each time step to facilitate the master in performing the majority of the book-keeping operations. In order to hold this data, a global array of size equal to the number of parcels/particles is allocated in each processor and the updated information is communicated to all the processors at each time step. Since the book-keeping and communication are not dependent on the number of processors used, this strategy provides only marginal increase in speedup of about 20% with increase in number of cores. However, time to compute particle/parcel parameters can still scale linearly as it is dependent on particles/parcels per each processor. The main advantage of the gather-scatter strategy is the ease of book-keeping which strictly ensures the presence of all the required particles (mass conservation) at each time step. However, since the data is allocated for all particles in each processor, the total number of particles handled is severely restricted based on the memory limitations of a given processor cluster. Although, this limitation can be relaxed in the point-to-point approach, in most spray calculations, the number of particles (droplets) present from injection to evaporation/combustion is limited. Thus, gather-scatter approach can provide reliable results with minimum implementation effort in these cases.

The point-to-point strategy involves communication of only the particles in the ghost cells to the adjacent neighbor. The particle data is allocated per each processor and so the total number of particles handled can scale linearly with the number of processors used. This is very advantageous in cases that have inevitably large number of particles. However, the implementation of the book-keeping is not trivial and is time consuming. At each time step, declaration of the intent to communicate, evaluation of the size of message to be communicated and actual communication of the message are to be performed which add extra latency. However, the communication cost is relatively small in comparison to the gather-scatter approach. The over-all performance and the memory management in the point-to-point strategy is expected to be superior. Both the gather-scatter and the point-to-point strategies suffer from load-balancing issues. If the particles are concentrated in a

particular group of processors the computational time may not scale favorably. This problem can be over come by adapting the processor distribution based on the particle concentration. However, care is needed as the gas-phase properties are needed to update the particle properties and adapting the processors should be accompanied by appropriate interpolation techniques necessary for two-way coupling. The details of the parallel Lagrangian tracking implementation, along with the code scaling, are discussed in Appendix B.

3.5.1 Time integration

The governing equations for Lagrangian dispersed phase discussed in Chapter 2 can be integrated using an Euler method [7], a Verlet method [117] or a higher order Runge-Kutta time integration scheme [94]. Euler method is a first order method with an error proportional to the square of the time step [7]. Thus, the accuracy of the Euler time integration scheme increases with decrease in time step. Since this places a restriction on the time step based on the accuracy required, Euler time integration scheme is not chosen here. Verlet integration methods are a popular choice to compute particle trajectories in many fields such as molecular dynamics and computer graphics. Verlet schemes that update the particle position by computing velocities at each time step without storing them are advantageous in cases with large number of particles due to the reduction in the memory requirements [117]. However, in the current studies, the particle velocities are important to determine the inter-phase coupling terms and the non-conservative terms. Hence, Verlet methods have no particular advantage over higher order Runge-Kutta time integration schemes. Here, the governing equations for Lagrangian dispersed phase are solved using a 4^{th} order Runge-Kutta time integration scheme due to the accuracy and the reliability of the scheme [19, 52, 94]. To explain this scheme, Eqns. (55) and (56) are written as

$$\frac{du_{p,i}}{dt} = a_{p,i}, \tag{122}$$

$$\frac{dT_p}{dt} = \dot{T}_p. \tag{123}$$

Now to integration from t to $t + \Delta t$ using 4^{th} order Runge-Kutta scheme, the following

four steps are executed

$$\textbf{Step 1:} \tag{124}$$

$$X_1 = \Delta t\left[u_{p,i}(t)\right]$$

$$U_1 = \Delta t\left[a_{p,i}(u_{p,i}, ...)\right]$$

$$T_1 = \Delta t\left[\dot{T}_p(T_p, ...)\right]$$

$$\textbf{Step 2:}$$

$$X_2 = \Delta t\left[u_{p,i}(t) + \frac{1}{2}U_1\right]$$

$$U_2 = \Delta t\left[a_{p,i}(u_{p,i} + \frac{1}{2}U_1, ...)\right]$$

$$T_2 = \Delta t\left[\dot{T}_p(T_p + \frac{1}{2}T_1, ...)\right]$$

$$\textbf{Step 3:}$$

$$X_3 = \Delta t\left[u_{p,i}(t) + \frac{1}{2}U_2\right]$$

$$U_3 = \Delta t\left[a_{p,i}(u_{p,i} + \frac{1}{2}U_2, ...)\right]$$

$$T_3 = \Delta t\left[\dot{T}_p(T_p + \frac{1}{2}T_2, ...)\right]$$

$$\textbf{Step 4:}$$

$$X_4 = \Delta t\left[u_{p,i}(t) + U_3\right]$$

$$U_4 = \Delta t\left[a_{p,i}(u_{p,i} + U_3, ...)\right]$$

$$T_4 = \Delta t\left[\dot{T}_p(T_p + T_3, ...)\right]$$

The updated values of $x_{p,i}$, $u_{p,i}$ and T_p at $t + \Delta t$ are then obtained as

$$\begin{aligned} x_{p,i}(t + \Delta t) &= x_{p,i}(t) + \frac{1}{6}X_1 + \frac{1}{3}X_2 + \frac{1}{3}X_3 + \frac{1}{6}X_4, \\ u_{p,i}(t + \Delta t) &= u_{p,i}(t) + \frac{1}{6}U_1 + \frac{1}{3}U_2 + \frac{1}{3}U_3 + \frac{1}{6}U_4, \\ T_p(t + \Delta t) &= T_p(t) + \frac{1}{6}T_1 + \frac{1}{3}T_2 + \frac{1}{3}T_3 + \frac{1}{6}T_4. \end{aligned} \tag{125}$$

If the particle mass transfer is non-zero then, the mass of the particle is also updated along with the other properties using similar procedure. The properties of the gas-phase

are interpolated using 2^{nd} order moving least squares interpolation. In some cases, when the particles are close to the blast wave or the shock wave, 1^{st} order interpolation is also used to avoid unphysical gas-phase properties near a given particle.

3.5.2 Time step for Lagrangian tracking

In the above equations one of the key requirement is to determine Δt for the time integration. Note that the gas-phase and the Eulerian dispersed phase provide a time step as given by Eqn. (91). Apart from this time step from Eulerian phase (Δt_{Euler}), each particle has time scale based on the particle evaporation (τ_{evap}), the mass transfer (τ_{life}) and the particle momentum (τ_{relax}). These time scales are given as [94]

$$\tau_{evap} = \frac{\rho_p C_v d_p}{6 h_p}, \tag{126}$$

$$\tau_{life} = \frac{4}{3}\pi r_p^3 \frac{\rho_p}{\dot{m}_p}, \tag{127}$$

$$\tau_{relax} = \frac{|u_{p,i} - u_{g,i}|}{|du_{p,i}/dt|}, \tag{128}$$

where $h_p = \kappa_g Nu/d_p$. τ_{life} restricts the size of the particle to remain positive and is estimated based on the mass transfer rate. In cases with the particle/droplet boiling point close to the surrounding temperature, the droplet temperature can abruptly rise if the Lagrangian time step is too large. τ_{evap} imposes a limit on the time step and prevents such abrupt rise in temperature and evaporation. The droplet or the particle relaxation time is obtained as an exact solution for the local linearized particle equations of motion in a uniform flow. τ_{relax} is the ratio of the particle slip velocity to the magnitude of the particle acceleration and restricts the time step based on the particle acceleration.

In addition to the above time scales based on the heat transfer, the mass transfer and the momentum/acceleration of the particle, another time scale based on the computational cell size, Δ, is also imposed. One of the challenges in the parallel implementation of Lagrangian tracking is to identify the computational cell corresponding to the new location of the particle after a given time integration step. Identification of the computational cell

is important as it is required for the interpolation of the source terms to the gas-phase and to compute the gas-phase properties at the particle location. If the particle moves several computational cells in a given time step, the region to search for the new location of the particle increases. For example, if the particle is allowed to cross two computational cells (instead of one) in a given time step, the search region increases to 5^3 (from 3^3) computational cells (2 cells in each positive and negative directions). This adds to the cost of tracking. Further, the communication cost also increases if the particle is present near the boundary of a given domain. Thus, to reduce the cost and the complexity, the particle is restricted to cross at most one computational cell in a given time step by defining the tracking time scale, τ_{cell} as

$$\tau_{cell} = \frac{0.5\Delta}{|u_{p,i}|}, \tag{129}$$

The time step for Lagrangian tracking is obtained as the minimum of all the time scales as

$$\Delta t_{Lagrangian} = \min(\Delta t_{Euler}, \tau_{evap}, \tau_{life}, \tau_{relax}, \tau_{cell}). \tag{130}$$

Note that the time step for Lagrangian time integration can be very small compared to the Euler time step from gas or Eulerian dispersed phase. In such cases, the integration for Lagrangian tracking is performed as sub-iterations and the source terms are evaluated after all the sub-iterations are completed. The number of sub-iterations for each Eulerian time integration is determined such that the sum of all the Lagrangian sub-time steps is same as the global Eulerian time step.

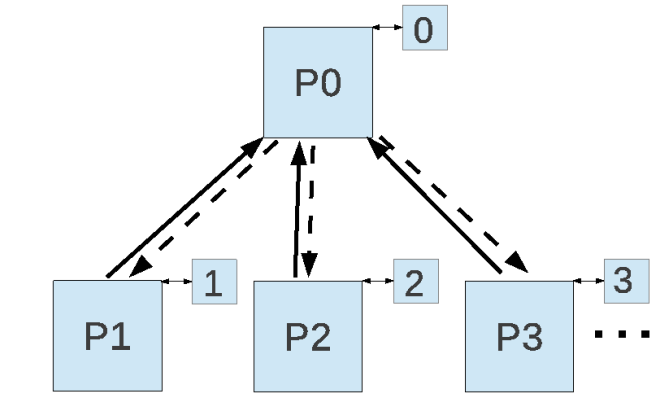

(a) Gather-Scatter

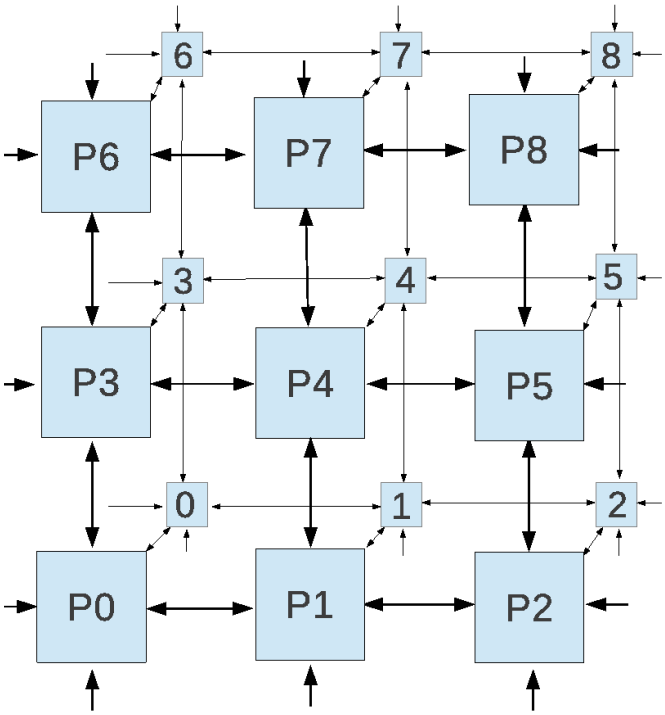

(b) Point-to-Point

Figure 11: Schematic of (a) gather-scatter and (b) point-to-point communication strategies for Lagrangian particle tracking. The boxes with P1 to P8 indicate the grid of processors performing computation for particles. A small box corresponding to each processor is shown to indicate the two-way coupling between the gas-phase and the dispersed-phase. The double sided arrow indicates two-way communication between the processors. The gathering operation is indicated with single arrow and scattering operation is indicated using single dashed arrow. P0 performs all the book-keeping operations and updates the full particle data array at each time step in Gather-Scatter approach. Note that there can be communication between corner neighbors (P4-P0, P4-P2, P4-P6 and P4-P8) in point-to-point method which is not illustrated.

CHAPTER IV

VERIFICATION AND VALIDATION

The numerical scheme and the overall computational strategy discussed in Chapter 2 are verified and validated in this chapter. This is an essential step before performing the studies which are the focus of this thesis. The verification tests are defined to assess the accuracy of the numerical implementation. In order to verify, the numerical results are compared to the expected theoretical results. The numerical results are also validated with the aid of experimental results. In this chapter, the studies describe the verification and the validation for both EE and EL solvers (see Table 3). The test cases for EE-EL solver, focusing on post-detonation flows, will be described in the following chapters.

4.1 Verification

The numerical approach is verified by simulating particle dispersal in uniform flow conditions. The tests for Lagrangian solver are aimed to verify the time integration procedure, the parallel communication and the boundary conditions. The tests for Eulerian dispersed phase solver are conducted to verify the scheme to track dilute and dense particle clouds. Results are also compared with theoretical values to determine the accuracy of the solvers.

4.1.1 Lagrangian solver

4.1.1.1 Dispersion in uniform flow

A non-inertial particle is initialized in a uniform gaseous flow of 100 m/s velocity. A domain 1.0 m long with a cross section of 10 cm $\times$ 10 cm is considered and is discretized with a $100 \times 10 \times 10$ Cartesian grid. Further, the domain length is equally split among 8 cores. The gases enter the domain from the left boundary where the flow parameters are specified. The parameters are extrapolated at the right boundary where the flow exits. All the boundaries perpendicular to the length of the domain are considered to be slip walls. The gas considered is air, and the pressure and the temperature of the gas are 10^5 Pa and 298 K, respectively.

Table 3: List of verification and validation cases for the Eulerian and the Lagrangian approaches used in this thesis.

Case	Lagrangian (L)/ Eulerian (E)	Dense/ Dilute	α_d or α_p	Purpose/Description
Verification				
Uniform flow	L	Dilute	-	Single non-inertial particle dispersion
Reflection	L	Dilute	-	Single inertial particle dispersion, communication and wall boundary condition
Uniform flow	L/E	Dilute	0.005	Inertial particle cloud convection
Uniform flow	L/E	Dense	0.05	Dense particle cloud convection
Validation				
Dispersion	L	Dilute	-	Single non-inertial shock-particle interaction
Boiko	L/E	Dense	0.03	Particle cloud dispersion by shock wave
Rouge	L/E	Dense	0.65	Particle cloud (near packing limit) dispersion by shock wave

The particle is initially placed at a distance of 2 cm from the inflow boundary and is tracked by core 1. Figure 12 shows the distance traveled by the particle and the velocity of the particle with time. Since the particle is non-inertial, the particle follows the gas-phase. Also, since the flow is uniform, the acceleration of the particle is expected to be zero. This is confirmed by this test. The velocity of the particle remains constant and the trajectory of the particle flows as straight line. The trajectory or the velocity are not altered at the core boundaries. The particle is transported across the domain with no change in properties due to the communication across the cores. This is the expected scenario. The solver performs very well and matches the expected behavior and the theoretical result.

4.1.1.2 Communication and reflection at boundaries

The aim of this test is to verify the particle communication, and reflection at the wall boundaries. Nylon particles of radius 10 μm are tracked in a quiescent flow. A two-dimensional square domain with length 1 cm is considered. The domain is set to have air

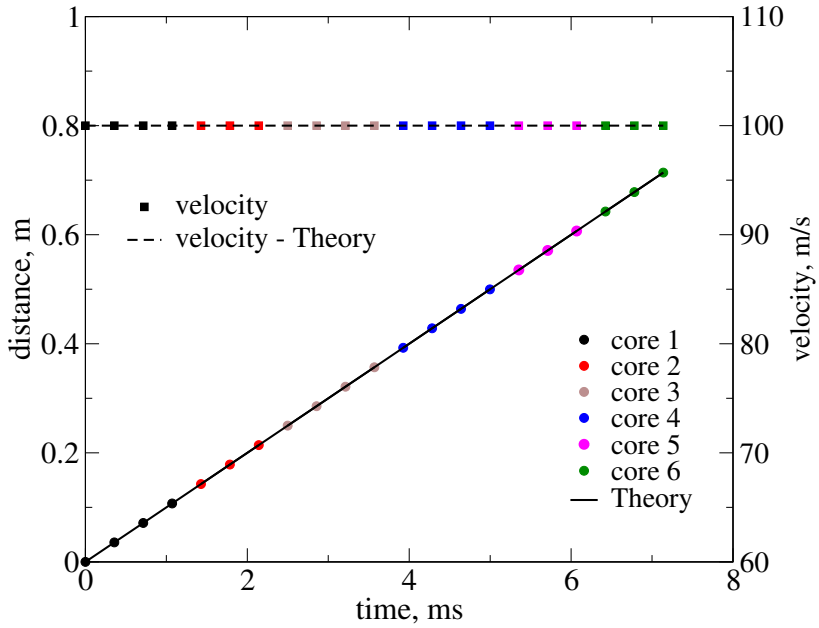

Figure 12: Dispersion of a non-inertial particle placed in a uniform flow

at 298 K and 10^5 Pa. The domain boundaries are slip walls and the domain is divided into 4 equal sub-domains. 4 cores are used in this test and each core handles one of the sub-domains. Four particles are initialized such that each core gets a particle to track. The particles are initially located at the coordinates (0.1, 0.4), (0.6, 0.1), (0.4, 0.9) and (0.9, 0.6) (in mm), and the velocity vectors of these particles are (-10.0, 10.0), (-10.0, -10.0), (10.0, 10.0) and (10.0, -10.0) (m/s), respectively. The initial location and the initial velocity of each particle is chosen with an aim to let the particles interact with the boundaries. The particles are inertial and the density of each particle is 1170.0 kg/m^3. The force on each particle is computed using the drag law described by Igra and Takayama [58].

The nylon particles placed in the domain move towards the walls and reflect from the walls as shown in Fig. 13. The particle reflection location on the wall is nearly at the boundary of two cores. After reflection, the particle is communicated to the neighboring core and the tracking continues. This verifies the particle reflection boundary condition at slip walls. The test has been repeated for no-slip walls with same the result. Further, the trajectory of particle is almost straight line as expected. A slight change in the velocity is noticed due to the quasi-steady drag.

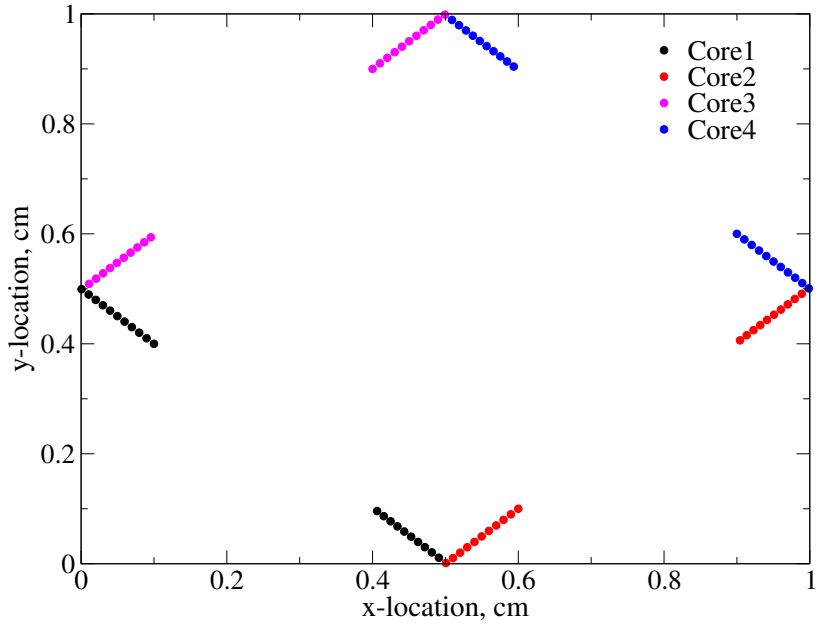

Figure 13: Reflection of inertial particles at the wall boundaries

4.1.2 Eulerian dispersed phase

The following tests are performed to verify the approach for the Eulerian dispersed phase. The tests verify the convection of a dilute and a dense particle cloud in a uniform flow. In both cases, the entire set of governing equations for Eulerian dispersed phase, discussed in Chapter 2, are used without any approximation.

4.1.2.1 Uniform flow

A dilute cloud of steel particles is convected in a uniform flow to verify the Eulerian dispersed phase solver. A two-dimensional domain 2.0 m long and 10.0 cm wide is considered and is discretized using a uniform Cartesian grid. Three grids, G1, G2 and G3, with resolutions, 5, 2.5 and 1.25 mm, are used to test the influence of grid on the particle cloud convection. The initial volume fraction of the dispersed phase is set to 0.5% and the velocity of the gas-phase and the dispersed-phase are set as 100.0 m/s. The domain is considered to comprise of air at 10^5 Pa and 293.0 K. The radius of each particle is 100.0 μ m. The force on each particle is evaluated using the drag law provided by Boiko et al. [23]. The flow in the domain is along the length of the domain. The flow enters the domain from the left boundary and

leaves from the right boundary. All the boundaries perpendicular to flow are considered to be slip walls.

The particle cloud is initially distributed between 0.4 m and 0.6 m, and is expected to move 1 m in 10 ms. Figure 14 shows that the particles move as predicted. The accuracy of the cloud boundaries increases with increase in resolution, i.e., Grid G3 gives the most accurate results. However, in all cases, the trajectory of the particle cloud is in good agreement with expected theoretical value. In this verification, result from EE is also compared with EL. To simulate the EL case, 120000 particles are uniformly distributed between 0.4 m and 0.6 m and tracked for 10 ms. The position of the particle cloud from EL is the most accurate as expected. Also, the result from G3 matches well with the EL result. Note that, although the dispersed phase volume fraction is 0.5 %, the flux correction and full set of governing equations are used in this case. This verifies the system of governing equations and the numerical scheme for flows in dilute regime.

4.1.2.2 Dense uniform flow

The convection of a dense particle cloud in uniform flow is verified in this test. The domain, the grid resolutions, the boundary conditions and the gas-phase flow parameters are same as that used in the verification test for dilute particle cloud convection. The initial volume fraction of the dispersed phase is set to 5.0% and the radius of each particle is 100.0 μm. The particle cloud is situated between 0.4 m and 0.6 m and convects to a location between 1.4 m and 1.6 m in 10 ms. Here again, grid G3 provides the most accurate results. In this case, unlike the dilute cloud convection, the flux correction in the numerical scheme is not negligible. However, the particle cloud is convected without any error verifying the implementation and accuracy of the governing equations and the simulation strategy. The dense cloud propagation is also tested using EL method by tracking 120000 computational particles (parcels) with 10 particles per parcel. The particle size and the particle cloud dimensions are same as in the EE cases. The particle cloud propagation obtained with EE and EL are in good agreement and this further verifies the EE method for dense particle cloud convection.

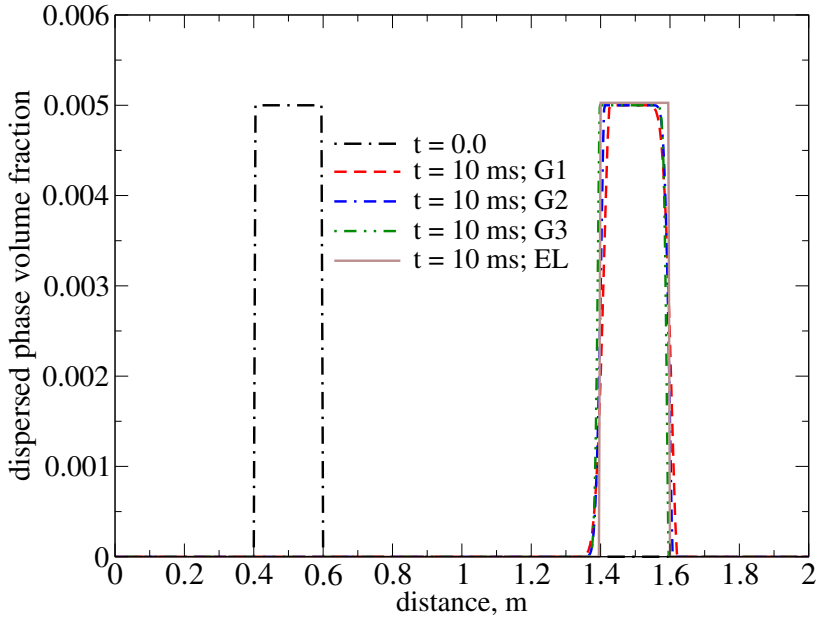

(a)

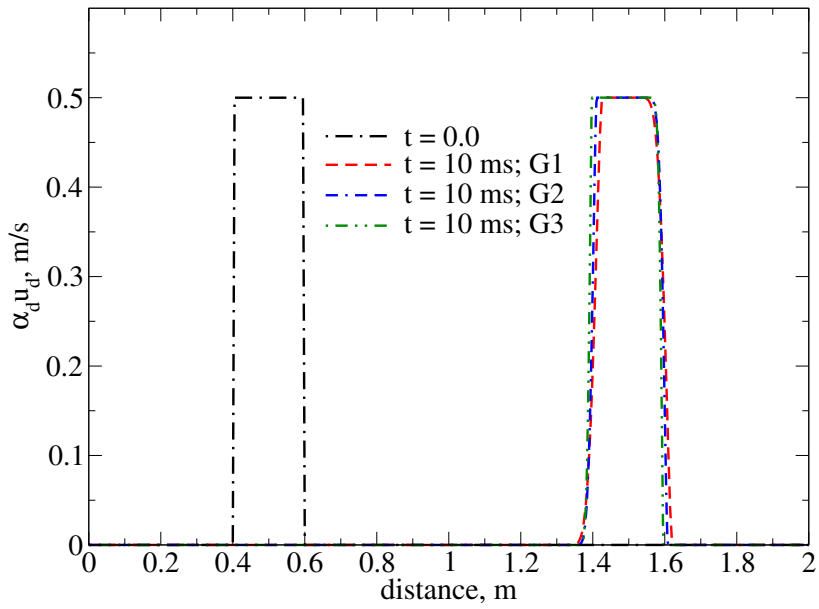

(b)

Figure 14: (a) Dispersed phase volume fraction and (b) the mass flow rate (normalized by the particle density) of the dispersed phase as the dilute particle cloud propagates in a uniform flow

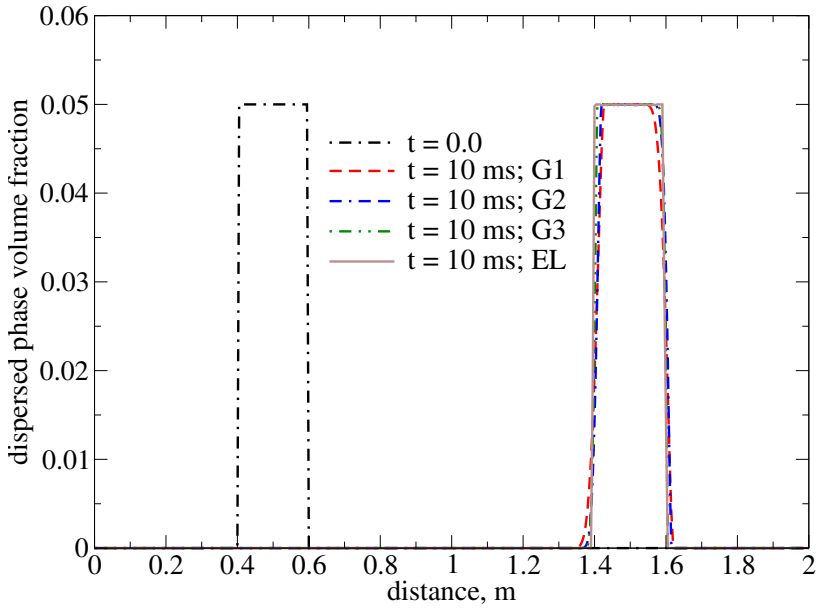

(a)

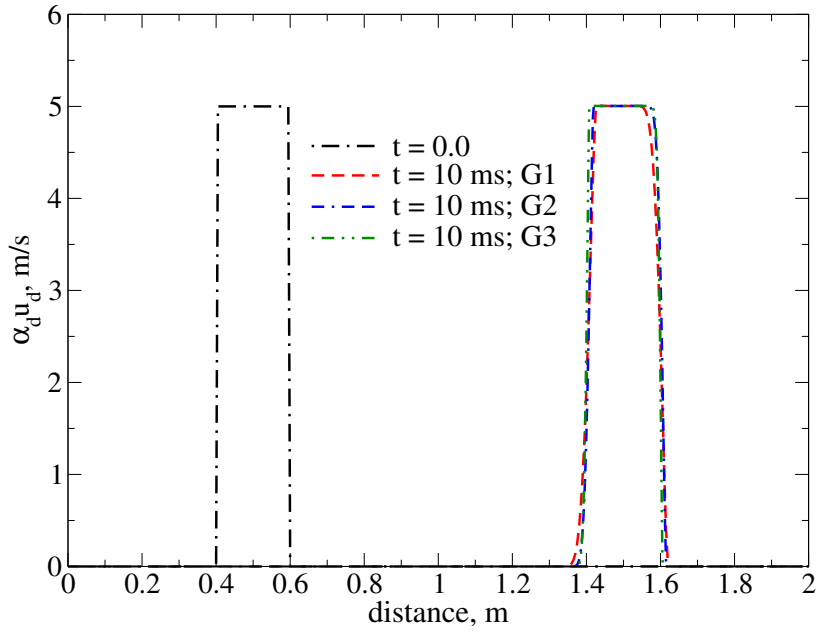

(b)

Figure 15: (a) Dispersed phase volume fraction and (b) the mass flow rate (normalized by the particle density) of the dispersed phase as the dense particle cloud propagates in a uniform flow

4.2 Validation

The validation cases discussed here are chosen to demonstrate the efficacy of the numerical strategy in modeling particle dispersion and the interaction of the flow with the particles. The cases are chosen to progressively span from dilute to dense flow regimes. The validation of EL is discussed in the dispersion, Boiko and Rouge tests. EE validation is discussed in Boiko and Rouge tests along with comparision of the results with EL. Further, validation of EE and comparisons with EL for post-detonation flows are discussed in detail in the following chapters.

4.2.1 Dispersion test

The dispersion of a particle by a shock is simulated to test the solvers ability to model the particle dispersal due to shock-particle interaction. The test is set based on the experiments conducted by Devals et al. [31]. The experiments were conducted in a 3.75 m long shock tube with a cross section 8 cm $\times$ 8 cm. A nylon particle was suspended from the ceiling of the shock tube with the aid of spider webs. A Mach 1.56 shock was allowed to interact with the particle and the trajectory of the particle was recorded. In order to simulate this experimental configuration, a domain with the dimensions same as that of the shock tube dimensions is considered and is resolved using a uniform Cartesian grid of size $375 \times 8 \times 8$. A nylon particle of radius 1 mm and density 1170 kg/m^3 is placed at a location 2.97 m from the high pressure closed end of the shock tube. All the boundaries of the domain are considered to be no-flux boundaries. In order to get a 1.56 Mach shock, a high pressure region is initialized based on the relation

$$\frac{p_4}{p_1} = \frac{2\gamma_1 M_1^2 - (\gamma_1 - 1)}{\gamma_1 + 1} \left[1 - \frac{(\gamma_4 - 1)}{(\gamma_1 + 1)} \frac{a_1}{a_4} \left(M_1 - \frac{1}{M_1}\right)\right]^{\frac{-2\gamma_4}{\gamma_4 - 1}}, \tag{131}$$

where M_1 is the shock Mach number, p_4 is the pressure in the high pressure (driver) section, p_1 is the pressure in the ambient shock tube (driven section), γ_1 is the ratio of the specific heats in the driven section, γ_4 is the ratio of the specific heats in the driver section, and a_1 and a_4 are the speeds of sound in the driven and the driver section, respectively. In this test, both the driven and driver section are filled with air and p_1 is 10^5 Pa. The temperature of

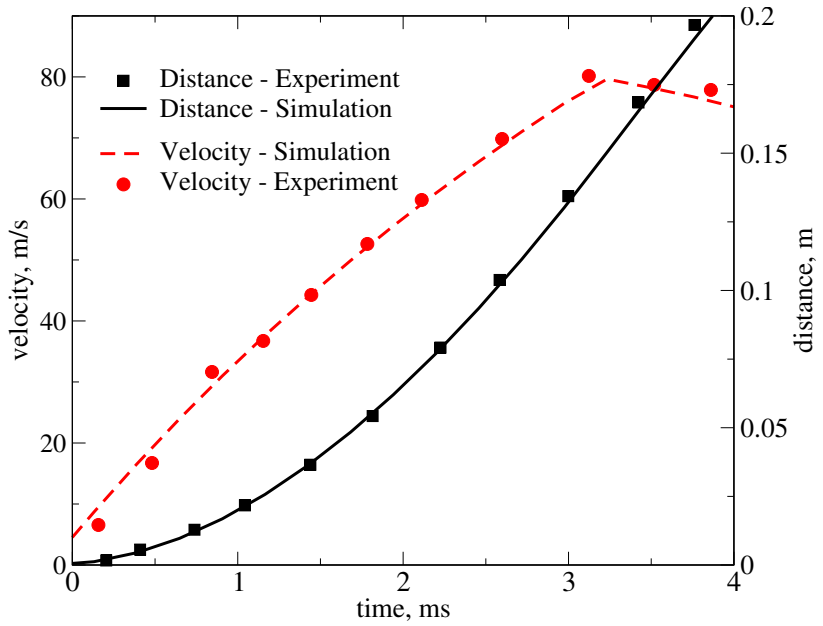

Figure 16: Dispersion of a nylon particle by a shock wave. Data from experiments by Devals et al. [31] is shown for comparison.

the gas and the particle are set to be 298.0 K. The force on the particle is computed based on the drag law provided by Igra and Takayama [58].

When the shock impacts the particle, the particle is accelerated and is swept downstream. The trajectory and the velocity of the particle as it travels along the length of the shock tube are shown in Fig. 16. The numerical results are in good agreement with the experimental observations. The particle velocity becomes almost constant for $t > 3.0$ ms due the shock reflection from the closed end of the shock tube. A small variation (about 2 m/s) in the particle velocity is still observed after the shock reflection due to the inertia of the particle. This feature is captured accurately by the Lagrangian solver.

4.2.2 Boiko test

In this test, the Lagrangian solver is validated by simulating the interaction of a marginally dense particle cloud with a shock wave. The setup for this test is based on the experiments performed by Boiko et al. [23]. A shock tube of length 6.5 m and cross section 52 mm $\times$ 52 mm was used in the experiment and an acrylic plastic particle cloud of initial volume fraction 3.0% was impacted by a Mach 2.8 shock. The radius of each particle is 150 μm

and the density is 1200 kg/m^3. For simulation, a domain with dimensions same as that of the shock tube is considered and is resolved using as grid of size 1250×10. The particle cloud is placed at a location 2 m from the high pressure end of shock tube. The initial width of the particle cloud is 13 mm and the cloud has 74600 particles. The driver section is filled with He and is initialized with high pressure p_4 obtained from Eqn. (131) such that a Mach 2.8 shock interacts with the particle cloud. The driven section is filled with air at 10^5 Pa. The driven section, the driver section and the particle cloud are at 298K, initially. All boundaries of the shock tube are set to be no-flux boundaries except the outflow where the flow properties are extrapolated. The acceleration of the particle is computed using the drag law provided by Boiko et al. [23].

The dispersion of the particle cloud after interaction with the shock wave is shown in Fig. 17. Here, unlike the single particle dispersion case, DEM is turned on and hence the gas-phase fluxes are influenced by the volume of the particles in the flow. The case shows the accuracy of the solver in simulating the particle dispersion for marginally dense clouds.

Boiko test is repeated with EE method using a grid with resolution, $\Delta = 250.0$ μm and the variation of the location of the particle cloud with time is compared with the results from EL method. While EL method accurately captures the particle cloud motion, EE method shows an agreement in initial stages of the cloud dispersal. As the volume fraction of the particle cloud decrease from 0.03 to below the dilute limit (i.e. 0.01), the error in the particle cloud location obtained using EE scheme increases from 1.5 % to 33.0 %. Since, the particle cloud location is dependent on the accurate estimation of the cloud extremities, the error with EE increases in this case. Note that the dilute dispersion with EE is not as accurate as EL as EL accounts for the motion of each particle and accurately determines the particle cloud edges.

4.2.3 Rouge test

Propagation of a shock wave through dense particle cloud is simulated using both EE and EL methods to validate both the methods and investigate the importance of the gas-phase flux correction based on the particle volume fraction. The setup for this test is based on the

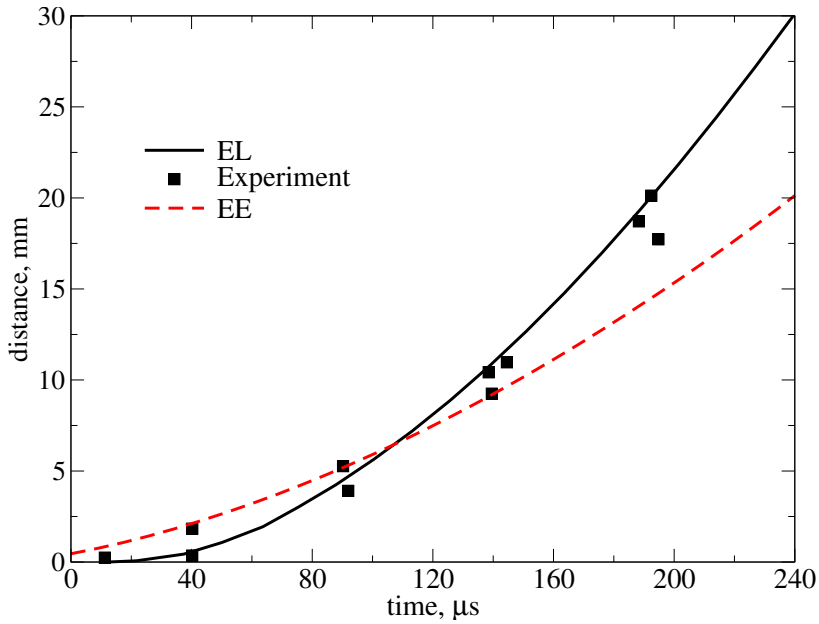

Figure 17: Dispersion of particle cloud by a shock wave. The experimental data is from [23]

experimental configuration described by Rouge et al. [101]. A vertical shock tube of length 6 m and cross section 13 cm $\times$ 13 cm has been employed in the experimental investigations. Glass particles of radius 750.0 μm are placed in the shock tube and are initially supported by a membrane. A Mach 1.3 shock is allowed to interact with the particles which initially form a bed of thickness 2 cm and volume fraction 65%. For simulations, the geometry of the domain is set to be same as the experimental configuration and is resolved using a grid of size $600 \times 13 \times 13$. In order to perform simulations using EL solver, 15540 computational particles, i.e., parcels, are initialized with 8 particles per parcel. The shock tube is filled with air and the pressure in the driver section is set based on Eqn. (131). The pressure in the driven section is 10^5 Pa, initially. The initial temperature of the particles and the gas is at 298 K. The velocity of the particles is computed based on the quasi-steady drag relation described by Crowe et al. [30]. All walls of the shock tube are set to be no-flux boundaries except the outflow (the end away from the high pressure driver section) where the flow properties are extrapolated.

The pressure at locations 11 cm below the particle bed and 72 cm above the particle bed

are recorded and compared with the experimental results. As the shock interacts with the dense particle bed, a transmitted shock propagates through the particle cloud and a reflected shock wave propagates upstream. In order to capture the pressure accurately, the gas-phase flux correction based on the volume fraction of the dispersed phase is very important. This is demonstrated in Fig. 18. In the case without DEM, the upstream pressure is under predicted and the downstream pressure is over predicted. Also, the downstream shock wave propagates through the particle cloud at relatively greater speed and reaches the upstream pressure trace point nearly 0.4 ms earlier. Thus, DEM is important to predict the gas-phase and the dispersed phase properties and its significance is increased with increase in the dispersed phase volume fraction.

For this test, the numerical simulations are performed using both EE and EL methods. The cases with EE are performed with and without the contribution from granular friction (p_f) and granular viscous dissipation terms ($\dot{\gamma}$ and ϕ). Figure 18 shows that the effect of friction and the granular viscous terms is not significant. Both EE and EL methods produce similar results and are in good agreement with the experimental results. The results with the combined EE-EL method, where the dispersed phase is transitioned from EE method to EL method if the Eulerian dispersed phase volume fraction reaches 0.01, are also in good agreement with the results from the experiment and the simulations using pure EE and pure EL methods.

4.3 Summary

The verification and validation tests described in this chapter provide the required confidence in the simulation strategy. In particular, the cases presented show that the parallel Lagrangian solver can accurately track particles across different cores. Also, the solver is able to handle both dense and dilute flow regimes. Both EE and EL are able to handle dispersed phase volume fractions up to 0.74 (the packing limit). However, the accuracy of EE is relatively poor in cases with $\alpha_d < 0.01$. The validation performed proves the efficacy of the solver to model particle dispersion and shock-particle interaction in flows with a wide range of dispersed phase volume fraction. Further, the cases show the need to used DEM.

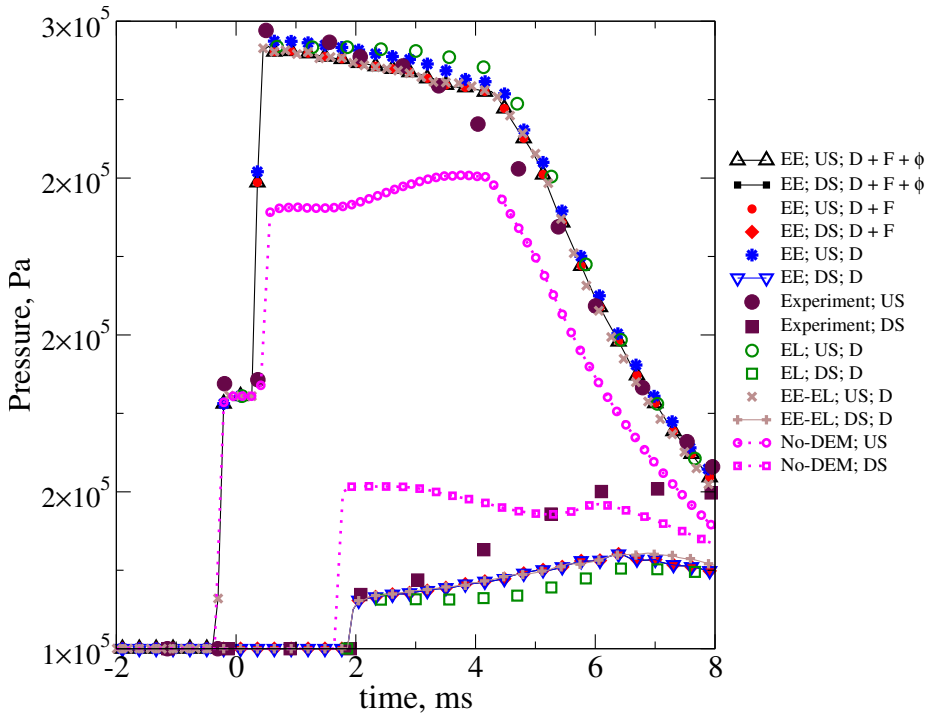

Figure 18: Comparision of pressures upstream (US) and downstream (DS) of a dense particle cloud. The experimental data is from [101]. The results with EE, EL and EE-EL are shown. Also, EL case without DEM is shown (No-DEM). Here, D, F and ϕ indicate the drag term, the friction term and the viscous dissipation of the granular energy. In each case, the terms considered are shown.

The validation and verification show that EE and EL provide similar results. In the following chapters, further analysis and comparision of EE and EL methods for post-detonation flows are discussed with an aim to describe appropriate range of dispersed phase volume fraction for each method.

CHAPTER V

COMPARISION OF EULERIAN-EULERIAN AND EULERIAN-LAGRANGIAN METHODS FOR POST-DETONATION FLOWS

The impulse generated by explosions is routinely augmented by the addition of metal particles. Explosive charges packed with metal particles are called heterogeneous explosives, and those without particles are called homogeneous explosives. In this chapter, first, simulation of post-detonation flows formed after detonation of homogeneous explosive charges is discussed. A blast wave followed by the hot detonation product gases are the main constituents of the post-detonation flow. The variation in the density of the gases and the acceleration of the flow induces hydrodynamic instabilities and generates a mixing zone. It has been established by past investigations [18, 64] that the flow is accelerated via RTI in the initial stages and later by RMI due to the shock-mixing zone interaction. Combustion of unburnt gases and hence the heat release due to afterburning is dependent on the mixing in the flow ensuing the explosion. Thus, it is vital to understand the development of the mixing zone and the blast wave propagation to characterize the post-detonation flow and afterburn. Further, studies with homogeneous charges are used to establish the problem setup used for the rest of this thesis.

Followed by the analysis of flow ensuing homogeneous explosion, numerical modeling of heterogeneous explosion is discussed. When detonated, heterogeneous charges, disperse the particles packed in them, which carry the momentum and the energy from the initial explosion. Before comparing EE and EL methods for simulation of explosive dispersal of dense particle clouds, the process of particle dispersal in the post-detonation flow of heterogeneous explosion using EL method is described. The volume fraction of the particles in the explosive charge is varied along with the radius of the metal particles to analyze the variation in the blast and the particle trajectories. In each case, EE and EL methods

are compared and the regimes where EE and EL predictions are in good agreement are identified.

5.1 Homogeneous explosive

An explosive charge is composed on highly reactive material. This material when ignited reacts rapidly and generates high pressure and high temperature zones leading to a blast wave. With suitable conditions, most modern explosives, detonate and deliver greater impact in comparision to explosions initiated without a detonation. The detonation front in the explosive charge can be described as a high pressure and a high temperature reaction zone separating the unburnt explosive and the detonation product gases. Unlike detonations in most gaseous mixtures, the detonation in a explosive material like NM, Tri-Nitro-Toluene (TNT) or High-Melting-Explosive (HMX), develops a strong blast wave with the the pressure at the primary blast front in the order of $10^9 - 10^{12}$ Pa. This high pressure is very useful to provide the required impact on target structures and can be further augmented by the afterburn processes.

Before proceeding to investigate the post-detonation flows with metal particles or droplets, analysis of pure gaseous post-detonation flow is discussed. Post-detonation flow emanating from the explosion of a 11.8 cm diameter spherical NM charge is considered for this purpose. The conditions used and the numerical setup to simulate the post-detonation flow are described in this section. Also, the flow and the processes that influence the afterburn are discussed.

5.1.1 Problem setup

Numerical simulation of homogeneous explosion involves accurate capture of the primary blast wave, the secondary shock wave and the mixing zone. The shock waves emanating from the center of the charge, hence forth called the origin, must retain their symmetry as expected. All the relevant scales of the mixing zone must be resolved. In order to satisfy these constraints, a sector grid, which confirms to the shape of the explosive charge, is used [18, 53]. The initial conditions, the grid resolution, and the boundary conditions used are described below. Note that the procedure to set the initial conditions, the sector grid

configuration, and the boundary conditions described in this section are identical to those used in the studies discussed in the subsequent sections and chapters. However, the domain size, the properties of the explosive charge, and the ambient conditions are varied and are provided for each case throughout the thesis.

5.1.1.1 Initial conditions

To carry out studies in the post-detonation flow, the initial detonated explosive charge is modeled using the Gas-Interpolated-Solid Stewart-Prasad-Asay (GISPA) method [18, 11, 123]. The detonation profiles obtained from GISPA method provide the initial flow properties, i.e., p_g, ρ_g, T_ga and $u_{r,g}$. Here, $u_{r,g}$ is the radial velocity of the gas-phase. Further, if metal particles are present in the explosive charge (Heterogeneous explosive), the initial dispersed phase velocity and the initial dispersed phase temperature are also solved for using GISPA method. Further details of GISPA are provided elsewhere [18, 11].

A domain of length 2.4 m in radial (R) direction and 45^o in the azimuthal (θ) and zenith (Φ) directions is considered. The radial extent of the domain is chosen based on the strength of the charge and past numerical simulations. For a NM charge of 11.8 cm diameter, the maximum radial extent of 2.4 m is sufficient to study the blast wave propagation and the mixing layer characteristics. The domain is resolved using a $1000 \times 60 \times 60$ grid, i.e., in R, θ and Φ directions, respectively. Grids of sizes $1000 \times 45 \times 45$ and $1000 \times 75 \times 75$ have also been considered. Figure 19 shows no variation in the flow features with different grid configurations, and $1000 \times 60 \times 60$ grid is considered for all studies since it is optimal for the problems under consideration. A full spherical grid of size $1000 \times 200 \times 200$ is also used here. The mixing zone characteristics and the blast propagation from the full sphere grid and the sector grid have been in good agreement. Since it is computationally expensive to carry out multiple simulations using full spherical grid, the studies conducted here use the sector grid.

The ambient conditions are set to be air at 10^5 Pa and 300 K. The charge dimensions and the ambient conditions are chosen based on experiments by Zhang et al. [129] which allows for comparisons with experimental data wherever available. JWL equation of state

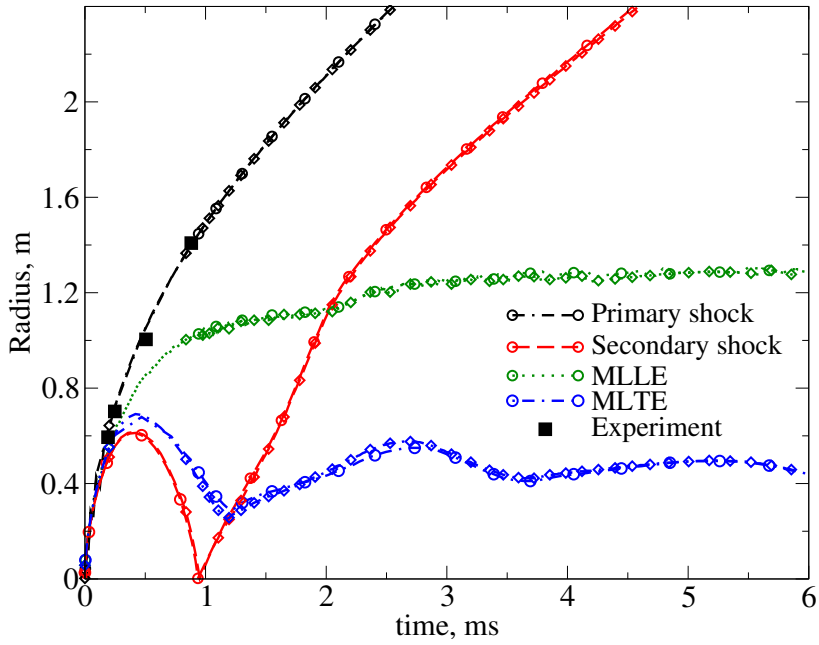

Figure 19: Position of the primary shock, secondary shock, leading edge of the mixing layer (MLLE) and trailing edge of the mixing layer (MLTE) in the post-detonation flow of a 11.8 diameter homogeneous NM explosive charge. The experimental results are from [129]. Results with $1000 \times 45 \times 45$ grid are indicated with diamonds and with $1000 \times 60 \times 60$ grid are indicated with squares.

is used in all cases presented in this chapter. The detonation product species are computed based on the dissociation reaction for NM given as

$$CH_3NO_2(NM) \rightarrow 0.5N_2 + CO + H_2O + 0.5H_2. \tag{132}$$

In addition to these species CO_2 and O_2 are also considered as they are present in the products of the afterburn and ambient air, respectively. A Gaussian perturbation is introduced in the species profile to model the natural imperfections on the charge surface or the variations at the molecular level, which enable the development of the hydrodynamic instabilities due to RTI and in later stages due to RMI.

5.1.1.2 Boundary conditions

One of the issues while using a grid confirming to spherical geometry is the boundary at the origin. Since structured Cartesian mesh is used to discretized the domain, it is not possible to perfectly align the grid with the charge and resolve the origin. To overcome

this problem, a small portion (of radius 2.4 mm) of the charge at the center is removed and a no-flux boundary condition is imposed. This method has been applied earlier with great success and can describe the post-detonation flow with good accuracy [15, 18, 53]. A no-flux boundary condition is also imposed in θ and Φ directions. At the boundary in the radial direction away from the origin, the flow properties are extrapolated. Note that the simulations performed with full sphere (without no-flux boundaries) [36, 37, 51] are in agreement with the studies discussed here and hence these boundary conditions are employed throughout this thesis.

If particles are present in the flow, the particles are assumed to undergo elastic reflection from the wall boundaries and are removed from the domain if they encounter the outflow. If the dispersed phase is computed using Eulerian approach, the properties at boundaries are set similar to the corresponding gas-phase properties.

5.1.2 Chronology of the post-detonation flow

When a spherical homogeneous charge is detonated, the events following the detonation can be summarized in four phases as (i) blast wave phase, (ii) implosion phase, (iii) res-shock phase and (iv) asymptotic mixing phase. The blast wave produced by the detonation propagates outwards away from the center along with the hot detonation product gases during the first phase. As the gases accelerate behind the blast wave, the initial perturbations at the contact surface of the detonation product gases and ambient air results in development of hydrodynamic instabilities. The variation in the location of the primary blast wave time is shown in Fig. 19 and is compared with the experimental data [129]. The trajectory of the blast wave is accurate. As the blast wave propagates further, an over-expansion of the expansion wave behind the blast results in the formation of a secondary shock wave. The secondary shock wave initially is swept away from the origin and later moves towards the origin. This motion leads to the implosion phase where the secondary shock reflects from the origin and propagates outwards. During the implosion phase, the gases are also pulled towards the origin and the width of the mixing layer increases. This is shown in Fig. 19. Here, the radial location of the mixing layer boundaries are calculated as r_{MLTE}

$= r|_{Y_{CO}=0.9Y^i_{CO}}$ and $r_{MLLE} = r|_{Y_{CO}=0.1Y^i_{CO}}$, where Y^i_{CO} is the initial mass fraction of CO in the detonation product gases. Figure 20 shows the flow features during the implosion phase. The generation of the bubble and spike structures in the flow due to RTI is noticed in Fig. 19 (a). Also, the formation of 'finger-like' projections is shown in Fig. 21.

The secondary shock wave propagates outwards from $t > 1.0ms$ and interacts with the mixing zone. During this re-shock phase, the structures already present in the flow interact with the shock wave and develop further hydrodynamic structures due to RMI. RMI enhances the mixing and afterburn in the flow. Also, the mixing zone develops a turbulence-like structure with the width of mixing zone being almost constant. This phase of asymptotic mixing shown in Fig. 20 (g)-(i) continues as the combustion due to the afterburn consumes the unburnt detonation product gases.

5.2 Heterogeneous explosive

Before comparing EE and EL methods for heterogeneous explosion modeling, the post-detonation flow formed due to the detonation of a 11.8 cm diameter NM charge packed with steel particles is discussed. The radius of each particle (r_p) is 231.5 μm and the initial dispersed phase volume fraction (α_{p_0}) is 0.62. The dispersed phase parameters are chosen based on the experimental studies by Zhang et al. [129]. The quasi-steady drag on each particle is computed using the drag law provided by Akhatov and Vainshtein [3]. The domain dimensions are 2.4m, 20^o and 20^o in R, θ and Φ directions, respectively. A grid of size $1000 \times 10 \times 10$ is used here and has been found to be sufficient for EL method [19]. The initial profile for the charge, the detonation product composition and the ambient environment is set as described in the case of homogeneous charge in the previous section. Also, the boundary conditions are identical to the those described in the previous section.

The detonation of the spherical heterogeneous NM charge results in a post-detonation flow with dense particle clouds. The chronology of this post-detonation flow can be described based on the location of the particle front and the blast front. In early stages, due to the inertia, the particles in the explosive charge lag behind the blast wave and the contact surface between the detonation product gases and ambient air. The acceleration of the contact

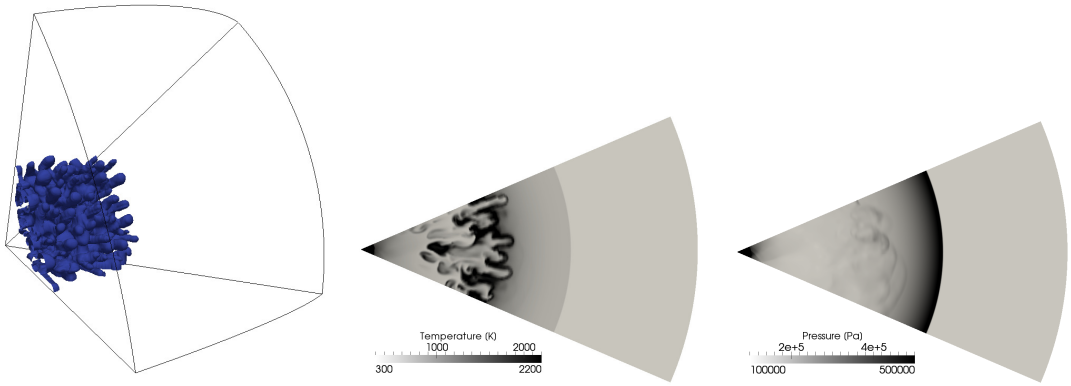

(a) $Y_{N_2} = 0.5$; t = 1.0 ms (b) T_g; t = 1.0 ms (c) p_g; t = 1.0 ms

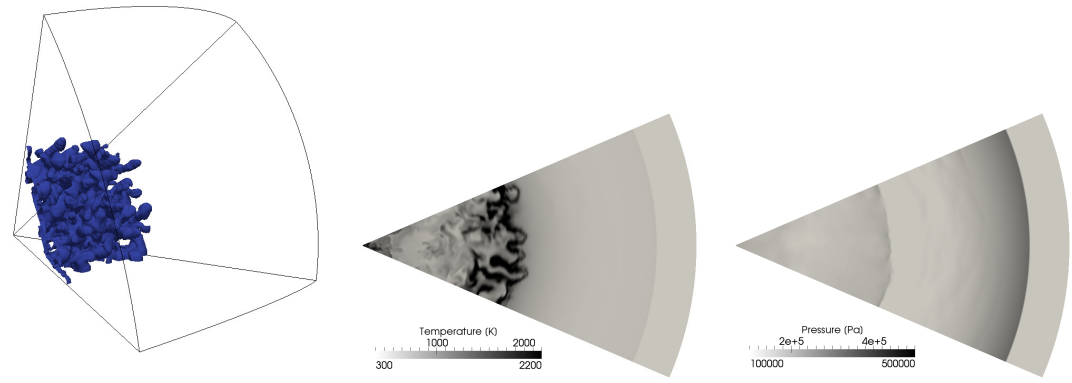

(d) $Y_{N_2} = 0.5$; t = 2.0 ms (e) T_g; t = 2.0 ms (f) p_g; t = 2.0 ms

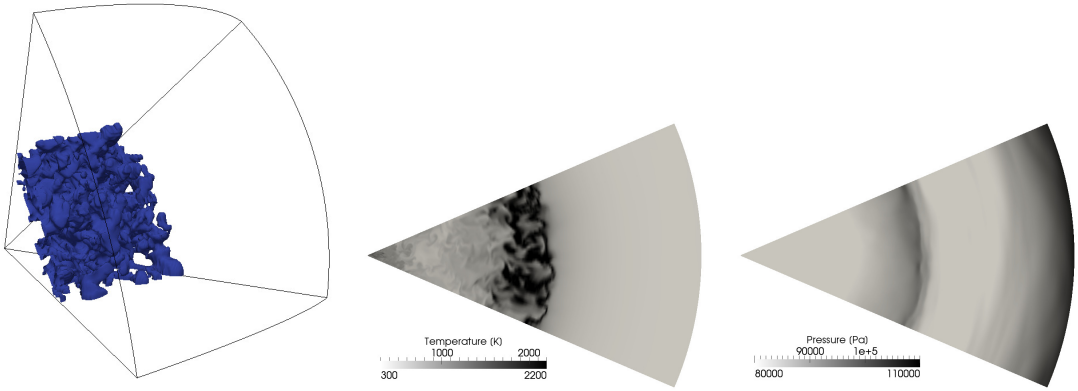

(g) $Y_{N_2} = 0.5$; t = 4.7 ms (h) T_g; t = 4.7 ms (i) p_g; t = 4.7 ms

Figure 20: Temperature, pressure and the mixing zone in the post-detonation flow of a 11.8 cm spherical NM charge. (a)-(c) correspond to implosion phase, (d)-(f) correspond to reshock phase, and (g)-(i) correspond to asymptotic phase. The scale of temperature and pressure is identical for all figures.

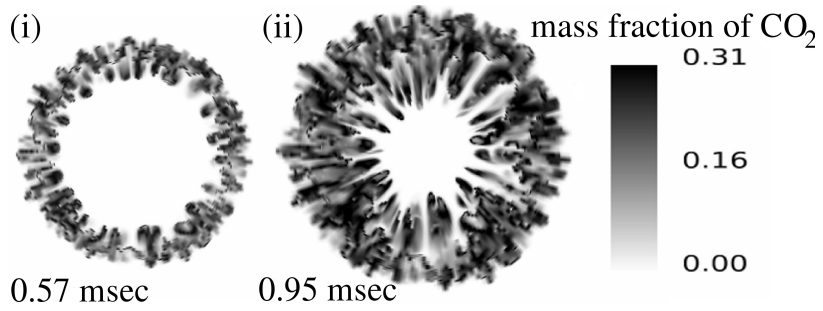

Figure 21: Formation of CO_2 due to afterburn in the post-detonation flow of a homogeneous nitromethane charge during (i) blast wave and (ii) implosion phases.

surface, as in the cases of homogeneous charges, results in the generation of hydrodynamic structures due to RTI. The particles absorb the momentum from the accelerating gases, and overtake the contact surface and the blast wave by t = 0.51 ms, as shown in Fig. 22. The inertia of the particles enables them to lead the blast wave at late times. The volume fraction of the dispersed phase is reduced as the particles disperse and the flow transitions to dilute regime away from the origin. These events in the post-detonation flow are shown in Fig. 23. Note that the particles are rarefied at the particle front (as shown in Fig. 23 (d)) and hence the particle front, in Fig. 22, is computed as the radial location that includes 98.0% of the particles in the flow.

5.3 Comparision of EE and EL methods

In order to compare EE and EL methods, described in Chapter 3, simulations are performed considering explosive charges with different initial dispersed phase volume fraction (α_{d_0} or α_{p_0}) and different particle sizes. These cases along with the parameters for each case are summarized in Table 4. The particle dispersion using each method and the role of dispersed phase parameters are discussed below.

5.3.1 Comparision of dispersion

The blast front obtained from the EE and EL method are almost identical and are shown in Fig. 24. The location of the blast front for each method is computed and shown in Fig. 22. The blast front trajectory predicted by EE and EL are in good agreement. In order to test the dependence of results using EE on the grid employed, the grid size has been

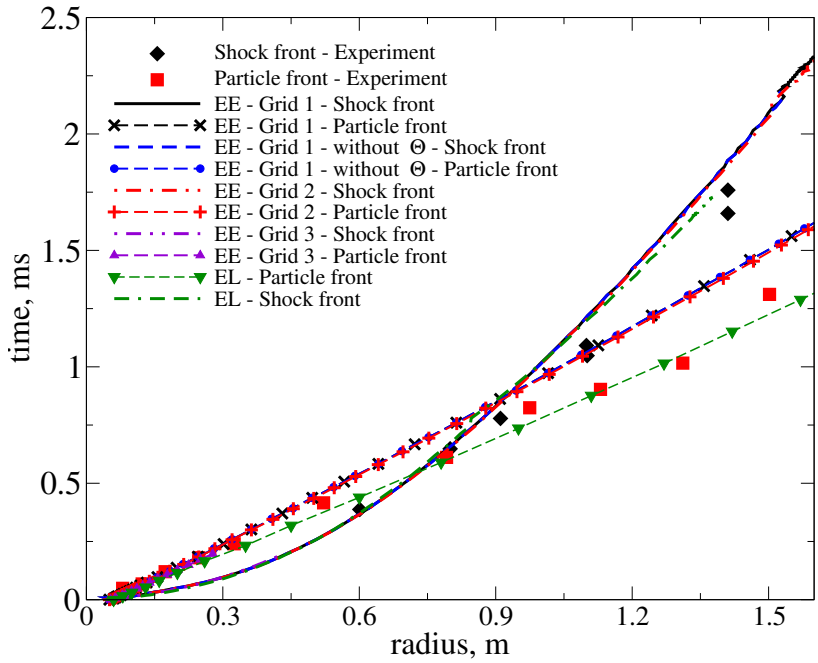

Figure 22: Location of the blast front and the particle front (with symbols) after detonation of a 11.8 cm diameter NM charge with steel particles (initial $\alpha_p = 62.0$ % and initial $r_p = 231.5$ μm). Experimental data is from [129].

Table 4: Parameters used to compare EE and EL methods to simulate the post-detonation flow.

Case	α_{p_0}	r_p μ m	particles per parcel	Number of parcels	Number of particles
VF1R1	0.62	231.5	3	30700	92100
VF1R2	0.62	100.0	12	95265	1143180
VF1R3	0.62	50.0	100	91454	9145400
VF2R1	0.31	231.5	3	15339	46017
VF2R2	0.31	100.0	12	47620	571440
VF2R3	0.31	50.0	100	45716	4571600
VF3R1	0.155	231.5	3	7658	22974
VF3R2	0.155	100.0	12	23798	285576
VF3R3	0.155	50.0	100	22847	2284700

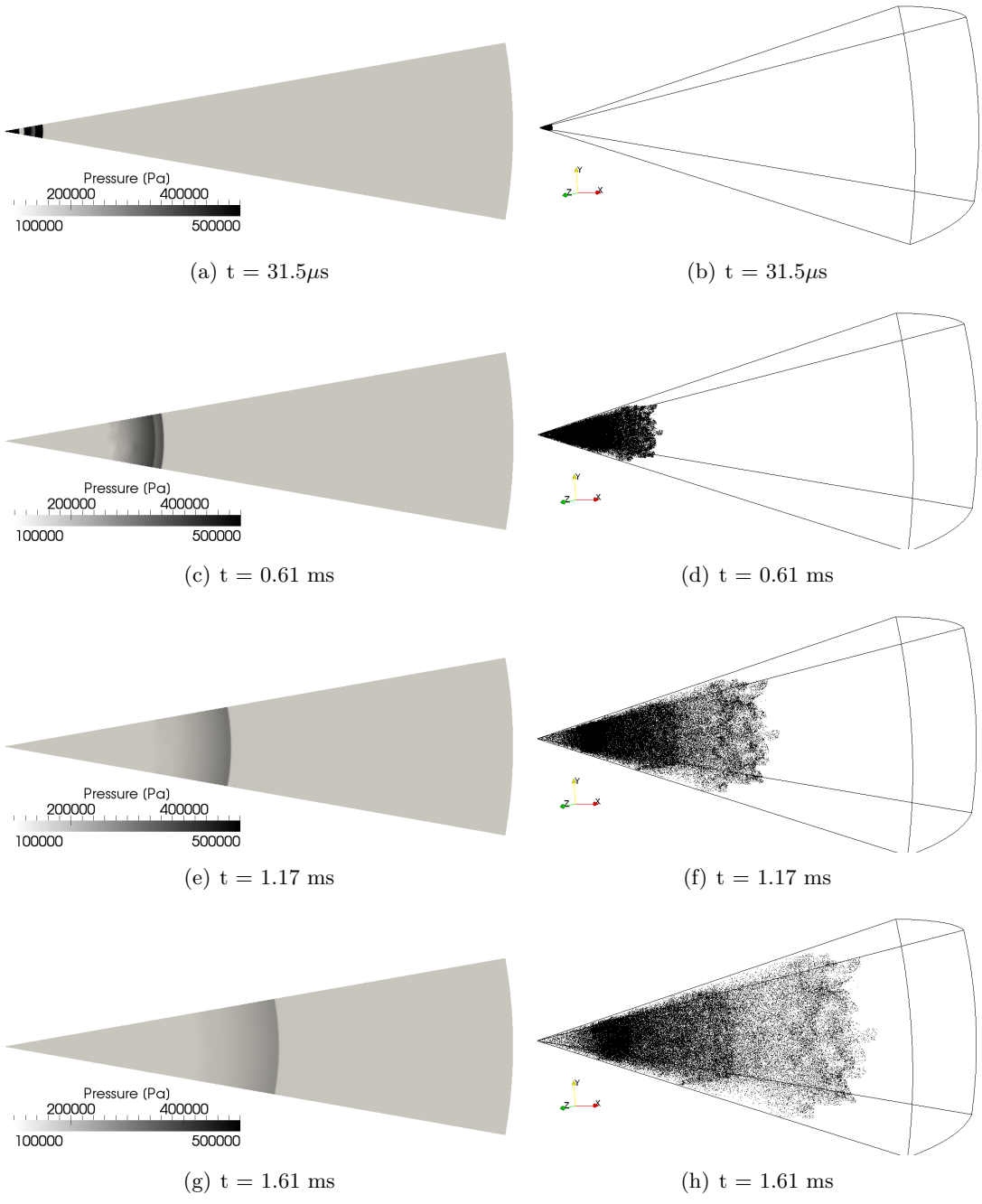

(a) t = 31.5μs (b) t = 31.5μs

(c) t = 0.61 ms (d) t = 0.61 ms

(e) t = 1.17 ms (f) t = 1.17 ms

(g) t = 1.61 ms (h) t = 1.61 ms

Figure 23: The blast front location (a, c, e, and g) and the location of the particles (b, d, f, and h) in the flow after detonation of a 11.8 cm heterogeneous NM charge with α_{p0} = 62.0 % and r_p = 231.5 μm.

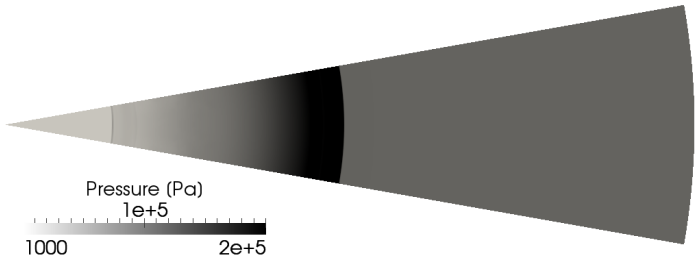

(a) EE

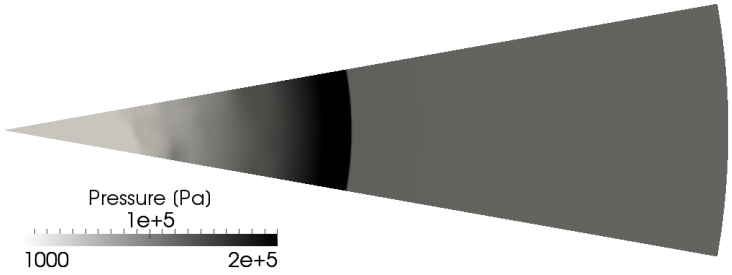

(b) EL

Figure 24: Comparision of the blast front location computed using EE and EL methods at t = 1.17 ms. The scale of pressure is identical in both the figures.

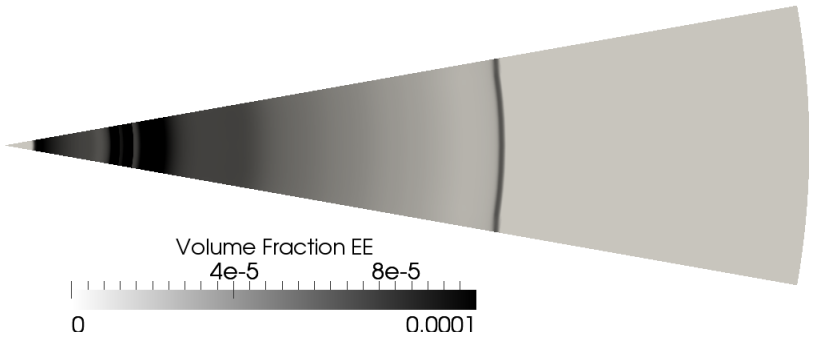

(a) EE

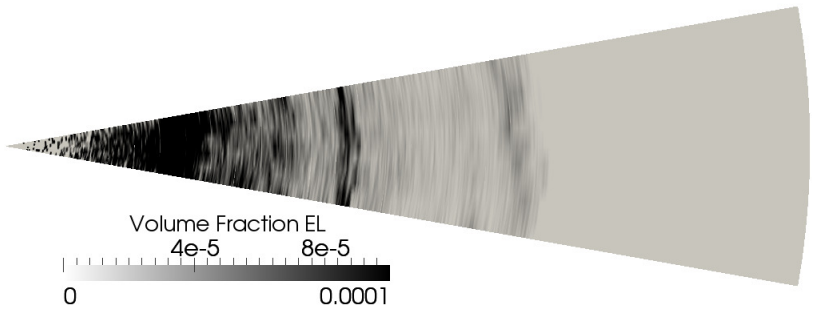

(b) EL

Figure 25: Comparision of the dispersed phase volume fraction computed using (a) EE and (b) EL methods, respectively, at t = 1.17 ms.

varied. Three grids of sizes $1000 \times 20 \times 20$ (G1), $1000 \times 10 \times 10$ (G1) and $2000 \times 20 \times 20$ (G3) are considered. The particle and the blast trajectories obtained using G1, G2 and G3 are in good agreement. Henceforth for EE cases, G1 is used for all the studies mentioned. The change in the blast front or the particle front has been negligible when EE method is used without the granular energy term. Thus, for the explosive particle dispersal, the granular energy does not play any significant role. This is due to the existence of the flow in dense regime for relatively short time i.e. about 100 μs. Note that the granular energy is dominant in dense flows, especially near the packing limit.

The dispersion of the particles in the post-detonation flow using EE and EL methods is compared by tracking the particle front. Also, the volume fraction of the gas-phase and the dispersed phase throughout the domain is compared (as shown in Fig. 25). The particle front location predicted by the EE method varied from the values predicted by the EL method. At $t = 1.25$ ms, the particle front simulated using EE is at the radial location, $R = 1.2$ m where as the particle front obtained using EL method is at $R = 1.5$ m. Thus, the value from EE method has an error of about 20.0 %. EL method is in good agreement with the experimental values (See Fig. 22) while the solution using EE provides a particle front moving relatively slowly. EE method is not accurate as the particle flow transitions to a dilute regime and rarefies. This is observed from the variation in the error in the particle front location from 14.0 % at $t = 0.5$ ms to 20.0 % at $t = 1.25$ ms. EE method is based on the continuum assumption for the particles and is applicable in cases with sufficient number of particles per computational cell. The number of particles, based on the point-particle assumption ($d_p \leq 0.1\eta_k$), for EE is nearly 500 for initial volume fraction 0.5. However, as discussed in Chapter 2, this criteria is relaxed since a fully resolved simulation for the current cases is not feasible in the foreseeable future. The predictions using EE, in most cases, are not reliable when the mean distance from the particles is in the order of the computational cell width. Since each individual particle is solved in EL method, EL method does not encounter this issue.

With a decrease in the particle size for the same initial volume fraction of the particles in the charge, the particle number density, i.e., number of particles per computational cell,

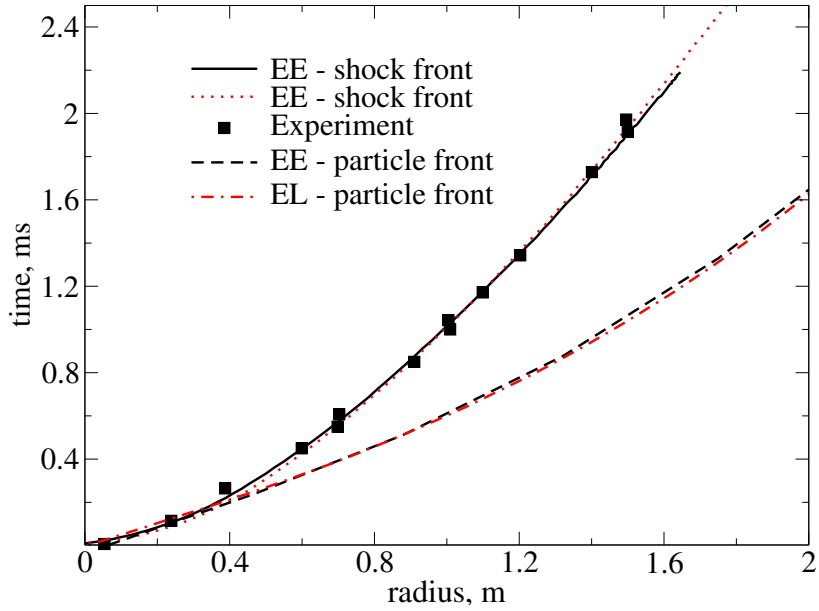

Figure 26: Location of the blast front and the particle front after detonation of a 11.8 cm diameter NM charge with steel particles (initial $\alpha_p = 62.0$ % and initial $r_p = 50.0$ μm). Experimental data from [129] is shown as squares.

increases. For example, a change in the particle size from 100 μm to 50 μm results in an 8 fold increase in the particle number density (for a given α_p and computational cell volume). It is expected that with increase in the particle number density the accuracy of EE method is improved. To test this, an explosive charge with $r_p = 50$ μm and initial dispersed phase volume fraction 0.62 is considered. The trajectory of the blast front obtained using both EE and EL methods in this case match well with the experimental observations (See Fig. 26). A comparision of the particle front trajectories obtained using EE and EL methods shows a good agreement (error at $t = 1.25$ ms is 1.7 %) unlike the case with $r_p = 231.5$ μm (with error 20.0% at $t = 1.25$ ms). Thus, with decrease in the particle size, for a given initial volume fraction, the accuracy of the solution using EE method increases.

5.3.2 Role of initial volume fraction

The propagation of the blast wave and the subsequent particle dispersion are influenced by the volume fraction of the particles in the explosive charge. To understand the effect of the particle volume fraction, explosive charges with initial dispersed phase volume fraction 0.62,

0.31 and 0.155 are considered. The energy and the momentum absorbed by the dispersed phase from the gas-phase increases with increase in the dispersed phase volume fraction. Also, for two given particle clouds, one denser than the other, the blast wave transmitted through the denser cloud is weaker. For example, at $t = 1.5$ ms, the blast wave from the charge with the initial $\alpha_p = 0.155$ reaches the radial location $R = 1.425$ m where as the blast wave from the charge with the initial $\alpha_p = 0.62$ reaches the radial location $R = 1.275$ m (See Fig. 27). This is due to the reflection of waves from the particle cloud and the amount of gas-phase flux transmitted. Thus, for a given particle size, the velocity of the blast front is reduced as the volume fraction is increased, i.e., about 10.0 % velocity reduction for a change in α_p from 0.155 to 0.62. The pressure at the blast wave is also reduced (about 0.1 MPa) with increase in the dispersed phase volume fraction from 0.155 to 0.62. The pressure at the blast wave and the variation in the blast wave location with time, shown in Figs. 27 and 28, show these effects.

The location of the blast front and the pressure at the blast front obtained using EE and EL are in good agreement (at most 5.0 % difference) for all volume fractions. This is expected as the gas-phase flux computation described by the numerical approach in Chapter 3 is identical for both EE and EL methods. This also shows that the dispersed phase volume fraction computed by both the methods, at least in marginally dense and dense regimes, is identical. Note that the blast wave characteristics could have significantly varied if the values of the dispersed phase volume fraction obtained from EE and EL methods varied significantly. Thus, both EE and EL methods perform well in predicting gas-phase properties and are in agreement as along as the flow is at least marginally dense.

The location of the particle front varied, for a given initial dispersed phase volume fraction, based on the amount of energy and momentum transferred to the dispersed phase. The particles initially in the charge and later after the formation of the blast wave absorb energy and momentum from the flow. With increase in the volume fraction for a given particle size, the amount of energy transferred is increased. Thus, the motion of the particle front for denser charges is relatively faster, i.e., as α_{p_0} or α_{d_0} increases from 0.155 to 0.62 the velocity of the particle front increases from 1000 m/s to 1250 m/s (for $r_p = 231.5$ μm).

The difference in the particle front velocity for different cases is evident for cases VF1-3R1 and VF1-3R2 in Table 4 and is shown in Figs. 30 and 31.

5.3.3 Role of initial particle size

For a given initial dispersed phase volume fraction, the effect of particle size on the blast wave propagation and the pressure, which determines the impulse, is not significant. The dominant effect of the dispersed phase on the propagation of the blast wave and the post-detonation flow is due to the blockage provided by the volume occupied by the particles. Thus, irrespective of the particle size, for the same volume fraction, the velocity of the blast wave and the pressure at the blast front are nearly equal. This is shown in Figs. 28 and 32.

The particle front, however, is influenced by the particle size. Small particles achieve equilibrium with the gas-phase at a faster rate. This allows for the particles with smaller radius, for the same initial dispersed phase volume fraction, to achieve relatively greater speed, and hence, higher velocities are recorded for the particle fronts with 50.0 μm particles. The particle fronts for $r_p = 100.0$ μm and $r_p = 231.5$ μm are also compared in Figs. 30 and 31, and show similar trends. The agreement between EE and EL is better for small particles at a given volume fraction. As already discussed, EE is better suited to problems with particles in non-rarefied zones. Hence, for $\alpha_d = 0.62$, 0.31 and 0.155, the error in the particle front location computed using the EE approach is reduced from about 20.0 % to nearly 1.0 % as the particle radius is decreased from 231.5 μm to 50.0 μm.

5.4 Summary

The post-detonation flow formed after the detonation of a 11.8 cm diameter spherical homogeneous explosive is simulated. A sector grid is used to perform the three-dimensional numerical simulations. The trajectory of the blast wave and the ensuing flow are accurately modeled. Different phases of the post-detonation flow are described. The formation of the secondary shock and the re-shock event leading to the asymptotic mixing regime are simulated. These simulations of homogeneous explosive in pure gaseous mixture not only provide the chronology of the post-detonation flow but also validate the numerical approach to simulate the post-detonation flow.

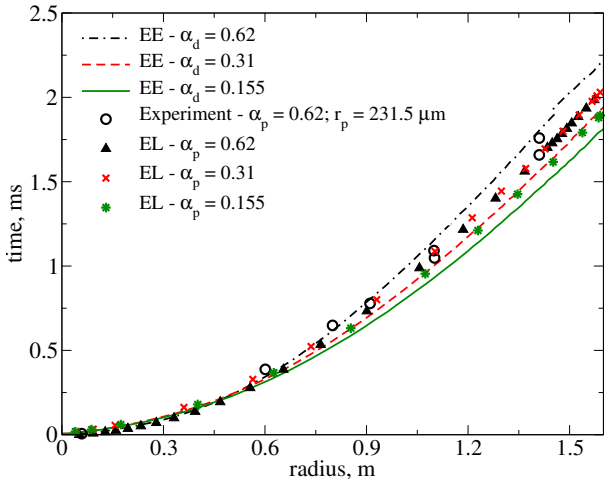

(a) $r_p = 231.5\ \mu$m

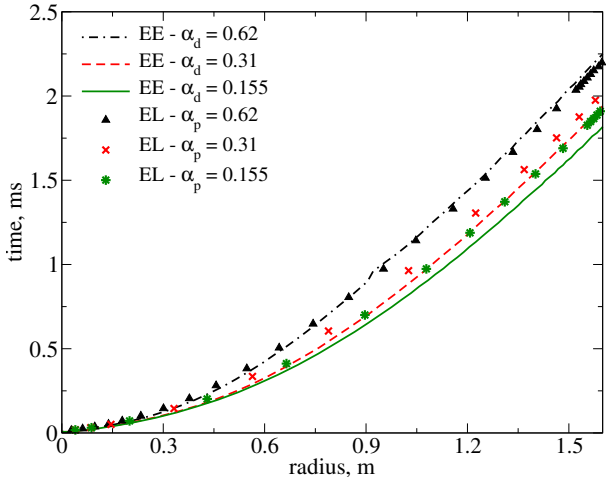

(b) $r_p = 100.0\ \mu$m

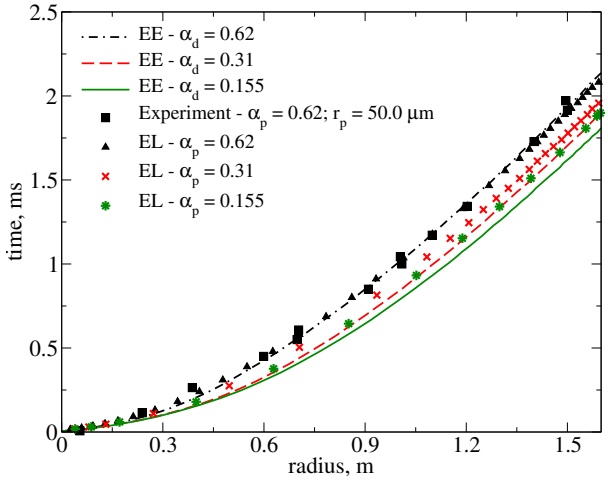

(c) $r_p = 50.0\ \mu$m

Figure 27: Location of the blast front after detonation of a 11.8 cm diameter NM charge with steel particles computed using EE and EL approaches for different initial dispersed phase volume fractions. Experimental data is from [129]. Note that α_p is the initial volume fraction of the dispersed phase (EL), α_d is the initial volume fraction of the dispersed phase (EE), and r_p is the particle radius.

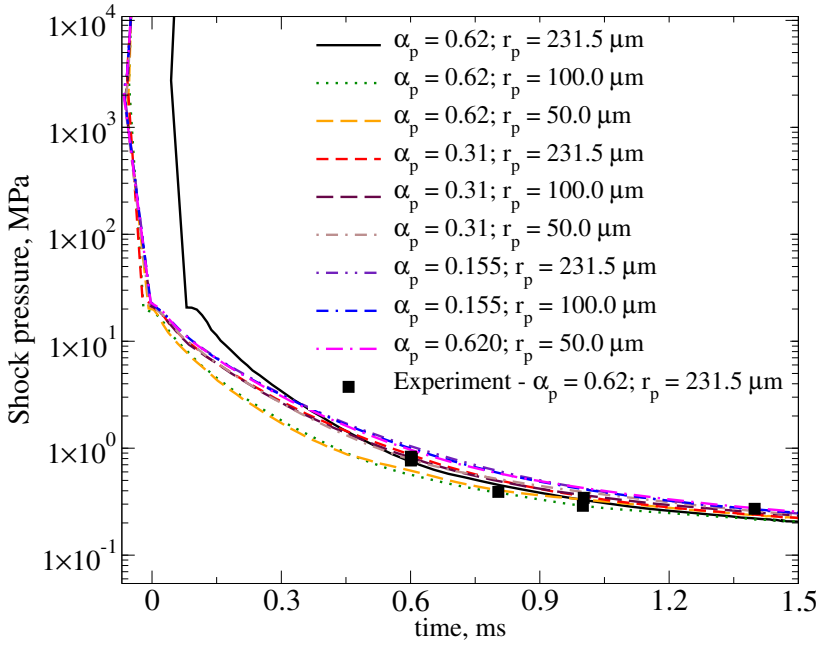

Figure 28: The pressure at the blast front after detonation of a 11.8 cm diameter NM charge with steel particles computed using EL approach. Experimental data is from [129]. Note that α_p is the initial volume fraction of the dispersed phase and r_p is the particle radius.

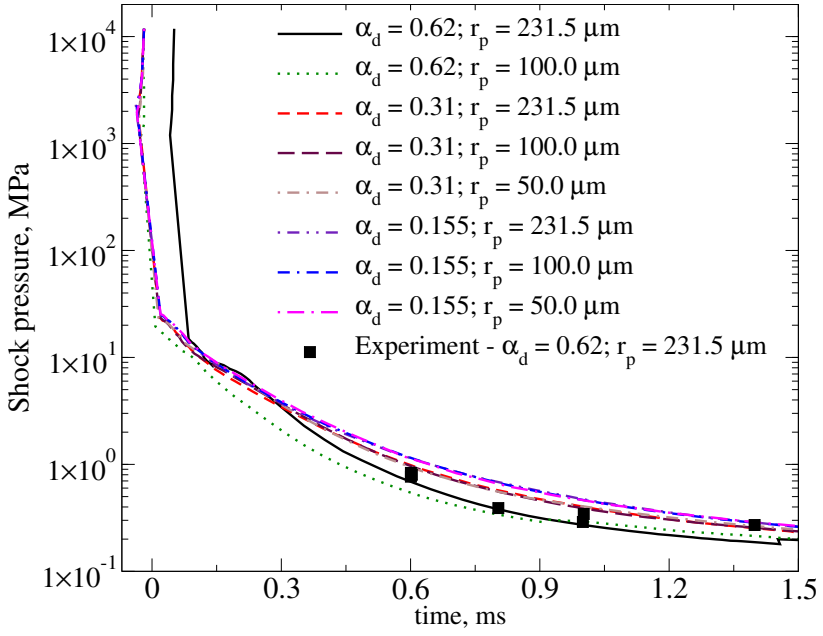

Figure 29: The pressure at the blast front after detonation of a 11.8 cm diameter NM charge with steel particles computed using EE approach. Experimental data is from [129]. Note that α_d is the initial volume fraction of the dispersed phase and r_p is the particle radius.

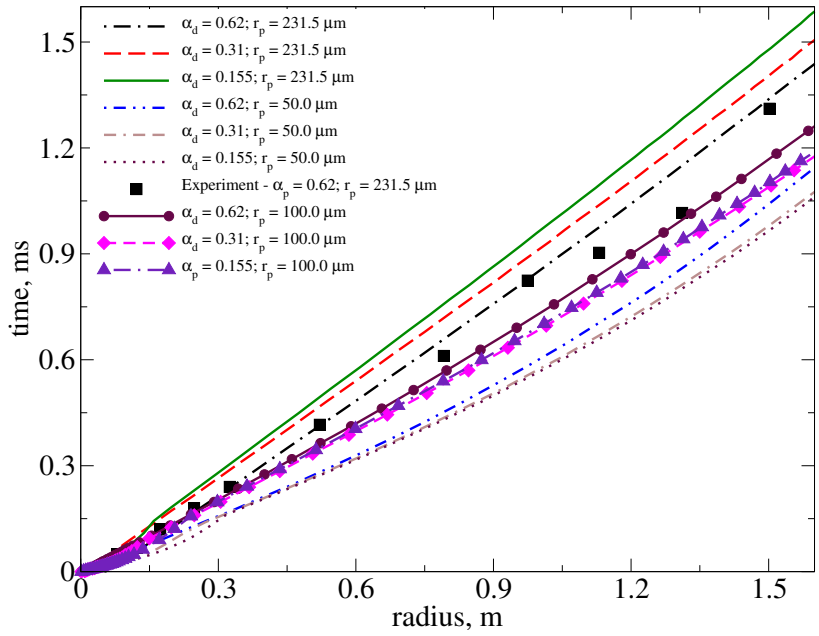

Figure 30: Location of the particle front after detonation of a 11.8 cm diameter NM charge with steel particles computed using EE approach. Experimental data is from [129]. Note that α_d is the initial volume fraction of the dispersed phase and r_p is the particle radius.

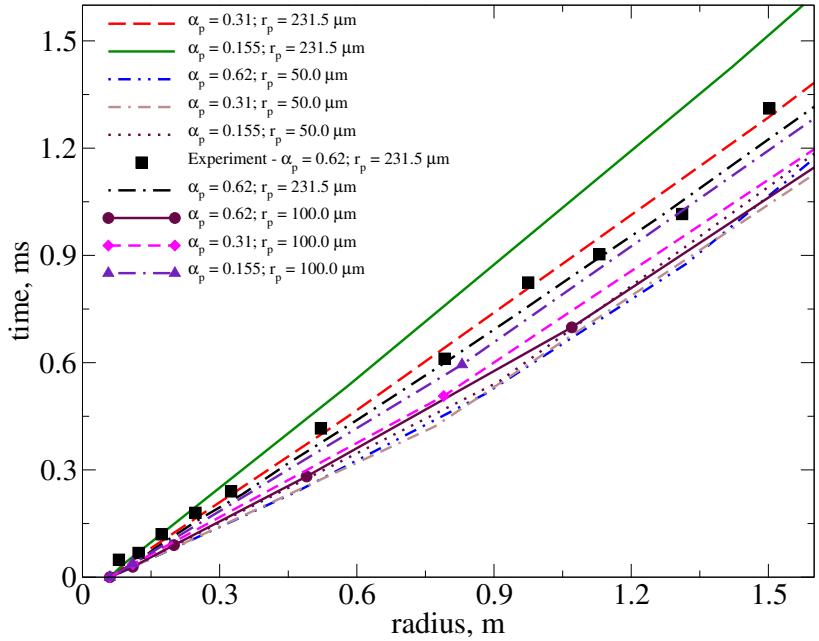

Figure 31: Location of the particle front after detonation of a 11.8 cm diameter NM charge with steel particles computed using EL approach. Experimental data is from [129]. Note that α_p is the initial volume fraction of the dispersed phase and r_p is the particle radius.

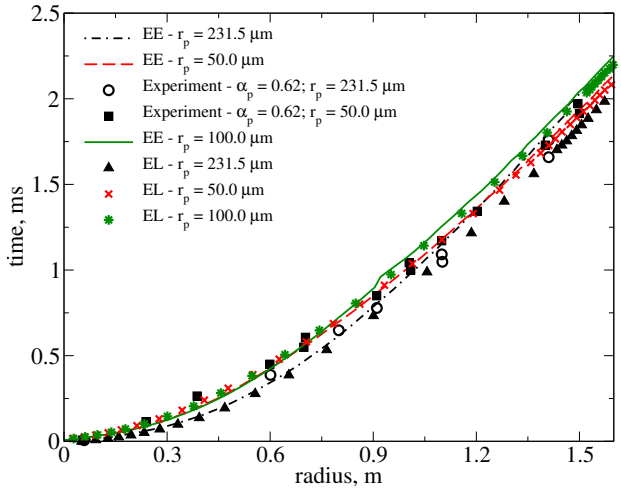

(a) $\alpha_p = 0.62$

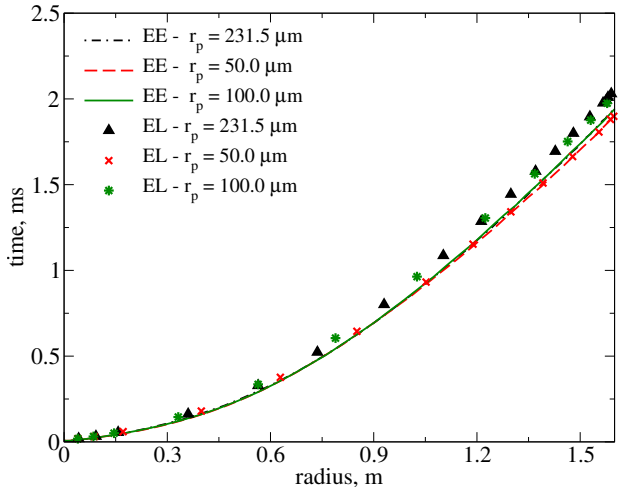

(b) $\alpha_p = 0.31$

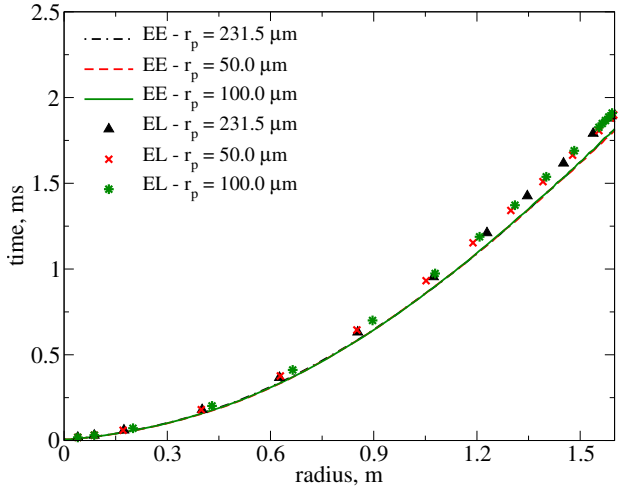

(c) $\alpha_p = 0.155$

Figure 32: Location of the blast front after detonation of a 11.8 cm diameter NM charge with steel particles computed using EE and EL approaches for different particle radius (r_p). Experimental data is from [129]. Note that α_d and α_p are the initial volume fraction of the dispersed phase using EE and EL, respectively.

The efficacy of EE and EL methods to solve for the post-detonation flow of explosive charges packed with dense clusters of inert (steel) particles is investigated in this chapter. A wide range of initial dispersed phase volume fractions and initial particle sizes are chosen to evaluate EE and EL methods. The trajectories of the blast wave and the over pressures obtained using different parameter sets agreed well with experiments. Further, the blast wave front location obtained using EE and EL are in good agreement for different cases. The particle fronts, however, differed based on the initial dispersed phase volume fraction and the initial particle radius. With increase in the volume fraction of the dispersed phase (from 0.155 to 0.62) and decrease in the particle size (from 231.5 μm to 50 μm), EE method converged with EL method, i.e., reduction in the error in the particle trajectory from 20.0 % to 1.0 %. Based on the analysis, EE method is suited for problems with particle radius in the order of 50 μm or less and with the dispersed phase volume fraction at least 1.0%. These limits on the volume fraction of the dispersed phase and the particle size help in the development of the combined EE-EL approach which is discussed in the next chapter.

CHAPTER VI

COMBINED EULERIAN-EULERIAN AND EULERIAN-LAGRANGIAN METHOD FOR POST-DETONATION FLOWS

In the previous chapter, EE and EL methods are used to investigate the post-detonation flow and the results from both the methods are compared. The computations using EE are fast and are accurate for dense to marginally dense flows. EL results are accurate over a wide range of dispersed phase volume fractions and particle size distributions. Further, EL method handles polydisperse flows and can handle combustion/evaporation of each particle efficiently. Thus, ideally, EL with correction for dense flow is preferred method to solve for the post-detonation flow. However, EL is computationally very expensive as the number of particles in the flow increases. Further, in some dense core regions, distribution of particles may be infeasible. Thus, EE approach is favored in these instances. In order to combine the advantages of both EE and EL methods, a combined EE-EL solver is developed and employed here. The combined approach uses EE in the dense regions where particles are clustered. The dispersed phase solution is transferred to EL method once the particles disperse away to form marginally dense or dilute flows.

In this chapter, the combined EE-EL method applied to simulation of the post-detonation flow formed after detonation of heterogeneous NM charges is discussed. The parameters used to transition from Eulerian dispersed phase to Lagrangian dispersed phase are analyzed. The efficacy of EE-EL method for different initial dispersed phase volume fractions and different particle radii is discussed. The accuracy of the approach to predict particle dispersion along with the variation in the computational resource requirement based on the different transition criteria are also discussed.

6.1 Transition between EE and EL

The procedure to transition from Eulerian dispersed phase to Lagrangian dispersed phase is determined by three parameters. These parameters are the transfer volume fraction, α_T, the transfer fraction, f_T, and the number of particles per parcel, P_p. The transfer volume fraction is upper limit of the volume fraction of the Eulerian dispersed phase, α_d, at which the particles are transferred to Lagrangian dispersed phase, i.e., particles are transferred if $\alpha_d \leq \alpha_T$. α_T indicates the region where the transition from EE to EL is desired. In general, the transition can be done from EE to EL and EL to EE based on α_T. However, in the current work, only EE to EL transition is considered. The cases of current interest provide a change in the flow field from dense to dilute as the particles disperse. Even though the particles can cluster during this dispersion, the volume fraction of the dispersed phase, after the initial dispersion, is within the dilute limit (≤ 0.01). Hence, the transition from EL to EE is not considered. Further, after the particle dispersal, EL is able to efficiently track all the particles (distributed over several processors) without the need to reduce the computational cost. This assumption of one way transition, i.e., only from EE to EL, is a limitation and can be relaxed in the future.

The transfer volume fraction ,α_T, has two limits. The upper limit of α_T is the maximum volume fraction of the dispersed phase in the flow, $\alpha_{d,max}$. If $\alpha_T = \alpha_{d,max}$, all particles are transferred to EL and the combined solver approaches the limit of being a pure EL method. The lower limit of α_T is 0.0 and if α_T is set to this value the combined approach is equivalent to pure EE method. With the values of α_T between 0.0 and $\alpha_{d,max}$, the combined method that is hybrid of EE and EL methods is generated. The value of α_T is set based on the computational cost, and the required accuracy

The transfer fraction is the fraction of particles in a computational cell transferred from Eulerian dispersed phase to Lagrangian dispersed phase. When the particles are added to the Lagrangian dispersed phase, the volume fraction of the Lagrangian dispersed phase, α_p, is incremented based on the number of particles added. The number of particles added to the Lagrangian dispersed phase is given as

$$N_p^* = \frac{3\alpha_d f_T Vol}{4\pi P_p r_p^3}. \tag{133}$$

Note that the nearest integer value of N_p^* is considered. As the particles are removed from Eulerian dispersed phase, α_d is updated as

$$\alpha_d^{new} = \alpha_d - \frac{4}{3}\pi P_p r_p^3 \frac{N_p^*}{Vol}. \tag{134}$$

The value of α_d^{new} is not $\alpha_d(1 - f_T)$ as N_p^* is an integer. The mass, the momentum, the energy and the granular energy of the Eulerian dispersed phase are adjusted based on the number of particles transferred to the Lagrangian dispersed phase. The conserved state variable matrix for dispersed phase, Q = ($\alpha_d\rho_d$, $\alpha_d\rho_d u_d$, $\alpha_d\rho_d v_d$, $\alpha_d\rho_d w_d$, $\alpha_d\rho_d e_d$, $\alpha_d\ \rho_d E_s$, $N_d)^T$, is updated to the new value, Q^{new}, after the transition as

$$Q^{new} = (\alpha_d^{new}\rho_d, \alpha_d^{new}\rho_d u_d, \alpha_d^{new}\rho_d v_d, \alpha_d^{new}\rho_d w_d, \alpha_d^{new}\rho_d e_d, \alpha_d^{new}\rho_d E_s, N_d - N_p^*)^T. \tag{135}$$

The velocity, the temperature and the radius and the position of each particle transferred to the Lagrangian dispersed phase are set based on the values from the Eulerian dispersed phase in a given computational cell. Thus, the summation of the conserved quantities before and after transition remains constant, i.e., Q is conserved. Note that the properties of the particles are set in an identical manner for both reactive/evaporating and non-reactive/inert particles. For reactive/evaporating particles, however, the radius in the dispersed phase is updated based on the number density and the particle mass. Thus, each computational cell may have different particle radius. Thus, for particles with mass transfer, a range of particle sizes result in Lagrangian tracking after the transition. If $f_T = 1.0$, then all the particles in a computational cell are transferred and $f_T = 0$ no particle is transferred. In some cases, to enhance stability values of f_T between 0 and 1 are chosen instead of transferring all the particles.

6.2 Explosive particle dispersal

The combined EE-EL approach is applied to investigate the particle dispersal in the post-detonation flow ensuing a heterogeneous NM explosion with steel particles. The problem

Table 5: Parameters used to specify the initial conditions of the dispersed phase for simulations using EE-EL approach.

Case	α_T	f_T	particles per parcel	Number of parcels	Number of particles
A00F000-1	0.00	-	1	91953	91953
A01F050-1	0.01	0.50	1	57125	57125
A01F075-1	0.01	0.75	1	77999	77999
A05F025-1	0.05	0.25	1	55280	55280
A05F050-1	0.05	0.50	1	89423	89423
A10F025-2	0.10	0.25	2	11553	23106
A10F050-2	0.10	0.50	2	33976	67952
A10F075-2	0.10	0.75	2	39509	79018
A10F100-1	0.10	1.00	1	81087	81087
A31F100-1	0.31	1.00	1	81073	81073
A31F100-3	0.31	1.00	3	16338	49014
A62F100-1	0.62	1.00	1	82795	82795
A62F100-3	0.62	1.00	3	32720	98160

Table 6: Parameters used to specify the initial conditions of the dispersed phase for simulations to investigate the effect of the initial r_p using EE-EL

Case	α_{p_0}	r_p μ m	particles per parcel	Number of parcels	Number of particles
A1R1	0.62	231.5	1	57125	57125
A1R2	0.62	50.0	60	162692	9761520
A2R2	0.62	50.0	40	57125	57125

setup used here is the one described in the previous chapter. All the particles are initially assumed to be in Eulerian dispersed phase and α_p is set to be zero. Particles of radius 231.5 μm and 50.0 μm are considered and the initial volume fraction of the dispersed phase is 0.62. The transition parameters are varied, as shown in Table 5, to study the effect of these parameters on the accuracy and the associated computational cost.

6.2.1 Effect of transition parameters

The particle front trajectories obtained using different α_T for a given f_T and P_p are shown in Fig. 33. With $\alpha_T = 0.01$, the results are almost identical to the pure EE case discussed in Chapter 6. As α_T is increased to 0.62, the particle front velocity increases and approaches

the value predicted by EL method. In case of $\alpha_T = 0.62$, almost all the particles are transferred to Lagrangian dispersed phase while the particles are within the charge. These particles are set to have relatively higher velocities based on the dispersed phase velocity in the computational cell they reside. Thus, the initial velocities of the particles are over-predicted and leads to the over prediction of the particle front velocity. However, for all other cases with $\alpha_T = 0.01$ to 0.32, the transition is made in the relatively dilute region and the particle trajectory is always between the values given by pure EE and pure EL methods. Note that the number of particles in the flow increases with increase in α_T as shown in Table 5. Thus, although α_T near 0.62 is preferred for accuracy, to reduce computational cost lower α_T values are preferred. The choice of α_T is a trade-off between the required accuracy and the computational feasibility.

The accuracy in the prediction of the particle dispersion is reduced with reduction in f_T as shown in Fig. 34. The value of $f_T = 1.0$ provides the results that tend towards the pure EL solution. However, increase in f_T also increases computational cost as the number of particles tracked increases. Thus, here again, as in the case of α_T, the choice of f_T is made based on the desired accuracy and the computational cost. Also, values of f_T near 1.0 in cases with α_T near $\alpha_{d,max}$ affect the stability of the solver due to the transfer of the mass, the momentum and the energy from the Eulerian to the Lagrangian dispersed phase. Hence, in such cases, for a smooth transition, values of f_T closer to one rather than $f_T = 1.0$ are considered.

Number of particles present in each parcel tracked using Lagrangian solver also affects the accuracy of the method. With increase in P_p, the number of particles in the flow is reduced but the error in the particle front location also increases. Here, again as in the case of f_T and α_T, $P_p = 1$ is preferred for accuracy but values of $P_p > 1$ are routinely considered to reduce the computational cost.

For particles with $r_p = 50.0$ μm, the trajectory predictions from EE, EL and EE-EL are in good match (see Fig. 36). The transition from EE to EL at different times for this case is shown in Fig. 37. The transition occurs in the region near the origin and is shown clearly in the zoomed views at t = 0.15 ms and 0.69 ms. Notice that the approach is confined

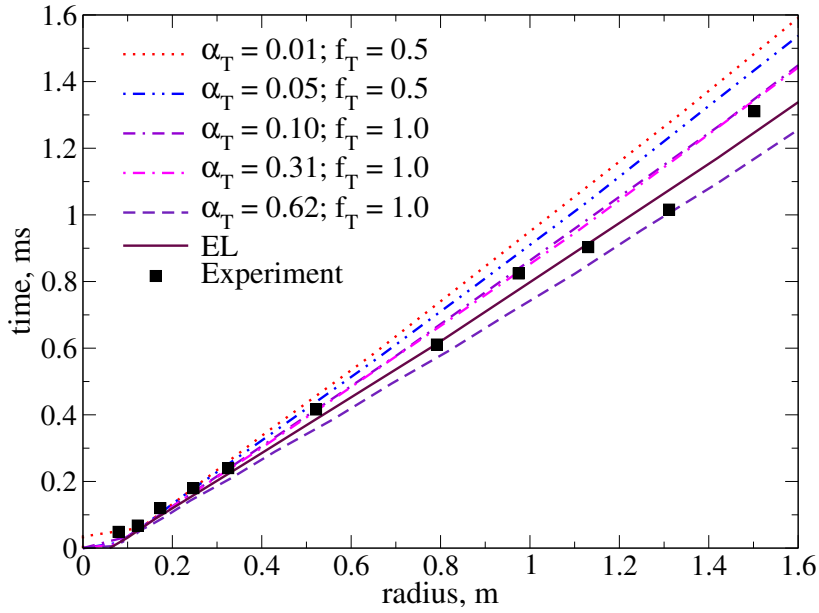

Figure 33: Location of the particle front after detonation of a 11.8 cm diameter NM charge with steel particles ($\alpha_p = 0.62$ and $r_p = 231.5$ μm) computed using EE-EL approach with different α_T. Experimental data is from [129]. $P_p = 1$ in all cases.

to EE near the origin and EL in the far-field. The overlap region between EE and EL is clear in Fig. 37, where the particles overlap the Eulerian dispersed phase volume fraction contours. In this case, although EE can be used for good global predictions, as discussed in the previous chapter, to capture local variations in the particles in dilute regions, EL is preferred. Also, if the particles evaporate or burn, EL can handle the polydisperse flow accurately. Hence in this case, the combined EE-EL solver is good to predict the global and the local particle trajectories with relatively lower computational cost. Thus, for dense clusters of particles of size $\mathcal{O}(50$ μm) or less, EE-EL method is optimal choice as it reduces the computational cost and provides accurate results.

6.2.2 Analysis of computational cost

The computational cost for EE, EL and EE-EL is analyzed for different transition parameters and is shown in Fig. 38. The total computational time required per iteration per computational cell increases with increase in α_T. Note that the cost here is computed per iteration and not per a constant time step. The time step for each iteration in all cases

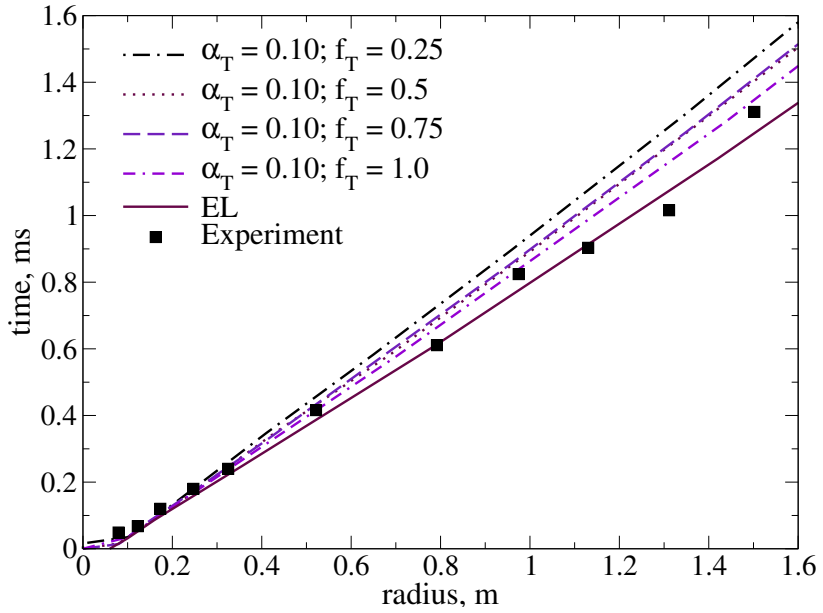

Figure 34: Location of the particle front after detonation of a 11.8 cm diameter NM charge with steel particles ($\alpha_p = 0.62$ and $r_p = 231.5$ μm) computed using EE-EL approach with different f_T. Experimental data is from [129].

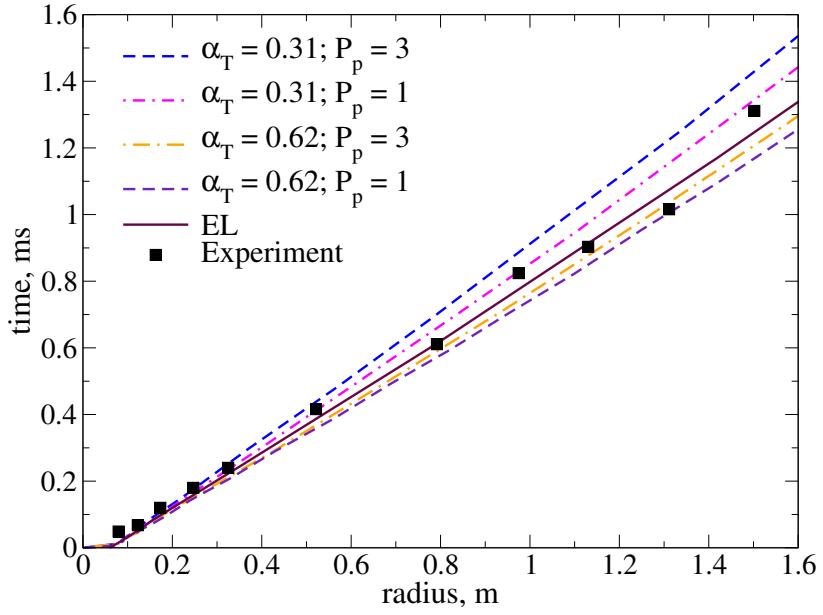

Figure 35: Location of the particle front after detonation of a 11.8 cm diameter NM charge with steel particles ($\alpha_p = 0.62$ and $r_p = 231.5$ μm) computed using EE-EL approach with different number of particles per parcel P_p. Experimental data is from [129].

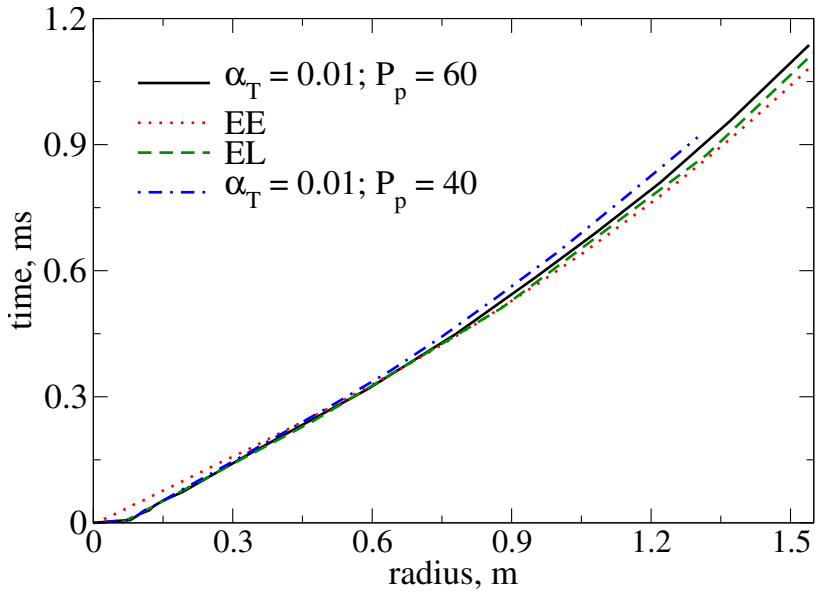

Figure 36: Location of the particle front after detonation of a 11.8 cm diameter NM charge with steel particles of radius 50 μm computed using EE-EL approach with different number of particles per parcel P_p. The transfer fraction (f_T) is set as 1.0.

varied from nearly 2.0×10^{-8} s to nearly 2.0×10^{-7} s. The variation in the time step occurred over 4000 iterations in all cases and each case is run till 10000 iterations to perform the cost analysis. After transition to the the higher value, the time step remained at almost 2.0×10^{-7} s for the rest of the simulation for all cases (EE, EL and EE-EL) shown in Fig. 38.

The cost of computation for EL with $P_p = 1$ is 7 times that of EE. In all cases, increase in P_p reduced the computational cost. An increase in P_p from 1 to 3 resulted in simulations 2.5 times faster using EL. For EE-EL, the reduction in computational cost with increase in P_p from 1 to 3 is about 2 times for $\alpha_T = 0.31$ and 3 times for $\alpha_T = 0.62$. Reduction in f_T and α_T also reduced the computational cost as the number of particles in the flow is reduced. Even though most particles are transferred for $f_T = 1.0$ and $\alpha_T = 0.62$, EE-EL method is still able to provide 10.0-30% reduction in computational cost due to the reduction in the computational cost in the early stages of the simulation when all the particles are clustered in few cores. Note that choice of transfer parameters that provides a better load balance for Lagrangian tracking is preferred to reduce the computational cost.

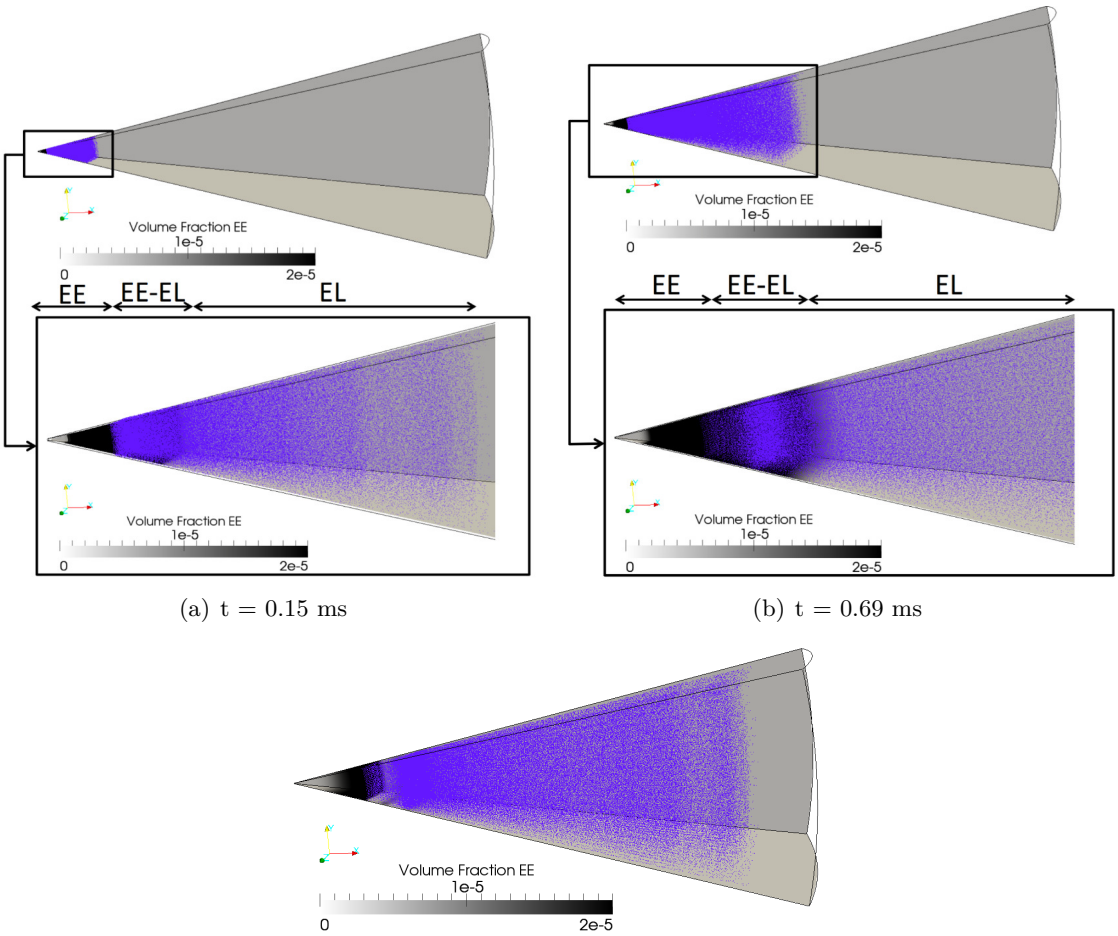

(a) t = 0.15 ms

(b) t = 0.69 ms

(c) t = 1.82 ms

Figure 37: Post-detonation flow at different times simulated using EE-EL approach. The transition from EE to EL is shown using the dispersed phase volume fraction (in gray scale) and the particles (shown in color). The initial charge is a 11.8 cm diameter NM charge with steel particles of radius 50 μm. The initial dispersed phase volume fraction is 0.62. Here, $\alpha_T = 0.01$, $f_T = 1.0$ and $P_p = 60$. Zoomed view of the transition at t = 0.15 ms and t = 0.69 ms is also shown for clarity along with the regions where EE, EL and EE-EL are active. Note that, over the entire domain, the full set of equations for EE-EL are used.

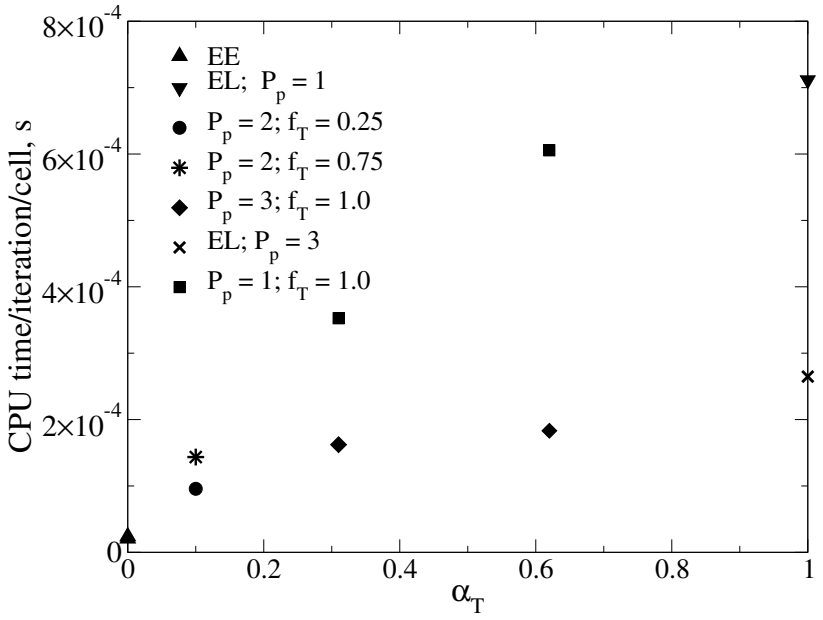

Figure 38: CPU time per iteration per computational cell for different transfer volume fractions (α_T). Values for EE, EL and EE-EL are shown. The values of P_p and f_T for EE-EL cases are shown. Note that α_T is 0.0 and 1.0 for EE and EL, respectively.

6.3 Summary

A combined EE-EL method is developed to mitigate the computational cost and accuracy issues associated with EE and EL methods. The transfer from EE to EL is made based on α_T, f_T and P_p. Increase in α_T increased the accuracy and the predicted solution spanned from the EE results to EL results as α_T is varied from 0.0 to $\alpha_{d,max}$. The choice of α_T is made based on the computational cost as values near $\alpha_{d,max}$, although provide better predictions, generate expensive simulations. The trends with f_T are found to be similar to that with α_T. However, since f_T also controls smooth transition in some cases, the choice of f_T is based on computational cost, accuracy and the smoothness of the transition. The combined EE-EL method has provided results with good agreement with EL method at relatively lower computational cost. Since global predictions with EE are good for particle sizes of the order of 50 μm and less, EE-EL is ideal to solve for dense clusters of small particles and can predict both global and local variations accurately.

CHAPTER VII

DILUTE PARTICLE CLOUD DISPERSION IN POST-DETONATION FLOW

Application of explosives to neutralize bio-agents adds the particle-flow interaction to the dynamics of the post-detonation flow. Neutralization of bio-agents is dependent on multiple factors such as the location of bio-agents with respect to the charge, the residence time of the bio-agents in the flow and the interaction of the bio-agents with the blast wave and the mixing zone. Hence, to quantify the neutralization and understand the neutralization process, study of the interaction of homogeneous explosion with ambient bio-agent aerosol clouds is essential. Mainly, the processes of dispersal and heat transfer which determine the fate of individual bio-agent particle should be modeled and studied.

In this chapter, the flow ensuing the detonation of a spherical homogeneous NM charge as it interacts with ambient bio-aerosol cloud is discussed. The simulations discussed in this chapter are performed using only the EL approach. The aspects of the mixing zone generation and the interaction of shock waves with hydrodynamic structures is described. The model employed to simulate the bio-aerosol is discussed in detail. The effects of the heat transfer on the aerosol and the dispersion of the aerosol in the flow based on the initial distance from the charge are analyzed and the neutralization is quantified for different cases.

7.1 Background

Spores produced by certain bacteria are known to pose severe threats to human health and safety [121]. Neutralization of these biological agents has been a vital component of many threat reduction scenarios. In real life conditions, one of the operational strategies is to use explosive charges to destroy spores in both confined and unconfined environments. Past experimental investigations suggest that the spore neutralization can be achieved by heating and chemical corrosion [107]. Detonation of explosive charges produces a high temperature gaseous environment along with possible corrosive detonation product gases,

both of which can be effectively used in multiple bio-agent defeat scenarios. However, there have been no reported studies in the open literature on the effects of explosive charges on spores. Such studies are essential and would enable the development of novel methods of spore neutralization.

Investigation of spore neutralization by explosive charges using experimental methods is challenging and in some cases not feasible due to the destructive nature of the flow. When experimental investigations are not viable, numerical simulations have been successfully employed to analyze the post-detonation flow dynamics [18, 64]. With the aid of the computational studies, the main stages of blast wave propagation and post-detonation combustion have been investigated in both confined and unconfined environments [18, 36, 64]. With the primary focus on the dispersion and the heating of bacterial spores by detonated explosive charges, this chronology of blast wave propagation and instability generation are modeled in this chapter following the procedure described in the previous chapter.

Bacteria are known to form spores that can survive harsh conditions, such as high temperatures, high pressures, and toxic chemical environments [87]. To address the challenges involved in spore destruction, many experimental and numerical studies in the past focused on the methods of spore kill and the effectiveness of these methods. Thermal inactivation of spores has been investigated in the past by exposing spores to temperatures in range of 90 - 200 °C for several seconds [121]. However, explosive charges are known to produce conditions with gas temperatures in the order of $10^3 - 10^4$ K. Also, most of the blast and post-detonation combustion events occur in the time span of few microseconds to few milliseconds. Therefore, it is not possible to accurately assess the spore kill rate by explosives based on the experiments, which are performed at different time scales and temperature ranges.

Recently, investigations on the interaction of spores with shock waves have been performed to estimate spore kill due to shock induced acceleration [110] and shock heated gas [80]. Sislian and co-workers used an impactor to study the spore break up by aerodynamic shocks and provided the critical acceleration (3.9 - 16 $\times$ 10^9 m/s^2) needed for bacterial

spore destruction [110]. Spore breakdown in a post-shock heated gas investigated by McCartt et al. provides the percentage of spores intact after heating for different post-shock temperatures [80]. These studies were aimed to understand spore kill in conditions analogous to conditions in post-detonation flows. However, explosive charges not only produce strong blast waves but also high temperature reacting regions, which can cause both thermal and mechanical spore rupture. Also, the hydrodynamic instabilities (RMI/RTI) in the post-detonation region can disperse spores and affect their survival. Thus, it is essential to consider the combined effect of dispersion, heating and mechanical impact to provide critical conditions for spore kill useful in operational conditions. Here, these aspects are investigated using three dimensional numerical simulations of interaction of spore clouds with post-detonation flow ensuing from explosive charges. A spore cloud is defined as a cluster of spores, which are organized to occupy a specified initial volume, and has a specified initial concentration and distribution. The motion and the temperature of the spores are evaluated using the Lagrangian tracking method, which can characterize the particle dispersion accurately in complex flows [52]. Past results suggest that the strength of the blast wave is reduced as it propagates outwards. Thus, the effect of the initial distance of the spore cloud from the explosive charge on spore kill is investigated in detail. However, before analyzing the interaction of the spore cloud with the post-detonation flow, a spore aerosol model is developed based on past experiments [80] and is evaluated in a shock tube configuration. The shock tube simulations are used to validate the spore aerosol model and quantify the uncertainties in the critical parameters, such as the aerosol size distribution and the spore neutralization temperature. The validated model is employed to study spore neutralization by explosive charges.

7.2 Spore aerosol modeling

In the studies discussed here, droplets of a spore-laden aqueous solution are introduced into the domain of interest, i.e., the reshock zone of the shock tube or in the vicinity of a detonated explosive charge. The spores are considered to be of the *Bacillus* species. Although most spores of this species are elliptical, in the current work, they are assumed

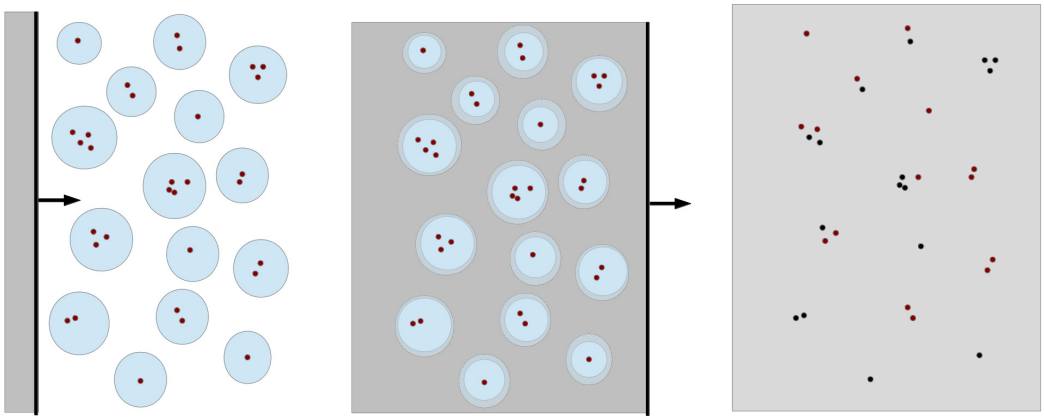

(a) Pre-shock Spore-laden aerosol (b) Droplet evaporation in post-shock zone (c) Exposed spore heating

Figure 39: Schematic of spore aerosol interaction with shock/blast wave and subsequent spore kill modeled in the current study. The arrows indicate the direction of motion and vertical line in (a) and (b) indicates shock/blast wave. The blue circles indicate aerosol droplets and the dotted circles indicate the mixture of evaporated water and ambient gases. The post-shock/post-blast wave region in shown in grey. Black dots indicate damaged spores and red dots indicate intact spores.

to be spherical with radius, $r_s = 0.4\ \mu m$ [25]. The spore aerosol considered has a particular droplet size distribution and a specific concentration of spores in the initial solution. Also, a specific initial concentration of spores in the domain is chosen. These parameters are set based on past experimental studies [44] so that the current results can be compared with the results available in the literature.

When the spore aerosol interacts with the hot gases in either a post-shock or a post-detonation flow, the water enveloping the spores evaporates and exposes the spores to the heat. Based on the aerosol droplet radius there could be multiple spores in a given droplet. These spores, after the evaporation of water, can stay clustered or disperse. As the temperature of the spores increases, based on the quantity of heat received by each spore, the spore kill can occur due to heating or mechanical rupture. These processes are illustrated in Fig. 39. When the spore-laden aerosol is nebulized, the droplets of aerosol are distributed in the domain of interest with each droplet having an initial radius, ${r_p}^0$. In general, ${r_p}^0$ can be specified based on a distribution function. However, as the exact distribution of the

droplet size is not known, ${r_p}^0$ (microns), based on a Gaussian distribution, is specified as

$$ {r_p}^0 = \min(\chi, \mu_\chi), \tag{136} $$

where χ is a Gaussian random variable with mean μ_χ and standard deviation σ_χ. As the values of μ_χ and σ_χ are not available, a range of values are used initially for the shock tube simulations and the values which provide good agreement with experimental results are then used in cases with explosive charges. Also, the initial atomization is assumed to reduce all droplets to a size less than μ_χ. Further, the number of spores per droplet (n_s^p) is set based on the concentration of the spores in the initial aqueous solution. In the current study, for an initial spore concentration of 10^{10} spores/ml, n_s^p varies from 1 to 5 [44]. Also, the concentration of the spores in the domain, χ_s^0, is varied from 10 to 10^6 spores/cm^3.

Due to the heat transfer to the droplets in the post-shock region, the water encapsulating the spores evaporates and this rate of mass transfer is given by Abramzon et al. [2]. The expressions for the Nusselt number (Nu), the Sherwood number (Sh) and the Spalding mass transfer number (B_M) for droplets are available elsewhere [2]. The quasi-steady drag on each particle is computed using the drag law provided by Boiko et al. [23] and added mass coefficient, C_A, is set to be 0.5. After the water evaporates, no mass transfer is considered from individual spores or spore clusters. Hence, these expressions for $\dot{m}_p$ and Nu are used until the radius of the droplet reduces to the effective radius of the spore cluster present inside the droplet, i.e., $r_p > r_s^c$. Here, the effective radius of the spore cluster is determined as

$$ r_s^c = r_s \left(\frac{n_s^p}{f_p} \right)^{1/3}, \tag{137} $$

where f_p is the packing fraction and is taken to be 1 when $n_s^p = 1$ and 0.74 otherwise, i.e., close packing assumption. The expression for Nu used when $r_p \leq r_s^c$ is provided elsewhere [52].

Once the spores are exposed to a high temperature gaseous environment, the temperature of the spores increases to a critical value (T_C). Past calculations of thermo-structural response of individual spores show that this critical temperature should result in the spore

membrane rupture and/or heating of the spore core leading to spore kill [67]. Experimental studies suggest that the loss of spore viability and structural damage occurs at gas temperatures of about 750K and above [43]. However, for the cases considered here, the exact quantity of heat needed to kill a spore or to reach T_C is not available. Hence, T_C is assumed as a variable parameter and a range of values are used in each case to obtain the percentage of spores killed. In cases presented here, any spore whose temperature exceeds T_C is assumed to be neutralized. Note that the loss of viability can occur before the spore is damaged [43]. Hence, in the current studies, the spores that are not intact are considered to have lost their viability and are neutralized. The sensitivity of spore kill to T_C is analyzed and the intact spore percentages are compared with shock tube experimental results such that this criteria can be used with confidence in cases with explosive charges.

7.3 Initial setup

7.3.1 Shock tube setup

A shock tube of length 2.6 m is considered in the current work to investigate the spore neutralization by shock waves. Initial pressure in the driver section is varied to obtain the desired shock Mach number (M_s). The shock tube is closed at both ends. Thus, the normal shock propagates from one end of the tube to the other end and reflects back. The lengths of driven and driver sections are chosen such that constant post-reshock properties are obtained for a given residence time. The residence time (t_r) considered in the current work, following experimental investigations [43], is $\sim$ 2.5 ms. M_s is varied from 1.5 to 2.1 such that the post-reshock temperature (T_5) varies from 600-1100 K. The spore-laden aerosol is introduced at the end of the shock tube away from the driver section. Note that, in all cases investigated here, the flow properties in post-reshock regime, $R5$, remain almost constant for the residence time considered. This is demonstrated for $M_s = 1.7$ in Fig. 40. The initial length (L^0) of the shock tube occupied by the aerosol and the number of droplets in the aerosol (n_p) are varied such that the initial concentration of the spores (${\chi_s}^0$) in the shock tube is of the desired value. The values of L^0, μ_χ, σ_χ, n_p, total number of spores considered (n_s^t) and ${\chi_s}^0$ for each case are provided in Table 7.

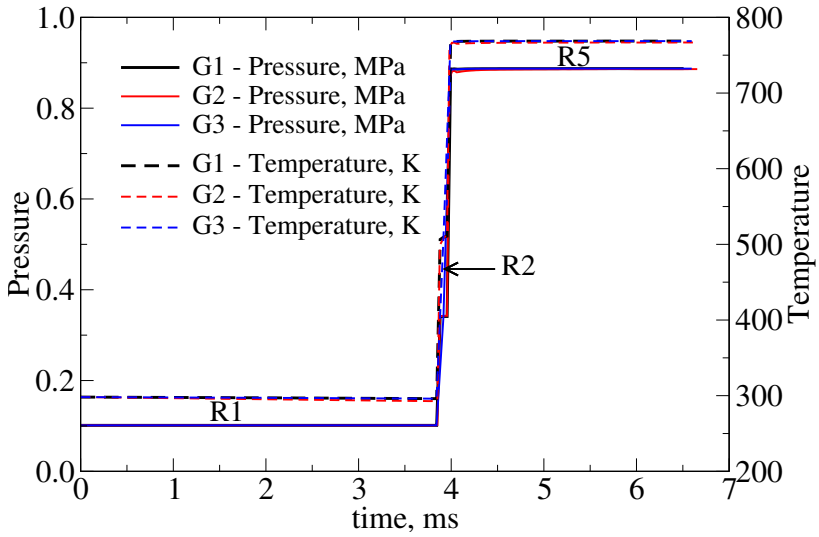

Figure 40: Variation of temperature and pressure in the shock tube at the location where spores are released for $M_s = 1.7$. Region R1 indicates the pre-shock condition, R2 indicates the post-shock condition and R5 indicates the post-reshock condition. The details of the grids G1, G2 and G3 are provided in Table 8.

The shock tube domain is discretized using a uniform mesh. The dimensions of the cross section and the width of each computational cell (Δ) used here are provided in Table 8. In all cases G1-G3, the flow properties are almost identical as shown in Fig. 40. Thus, for the rest of the studies presented here, the grid setup as in Case G1 is used. As the focus of the current studies is the neutralization of spores in unconfined post-detonation flows, only the particle dispersion effects away from the wall boundaries are considered, and all the walls of the shock tube are assumed to be slip walls.

7.3.2 Setup for simulations with explosive charges

A homogeneous spherical NM charge of diameter 11.8 cm is considered in the current investigations. The detonation energy and the initial density of the NM charge are 4.35 MJ/kg and 1128.0 kg/m^3, respectively [18]. Note that, in the post-detonation flow analysis, all the temporal and spatial scales provided correspond to this detonation energy, initial charge density and initial charge volume. The detonated charge is initialized in an unconfined domain, which is modeled by a three dimensional spherical sector (2.4 m$\times 45^o \times 45^o$). A structured mesh ($1000 \times 60 \times 60$) is used to resolve the domain. The initial composition

Table 7: Parameters used to specify the initial conditions of the dispersed phase in the shock tube (ST) studies.

Case	n_p	μ_χ	σ_χ	n_s^t	L^0 (cm)	${\chi_s}^0$ ($\times 10^6/cm^3$)
ST1	2500	5.0	0.5	2500	5.0	0.185
ST2	2500	5.0	0.5	9070	5.0	0.670
ST3	4000	5.0	0.5	14504	5.0	1.000
ST4	4000	5.0	0.5	14504	5.0	1.000
ST5	4000	5.0	0.6	14504	5.0	1.000
ST6	4000	5.0	0.7	14504	5.0	1.000
ST7	4000	5.0	0.4	14504	5.0	1.000
ST8	4000	5.0	0.5	14504	10.0	0.500
ST9	4000	5.2	0.5	14504	5.0	1.000
ST10	4000	4.8	0.5	14504	5.0	1.000

Table 8: Shock tube cross sections and grid resolution used in the current studies.

Case	Dimensions	cross section (mm)	Δ (μm)
G1	1D	0.52×0.52	520.0
G2	3D	1.56×1.56	520.0
G3	1D	1.04×1.04	1040.0

Table 9: Parameters used to specify the initial conditions of the dispersed phase in the simulation with explosive charges.

Case	n_p	n_s^t	L^0 (mm)	${\chi_s}^0$ ($\times 10^3/cm^3$)	d^0 (cm)
NM0C1	4000	14504	3.0	0.545	12.0
NM1C1	4000	14504	3.0	0.138	24.0
NM2C1	4000	14504	3.0	0.035	48.0
NM3C1	4000	14504	3.0	0.009	96.0
NM4C1	4000	14504	3.0	0.015	72.0
NM5C1	4000	14504	3.0	0.244	18.0
NM6C1	4000	14504	3.0	0.180	21.0
NM7C1	4000	14504	3.0	0.218	19.0
NM8C1	4000	14504	3.0	0.062	36.0
NM0C2	8000	29008	3.0	1.090	12.0
NM1C2	8000	28828	3.0	0.276	24.0
NM2C2	8000	28828	3.0	0.070	48.0
NM4C2	8000	29171	3.0	0.031	72.0
NM5C2	8000	29346	3.0	0.494	18.0
NM6C2	8000	29008	3.0	0.360	21.0
NM8C2	8000	29008	3.0	0.124	36.0
NM0C4	32000	116032	3.0	4.360	12.0
NM0C6	128000	464128	3.0	17.440	12.0
NM1C4	32000	116032	3.0	0.552	24.0
NM1D2	4000	14504	6.0	0.068	24.0
NM1D3	8000	29008	12.0	0.068	24.0

Table 10: Spore density (ρ_s) and heat capacity (C_s) used in the current studies.

Case	ρ_s (kg/m^3)	C_s (J/kg/K)
ST1-10	1000.0	4180.0
ST11	1300.0	4180.0
ST12	1000.0	2500.0
ST13	1300.0	2500.0

of the product gases in the homogeneous charge is same as that described in Chapter 5. The ambient gas is specified to be air at 1.01325 MPa and 300 K. The spore-laden aerosol is initially distributed in the ambient flow at a specific radial distance, d^0, away from the initial charge. The thickness (L^0) of the aerosol cloud is specified based on the initial concentration (χ_s^0) and the total number of spores in the cloud (n_s^t). These parameters for each case investigated are presented in Table 9.

7.4 Spore neutralization in shock tube

The shock tube studies are set to compare with the available experimental results and used to analyze the significance of the modeling parameters discussed earlier. The intact spore ratio (I_s) = $(100.0 \times n_s^i)/n_s^t$, where n_s^i is number of intact spores after time $t = t_r$, in each case is evaluated and the role of each modeling parameter is discussed. Note that the value of I_s ranges from 0 to 100, i.e., complete neutralization to no neutralization.

A normal shock of Mach number, M_s, is simulated in a shock tube closed at both ends and filled with argon to study the spore-laden aerosol neutralization in post-shock flow. Here, the shock wave is allowed to reflect from the closed end to produce a reflected shock and a post-reshock flow with a temperature ($T_5 \sim$ 600-1200K) considerably higher than the post-shock ($T_2 \sim$ 440-650K) temperature. Initially, the spore-laden aerosol droplets are distributed uniformly over L^0 and span the entire cross section of the shock tube. As the aerosol droplets interact with the shock heated gas, the water surrounding the spores evaporates resulting in a reduction in the droplet radius and an increase in the droplet temperature. As M_s is increased, the rate of change in the average droplet size and the average droplet temperature increase due to the increase in the post-shock/post-reshock gas

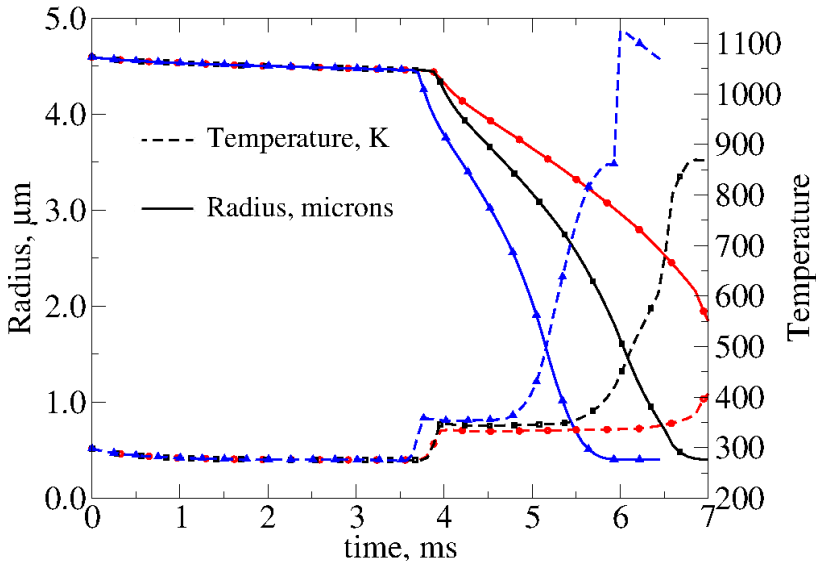

Figure 41: Variation of average particle radius and average particle temperature with time for $M_s = 1.6$ (red, dots), 1.8 (black, squares) and 2.0 (blue, triangles). Initial conditions correspond to Case ST4.

temperature (see Fig. 41). Here, the average quantities are the average values evaluated over all the droplets. Note that for $M_s = 1.6$, even after 7 ms, the average droplet temperature is about 400 K. Thus, I_s is nearly 100 for $M_s = 1.6$. Similarly, for $M_s = 2.0$, the average droplet temperature is about 1100 K after 6.5 ms and I_s is nearly 0.

One of the important criteria determining the survival of spore is T_C. Values of T_C in the range 650 K to 690 K show a negligible change (about 0.2) in I_s, as shown in Fig. 42, computed for T_5 ranging from 650 K to 1100 K. Thus, in all the current studies, $T_C = 670$ K is used to determine the number of intact spores at any given time. The significance of the acceleration due to the pressure gradient (PG) and the added-mass (AM) effect on the intact spore percentages for different T_5 is investigated by considering simulations with individual acceleration terms. Figure 43 shows that the difference in the predicted values of the number of intact spores is negligible and the calculations with only the quasi-steady drag, the dominant acceleration term, provide results with good accuracy. Thus, for all other studies reported here on, in this chapter, the acceleration due to PG and AM effects are neglected. During the short time interval when the particles are stalled by the gases moving in the direction opposite to the particle motion (especially, before reshock in cases

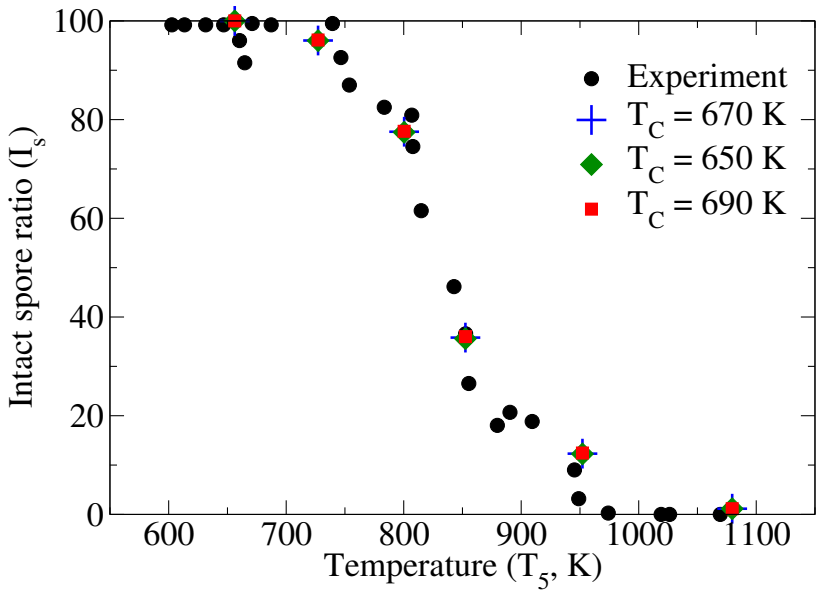

Figure 42: Percentage of spores left intact for different post-reshock temperatures (T_5) for different spore neutralization temperatures, T_C. Results from experiments [43] are shown for comparision.

with explosives), the gravitational force can alter the particle trajectory. However, since the particles are stalled for few micro seconds, the change in the trajectory does not affect the total spore survivability. Thus for the cases considered here, the effect of the gravitational force on the aerosol is also neglected.

The spore density (ρ_s) and heat capacity (C_s) are varied as shown in Table 10. These values are considered based on the values provided by earlier investigations [67]. Change in both ρ_s and C_s result in a negligible change in I_s, as shown in Fig. 44, and hence the values in Case ST4 are used in all the cases with post-detonation flows. The effect of the spore-aerosol modeling parameters is investigated by varying χ_s^0, μ_χ and σ_χ as shown in Table 7. The maximum change in I_s, in comparison to Case ST4, is 10.0 when σ_χ is varied from 0.4 to 0.7 for $\mu_\chi = 5.0$. Also, when μ_χ is varied from 4.8 to 5.2, the maximum change in I_s, compared to Case ST4, is 30.0. Both, μ_χ and σ_χ determine the range and the maximum size of the droplets in the aerosol. With an increase in the droplet size, the time required to evaporate the water encapsulating the spores increases. Thus, the time needed to expose the spores increases with an increase in the droplet size. Hence, the

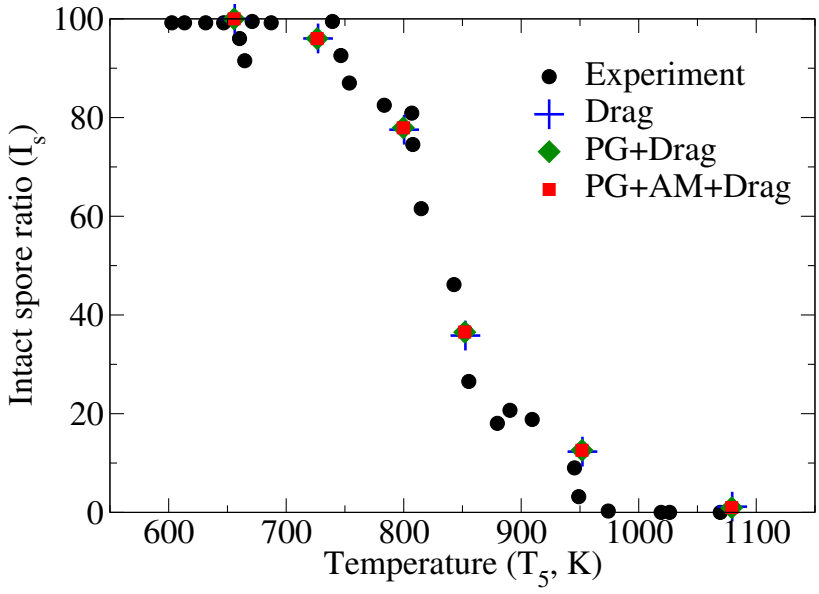

Figure 43: Percentage of spores left intact for different post-reshock temperatures (T_5) for different particle acceleration terms considered. Here, PG indicates the pressure gradient term and AM indicates the added-mass effect. The residence time of spores in reshock zone is nearly 2.5 ms. Results from experiments [43] are shown for comparision.

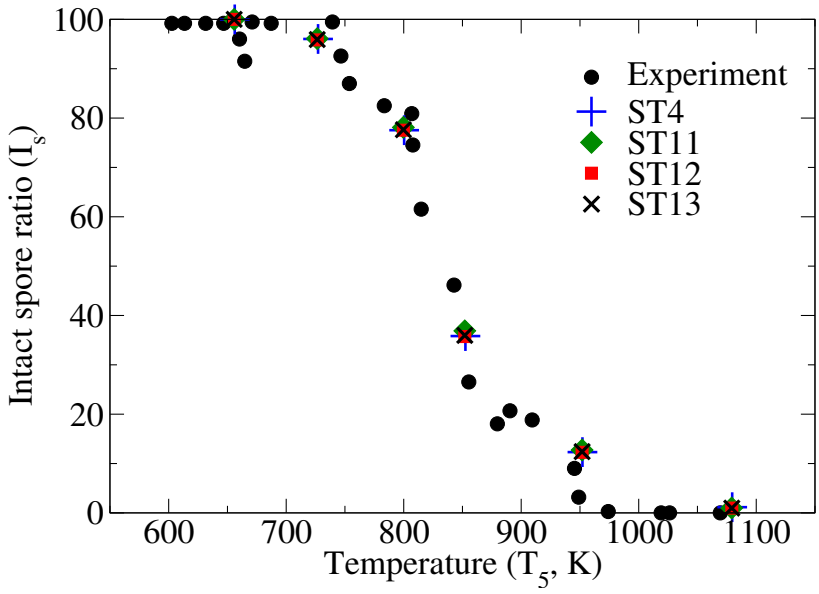

Figure 44: Percentage of spores left intact for different post-reshock temperatures (T_5) for different physical properties (shown in Table 10) of spores. Results from experiments [43] are shown for comparision.

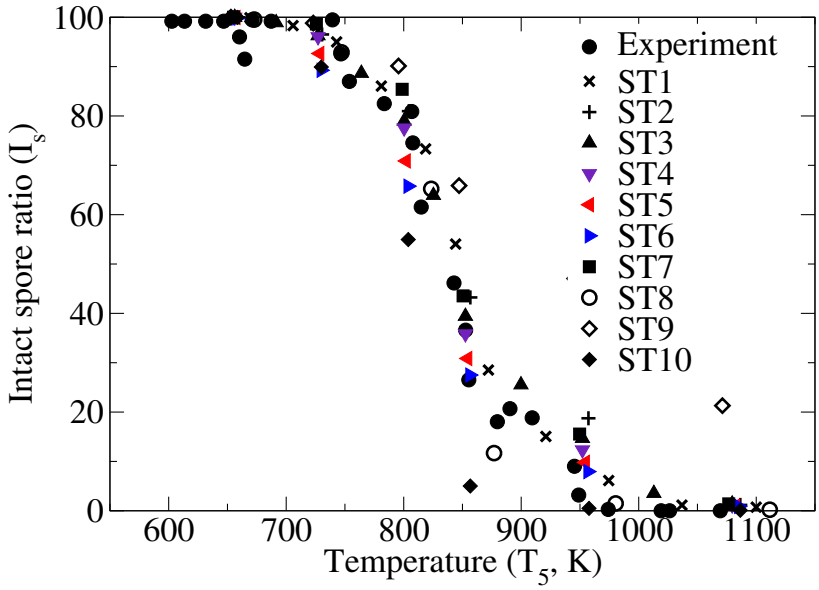

Figure 45: Percentage of spores left intact for different post-reshock temperatures (T_5) for cases shown in Table 7. The residence time of spores in reshock zone is nearly 2.5 ms. Results from experiments [43] are shown for comparision.

Table 11: Modeling parameters affecting the intact spore ratio. Experimental results [43] (ΔI_s^E) and Case ST4 (ΔI_s^N) are used as a reference to compute the maximum difference in I_s over all M_s for each parameter.

Parameter	Definition	Range	ΔI_s^E	ΔI_s^N
T_C	Critical spore temperature (K)	650-690	3.5	0.2
C_s	Heat capacity of spore (J/kg/K)	2500.0-4180.0	3.7	0.2
ρ_s	Density of spore (kg/m^3)	1000.0-1300.0	3.7	1.0
μ_χ	Mean spore aerosol droplet radius (μm)	4.8-5.2	21.0	30.0
σ_χ	Standard deviation of aerosol droplet radius	0.4-0.7	9.0	10.0
χ_s^0	Initial concentration of spores in the domain ($10^6/cm^3$)	0.185-1.0	6.0	2.0
L^0	Initial spore cloud length (cm)	5.0-10.0	6.0	2.0
n_s^p	Spores per aerosol droplet	1-5	5.0	1.0

dependence of I_s on μ_χ and σ_χ is significant with $\mu_\chi = 5.0$ and $\sigma_\chi = 0.5$ showing a good agreement with the experimental values. Hence, these values of μ_χ and σ_χ are used for all cases investigated in post-detonation flows. When all the water evaporates, the spores in a given droplet remain clustered or disperse. The spores are allowed to remain clustered in Case ST3 and are dispersed in Case ST4 to evaluate the differences in the number of intact spores. Between Case ST3 and Case ST4, the maximum difference in I_s is 4.4 (at $M_s = 1.9$) with the average difference in $I_s = 1.31$ (over all M_s). Since the average difference is not significant, for studies in post-detonation flows, the spores are assumed to be dispersed.

To summarize, the standard deviation and the mean of the initial droplet size are important parameters determining the time required to neutralize the spores, whereas the parameters such as ρ_s, C_s, T_C, L^0 and n_s^p have a negligible effect on I_s. The sensitivity analysis indicates that the number of intact spores for different post-shock conditions agree reasonably with the experimental results (See Fig. 45) over a wide range of parameters as shown in Table 11. Especially, the values for the representative case, Case ST4, are in good agreement, and hence, the set of spore-aerosol parameters used in this case are used for all the cases investigated in post-detonation flows.

7.5 Spore neutralization by explosive charges

Spore neutralization in post-detonation flow is investigated by varying the initial distance of the spore cloud, d^0, the initial spore cloud concentration, χ_s^0, and the initial spore cloud width in the radial direction, L^0, as shown in Table 9. Here, a spore cloud is a cluster of spore-laden aerosol droplets uniformly distributed in the azimuthal and the zenith directions and placed at radial distance d^0 from the center of the explosive charge.

7.5.1 Effect of initial spore concentration and initial spore cloud width

When the explosive charge is detonated in the vicinity of the spore cloud, the blast wave from the explosion propagates outwards from the charge and a post-detonation flow comprising of hot detonation product gases is generated. The events in this post-detonation flow can be categorized into 4 phases: (a) primary phase, (b) implosion phase, (c) reshock phase and (d) asymptotic phase (see Fig. 46). Initially, during the primary phase, the detonation

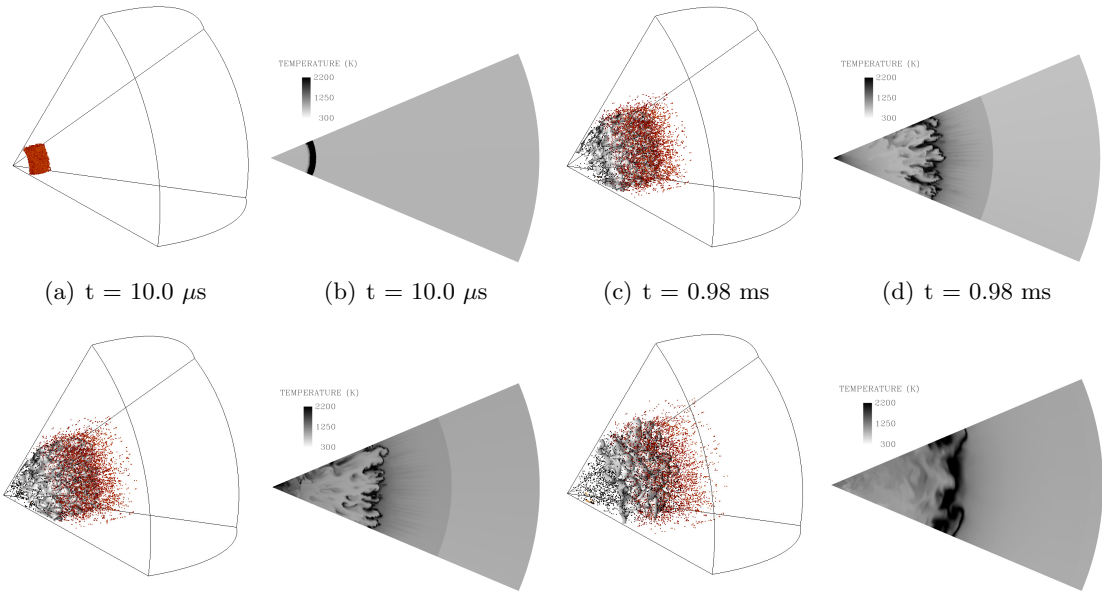

(a) t = 10.0 μs (b) t = 10.0 μs (c) t = 0.98 ms (d) t = 0.98 ms

(e) t = 1.3 ms (f) t = 1.3 ms (g) t = 4.7 ms (h) t = 4.7 ms

Figure 46: Position of damaged (black) and intact (red) spores in post-detonation flow for Case NM1C2. The mixing zone is indicated by iso-surface of N_2 ($Y_{N_2} = 0.5$). (a)-(b) correspond to primary phase, (c)-(d) correspond to implosion phase, (e)-(f) correspond to reshock phase, and (g)-(h) correspond to asymptotic phase.

product gases propagate outward along with the primary shock (PS) and engulf the spore aerosol cloud. The aerosol droplets are heated by the resulting high temperature gaseous environment and the evaporation of the water encapsulating the spores is initiated. During this phase, a secondary shock (SS) is formed due to the over expansion of the local flow by the inward moving rarefaction. The aerosol cloud, overtaken by the contact surface between detonation product gases and the ambient air, perturbs the contact surface and results in the formation of RTI [15] and the mixing/combustion zone. The afterburn of CO and H_2 further increases the temperature of the mixing zone.

At t $\sim$ 0.4 ms, the secondary shock starts propagating inwards, as shown in Fig. 47, as the core pressure is reduced by the rarefaction. This initiates the implosion phase, where the aerosol cloud is dragged towards the origin along with the mixing layer. However, the aerosol droplets, which acquired sufficient momentum due to the interaction with the outward propagating gases, remain outside the mixing zone and continue propagating outward. This motion of the leading edge of the mixing layer (MLLE), the trailing edge of the mixing layer

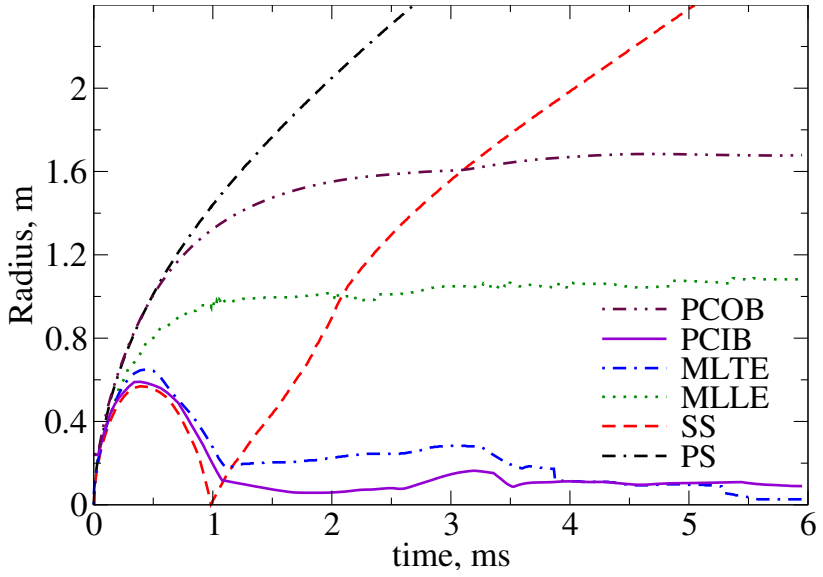

(a)

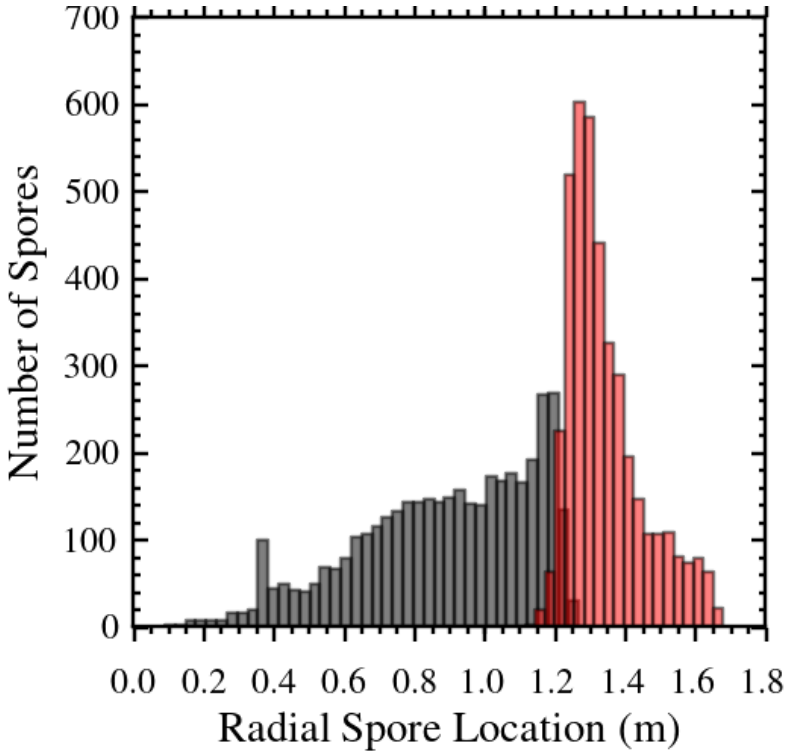

(b)

Figure 47: (a) Position of the Primary Shock (PS), the Secondary Shock (SS), the leading and the trailing end of the mixing layer (MLLE and MLTE), the inner and the outer boundaries of the particle cloud (PCIB and PCOB) at different time for Case NM1C2. (b) Histograms showing the distribution of the intact (red) and the damaged (black) spores based on their radial location at t = 6 ms. The radial positions are obtained by averaging the quantities in the azimuthal and the zenith directions.

(MLTE), the inner boundary of the spore cloud (PCIB) and the outer boundary of the spore cloud (PCOB) are shown in Fig. 47. The inner and the outer spore cloud boundaries are evaluated as the minimum and the maximum of the radial location of all the spores, respectively.

After propagating towards the origin, at t $\sim$ 1.0 ms, the secondary shock reflects back from the origin and interacts with the flow structures. The aerosol droplets, dragged towards the origin in the implosion phase, are pushed into the high temperature mixing zone. Also, the outward propagating secondary shock further drags the aerosol droplets, dispersed beyond the mixing zone, outward. The mixing zone, after interaction with the secondary shock in the reshock phase, settles into an asymptotic mixing phase, where the combustion is sustained by the continuous mixing of the detonation product gases and the ambient air. In all the phases of the post-detonation flow, the spores are exposed to the hot gases. However, the spores in the aerosol droplets with relatively higher water content take considerable time to get exposed. The neutralization of the spores in these droplets is facilitated by the asymptotic phase, where sustained mixing enables relatively longer residence time in the hot gases. Further, during the asymptotic phase, as the aerosol outside the mixing zone moves outwards, spores outside the mixing zone escape and remain intact. After 5.5 ms, most of the spores within the mixing zone are neutralized and the number of intact spores reaches an asymptotic value as shown in Fig. 48.

When the initial concentration of the spore cloud is increased from 0.276 $\times 10^3/cm^3$ to 0.552 $\times 10^3/cm^3$ (Cases NM1C2 and NM1C4), I_s increases from 52.3 to 53.6 at t = 6 ms. This negligible change is attributed to the difference in the number of spores that escape the mixing zone and the neutralization. Variation of χ_s^0 in other cases, shown in Table 9, also shows a negligible change in I_s (see Fig. 48). Similarly, changing L^0 from 3.0 mm to 12.0 mm results in a nominal increase in I_s from 52.3 to 54.6 (Cases NM1C2 and NM1D3). Here, again, the change in the number of intact spores is attributed to the change in the number of spores dispersed away from the mixing zone. Thus, when χ_s^0 and L^0 are varied for a fixed d^0, the variation in I_s is not significant. This is expected because of the dilute nature of the spore-laden flow considered here.

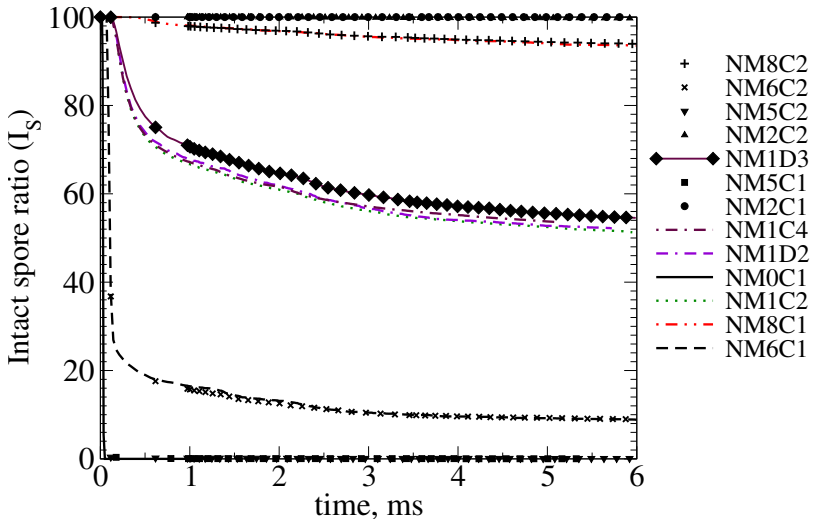

Figure 48: Variation of percentage of spores left intact with time for cases shown in Table 9.

7.5.2 Effect of initial distance from the charge

When the initial radial location of the spore-laden aerosol cloud, d^0, is varied from 12 cm to 98.0 cm, I_s changes from 0.0 to 100.0. Here, the post-detonation flow can be divided into three distinct regions based on the number of spores neutralized. These regions are (1) ISR1 ($d^0 \leq 3.0R_C$), (2) ISR2 ($3.0R_C < d^0 < 8.0R_C$) and (3) ISR3 ($d^0 \geq 8.0R_C$). In ISR1, the aerosol is initially located near the explosive charge, and most of the spores are neutralized in the primary phase after the initial engulfment. The droplets are not scattered away from the mixing zone and remain within the mixing layer boundaries as shown in Fig. 49. This enables maximum heat exposure and almost complete spore neutralization. Thus in ISR1, $I_s \sim 0.0$.

In ISR2, the spores are partially located within the mixing zone (see Fig. 47). The spore neutralization occurs over the primary, the implosion, the reshock and the asymptotic phases. Within this region, as d^0 is increased from $3.0R_C$ to $8.0R_C$, the proportion of spores neutralized in the primary phase decreases from 100.0 % to $\sim$ 0.0 %. Thus, the role of the mixing zone in spore neutralization increases. When $d^0 \geq 8.0R_C$, i.e., in ISR3, the aerosol is dispersed beyond the mixing zone by t $\sim$ 0.2 ms as shown in Fig. 50. The temperature in the post-PS and post-SS flow is relatively low in comparison to the temperature within

the mixing zone and sufficient heat is not transferred to the aerosol. Thus, $I_s \sim 100.0$ in ISR3.

In summary, the initial concentration of the aerosol and the initial width of the spore cloud have a negligible effect on the spore survival. Since the cases considered here fall in the dilute regime of two-phase flows, this is expected. However, depending on the aerosol droplet dispersal within and beyond the mixing/combustion zone in the post-detonation flow, a change in the initial radial distance from the charge affects the spore survival. Three regions, ISR1, ISR2 and ISR3 are defined, shown in Fig. 51, which provide a continuous change in I_s from 0 to 100 as d^0 is increased from 12 cm to 96.0 cm ($\sim 2.0R_C$ to $\sim 16.0R_C$).

7.6 Summary

With the aid of the methodology and the setup developed for homogeneous explosives in pure gaseous mixtures, bacterial spore neutralization in post-shock and post-detonation flows is investigated numerically. The key components of the interaction of a spore-laden aerosol with shock/blast waves are simulated by accounting for the heat and the mass transfer between the phases. The spore-laden aerosol is modeled based on parameters such as the concentration of spores and the aerosol droplet size distribution so that the results can be compared with the available experimental results. The intact spore percentages obtained in the shock tube studies agree well with the experiments over a wide range of modeling parameters. These investigations provide sufficient confidence to employ the spore-laden aerosol model to study spore neutralization in post-detonation flows of explosive charges.

In post-detonation flows, the initial concentration of the spores is shown to have a negligible effect on the overall spore survival. However, the initial distance from the explosive charge has a substantial effect on the intact spore ratio. When the spore cloud is placed within a distance of $3R_C$, nearly all the spores are damaged in about 0.2 ms. When spores are placed at distances of $8R_C$ and above, $I_s \sim 100.0$ as all the aerosol droplets are found to be scattered beyond the mixing zone before complete evaporation occurs. In the case with the initial radial distance from the charge between $3R_C$ and $8R_C$, I_s varies from ~ 0.0 to ~ 100.0. In these cases, a portion of spores is always found within the mixing/combustion

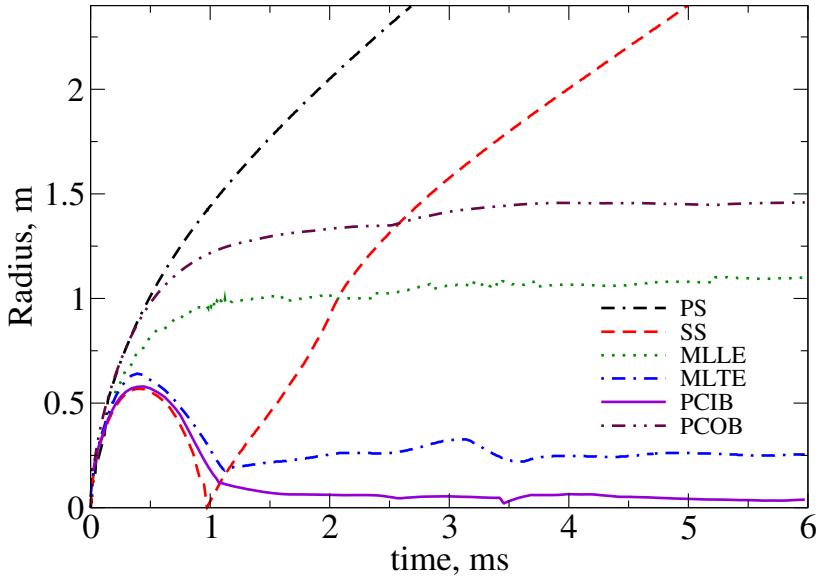

(a)

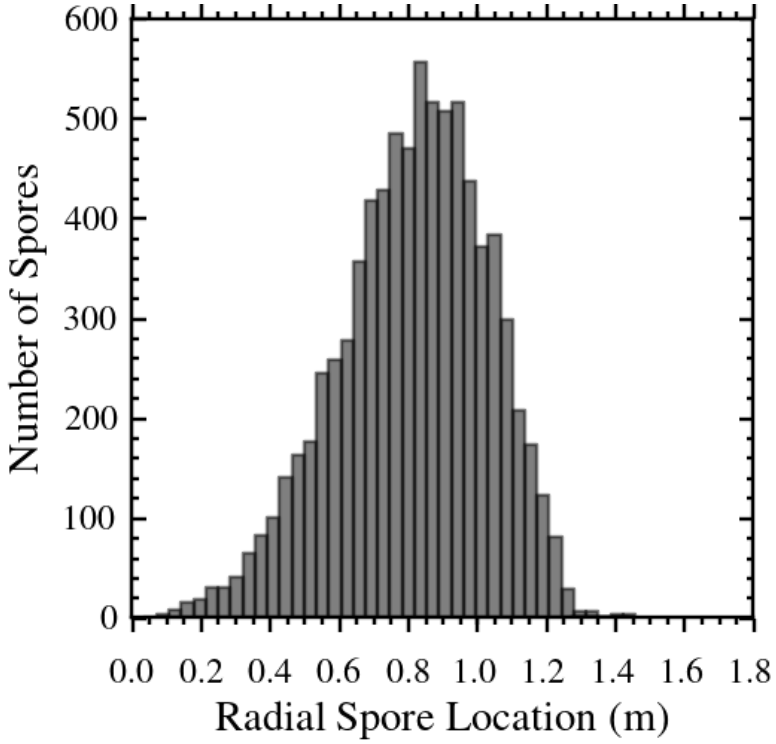

(b)

Figure 49: (a) Position of the Primary Shock (PS), the Secondary Shock (SS), the leading and the trailing end of mixing layer (MLLE and MLTE), the inner and the outer boundaries of the particle cloud (PCIB and PCOB) at different time for Case NM5C2. (b) Histogram showing the distribution of the spores based on their radial location at t = 6 ms. The radial positions are obtained by averaging the quantities in the azimuthal and the zenith directions.

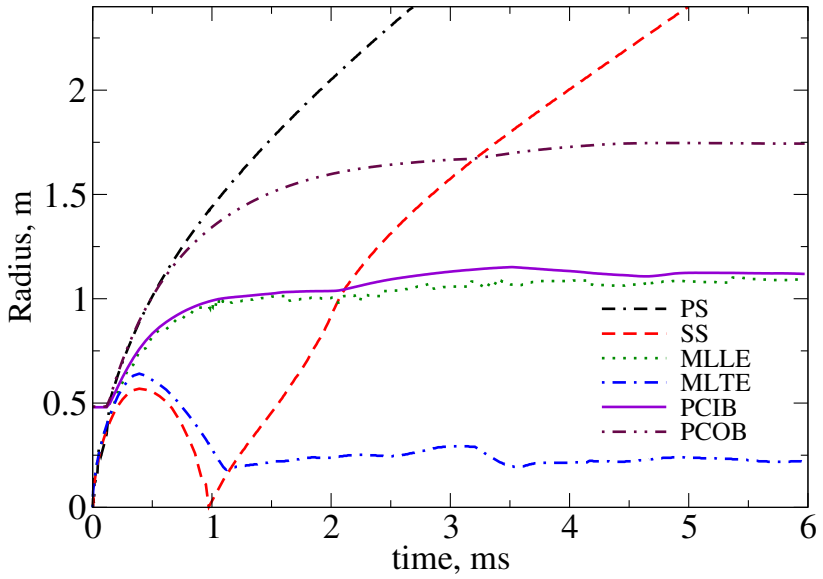

(a)

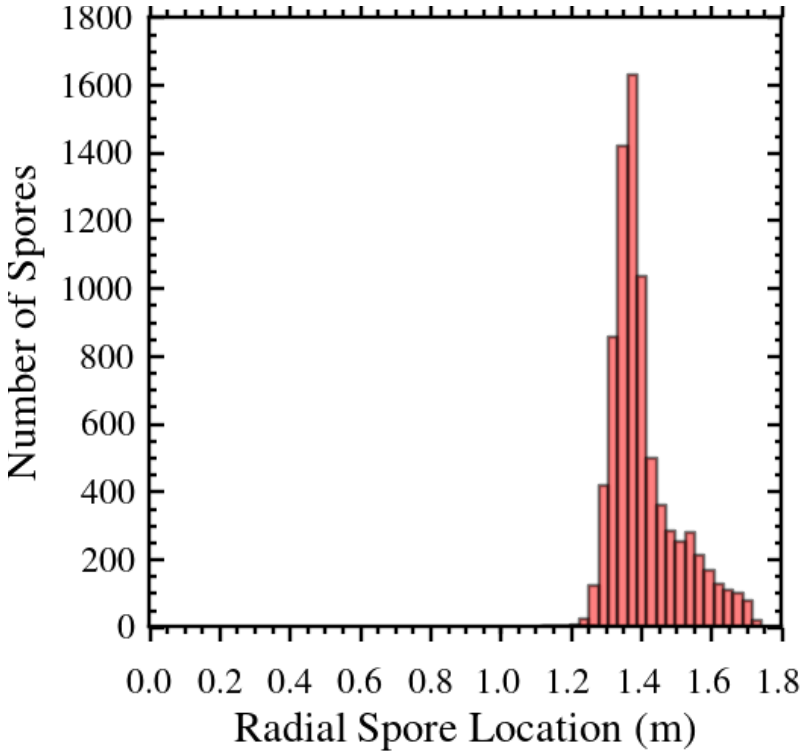

(b)

Figure 50: (a) Position of the Primary Shock (PS), the Secondary Shock (SS), the leading and the trailing end of mixing layer (MLLE and MLTE), the inner and the outer boundaries of the particle cloud (PCIB and PCOB) at different time for Case NM2C2. (b) Histogram showing the distribution of the spores based on their radial location at t = 6 ms. The radial positions are obtained by averaging the quantities in the azimuthal and the zenith directions.

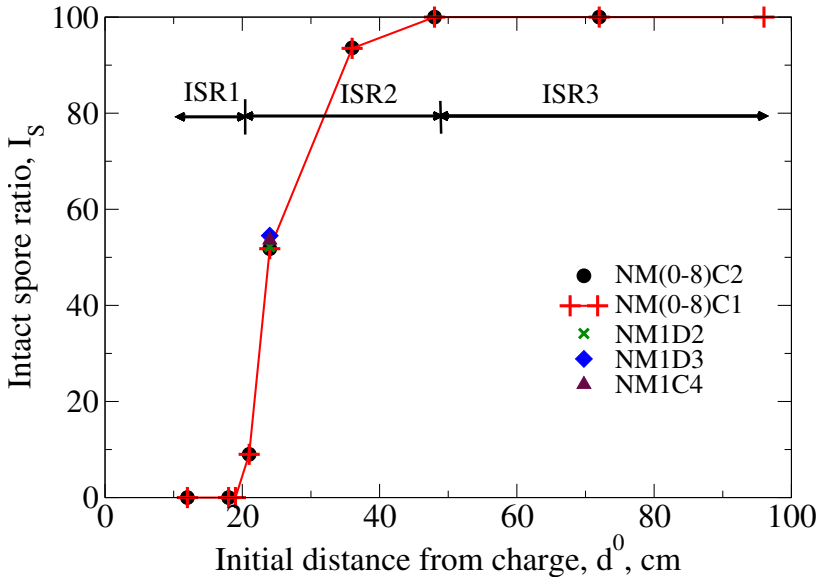

Figure 51: Percentage of spores left intact for different initial distance from the charge (d^0) for cases shown in Table 9. The Intact Spore Regions (ISR1, ISR2 and ISR3), based on d^0, are also labeled.

zone. Thus, three regions of spore neutralization are simulated in the post-detonation flow based on initial distance from the explosive charge. The investigations presented here are in the dilute regime, and hence, changes in the spore concentration produce little effect on I_s.

CHAPTER VIII

AFTERBURN IN POST-DETONATION FLOW

Dispersion and combustion of aluminum particles in the post-detonation flow are discussed in this chapter. Heterogeneous charges with dilute and dense loading of aluminum particles are considered. The particle combustion is modeled based on the kinetic and diffusive limited burning regimes. The first section of this chapter is dedicated to the analysis of the effect of the particle size and the initial distance of the particle from the explosive charge on the particle combustion. In the next section, the dispersion and combustion of aluminum particles, initially packed to form a dilute cluster, are studied. The third section, combustion of dense aluminum particle clusters is analyzed. Here, comparisons are made with afterburn in the corresponding cases with steel particles. In all cases the effects of the particle mass fraction (η) or particle volume fraction (α_p or α_d) and the initial particle radius (r_{p_0}) are described.

8.1 Aluminum particle combustion

Aluminum particle combustion is known to occur in two regimes, kinetic-limited regime and diffusion-limited regime [130]. When the mass transfer and combustion occurs in the kinetic-limited regime, the particle temperature plays a critical role and in the diffusion-limited regime the particle combustion is determined by the concentration of the oxidizer. In both the limits, the mass transfer is dependent on the particle size. At a given temperature, reduction in the particle size results in the kinetic limited burning. However, the particles in the post-detonation flow do not have uniform temperature and the temperature of the particle is initially almost same as the ambient gas temperature. The particle temperature increases as it interacts with the post-detonation flow and hence the relation between the mass transfer rate and the particle size is not trivial. Also, since the particle temperature and the residence time varies with a change in the initial location, the distance from the initial charge also determines the effective mass transfer. Thus, the initial particle radius

and the distance from the charge are varied to study the aluminum burning regimes in the post-detonation flow.

The setup used in this problem is same as that described in Chapter 6 for heterogeneous charges except the initial detonation profile used in Chapter 5 for homogeneous charge is used. The location and the initial radius of aluminum particle for different cases considered are provided in Table 12.

8.1.1 Effect of particle size

The temperature of the particle and the radius of the particle are the dominant parameters in determining the mass transfer and the particle combustion. These two parameters along with the change in the particle location with time are shown in Figs. 52 - 54. When r_{p_0} is decreased from 50.0 μm to 1.0 μm, the reduction in the particle radius is increased from almost 0 to 90.0 %. The mass transfer from the particle is dependent on temperature of the particle. Smaller particles tend to equilibrate with the flow at a faster rate. Thus, the temperature of particle increases with decrease in r_{p_0} from 50.0 μm to 1.0 μm (from 450.0 K to 3100.0 K for $d_0 = 10.0$ cm). Hence, the mass transfer is also reduced with increase in the particle size. For example, the total mass transfer for $r_{p_0} = 50.0$ μm is in the range of $10^{-13} - 10^{-11}$ kg/s where as in cases with $r_{p_0} = 16.0$ μm it is in the range of $10^{-9} - 10^{-7}$ kg/s. Since the mass transfer acts to decrease the particle radius, the reduction in the particle radius for small particles is greater, i.e., a drop of 90.0 % radius for $r_{p_0} = 1.0$ μm in comparison to 32.0 % for radius for $r_{p_0} = 4.0$ μm.

The effective mass transfer from each particle is computed based on the the kinetic-limited mass transfer and the diffusion-limited mass transfer. If the mass transfer due to diffusion is much greater than the mass transfer due to kinetics ($\dot{m}_D \gg \dot{m}_K$), the effective mass transfer is kinetic-limited and the trend of $\dot{m}_p$ follows that of $\dot{m}_K$. However, if $\dot{m}_D \ll \dot{m}_K$, $\dot{m}_p \approx \dot{m}_D$. This is shown in Figs. 55 - 57. Only for $r_{p_0} = 1.0$ μm and $r_{p_0} = 2.0$ μm, the temperature of the particle is high enough (≥ 1100 K) to obtain a diffusion-limited mass transfer. In all other cases, $\dot{m}_D \gg \dot{m}_K$, and thus $\dot{m}_p$ follows that of $\dot{m}_K$. This is against expected trend with increase in particle radius at a fixed temperature. Thus, in the

Table 12: Parameters used to specify the initial conditions of the dispersed phase to investigate the effect of r_{p_0} and d_0 on aluminum particle combustion.

Case	d_0 cm	r_{p_0} μ m
D1R1	10.0	50.0
D1R2	10.0	32.0
D1R3	10.0	16.0
D1R4	10.0	8.0
D1R5	10.0	4.0
D1R6	10.0	2.0
D1R7	10.0	1.0
D2R1	30.0	50.0
D2R2	30.0	32.0
D2R3	30.0	16.0
D2R4	30.0	8.0
D2R5	30.0	4.0
D2R6	30.0	2.0
D2R7	30.0	1.0
D3R1	50.0	50.0
D3R2	50.0	32.0
D3R3	50.0	16.0
D3R4	50.0	8.0
D3R5	50.0	4.0
D3R6	50.0	2.0
D3R7	50.0	1.0

post-detonation flow, the change in the temperature of the particle dominates the particle size affect and determines the effective mass transfer and particle burning rate.

8.1.2 Effect of initial distance from the charge

When particles move away from the charge, the temperature of the particle is reduced from 4 to 10 times the initial value to about 1.5 times the initial value. This is due to fact that the temperature in the post-detonation flow decreases with increase in the radial distance away form the origin. Here again the temperature provides a dominant effect and the mass transfer transitions to the kinetic-limited regime from the diffusion-limited regime as the initial distance from the charge increases. This is clear in cases with $d_0 = 50.0$ cm, shown in Fig. 57, where even cases with $r_{p_0} = 1.0$ and 2.0 μm follow an effective hybrid mass transfer instead of the diffusion-limited mass transfer.

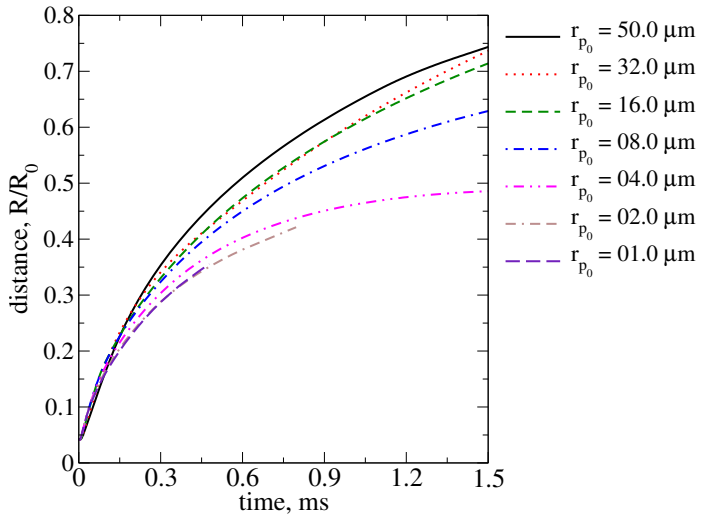

(a) $d_0 = 10$ cm

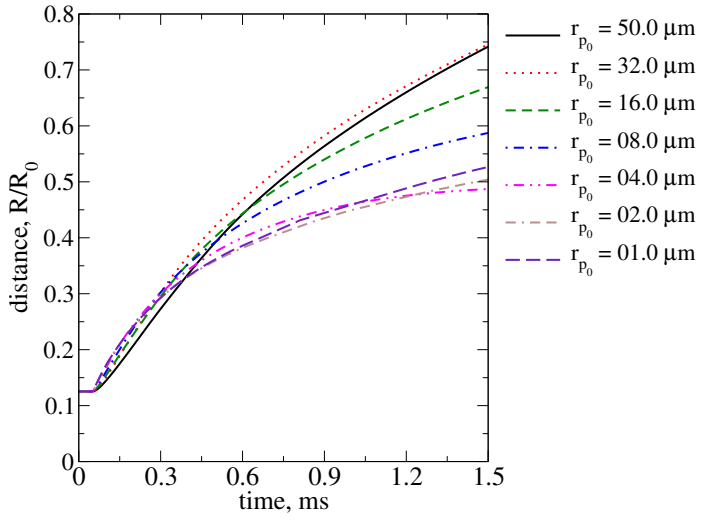

(b) $d_0 = 30$ cm

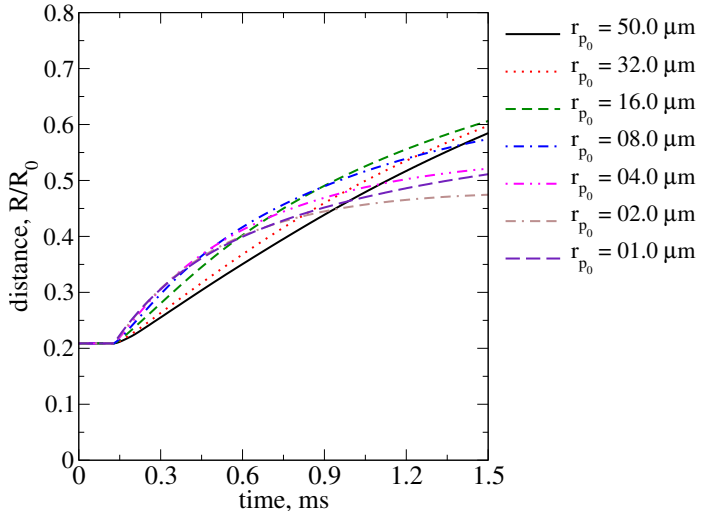

(c) $d_0 = 50$ cm

Figure 52: Change in the radial location (normalized by the radius of the domain) of the aluminum particle with time for different initial particle radius (r_{p_0}).

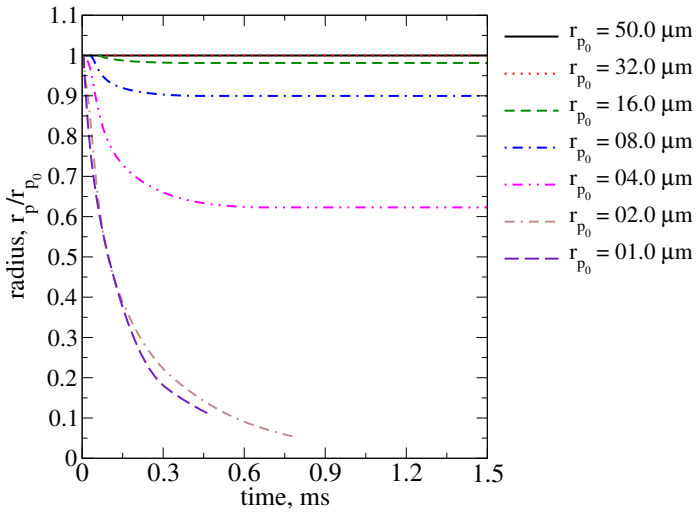

(a) d_0 = 10 cm

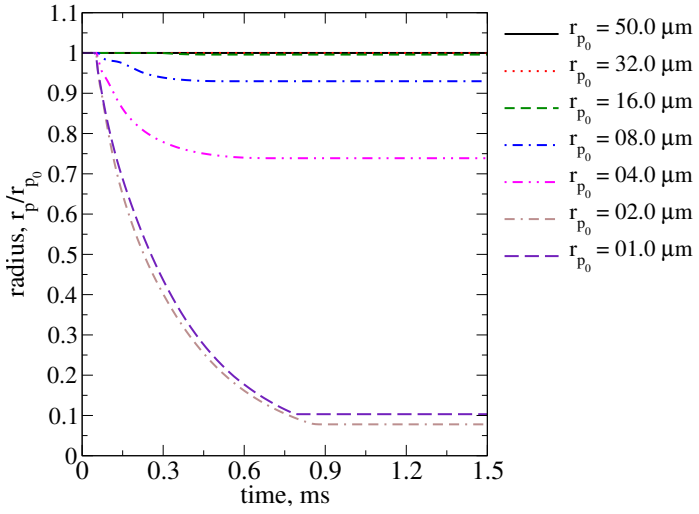

(b) d_0 = 30 cm

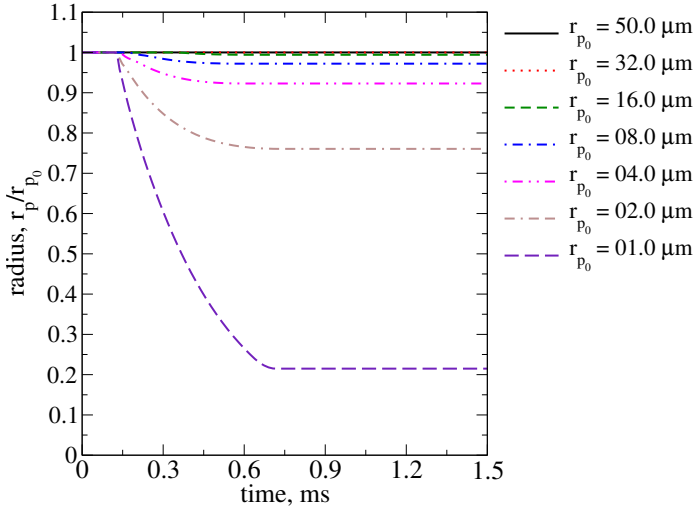

(c) d_0 = 50 cm

Figure 53: Change in the radius (normalized by initial radius of the particle) of the aluminum particle with time for different initial particle radius (r_{p_0}).

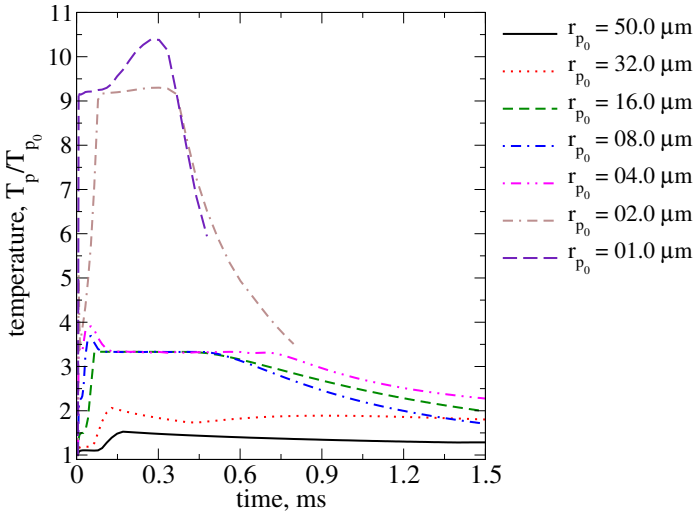

(a) $d_0 = 10$ cm

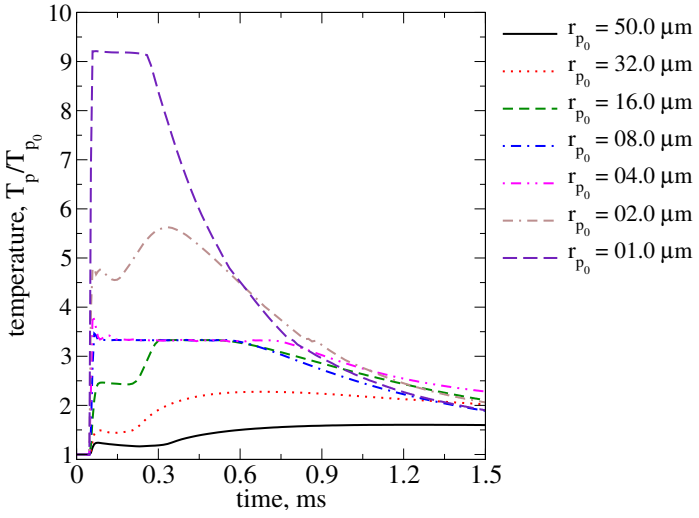

(b) $d_0 = 30$ cm

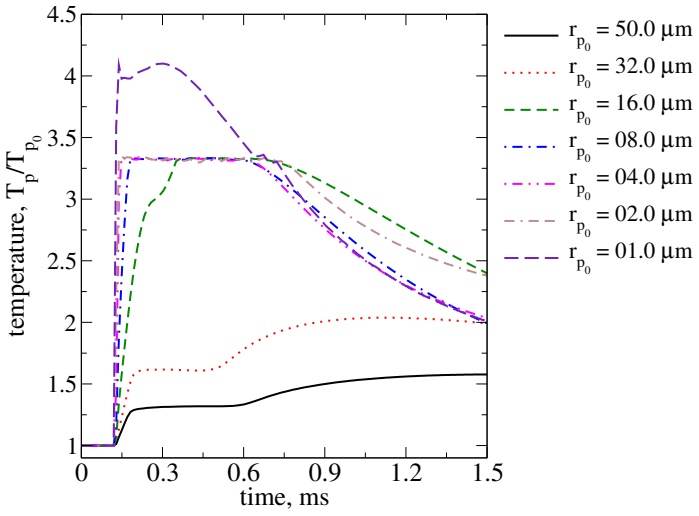

(c) $d_0 = 50$ cm

Figure 54: Change in the temperature (normalized by the initial particle temperature) of the aluminum particle with time for different initial particle radius (r_{p_0}).

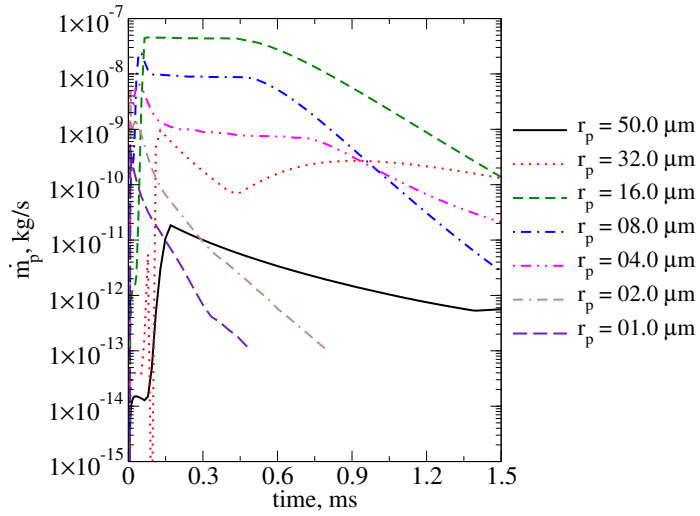

(a) $\dot{m}_p$

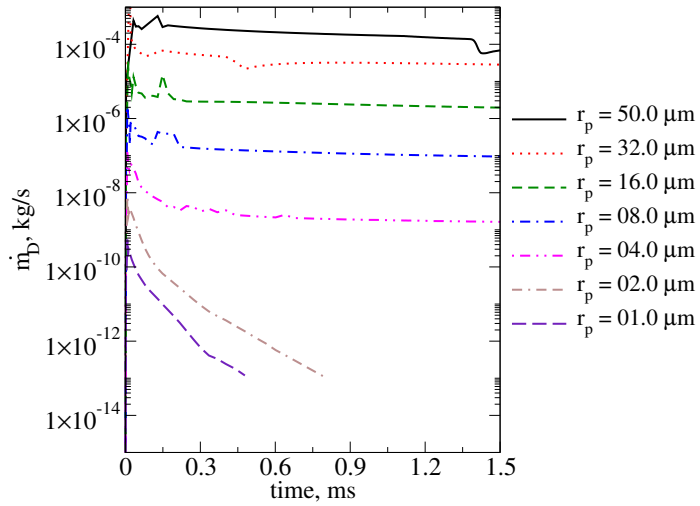

(b) $\dot{m}_D$

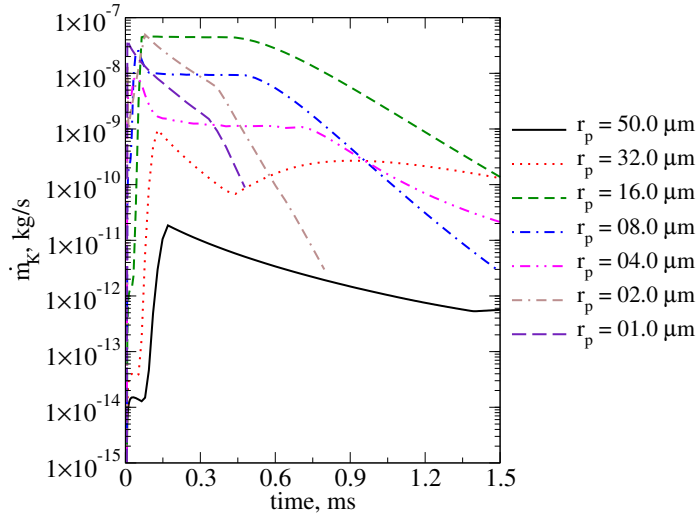

(c) $\dot{m}_K$

Figure 55: Change in mass transfer rate with time for aluminum particle placed initially at 10 cm from the charge center.

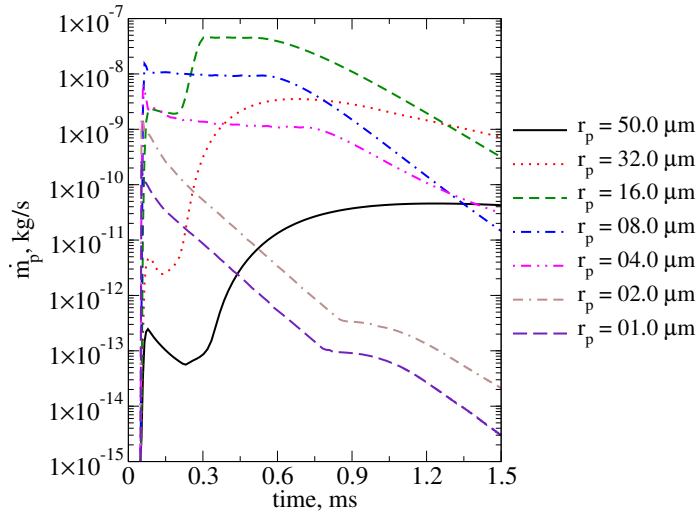

(a) $\dot{m}_p$

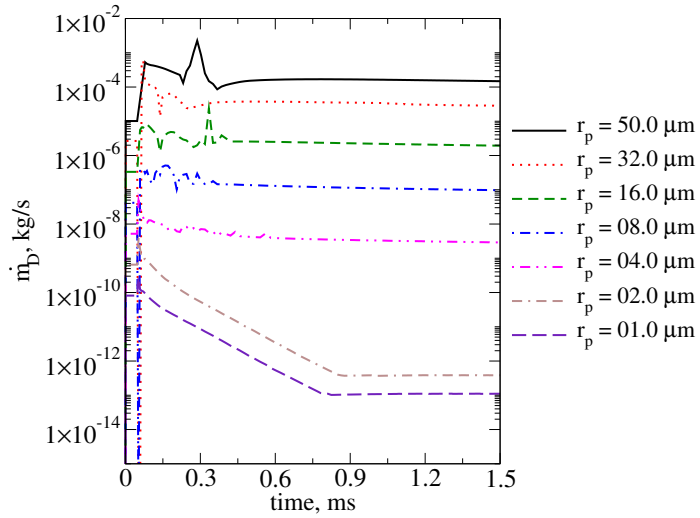

(b) $\dot{m}_D$

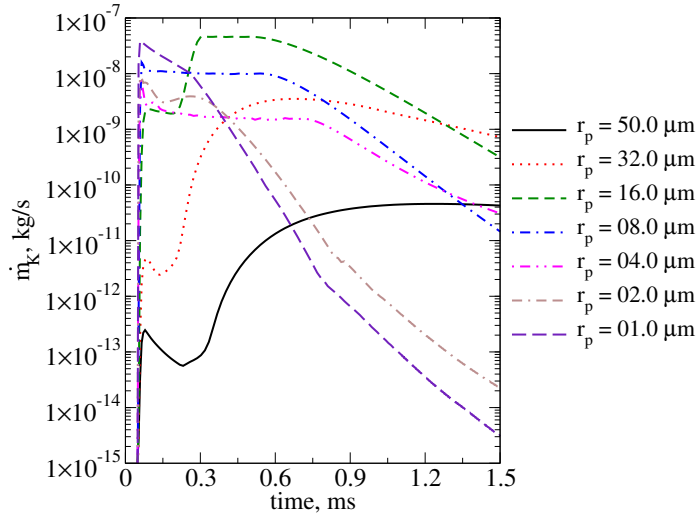

(c) $\dot{m}_K$

Figure 56: Change in mass transfer rate with time for aluminum particle placed initially at 30 cm from the charge center.

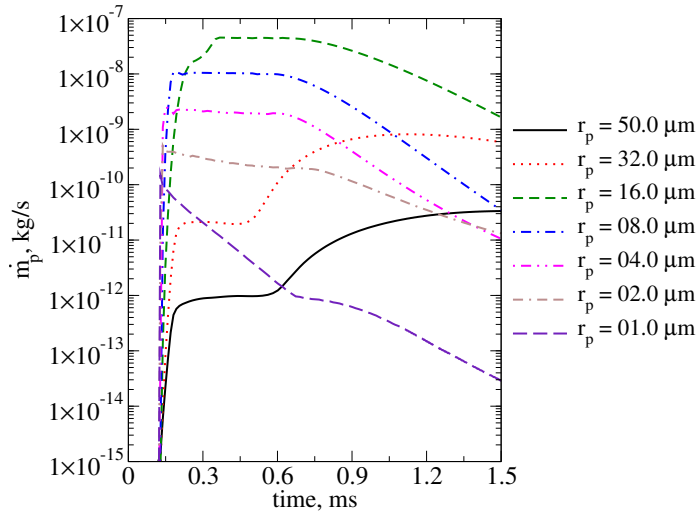

(a) $\dot{m}_p$

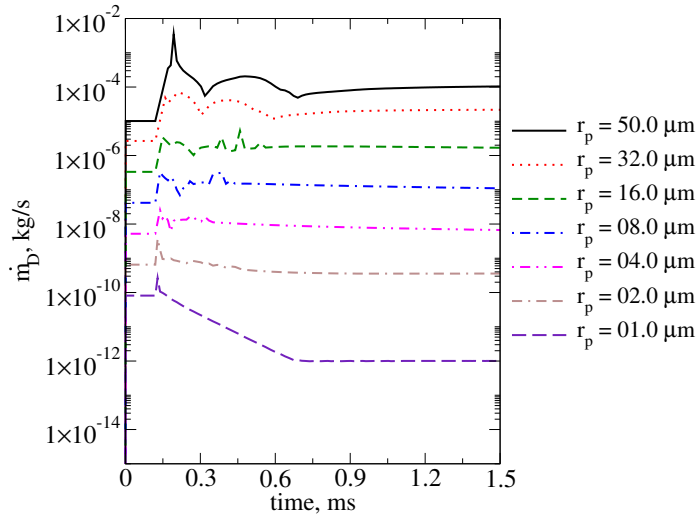

(b) $\dot{m}_D$

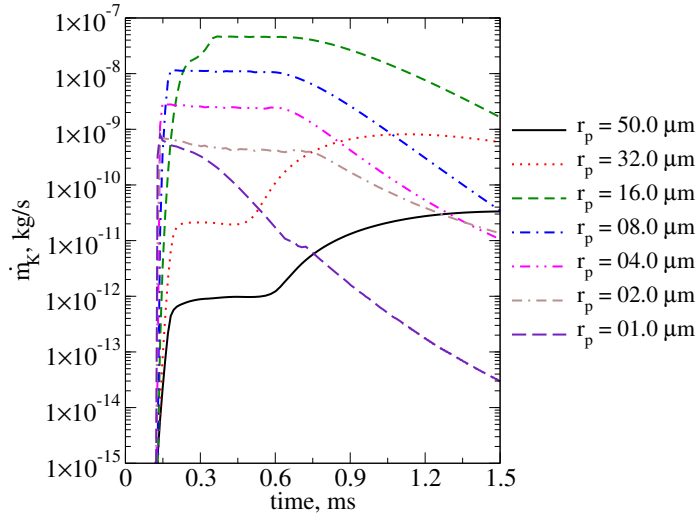

(c) $\dot{m}_K$

Figure 57: Change in mass transfer rate with time for aluminum particle placed initially at 50 cm from the charge center.

8.2 Dilute particle cloud dispersion and combustion

In order to study the particle combustion in dilute post-detonation flow, NM charges with aluminum particles are considered. The particles are initially placed uniformly within the charge. The domain dimensions and the grid resolution employed here are identical to the one descried for the homogeneous charge cases discussed in Chapter 5. As indicated in Table 1, mass fraction of the particles, η, and the initial particle radius, r_{p_0}, are varied, and the resulting post-detonation flow is studied in each case.

One of the ways to characterize the amount of mixing in the post-detonation flow is by computing the region in the flow where ambient gases mix with the detonation product gases. This is achieved by defining, degree of mixedness (DM), and is expressed as [16]:

$$DM = \frac{\left[\frac{\int Y_{CO}(Y_{N_2}-Y^i_{N_2})dV}{\int dV}\right]}{\left[\left(\frac{\int Y_{CO}dV}{\int dV}\right)\left(\frac{\int (Y_{N_2}-Y^i_{N_2})dV}{\int dV}\right)\right]}, \tag{138}$$

where Y_{CO} and Y_{N_2} are, respectively, the instantaneous mass fractions of CO and N_2 and $Y^i_{N_2}$ is the mass fraction of N_2 in the initial detonation products. When a heterogeneous charge explodes, the solid particles present within the charge are driven out. As these particles disperse outward, they perturb the contact surface between the detonation products and ambient air. Thus, increase in the number of particles results in increased perturbations and hence increase in mixing. Thus, in Cases 2 and 3, due to increased mixing, as a result of more number of particles in comparison to Case1, CO is converted to CO_2 and DM, in Fig. 58, decreases initially till time (t) = 0.5 ms. However, in Case 3, the $5\mu m$ particles burn quickly in comparison to $10\mu m$ particles. The Al combustion consumes O_2 needed for CO_2 production and thus DM in Case 3 increases above the values of DM for Cases 1 and 2 at t = 2.5 ms and 1.75 ms, respectively. In Case 2, the value of DM remains lower than that of Case 1 because of greater mixing and same burn rate for Al. Thus, for a fixed η, DM increased with decrease in r_{p_0} after the implosion phase and for a fixed initial r_{p_0}, DM decreased with increase in η.

As the blast wave is driven outwards, the initial mixing of aluminum particles with air and detonation products results in particle burning and increase in the mass fraction of

Table 13: Initial radius of particles (r_{p_0}), mass loading and number of particles tracked in each case. Particles are tracked by tracking parcels. Here, each parcel contains 50 particles.

Case	η	r_{p_0} (μm)	Number of parcels
1	1.0	10.0	86881
2	2.0	10.0	173762
3	1.0	5.0	695048

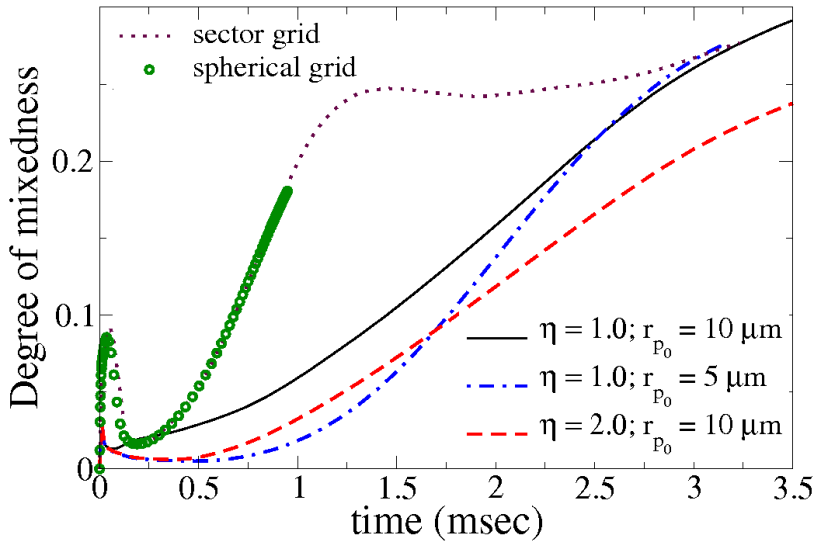

Figure 58: Variation of degree of mixedness with time. Dots and circles (sector and spherical grids) indicate cases with homogeneous explosive.

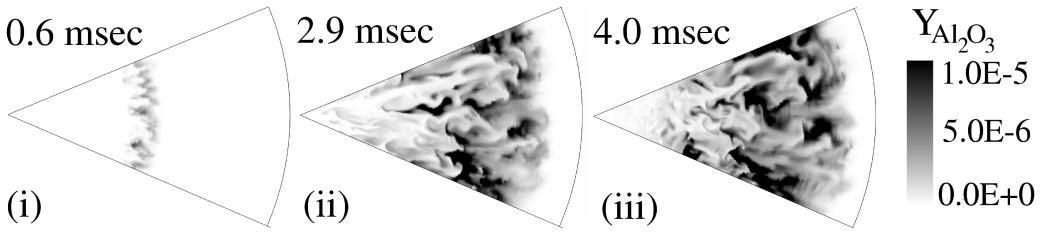

Figure 59: Formation of Al_2O_3 due to the combustion of Al in the post-detonation flow of a heterogeneous nitromethane charge (Case 1) during (i) blast wave, (ii) implosion, and (iii) re-shock phases.

Al_2O_3 ($Y_{Al_2O_3}$). This is followed by the implosion phase in which the particles are drawn towards the center along with the gases and hence the particle burning is enhanced. As the secondary-shock is formed after the implosion phase, the re-shock drives the particles outwards and the particle burning continues in the mixing layer. These phases are shown in Fig. 59. Figure 60 shows that the particle dispersion, which determines Al availability and mixing, determines the amount of oxidizer (O_2 for 'aerobic', and H_2O and CO_2 for 'anaerobic' reactions) available, on the particle combustion. In Case 3, even though mixing is greater than Case 1 due to larger number of particles, the burning rate is high and thus the outer boundary overtakes the outer boundary of Case 1. Also, 5 μm particles are entrained and dragged towards center easily in comparison to 10 μm particles. Hence, the inner boundary in Case 3 is drawn below the inner boundary of Cases 1 and 2 during the implosion phase. Again during the re-shock phase, as 5 μm particles have relatively less inertia, the inner boundary overtakes the inner boundaries of Cases 1 and 2. In Case 2, the burn rate of particles is same as in Case 1. Hence higher mixing results in both the inner and outer boundaries of Case 2 to be within the inner and outer boundaries of Case 1. Thus, burn rate and mixing which directly depend on η and r_{p_0} determine the afterburn and particle combustion.

8.3 Dense particle cloud dispersion and combustion

Dispersion and combustion of particles dispersed by the explosion are investigated by considering spherical NM charge of diameter 11.8 cm packed with particles of initial radius (r_{p_0}) 2.0 μm-8.0 μm. Particles form a dense cluster in the explosive charge with the volume fraction of the particles in the charge being 15.5 % or 31.0 %. The initial dispersed phase volume fraction (α_{p_0}) chosen here is half and one-fourth that of the case discussed in Chapters 5 and 6. Number of particles per parcel is varied in each case and the values range from 1800 to 7200. The initial volume fractions and the number of particles per parcel are chosen based on computational feasibility. The radius of particles is chosen such that the combustion is in kinetic-controlled regime or in the hybrid regime. The values of different parameters for each case are summarized in Table 14. Note that, in all cases, the number of

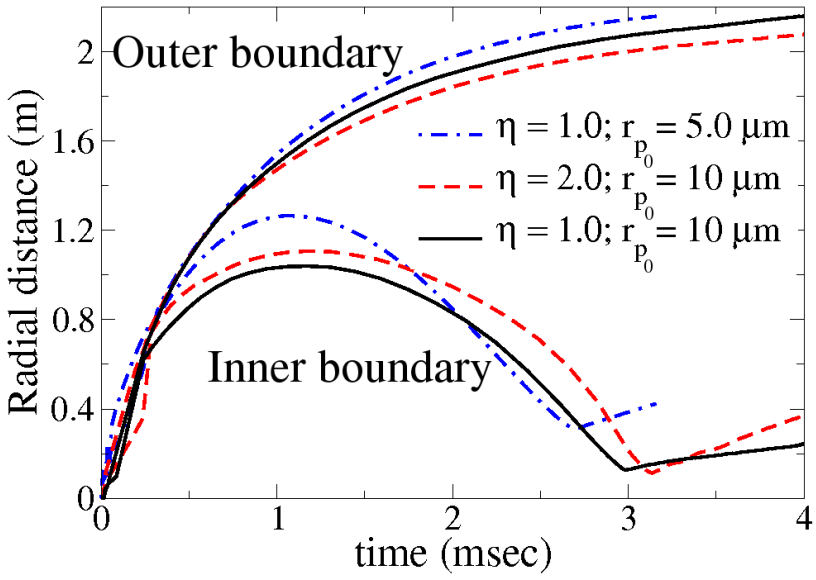

Figure 60: Variation of the inner and the outer boundaries of Al combustion with time. Here, the inner most and the outer most radial locations where the mass fraction of Al_2O_3 is at least 5% of maximum mass fraction of Al_2O_3 is defined as the inner and the outer boundary, respectively.

particles in the post-detonation flow varies from 5.8 billion to 187.6 billion. Even the number of parcels vary from about 1.6 million to 26 million. Hence, the massively parallel EL approach and the EE-EL method described in the previous chapters are used here. These methods render these cases, which are computationally prohibitive before, feasible.

Studies discussed in this section are performed using a domain, a grid and boundary conditions identical to the case of Homogeneous charge discussed in Chapter 5. However, in each case, the initial detonation profile and the initial profile for dispersed phase properties are obtained using the GISPA method. The quasi-steady drag on each particle is computed using the drag law provided by Akhatov and Vainshtein [3]. The rest of this section describes the influence of the particles on the processes in the post-detonation flow and the effects of the choice of r_{p_0} and α_{p_0}.

8.3.1 Post-detonation flow with dense particle clouds

The events in the post-detonation flow are influenced by the presence of the particles. The shock waves in the flow interact with the particles and are attenuated. The transfer of the

momentum and the energy between the phases also affects the mixing zone. The chronology of the post-detonation flow with dense clouds of inert/reactive particles can be described as follows:

1. **Blast wave:** As discussed in the case of a homogeneous charge, the detonation of a heterogeneous charge generates a strong blast wave driven outward away from the origin. The detonation product gases follow this blast wave and interact with the ambient air. The particles are also driven outward and are initially contained within the contact surface between the detonation products and air. The particles absorb the momentum and the energy from the accelerating gases and are dispersed beyond the contact surface. A mixing zone is produced due to the perturbations induced by the particles. Also, the initial perturbations in the contact surface due to the imperfections on the charge surface along with the acceleration of the gases generates the mixing zone. The mixing zone formed at 0.68 ms, for case with both steel and aluminum particles, is shown in Fig. 61. Here, till 0.68 ms, both steel and aluminum cases show identical features. The combustion in the mixing zone is shown in Fig. 62 and most of the reactions are concentrated at the thin contact between the detonation products and air.

2. **Implosion:** As the blast wave propagates a rarefaction propagates towards the origin and leads to an implosion. The implosion and the formation of the secondary shock wave are delayed by about 0.5 - 1.0 ms for heterogeneous charges studies here in comparision to the homogeneous charge. This is a result of particles attenuating the propagating secondary shock wave. Also, in comparison to aluminum, steel particles have delayed the processes by about 0.3-0.5 ms because of the additional inertia, and the associated momentum and energy transfer from the gases. Figure 61 shows that at 2.0 ms, the case with aluminum particles has already imploded with a secondary shock moving outward, where as in the case with steel particles the shock wave is about to reach the origin. The stretched combustion zone formed by t = 2.0 ms is shown in Fig. 62. Relatively, 100 to 200 K higher temperature, due to the particle

combustion, in the case with aluminum particles is also noticed.

3. **Reshock:** As the secondary shock propagates outwards away from the origin, it interacts with the particles and the mixing zone. The particles are further propelled away from the origin, as shown in Fig. 63, along with the mixing zone. The secondary shock interaction with the mixing zone results in the RMI, and the mixing in the flow reaches a peak value just before the reshock. The mixing quantified using the parameter DM is shown in Fig. 64, and the peak values are at $DM = 0.3$.

4. **Asymptotic mixing:** The reshock phase leads to asymptotic mixing of the gases and the particles in the flow. Here, the combustion is continued with only a minor variation of about 0.05 m to 0.1 m in the thickness of the mixing zone. Both the primary and the secondary shock waves move far beyond the particle cloud and the mixing zone. Particles also spread beyond the combustion zone (fireball) as shown in Figs. 63 (i) and (j).

During all these phases, particles act to enhance the mixing zone. In comparision to the case with the homogeneous charge, the peak value of DM is about 0.05 higher for cases with particles. However, the mass of CO_2 produced in the case of homogeneous charge is highest as shown in Fig. 65. Here, the mass of CO_2 in the flow is computed as

$$m_{CO_2} = \int \alpha_g \rho_g Y_{CO_2} dV, \tag{139}$$

where the integration is performed over the entire domain. Note that the inert nature of steel particles results in about 20.0 to 25.0 % less CO_2 in comparison to the aluminum particle cases.

8.3.2 Effects of initial volume fraction and particle size

The post-detonation flow has relatively more number of particles and relatively higher dispersed phase volume fractions when the initial volume fraction of the particles in the charge is increased. This results in attenuation of waves propagating through the gas-particle mixture. Further, the transmitted shock strength decreases due to the increased

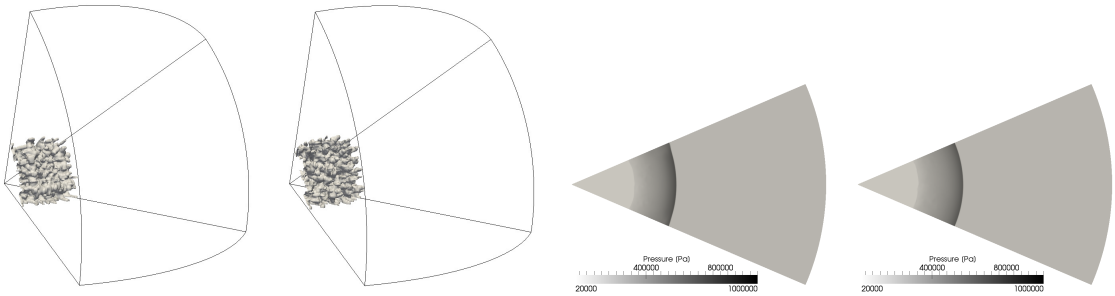

(a) t = 0.68 ms; Y_{N_2}; SV2R3 (b) t = 0.68 ms; Y_{N_2}; AV2R3 (c) t = 0.68 ms; p_g; SV2R3 (d) t = 0.68 ms; p_g; AV2R3

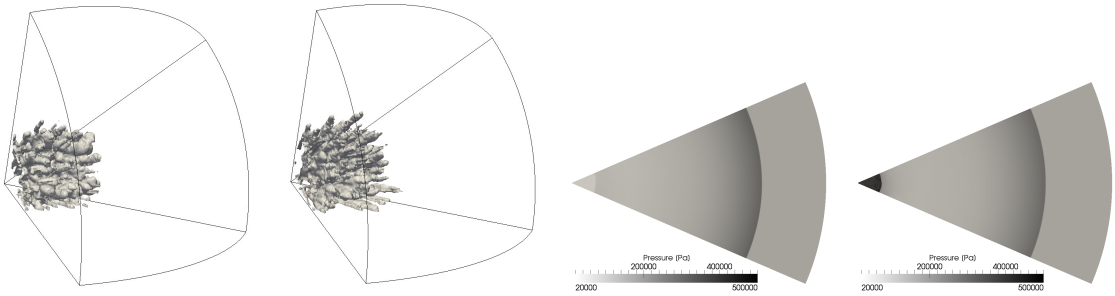

(e) t = 2.0 ms; Y_{N_2}; SV2R3 (f) t = 2.0 ms; Y_{N_2}; AV2R3 (g) t = 2.0 ms; p_g; SV2R3 (h) t = 2.0 ms; p_g; AV2R3

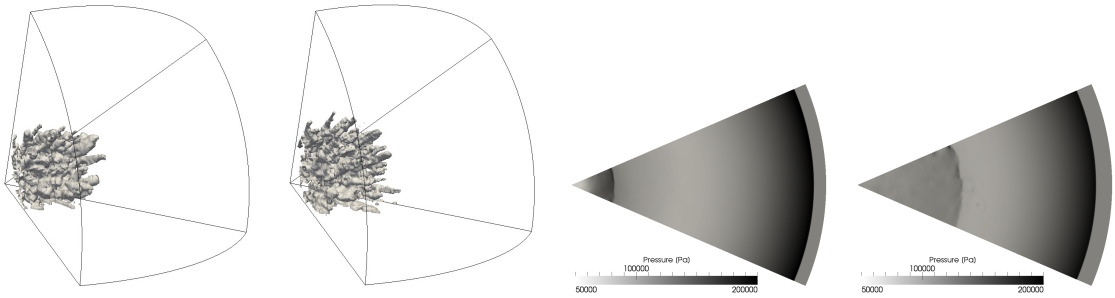

(i) t = 3.0 ms; Y_{N_2}; SV2R3 (j) t = 3.0 ms; Y_{N_2}; AV2R3 (k) t = 3.0 ms; p_g; SV2R3 (l) t = 3.0 ms; p_g; AV2R3

Figure 61: Pressure showing the blast front and mixing layer shown using iso-surface of $Y_{N_2} = 0.5$ for Cases SV2R3 and AV2R3 shown in Table 14.

Table 14: Parameters used to specify the initial conditions of the dispersed phase in the simulation with heterogeneous explosive charges.

Case	α_{p_0}	η	r_p μ m	P_p	Number of parcels	Number of particles	Particle type
SV1R1	0.155	958.9	2.0	7200	26052048	187574745600	steel
SV1R2	0.155	958.9	4.0	1800	13026024	46893686400	steel
SV1R3	0.155	958.9	8.0	1800	1627524	2929543200	steel
SV2R3	0.310	1917.7	8.0	3600	1627524	5859086400	steel
AV1R3	0.155	328.8	8.0	1800	1627524	2929543200	aluminum
AV2R3	0.310	657.6	8.0	3600	1627524	5859086400	aluminum

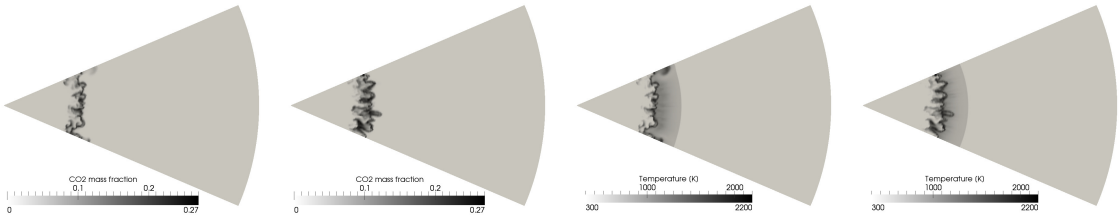

(a) t = 0.68 ms; Y_{CO_2}; SV2R3 (b) t = 0.68 ms; Y_{CO_2}; AV2R3 (c) t = 0.68 ms; T_g; SV2R3 (d) t = 0.68 ms; T_g; AV2R3

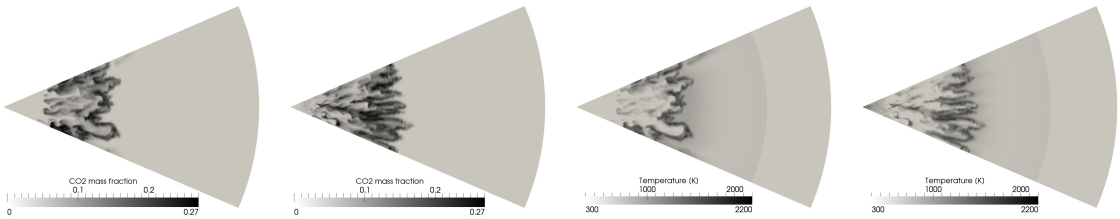

(e) t = 2.0 ms; Y_{CO_2}; SV2R3 (f) t = 2.0 ms; Y_{CO_2}; AV2R3 (g) t = 2.0 ms; T_g; SV2R3 (h) t = 2.0 ms; T_g; AV2R3

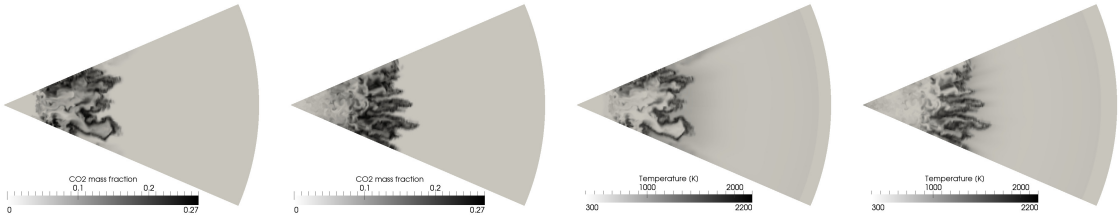

(i) t = 3.0 ms; Y_{CO_2}; SV2R3 (j) t = 3.0 ms; Y_{CO_2}; AV2R3 (k) t = 3.0 ms; T_g; SV2R3 (l) t = 3.0 ms; T_g; AV2R3

Figure 62: Temperature of the gases and the mass fraction of CO_2 in the post-detonation flow for Cases SV2R3 and AV2R3 shown in Table 14.

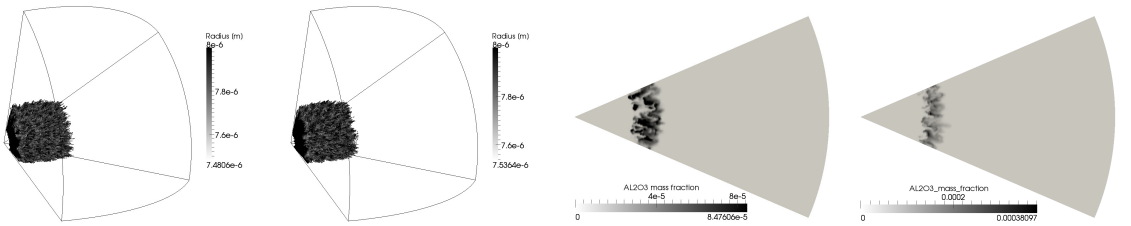

(a) t = 0.68 ms; AV1R3 (b) t = 0.68 ms; AV2R3 (c) t = 0.68 ms; $Y_{Al_2O_3}$; AV1R3 (d) t = 0.68 ms; $Y_{Al_2O_3}$; AV2R3

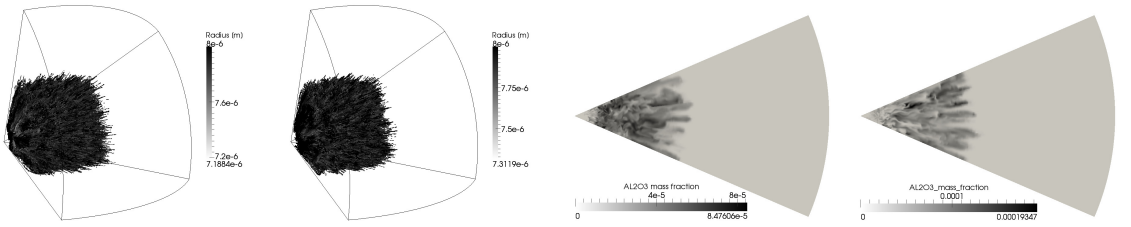

(e) t = 2.0 ms; AV1R3 (f) t = 2.0 ms; AV2R3 (g) t = 2.0 ms; $Y_{AL_2O_3}$; AV1R3 (h) t = 2.0 ms; $Y_{Al_2O_3}$; AV2R3

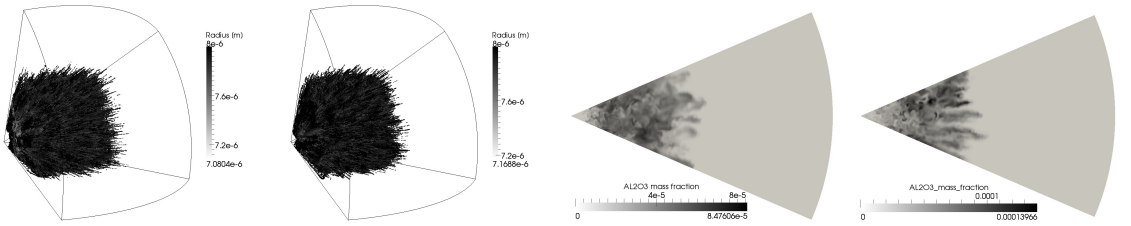

(i) t = 3.0 ms; AV1R3 (j) t = 3.0 ms; AV2R3 (k) t = 3.0 ms; $Y_{Al_2O_3}$; AV1R3 (l) t = 3.0 ms; $Y_{Al_2O_3}$; AV2R3

Figure 63: The mass fraction of Al_2O_3 and particles in the post-detonation flow for Cases AV1R3 and AV2R3 shown in Table 14.

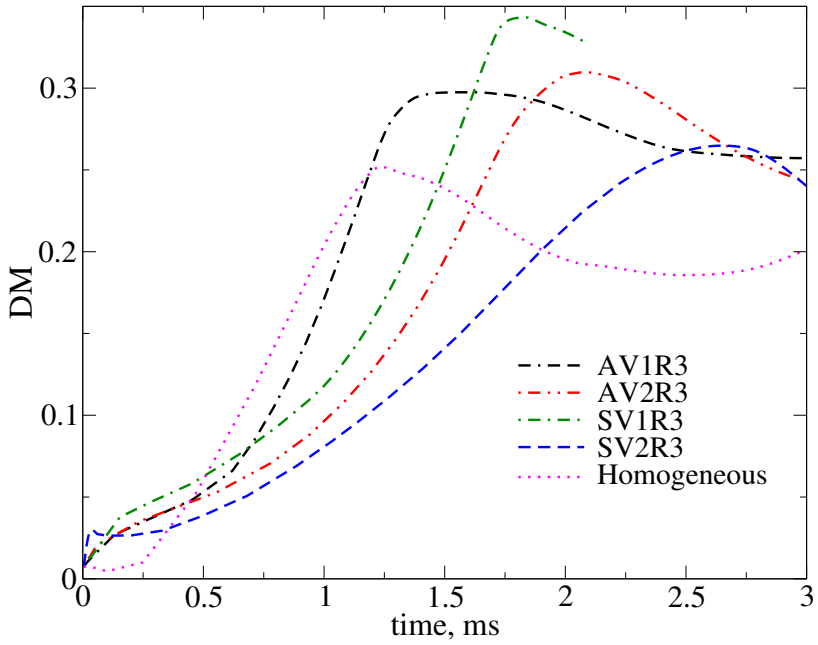

Figure 64: Variation of degree of mixed ness with time for different cases listed in Table 14. *Homogeneous* refers the homogeneous charge case discussed in Chapter 5.

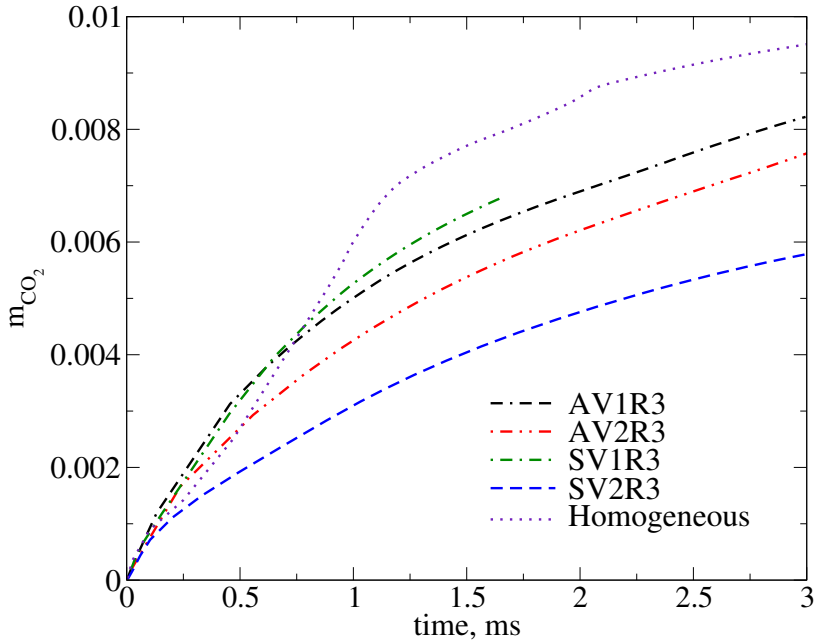

Figure 65: Variation in the mass of CO_2 (in Kg) in the post-detonation flow with time for different cases listed in Table 14. *Homogeneous* refers the homogeneous charge case discussed in Chapter 5.

dispersed phase volume fraction. Thus, the process of implosion and the reshock are delayed for charges with higher α_{p_0}, and the peak DM is delayed by 1.0 ms. This is true for both steel and aluminum particles and is shown in Fig. 64. Also, the peak value of DM is reduced by 0.02 to 0.05 when α_{p_0} is doubled.

Both α_{p_0} and r_{p_0} effect the temperature in the post-detonation flow. High temperatures are desired in the flow as it supports the explosion and provides the high temperature zone required in many applications. Here, the temperature in the flow is analyzed by averaging the temperature over all θ and Φ at each radial location and the zenith and azimuthally averaged temperature is given as

$$T_g^\dagger(r) = \frac{\int T_g dV^\dagger}{\int dV^\dagger}, \tag{140}$$

where $dV^\dagger$ is the volume of a section between radial location r and $r + dr$. For both steel and aluminum particles, with increase in α_{p_0} from 0.155 to 0.31, the peak value of $T_g^\dagger(r)$ is reduced by about 200 K (see Fig. 66). For a fixed α_{p_0}, increase in the number of particles in the flow occurs, when particle radius is reduced. Thus, the effective surface for heat transfer increases and results in lower temperature. In case of steel particles, the peak temperature is lowered by about 50 K with reduction in particle radius from 8.0 μm to 2.0 μm.

8.4 Summary

Three-dimensional numerical simulations of blast wave propagation ensuing from detonation of a heterogeneous nitromethane charge of 5.9 cm radius with aluminum particles are presented. Explosions generated hydrodynamic instabilities (RTI and RMI) which resulted in mixing of detonation products and ambient air. The instability induced mixing enhanced the afterburn. The simulations in dilute mixtures suggest that the combustion of Al is controlled by the particle dispersion and mixing of gases. In each case, mixing controls the amount of oxidizer available for different species to react and the net effect determines the extent of afterburn (Al or CO).

Influence of dense particle clouds on the post-detonation mixing, and aluminum particle combustion are investigated. The degree of mixing is enhanced by about 0.05 due to the

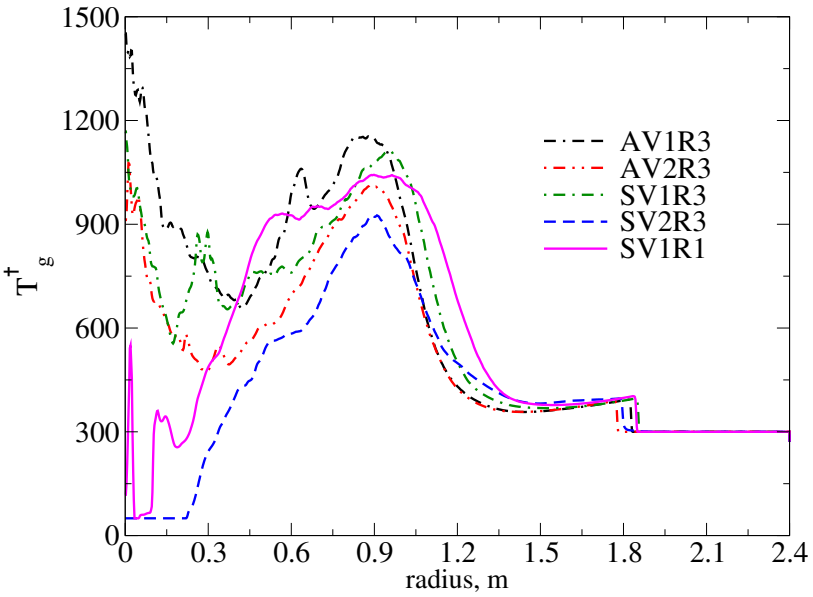

Figure 66: Variation in the average (in Φ and θ directions) gas-phase temperature ($T_g^\dagger$ in K) with radius at t = 2.0 ms for different cases listed in Table 14.

particle induced mixing and low density aluminum particles increased DM better than steel particles. The temperature in the post-detonation flow is also enhanced about 100 to 200 K due to particle combustion. Increase in the particle volume fraction and decrease in the particle size resulted in reduction in the post-detonation flow temperature. However, this change is pronounced for inert particles (a difference of nearly 50 K) than for reactive particles.

The results discussed in this chapter show the role of dense particle clouds in the post-detonation flow and demonstrate the effects of micron sized inert and reactive particles on the post-detonation flow temperatures. The investigations also show the efficacy of the numerical approach in simulating the post-detonation flow with millions of reactive particles, and provide confidence to employ the method in other complex cases.

CHAPTER IX

CONCLUSIONS AND FUTURE DIRECTIONS

9.1 Conclusions

The problem of particle dispersal by explosives is challenging due to the wide range of dispersed phase volume fractions and the particle sizes encountered. The particle volume fractions span from near packing limit to very dilute rarefied flow. The number of particles in some cases is in the order of a billion and solving for all the particles is computationally infeasible with current state-of-the-art computational resources. These problems are addressed using robust Eulerian-Eulerian and Eulerian-Lagrangian methods. The methods chosen are capable of adjusting the gas-phase properties based on the volume of the particles present in the flow. In addition to these individual methods, a combined Eulerian-Eulerian and Eulerian-Lagrangian method is developed to solve the problem of local clusters of small particles. The accuracy and the computational cost of the overall method are analyzed and the method is applied to the investigate post-detonation flows.

In order to account for the volume fraction of the dispersed phase, the gas-phase fluxes are adjusted based on the Discrete Equations Method. The gas-phase flux computation is adjusted by solving for the volume fraction as a piece-wise continuous variable and determining the direction and the amount of flux based on the type of interface encountered at each computational cell interface. The numerical method ($AUSM^+$-up scheme) employed to solve for Eulerian dispersed phase is chosen such that the method can span the regions with and without particles. This is needed as the wave speed in granular mixtures approaches zero as the volume fraction of dispersed phase tends to zero. The gas-phase solver is coupled with the dispersed phase via transfer of the mass, the momentum and the energy, and is influenced by the volume occupied by the particles. A massively parallel Lagrangian solver is implemented to solve for the particles using EL method. The parallel Lagrangian solver is designed to handle millions of particles, albeit when distributed over several cores. Eulerian

dispersed phase solver is coupled with the Lagrangian dispersed phase solver to solve for large number of mono-disperse particles distributed in a small region that is handled by few processors.

Extensive verification and validation are performed to assess the accuracy, the robustness and the computational cost of the numerical approach. Validation cases based on experimental results are presented and test the solver for dilute and dense shock-particle cloud interactions. The validation studies show negligible effect of granular energy terms on the shock-particle interaction. Granular energy is important near packing limits and since the flow transitions to a dilute regime, soon after the interaction with the shock wave, the significance of the granular energy is reduced. However, complete formulation is used for all the studies performed.

The studies carried out to address the particle dispersion and combustion in post-detonation flows are discussed in 4 chapters in this thesis, i.e., Chapters 5-8. These chapters correspond to the 4 objectives listed in Chapter 1. Since EL method alone cannot handle the number of particles encountered in the flow, heterogeneous explosions are studied using EE-EL solver. However, before applying EE-EL method, EE and EL methods for the post-detonation flow are compared. Both EE and EL methods are in agreement while predicting gas-phase properties. Since the gas-phase is effected by the volume fraction of the dispersed phase and the source terms from the dispersed phase, this is expected. The predictions of dispersed phase properties from EE and EL differed mainly in dilute regime of the flow. For initial dispersed volume fraction 0.62, reduction in particle radius from 231.5 μm to 50.0 μm enabled EE to provide better predictions. EE is found to provide good global predictions with particle sizes of the order of 50 μm and below, since the number of particles in these flows is sufficient to avoid rarefied particle dispersion. However, since the local fluctuations are not accurately captured by EE method, EL is still required. EE-EL method, which has the merits of both EE and EL methods, is applied to study the particle dispersion in the post-detonation flow. The combined method spans from EE limit to EL limit based on the choice of the transfer parameters. The transfer volume fraction, the transfer fraction and the number of particles per parcel determine the overall accuracy and the computational

cost. A transition volume fraction of 0.01 has been an optimal choice in most cases and is suggested for future cases with spray dispersion. EL method is the most expensive and with decrease in the transfer volume fraction the computational cost is reduced with EE being the least expensive (about 7 times less expensive than EL) method. Overall these studies satisfactorily address the issues discussed in Objectives 1 and 2.

Next, investigations are focused on dilute particle cloud dispersal, as described in the third objective, and are handled by EL solver. The dispersal of bacterial aerosol in post-shock and post-detonation flows is investigated and the spore neutralization is quantified. The aerosol is modeled based on the experimental data and each aerosol drop is considered to comprise of a water droplet enveloping bacterial spores. A spherical homogeneous NM charge of diameter 11.8 cm is simulated and the effect of the distance from the charge is analyzed. The spore neutralization is found to be effective when the aerosol is distributed within a distance of 4 charge diameters. Spore clouds located more than 4 charge diameters are left intact with almost no neutralization while spore clouds within a distance of 1.5 charge diameters are completely neutralized.

Finally, the simulation strategy is applied to investigate aluminum particle combustion in the post-detonation flow and satisfy the goals mentioned in the final objective. A hybrid kinetic-diffusive burning model for aluminum combustion is investigated. The particles are burnt in kinetic or diffusive limit based on the distance from the charge and the size of the particle. Small particles, i.e. $r_p < 4.0$ μm, placed away from the charge, attain high temperatures in a short time and thus burn in a diffusion-limited regime. Simulations of charges packed with dense aluminum and steel particles showed an increase in mixing (DM by 0.05). Also, packing the explosive charge with aluminum particles ($r_{p_0} = 8.0$ μm) has resulted in increase in the post-detonation temperature by 100 K to 200 K.

Investigation of dense aluminum particle combustion and dense metal particle cloud dispersion in the post-detonation flow has been made computationally feasible by the approach developed here. The comparision of EE and EL method have also provided the regimes of volume fraction and range of particle sizes where each method is better suited. With reduction in the computational cost and the ability to provide accurate gaseous and

dispersed phase properties, the approach developed is verified for its efficacy to solve for complex multi-phase problems over a wide range of dispersed phase volume fractions and particle sizes.

9.2 Recommendations for future research

The approach developed to accomplish the objectives of this thesis has a wide range of applications. Although, the focus of the current investigations have been post-detonation flows, the method can be extended to solve for a wide variety of multi-phase flows. Further, addition of specific physical models would enable investigation of new physical phenomena. Some of these numerical and physical models for further research are suggested here.

- **Material interface modeling**

  Although the method developed can handle dense and dilute two phase flows, the dispersed phase flow is described as a group of particles. Thus, to simulate flows with liquid sheets or continuous solid blocks, an interface tracking procedure is needed in addition to the equations solved. Also, the granular energy equation and the internal energy equation for the dispersed phase should be replaced by a single total energy which couples with the pressure in the dispersed phase. Thus, the current equations can be extended to a 7 equation model with material interface tracking to model problems where pure materials exist in a given computational cell. Further, a hybrid model of the current EE-EL approach and the 7 equation material interface method would enable investigation of problems like liquid jet atomization and combustion as it spans from pure material to a rarefied gas-particle flow.

- **Adaptive load balancing for Lagrangian tracking**

  The EL method developed here is efficient to track millions of particles if sufficient processors and memory are provided. However, this is not always feasible as the domain decomposition for the current parallel Lagrangian solver confirms with the domain decomposition for the gas-phase. Although, this makes the interpolation and the communication of the gas-phase properties to the particles and the source terms

to the gas-phase easier, the load on a given processor due to the particles and the gas-phase is, generally, not similar. Thus, for problems, especially with localized particle concentrations, it is preferred to have a processor distribution or a domain decomposition for Lagrangian tracking based on the locations of the particles. This can be performed by adding an additional set of processor mapping for Lagrangian solver and identifying the relation between the gas-phase domain decomposition and the dispersed phase domain decomposition.

- **Adaptive Mesh Refinement (AMR) with dispersed phase**

  Many problems of practical interest involve complex geometries. Also, the flow features, like a blast wave, may not always confirm to the grid used and the resolution requirements can vary across the domain based on the flow. AMR is an efficient way to handle all these issues and is routinely used to solve complex problems. EE-EL solver, if combined with an AMR solver, would provide a powerful tool to solve a wide range of problems, such as Deflagration-to-Detonation Transition (DDT) in gas-particle mixtures, which are otherwise unfeasible due to the computational cost.

- **Agglomeration, breakup and fragmentation**

  In the problems considered in this thesis, the agglomeration, the breakup and the fragmentation of solid particles or liquid droplets is not considered. However, solid particles can fragment or agglomerate upon impact with target structures and liquid droplets breakup/agglomerate based on the flow conditions. The solver can be extended by addition of these models to investigate particle impact on targets and liquid jet breakup and atomization.

- **Turbulence modeling and closures for dispersed phase**

  The focus of this thesis has been on the post-detonation flows and the ambient turbulence is not considered. However, to investigate turbulent flows, flow quantities at sub-grid scales must be considered, and for this, the governing equations for the dispersed phase need modification with appropriate filtered terms and closures. With

these closures, EE-EL combined approach can be applied to investigate dense and dilute turbulent gas-particle flows.

- **Condensed phase detonation modeling**

  The initial detonation profiles used in this thesis are obtained by solving governing equations in 1D. This assumption is valid for spherical charges but for charges with other shapes, 1D profiles do not describe the blast wave and the mixing zone propagation. Thus, the initial detonation solution in 3D is required. This can be solved by using a combination of Equations of State each suited for a specific density regime in the flow. By extending the solver to solve for detonations in condensed phase material, many scenarios of practical interest with different charge shapes can be modeled.

APPENDIX A

DRAG AND HEAT TRANSFER CORRELATIONS FOR DISPERSED PHASE

In order to compute the quasi-steady drag on each particle using either EE or EL methods, correlations are needed and are available in literature. Similarly, for convective heat transfer between the phases, correlations for Nusselt number (Nu) are required. Also, the added mass coefficient, required to compute the added mass effect, is needed. These correlations are expressed as a function of Reynolds number, Re, particle relative Mach number, M, and the dispersed phase volume fraction, α_s. Based on the flow conditions, different correlations have been developed by past researchers and the correlations used/implemented in the present studies are summarized below.

A.1 Correlations for the drag coefficient (C_D)

1. **Akhatov and Vainshtein [3]:** C_D as a function of Re and and α_s for Deflagration-to-Detonation transition in two-phase reactive mixtures.

$$
\begin{aligned}
C_D &= \frac{24}{Re} + \frac{4.4}{Re^{0.5}} + 0.42, \quad \alpha_s \leq 0.08 \\
&= \frac{4}{3(1-\alpha_s)}\left(1.75 + \frac{150\alpha_s}{Re(1-\alpha_s)}\right), \quad \alpha_s \geq 0.45 \\
&= \frac{1}{0.37}\left[\frac{4(\alpha_s - 0.08)}{3(1-\alpha_s)}\left(1.75 + \frac{150\alpha_s}{Re(1-\alpha_s)}\right)\right. \\
&\quad \left. +(0.45-\alpha_s)\left(\frac{24}{Re} + \frac{4.4}{Re^{0.5}} + 0.42\right)\right], \quad 0.08 < \alpha_s < 0.45
\end{aligned}
\tag{141}
$$

2. **Boiko et al. [23]:** C_D as a function of Re and and M to model the interaction of particle cloud (dilute to marginally dense) with a shock wave.

$$C_D = \left(\frac{24.0}{Re} + \frac{4.0}{Re^{0.5}} + 0.38\right)\left[1.0 + \exp\left(\frac{-0.43}{M^{4.67}}\right)\right] \tag{142}$$

3. **Clift et al. [28]:** For flow past a sphere as a function of Re.

$$C_D = \frac{24}{Re}\left[(1 + 0.15Re^{0.687}) + \frac{0.0175Re}{1 + 42500Re^{-1.16}}\right] \tag{143}$$

4. **Crowe et al. [30]:** Obtained from pressure drop in a particle bed for dense flows ($\alpha_s < 0.8$) as a function of Re and α_s.

$$C_D = \frac{24}{Re}\left(8.33\frac{\alpha_s}{1-\alpha_s} + 0.0972Re\right) \tag{144}$$

5. **Igra and Takayama [58]:** For shock-particle interaction in dilute flows as a function of Re.

$$\log_{10}(C_D) = 7.8231 - 5.8137\log_{10}(Re) + 1.4129[\log_{10}(Re)]^2 - 0.1146[\log_{10}(Re)]^3 \tag{145}$$

6. **Parmar et al. [73, 92]:** Drag law for shock-particle interaction in dense flows as a function of Re, α_s and M.

$$C_D = C_{D,std}\xi_1(M, Re)\xi_2(\alpha_s), \tag{146}$$

where

$$C_{D,std} = \frac{24}{Re}\left[(1 + 0.15Re^{0.687}) + \frac{0.0175Re}{1 + 42500Re^{-1.16}}\right], \tag{147}$$

$$\begin{aligned}
\xi_1(M, Re) &= 1 + (C_{D,M_{cr}}/C_{D,std} - 1)M/M_{cr} \quad \text{if } M \le M_{cr}, \\
&= C_{D,M_{sub}}/C_{D,std} \quad \text{if } M_{cr} < M \le 1.0, \\
&= C_{D,M_{sup}}/C_{D,std} \quad \text{if } 1.0 < M \le 1.75,
\end{aligned} \tag{148}$$

$$\xi_2(\alpha_s) = \frac{1 + 2\alpha_s}{(1 - \alpha_s)^2}. \tag{149}$$

$C_{D,M_{cr}}$, $C_{D,M_{sub}}$, and $C_{D,M_{sup}}$, in the above equations, are given as

$$C_{D,M_{cr}} = \frac{24.0}{Re}(1.0 + 0.15Re^{0.684}) + \frac{0.513}{1.0 + 483.0Re^{-0.669}}, \tag{150}$$

$$C_{D,M_{sub}} = C_{D,cr} + (C_{D,M=1} - C_{D,M_{cr}})\chi_{sub}, \tag{151}$$

$$C_{D,M_{sup}} = C_{D,M=1} + (C_{D,M=1.75} - C_{D,M=1})\chi_{sup}, \tag{152}$$

where $C_{D,M=1}$, $C_{D,M=1.75}$, χ_{sub} and χ_{sup} are expressed as

$$C_{D,M=1.75} = \frac{24.0}{Re}\left(1.0 + 0.107Re^{0.867}\right) + \frac{0.646}{1.0 + 861.0Re^{-0.634}}, \tag{153}$$

$$C_{D,M=1} = \frac{24.0}{Re}\left(1.0 + 0.118Re^{0.813}\right) + \frac{0.69}{1.0 + 3550.0Re^{-0.793}}, \tag{154}$$

$$\chi_{sub}(M, Re) = \sum_{i=1}^{3} f_{i,sub}(M) \prod_{\substack{j \neq i \\ j=1}} \frac{\log(Re) - C_{j,sub}}{C_{i,sub} - C_{j,sub}}, \tag{155}$$

$$\chi_{sup}(M, Re) = \sum_{i=1}^{3} f_{i,sup}(M) \prod_{\substack{j \neq i \\ j=1}} \frac{\log(Re) - C_{j,sup}}{C_{i,sup} - C_{j,sup}}. \tag{156}$$

Here, the expressions for $f_{i,sub}(i = 1, 3)$ and $f_{i,sup}(i = 1, 3)$ are

$$f_{1,sub}(M) = -1.884 + 8.422M - 13.7M^2 + 8.162M^3, \tag{157}$$

$$f_{2,sub}(M) = -2.228 + 10.35M - 16.96M^2 + 9.84M^3, \tag{158}$$

$$f_{3,sub}(M) = 4.362 - 16.91M + 19.84M^2 - 6.296M^3, \tag{159}$$

$$f_{1,sup}(M) = -2.963 + 4.392M - 1.169M^2 - 0.027M^3 - 0.233\exp[(1.0 - M)/0.011], \tag{160}$$

$$f_{2,sup}(M) = -6.617 + 12.11M - 6.501M^2 + 1.182M^3 - 0.174\exp[(1.0 - M)/0.01], \tag{161}$$

$$f_{3,sup}(M) = -5.866 + 11.57M - 6.665M^2 + 1.312M^3 - 0.350\exp[(1.0 - M)/0.012. \tag{162}$$

Note that the values of $C_{1,sub}$, $C_{2,sub}$, $C_{3,sub}$, $C_{1,sup}$, $C_{2,sup}$ and $C_{3,sup}$ are 6.48, 9.28, 12.21, 6.48, 9.28 and 12.21, respectively.

7. **Putnam [96]:** Correction to Stokes drag law [82] for high Re, i.e., $Re < 3 \times 10^5$.

$$\begin{aligned} C_D &= \frac{24.0}{Re}\left(1.0 + \frac{1}{6}Re^{2.0/3.0}\right) \text{ if } Re < 1000, \\ &= 0.0183Re \text{ if } 1000 \leq Re < 3 \times 10^5. \end{aligned} \tag{163}$$

8. **Stokes drag law [82]:** For flow over a sphere at low Re ($Re < 1.0$).

$$C_D = \frac{24}{Re}. \tag{164}$$

A.2 Correlations for Nusselt number (Nu)

1. **Akhatov and Vainshtein [3]:** Nu as a function of Re and and Pr for Deflagration-to-Detonation transition in two-phase reactive mixtures.

$$\begin{aligned} Nu &= 2.0 + 0.106RePr^{0.333}, \qquad Re \leq 200.0; \\ &= 2.274 + 0.6Re^{0.67}Pr^{0.333}, \quad Re > 200.0. \end{aligned} \tag{165}$$

2. **Yuen and Chen [125]:** Nusselt number correlation as a function of Re and Pr for evaporating liquid droplets.

$$Nu = 2.0 + 0.6Re^{0.5}Pr^{0.333}. \tag{166}$$

A.3 Correlations for added mass coefficient (C_A)

1. **Crowe et al. [30]:** Added mass coefficient for flow past a sphere without considering the effects of M and α_s.

$$C_A = \frac{1}{2} \tag{167}$$

2. **Ling et al. [73]:** C_A as a function of M and α_s for shock-particle interaction in dense flows.

$$C_A = \frac{1}{2}(1.0 + 1.8M^2 + 7.6M^4)(1 + 2\alpha_s) \tag{168}$$

APPENDIX B

PARALLEL LAGRANGIAN TRACKING AND SCALING

B.1 Procedure

Parallel implementation of Lagrangian tracking is essential to increase the speed of execution and feasible number of particles in the domain. In order to simplify the communication/interpolation of the source terms to the gas-phase and the gas-phase properties to the particles, the domain decomposition used for the gas-phase is also used in the Lagrangian implementation. Thus, the neighbors of a particular section of the domain (say a block) in the gas-phase communication are same as those for the particle communication. Once the computational cell corresponding to the particle location is identified, the required terms are interpolated based on the cell indices (i, j, k). Also, if particles cross the block boundary, the cell indices exceed the indices for the block, and the particles are communicated to the corresponding neighbor. The pseudo-code, Algorithm 1, shows the series of operations performed to track particles using the parallel implementation.

B.2 Code scaling

Homogeneous isotropic turbulence with 5.2 million particles is simulated to compute the speed-up of the code. The speed-up is defined as

$$\text{speed-up} = \frac{\text{Time for execution on } N_{ref} \text{ processors}}{\text{Time for execution on } N \text{ processors}}, \tag{169}$$

where N_{ref} is the reference number of processors. Here, the domain is a cube of length 1.6 mm and is discretized using 256^3 grid points and $N_{ref} = 62$. The turbulence is set based on the past results from literature [39]. The domain boundaries are set to be periodic. Particles are inertial and are uniformly distributed throughout the domain. The number of particles per processor remains nearly constant throughout the simulation. The speed-up of the code on Spirit (SGI Ice X) and Garnet (Cray XE6) is shown in Fig. 67. The scaling of the code

Algorithm 1 Parallel Lagrangian tracking

```
1: procedure LAGRANGIAN TRACKING
2:     for each block N in the domain do
3:         for each particle p in the block N do
4:             while total particle time step < Eulerian time step do
5:                 InterpolateGasPropertiesToParticle()
6:                 ComputeParticleAccelerationTerms()
7:                 ComputeHeatAndMassTransferTerms()
8:                 ComputeParticleTimeStep()
9:                 UpdateTotalParticleTimeStep()
10:                UpdateSourceTermsInGasPhase()
11:                IntegrateLagrangianGoverningEquations()
12:                if particle evaporated then
13:                    Remove particle
14:                end if
15:                LocateParticle()
16:                CheckParticleBoundaryCondition()
17:                if particle in the boundary cells then
18:                    Based on the boundary cells find the neighbor to communicate
19:                    Add the particle to the transfer list corresponding to the neighbor
20:                end if
21:            end while
22:        end for
23:        CommunicateParticleLists()
24:        CheckTotalNumberOfParticlesAfterCommunication()
25:        if Print criteria satisfied then
26:            WriteParticlePropertiesToFiles()
27:        end if
28:    end for
29: end procedure
```

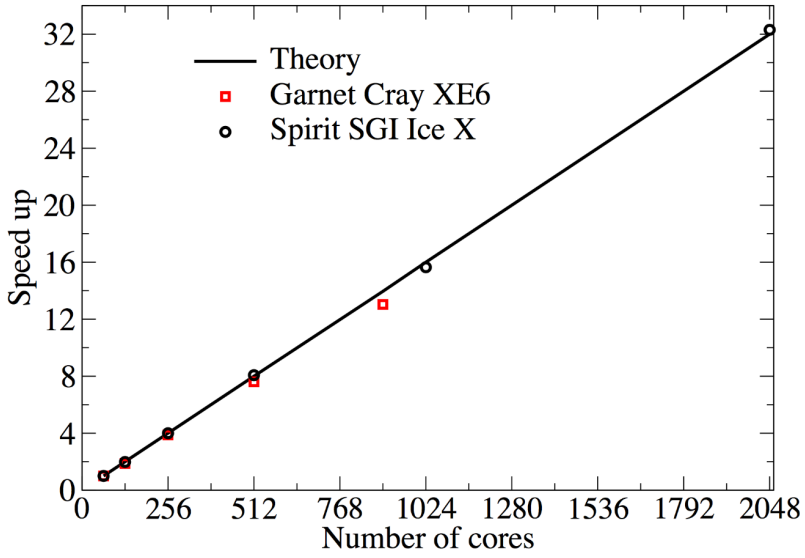

Figure 67: Speed up of the EL solver with parallel Lagrangian tracking on Spirit (SGI Ice X) and Garnet (Cray XE6). Number of particles tracked is 5.2 million.

nearly follows the theoretical values and compares well with the theoretical prediction over the wide range of processors considered, i.e., from 64 to 2048. Most of the cases presented here have been run using at most 1000 processors, where the code has excellent performance. The scaling of the code gives the confidence to run large scale computations with minimum effect on the computational cost.

APPENDIX C

COPYRIGHT PERMISSIONS

Copyright permissions for the following are obtained and used in this thesis:

1. Figures 1, 3 and 7 from Zhang et al., Shock Waves, 25, 2014 [132]
2. Full text, tables and figures from Gottiparthi et al., Shock Waves, 25, 2014 [53]
3. Full text, figures and tables from Gottiparthi and Menon, AIP conference proceedings, 2012 [51]

The permissions are attached in the following pages.

SPRINGER LICENSE
TERMS AND CONDITIONS

Jul 03, 2015

This is a License Agreement between Kalyana C Gottiparthi ("You") and Springer ("Springer") provided by Copyright Clearance Center ("CCC"). The license consists of your order details, the terms and conditions provided by Springer, and the payment terms and conditions.

All payments must be made in full to CCC. For payment instructions, please see information listed at the bottom of this form.

License Number	3661560774780
License date	Jul 03, 2015
Licensed content publisher	Springer
Licensed content publication	Shock Waves
Licensed content title	Large-scale spray detonation and related particle jetting instability phenomenon
Licensed content author	F. Zhang
Licensed content date	Jan 1, 2014
Volume number	25
Issue number	3
Type of Use	Thesis/Dissertation
Portion	Figures
Author of this Springer article	No
Order reference number	None
Original figure numbers	figures 1, 3 and 7
Title of your thesis / dissertation	A Study of Dispersion and Combustion of Particle Clouds in Post-Detonation flows
Expected completion date	Aug 2015
Estimated size(pages)	200
Total	0.00 USD
Terms and Conditions	

Introduction

The publisher for this copyrighted material is Springer Science + Business Media. By clicking "accept" in connection with completing this licensing transaction, you agree that the following terms and conditions apply to this transaction (along with the Billing and Payment terms and conditions established by Copyright Clearance Center, Inc. ("CCC"), at the time that you opened your Rightslink account and that are available at any time at http://myaccount.copyright.com).

Limited License
With reference to your request to reprint in your thesis material on which Springer Science and Business Media control the copyright, permission is granted, free of charge, for the use indicated in your enquiry.

Licenses are for one-time use only with a maximum distribution equal to the number that you identified in the licensing process.

This License includes use in an electronic form, provided its password protected or on the university's intranet or repository, including UMI (according to the definition at the Sherpa website: http://www.sherpa.ac.uk/romeo/). For any other electronic use, please contact Springer at (permissions.dordrecht@springer.com or permissions.heidelberg@springer.com).

The material can only be used for the purpose of defending your thesis limited to university-use only. If the thesis is going to be published, permission needs to be re-obtained (selecting "book/textbook" as the type of use).

Although Springer holds copyright to the material and is entitled to negotiate on rights, this license is only valid, subject to a courtesy information to the author (address is given with the article/chapter) and provided it concerns original material which does not carry references to other sources (if material in question appears with credit to another source, authorization from that source is required as well).

Permission free of charge on this occasion does not prejudice any rights we might have to charge for reproduction of our copyrighted material in the future.

Altering/Modifying Material: Not Permitted
You may not alter or modify the material in any manner. Abbreviations, additions, deletions and/or any other alterations shall be made only with prior written authorization of the author(s) and/or Springer Science + Business Media. (Please contact Springer at (permissions.dordrecht@springer.com or permissions.heidelberg@springer.com)

Reservation of Rights
Springer Science + Business Media reserves all rights not specifically granted in the combination of (i) the license details provided by you and accepted in the course of this licensing transaction, (ii) these terms and conditions and (iii) CCC's Billing and Payment terms and conditions.

Copyright Notice:Disclaimer
You must include the following copyright and permission notice in connection with any reproduction of the licensed material: "Springer and the original publisher /journal title, volume, year of publication, page, chapter/article title, name(s) of author(s), figure number(s), original copyright notice) is given to the publication in which the material was originally published, by adding; with kind permission from Springer Science and Business Media"

Warranties: None

Example 1: Springer Science + Business Media makes no representations or warranties with respect to the licensed material.

Example 2: Springer Science + Business Media makes no representations or warranties with respect to the licensed material and adopts on its own behalf the limitations and disclaimers established by CCC on its behalf in its Billing and Payment terms and conditions for this licensing transaction.

Indemnity
You hereby indemnify and agree to hold harmless Springer Science + Business Media and CCC, and their respective officers, directors, employees and agents, from and against any and all claims arising out of your use of the licensed material other than as specifically authorized pursuant to this license.

No Transfer of License
This license is personal to you and may not be sublicensed, assigned, or transferred by you to any other person without Springer Science + Business Media's written permission.

No Amendment Except in Writing
This license may not be amended except in a writing signed by both parties (or, in the case of Springer Science + Business Media, by CCC on Springer Science + Business Media's behalf).

Objection to Contrary Terms
Springer Science + Business Media hereby objects to any terms contained in any purchase order, acknowledgment, check endorsement or other writing prepared by you, which terms are inconsistent with these terms and conditions or CCC's Billing and Payment terms and conditions. These terms and conditions, together with CCC's Billing and Payment terms and conditions (which are incorporated herein), comprise the entire agreement between you and Springer Science + Business Media (and CCC) concerning this licensing transaction. In the event of any conflict between your obligations established by these terms and conditions and those established by CCC's Billing and Payment terms and conditions, these terms and conditions shall control.

Jurisdiction
All disputes that may arise in connection with this present License, or the breach thereof, shall be settled exclusively by arbitration, to be held in The Netherlands, in accordance with Dutch law, and to be conducted under the Rules of the 'Netherlands Arbitrage Instituut' (Netherlands Institute of Arbitration).***OR:***

All disputes that may arise in connection with this present License, or the breach thereof, shall be settled exclusively by arbitration, to be held in the Federal Republic of Germany, in accordance with German law.

Other terms and conditions:

v1.3

Questions? customercare@copyright.com or +1-855-239-3415 (toll free in the US) or +1-978-646-2777.

SPRINGER LICENSE
TERMS AND CONDITIONS

Jul 10, 2015

This is a License Agreement between Kalyana C Gottiparthi ("You") and Springer ("Springer") provided by Copyright Clearance Center ("CCC"). The license consists of your order details, the terms and conditions provided by Springer, and the payment terms and conditions.

All payments must be made in full to CCC. For payment instructions, please see information listed at the bottom of this form.

License Number	3665260087954
License date	Jul 10, 2015
Licensed content publisher	Springer
Licensed content publication	Shock Waves
Licensed content title	On the neutralization of bacterial spores in post-detonation flows
Licensed content author	K. C. Gottiparthi
Licensed content date	Jan 1, 2014
Volume number	24
Issue number	5
Type of Use	Thesis/Dissertation
Portion	Full text
Number of copies	100
Author of this Springer article	Yes and you are the sole author of the new work
Order reference number	None
Title of your thesis / dissertation	A Study of Dispersion and Combustion of Particle Clouds in Post-Detonation flows
Expected completion date	Aug 2015
Estimated size(pages)	200
Total	0.00 USD
Terms and Conditions	

Introduction

The publisher for this copyrighted material is Springer Science + Business Media. By clicking "accept" in connection with completing this licensing transaction, you agree that the following terms and conditions apply to this transaction (along with the Billing and Payment terms and conditions established by Copyright Clearance Center, Inc. ("CCC"), at the time that you opened your Rightslink account and that are available at any time at http://myaccount.copyright.com).

Limited License

With reference to your request to reprint in your thesis material on which Springer Science and Business Media control the copyright, permission is granted, free of charge, for the use indicated in your enquiry.

Licenses are for one-time use only with a maximum distribution equal to the number that you identified in the licensing process.

This License includes use in an electronic form, provided its password protected or on the university's intranet or repository, including UMI (according to the definition at the Sherpa website: http://www.sherpa.ac.uk/romeo/). For any other electronic use, please contact Springer at (permissions.dordrecht@springer.com or permissions.heidelberg@springer.com).

The material can only be used for the purpose of defending your thesis limited to university-use only. If the thesis is going to be published, permission needs to be re-obtained (selecting "book/textbook" as the type of use).

Although Springer holds copyright to the material and is entitled to negotiate on rights, this license is only valid, subject to a courtesy information to the author (address is given with the article/chapter) and provided it concerns original material which does not carry references to other sources (if material in question appears with credit to another source, authorization from that source is required as well).

Permission free of charge on this occasion does not prejudice any rights we might have to charge for reproduction of our copyrighted material in the future.

Altering/Modifying Material: Not Permitted
You may not alter or modify the material in any manner. Abbreviations, additions, deletions and/or any other alterations shall be made only with prior written authorization of the author(s) and/or Springer Science + Business Media. (Please contact Springer at (permissions.dordrecht@springer.com or permissions.heidelberg@springer.com)

Reservation of Rights
Springer Science + Business Media reserves all rights not specifically granted in the combination of (i) the license details provided by you and accepted in the course of this licensing transaction, (ii) these terms and conditions and (iii) CCC's Billing and Payment terms and conditions.

Copyright Notice:Disclaimer
You must include the following copyright and permission notice in connection with any reproduction of the licensed material: "Springer and the original publisher /journal title, volume, year of publication, page, chapter/article title, name(s) of author(s), figure number(s), original copyright notice) is given to the publication in which the material was originally published, by adding; with kind permission from Springer Science and Business Media"

Warranties: None

Example 1: Springer Science + Business Media makes no representations or warranties with respect to the licensed material.

Example 2: Springer Science + Business Media makes no representations or warranties with

respect to the licensed material and adopts on its own behalf the limitations and disclaimers established by CCC on its behalf in its Billing and Payment terms and conditions for this licensing transaction.

Indemnity
You hereby indemnify and agree to hold harmless Springer Science + Business Media and CCC, and their respective officers, directors, employees and agents, from and against any and all claims arising out of your use of the licensed material other than as specifically authorized pursuant to this license.

No Transfer of License
This license is personal to you and may not be sublicensed, assigned, or transferred by you to any other person without Springer Science + Business Media's written permission.

No Amendment Except in Writing
This license may not be amended except in a writing signed by both parties (or, in the case of Springer Science + Business Media, by CCC on Springer Science + Business Media's behalf).

Objection to Contrary Terms
Springer Science + Business Media hereby objects to any terms contained in any purchase order, acknowledgment, check endorsement or other writing prepared by you, which terms are inconsistent with these terms and conditions or CCC's Billing and Payment terms and conditions. These terms and conditions, together with CCC's Billing and Payment terms and conditions (which are incorporated herein), comprise the entire agreement between you and Springer Science + Business Media (and CCC) concerning this licensing transaction. In the event of any conflict between your obligations established by these terms and conditions and those established by CCC's Billing and Payment terms and conditions, these terms and conditions shall control.

Jurisdiction
All disputes that may arise in connection with this present License, or the breach thereof, shall be settled exclusively by arbitration, to be held in The Netherlands, in accordance with Dutch law, and to be conducted under the Rules of the 'Netherlands Arbitrage Instituut' (Netherlands Institute of Arbitration).***OR:***

All disputes that may arise in connection with this present License, or the breach thereof, shall be settled exclusively by arbitration, to be held in the Federal Republic of Germany, in accordance with German law.

Other terms and conditions:

v1.3

Questions? customercare@copyright.com or +1-855-239-3415 (toll free in the US) or +1-978-646-2777.

SPRINGER LICENSE
TERMS AND CONDITIONS

Jul 23, 2015

This is a License Agreement between Kalyana C Gottiparthi ("You") and Springer ("Springer") provided by Copyright Clearance Center ("CCC"). The license consists of your order details, the terms and conditions provided by Springer, and the payment terms and conditions.

All payments must be made in full to CCC. For payment instructions, please see information listed at the bottom of this form.

License Number	3674610298421
License date	Jul 23, 2015
Licensed content publisher	Springer
Licensed content publication	Shock Waves
Licensed content title	On the neutralization of bacterial spores in post-detonation flows
Licensed content author	K. C. Gottiparthi
Licensed content date	Jan 1, 2014
Volume number	24
Issue number	5
Type of Use	Thesis/Dissertation
Portion	Figures
Author of this Springer article	Yes and you are the sole author of the new work
Order reference number	None
Original figure numbers	figures 1, 2, 3, 4, 5, 6, 7, 8, 9, 10, 11, 12, 13 and Tables 1, 2, 3, 4, 5
Title of your thesis / dissertation	A Study of Dispersion and Combustion of Particle Clouds in Post-Detonation flows
Expected completion date	Aug 2015
Estimated size(pages)	200
Total	0.00 USD
Terms and Conditions	

Introduction

The publisher for this copyrighted material is Springer Science + Business Media. By clicking "accept" in connection with completing this licensing transaction, you agree that the following terms and conditions apply to this transaction (along with the Billing and Payment terms and conditions established by Copyright Clearance Center, Inc. ("CCC"), at the time that you opened your Rightslink account and that are available at any time at http://myaccount.copyright.com).

Limited License
With reference to your request to reprint in your thesis material on which Springer Science and Business Media control the copyright, permission is granted, free of charge, for the use indicated in your enquiry.

Licenses are for one-time use only with a maximum distribution equal to the number that you identified in the licensing process.

This License includes use in an electronic form, provided its password protected or on the university's intranet or repository, including UMI (according to the definition at the Sherpa website: http://www.sherpa.ac.uk/romeo/). For any other electronic use, please contact Springer at (permissions.dordrecht@springer.com or permissions.heidelberg@springer.com).

The material can only be used for the purpose of defending your thesis limited to university-use only. If the thesis is going to be published, permission needs to be re-obtained (selecting "book/textbook" as the type of use).

Although Springer holds copyright to the material and is entitled to negotiate on rights, this license is only valid, subject to a courtesy information to the author (address is given with the article/chapter) and provided it concerns original material which does not carry references to other sources (if material in question appears with credit to another source, authorization from that source is required as well).

Permission free of charge on this occasion does not prejudice any rights we might have to charge for reproduction of our copyrighted material in the future.

Altering/Modifying Material: Not Permitted
You may not alter or modify the material in any manner. Abbreviations, additions, deletions and/or any other alterations shall be made only with prior written authorization of the author(s) and/or Springer Science + Business Media. (Please contact Springer at (permissions.dordrecht@springer.com or permissions.heidelberg@springer.com)

Reservation of Rights
Springer Science + Business Media reserves all rights not specifically granted in the combination of (i) the license details provided by you and accepted in the course of this licensing transaction, (ii) these terms and conditions and (iii) CCC's Billing and Payment terms and conditions.

Copyright Notice:Disclaimer
You must include the following copyright and permission notice in connection with any reproduction of the licensed material: "Springer and the original publisher /journal title, volume, year of publication, page, chapter/article title, name(s) of author(s), figure number(s), original copyright notice) is given to the publication in which the material was originally published, by adding; with kind permission from Springer Science and Business Media"

Warranties: None

Example 1: Springer Science + Business Media makes no representations or warranties with respect to the licensed material.

Example 2: Springer Science + Business Media makes no representations or warranties with respect to the licensed material and adopts on its own behalf the limitations and disclaimers established by CCC on its behalf in its Billing and Payment terms and conditions for this licensing transaction.

Indemnity
You hereby indemnify and agree to hold harmless Springer Science + Business Media and CCC, and their respective officers, directors, employees and agents, from and against any and all claims arising out of your use of the licensed material other than as specifically authorized pursuant to this license.

No Transfer of License
This license is personal to you and may not be sublicensed, assigned, or transferred by you to any other person without Springer Science + Business Media's written permission.

No Amendment Except in Writing
This license may not be amended except in a writing signed by both parties (or, in the case of Springer Science + Business Media, by CCC on Springer Science + Business Media's behalf).

Objection to Contrary Terms
Springer Science + Business Media hereby objects to any terms contained in any purchase order, acknowledgment, check endorsement or other writing prepared by you, which terms are inconsistent with these terms and conditions or CCC's Billing and Payment terms and conditions. These terms and conditions, together with CCC's Billing and Payment terms and conditions (which are incorporated herein), comprise the entire agreement between you and Springer Science + Business Media (and CCC) concerning this licensing transaction. In the event of any conflict between your obligations established by these terms and conditions and those established by CCC's Billing and Payment terms and conditions, these terms and conditions shall control.

Jurisdiction
All disputes that may arise in connection with this present License, or the breach thereof, shall be settled exclusively by arbitration, to be held in The Netherlands, in accordance with Dutch law, and to be conducted under the Rules of the 'Netherlands Arbitrage Instituut' (Netherlands Institute of Arbitration).***OR:***

All disputes that may arise in connection with this present License, or the breach thereof, shall be settled exclusively by arbitration, to be held in the Federal Republic of Germany, in accordance with German law.

Other terms and conditions:

v1.3

Questions? customercare@copyright.com or +1-855-239-3415 (toll free in the US) or +1-978-646-2777.

AIP PUBLISHING LLC LICENSE TERMS AND CONDITIONS

Jul 23, 2015

All payments must be made in full to CCC. For payment instructions, please see information listed at the bottom of this form.

License Number	3674610731845
Order Date	Jul 23, 2015
Publisher	AIP Publishing LLC
Publication	AIP Conference Proceedings
Article Title	Simulations of heterogeneous detonations and post-detonation turbulent mixing and afterburning
Author	Kalyana Chakravarthi Gottiparthi,Suresh Menon
Online Publication Date	Mar 29, 2012
Volume number	1426
Issue number	1
Type of Use	Thesis/Dissertation
Requestor type	Author (original article)
Format	Print and electronic
Portion	Excerpt (> 800 words)
Will you be translating?	No
Title of your thesis / dissertation	A Study of Dispersion and Combustion of Particle Clouds in Post-Detonation flows
Expected completion date	Aug 2015
Estimated size (number of pages)	200
Total	0.00 USD

Terms and Conditions

AIP Publishing LLC -- Terms and Conditions: Permissions Uses

AIP Publishing LLC ("AIPP"") hereby grants to you the non-exclusive right and license to use and/or distribute the Material according to the use specified in your order, on a one-time basis, for the specified term, with a maximum distribution equal to the number that you have ordered. Any links or other content accompanying the Material are not the subject of this license.

1. You agree to include the following copyright and permission notice with the reproduction of the Material:"Reprinted with permission from [FULL CITATION]. Copyright [PUBLICATION YEAR], AIP Publishing LLC." For an article, the copyright and permission notice must be printed on the first page of the article or book chapter. For photographs, covers, or tables, the copyright and permission notice may appear with the Material, in a footnote, or in the reference list.
2. If you have licensed reuse of a figure, photograph, cover, or table, it is your responsibility to ensure that the material is original to AIPP and does not contain the copyright of another entity, and that the copyright notice of the figure, photograph, cover, or table does not indicate that it was reprinted by AIPP, with permission, from another source. Under no circumstances does AIPP, purport or intend to grant permission to reuse material to which it does not hold copyright.
3. You may not alter or modify the Material in any manner. You may translate the Material into another language only if you have licensed translation rights. You may not use the

Material for promotional purposes. AIPP reserves all rights not specifically granted herein.

4. The foregoing license shall not take effect unless and until AIPP or its agent, Copyright Clearance Center, receives the Payment in accordance with Copyright Clearance Center Billing and Payment Terms and Conditions, which are incorporated herein by reference.
5. AIPP or the Copyright Clearance Center may, within two business days of granting this license, revoke the license for any reason whatsoever, with a full refund payable to you. Should you violate the terms of this license at any time, AIPP, AIP Publishing LLC, or Copyright Clearance Center may revoke the license with no refund to you. Notice of such revocation will be made using the contact information provided by you. Failure to receive such notice will not nullify the revocation.
6. AIPP makes no representations or warranties with respect to the Material. You agree to indemnify and hold harmless AIPP, AIP Publishing LLC, and their officers, directors, employees or agents from and against any and all claims arising out of your use of the Material other than as specifically authorized herein.
7. The permission granted herein is personal to you and is not transferable or assignable without the prior written permission of AIPP. This license may not be amended except in a writing signed by the party to be charged.
8. If purchase orders, acknowledgments or check endorsements are issued on any forms containing terms and conditions which are inconsistent with these provisions, such inconsistent terms and conditions shall be of no force and effect. This document, including the CCC Billing and Payment Terms and Conditions, shall be the entire agreement between the parties relating to the subject matter hereof.

This Agreement shall be governed by and construed in accordance with the laws of the State of New York. Both parties hereby submit to the jurisdiction of the courts of New York County for purposes of resolving any disputes that may arise hereunder.

Questions? customercare@copyright.com or +1-855-239-3415 (toll free in the US) or +1-978-646-2777.

AIP PUBLISHING LLC LICENSE TERMS AND CONDITIONS

Jul 23, 2015

All payments must be made in full to CCC. For payment instructions, please see information listed at the bottom of this form.

License Number	3674611151711
Order Date	Jul 23, 2015
Publisher	AIP Publishing LLC
Publication	AIP Conference Proceedings
Article Title	Simulations of heterogeneous detonations and post-detonation turbulent mixing and afterburning
Author	Kalyana Chakravarthi Gottiparthi,Suresh Menon
Online Publication Date	Mar 29, 2012
Volume number	1426
Issue number	1
Type of Use	Thesis/Dissertation
Requestor type	Author (original article)
Format	Print and electronic
Portion	Figure/Table
Number of figures/tables	6
Title of your thesis / dissertation	A Study of Dispersion and Combustion of Particle Clouds in Post-Detonation flows
Expected completion date	Aug 2015
Estimated size (number of pages)	200
Total	0.00 USD

Terms and Conditions

AIP Publishing LLC -- Terms and Conditions: Permissions Uses

AIP Publishing LLC ("AIPP"") hereby grants to you the non-exclusive right and license to use and/or distribute the Material according to the use specified in your order, on a one-time basis, for the specified term, with a maximum distribution equal to the number that you have ordered. Any links or other content accompanying the Material are not the subject of this license.

1. You agree to include the following copyright and permission notice with the reproduction of the Material:"Reprinted with permission from [FULL CITATION]. Copyright [PUBLICATION YEAR], AIP Publishing LLC." For an article, the copyright and permission notice must be printed on the first page of the article or book chapter. For photographs, covers, or tables, the copyright and permission notice may appear with the Material, in a footnote, or in the reference list.
2. If you have licensed reuse of a figure, photograph, cover, or table, it is your responsibility to ensure that the material is original to AIPP and does not contain the copyright of another entity, and that the copyright notice of the figure, photograph, cover, or table does not indicate that it was reprinted by AIPP, with permission, from another source. Under no circumstances does AIPP, purport or intend to grant permission to reuse material to which it does not hold copyright.
3. You may not alter or modify the Material in any manner. You may translate the Material into another language only if you have licensed translation rights. You may not use the

Material for promotional purposes. AIPP reserves all rights not specifically granted herein.

4. The foregoing license shall not take effect unless and until AIPP or its agent, Copyright Clearance Center, receives the Payment in accordance with Copyright Clearance Center Billing and Payment Terms and Conditions, which are incorporated herein by reference.
5. AIPP or the Copyright Clearance Center may, within two business days of granting this license, revoke the license for any reason whatsoever, with a full refund payable to you. Should you violate the terms of this license at any time, AIPP, AIP Publishing LLC, or Copyright Clearance Center may revoke the license with no refund to you. Notice of such revocation will be made using the contact information provided by you. Failure to receive such notice will not nullify the revocation.
6. AIPP makes no representations or warranties with respect to the Material. You agree to indemnify and hold harmless AIPP, AIP Publishing LLC, and their officers, directors, employees or agents from and against any and all claims arising out of your use of the Material other than as specifically authorized herein.
7. The permission granted herein is personal to you and is not transferable or assignable without the prior written permission of AIPP. This license may not be amended except in a writing signed by the party to be charged.
8. If purchase orders, acknowledgments or check endorsements are issued on any forms containing terms and conditions which are inconsistent with these provisions, such inconsistent terms and conditions shall be of no force and effect. This document, including the CCC Billing and Payment Terms and Conditions, shall be the entire agreement between the parties relating to the subject matter hereof.

This Agreement shall be governed by and construed in accordance with the laws of the State of New York. Both parties hereby submit to the jurisdiction of the courts of New York County for purposes of resolving any disputes that may arise hereunder.

Questions? customercare@copyright.com or +1-855-239-3415 (toll free in the US) or +1-978-646-2777.

REFERENCES

[1] Abgrall, R. and Saurel, R., "Discrete equations for physical and numerical compressible multiphase mixtures," *Journal of Computational Physics*, vol. 186, no. 2, pp. 361–396, 2003.

[2] Abramzon, B. and Sirignano, W. A., "Droplet vaporization model for spray combustion calculations," *International Journal of Heat and Mass Transfer*, vol. 32, pp. 1605–1618, 1989.

[3] Akhatov, I. S. and Vainshtein, P. B., "Transition of porous explosive combustion into detonation," *Combustion Explosions and Shock Waves*, vol. 20, no. 1, pp. 63–69, 1984.

[4] Akiki, M. and Menon, S., "A model for hot spot formation in shocked energetic materials," *Combustion and Flame*, 2015.

[5] Anderson, J. D., *Computational Fluid Dynamics: The Basics with Applications*. McGraw Hill, 1994.

[6] Apte, S. V. and Moin, P., *Handbook of Atomization and Sprays*, ch. Spray Modeling and predictive simulations in realistic gas-turbine engines, pp. 811–835. Springer, 2011.

[7] Atkinson, K., *An Introduction to Numerical Analysis*. New York: John Wiley & Sons, 1989.

[8] Baer, M. R. and Nunziato, J. W., "A two-phase mixture theory for the deflagration-to-detonation transition (DDT) in reactive granular materials," *International Journal of Multiphase Flow*, vol. 12, no. 6, pp. 861–889, 1986.

[9] Bailey, A. B. and Hiatt, J., "Sphere drag coefficient for a broad range of mach and reynolds numbers," *AIAA Journal*, vol. 10, pp. 1436–1440, 1972.

[10] Balachandar, S. and Eaton, J. K., "Turbulent dispersed multiphase flow," *Annual Review of Fluid Mechanics*, vol. 42, pp. 111–133, 2010.

[11] Balakrishnan, K., *On the high fidelity simulation of chemical explosions and their interaction with solid particle clouds*. PhD thesis, Georgia Institute of Technology, Atlanta, Georgia, U.S.A, 2010.

[12] Balakrishnan, K., "Diffusion- and kinetics-limited combustion of an explosively dispersed aluminum particle," *Journal of Propulsion and Power*, vol. 30, no. 2, pp. 522–526, 2014.

[13] Balakrishnan, K., "Explosively-driven Rayleigh-Taylor instability in gas-particle mixtures," *Physics of Fluids*, vol. 26, no. 043303, 2014.

[14] Balakrishnan, K., Kuhl, A. L., Bell, J. B., and Beckner, V. E., "An empirical model for ignition of explosively dispersed aluminum particle clouds," *Shock Waves*, vol. 22, no. 6, pp. 591–603, 2012.

[15] Balakrishnan, K. and Menon, S., "On the role of ambient reactive particles in the mixing and afterburn behind explosive blast waves," *Combustion Science and Technology*, vol. 182, no. 2, pp. 186–214, 2010.

[16] Balakrishnan, K. and Menon, S., "On turbulent chemical explosions into dilute aluminum particle clouds," *Combustion Theory and Modeling*, vol. 14, no. 4, pp. 583–617, 2010.

[17] Balakrishnan, K. and Menon, S., "Characterization of the mixing layer resulting from the detonation of heterogeneous explosive charges," *Flow Turbulence and Combustion*, vol. 87, no. 4, pp. 639–671, 2011.

[18] Balakrishnan, K., Nance, D. V., and Menon, S., "Numerical study of blast characteristics from detonation of homogeneous explosives," *Shock Waves*, vol. 20, pp. 147–162, 2010.

[19] Balakrishnan, K., Nance, D. V., and Menon, S., "Simulation of impulse effects from explosive charges containing metal particles," *Shock Waves*, vol. 20, pp. 217–239, 2010.

[20] Balakrishnan, K., Ukai, S., and Menon, S., "Clustering and combustion of dilute aluminum particle clouds in a post-detonation flow field," *Proceedings of the Combustion Institute*, vol. 33, pp. 2255–2263, 2011.

[21] Benkiewicz, K. and Hayashi, A. K., "Parametric studies of aluminum combustion model for simulations of detonation waves," *AIAA Journal*, vol. 44, no. 3, pp. 608–619, 2006.

[22] Bhattacharya, A., *Gunpowder, Explosives and the State: A Technological History*, ch. Gun powder and its applications in ancient India. Burlington, VT, USA: Ashgate publishing company, 2006.

[23] Boiko, V. M., Kiselev, V. P., Keselev, S. P., Papyrin, A. P., Poplavsky, S. V., and Fomin, V. M., "Shock wave interaction with a cloud of particles," *Shock Waves*, vol. 7, pp. 275–285, 1997.

[24] Briand, A., Veyssiere, B., and Khasianov, B. A., "Modelling of detonation cellular structure in aluminum suspensions," *Shock Waves*, vol. 20, pp. 521–529, 2010.

[25] Carrera, M., Zandomeni, R. O., Fitzgibbon, J., and Sagripanti, J. L., "Difference between the spore sizes of Bacillus anthracis and other Bacillus species," *Journal of Applied Microbiology*, vol. 102, pp. 303–312, 2007.

[26] Chang, C.-H. and Liou, M.-S., "A robust and accurate approach to computing compressible multiphase flow: Stratified flow model and AUSM$^+$ -up scheme," *Journal of Computational Physics*, vol. 225, pp. 840–873, 2007.

[27] Chinnayya, A., Daniel, E., and Saurel, R., "Modelling detonation waves in heterogeneous energetic materials," *Journal of Computational Physics*, vol. 196, pp. 490–538, 2004.

[28] Clift, R.and Grace, J. R. and Weber, M. E., *Bubbles Drops and Particles*. New York: Academic, 1978.

[29] Collins, J., Ferguson, R., Chien, K., Kuhl, A., Krispin, J., and Glaz, H., "Simulation of shock-induced dusty gas flows using various models," *25th AIAA Fluid Dynamics Conference, Colarado Springs, CO*, 1994.

[30] Crowe, C. T., Sommerfeld, M., and Tsuji, Y., *Multiphase Flows with Droplets and Particles*. Boca Raton: CRC Press, 1998.

[31] Devals, C., Jourdan, G., Estivalezes, J. L., Meshkov, E. E., and Houas, L., "Shock tube spherical particle accelerating study for drag coefficient determination," *Shock Waves*, vol. 12, pp. 325–331, 2003.

[32] Dewey, J. M., "The air velocity in blast waves from TNT explosions," *Proceedings of the Royal Society of London A*, vol. 279, pp. 366–385, 1964.

[33] Ding, J. and Gidaspow, D., "A bubbling fluidization model using kinetic theory of granular flow," *AIChE Journal*, vol. 36, no. 4, pp. 523–538, 1990.

[34] Donahue, L., Zhang, F., and Ripley, R. C., "Numerical models for afterburning of TNT detonation products in air," *Shock Waves*, vol. 23, pp. 559–573, 2013.

[35] El-Asrag, H., Menon, S., Lu, T., and Law, C. K., "Simulation of soot formation in turbulent flame," *Combustion and Flame*, vol. 150, pp. 108–126, 2007.

[36] Fedina, E. and Fureby, C., "Investigating ground effects on mixing and afterburning during a TNT explosion," *Shock Waves*, vol. 23, pp. 251–261, 2013.

[37] Fedina, E., Gottiparthi, K. . C., Fureby, C., and Menon, S., *Coarse Grained Simulations and Turbulent Mixing*, ch. Combustion in afterburn behind explosive blasts. Cambridge, United Kingdom: Cambridge University Press, 2015.

[38] Fedorov, A. V. and Kratova, Y. V., "Calculation of detonation wave propagation in a gas suspension of aluminum and inert particles," *Combustion, Explosion and Shock Waves*, vol. 49, no. 3, pp. 335–347, 2013.

[39] Ferrante, A. and Elghobashi, S., "On the physical mechanisms of two-way coupling in particle-laden isotropic turbulence," *Physics of Fluids*, vol. 15, pp. 315–329, 2003.

[40] Frost, D. L., Gregoire, Y., Petel, O., Goroshin, S., and Zhang, F., "Particle jet formation during explosive dispersal of solid particles," *Physics of Fluids*, vol. 24, p. 091109, 2012.

[41] Frost, D. L., Zarei, Z., and Zhang, F., "Instability of combustion products interface from detonation of heterogeneous explosives," in *20th International Colloquium on the Dynamics of Explosions and Reactive Systems*, (Montreal, Canada), 2005.

[42] Gamezo, V. N., Khokhlov, A. M., Oran, E. S., Chtchelkanova, A. Y., and Rosenberg, E. O., "Thermonuclear supernovae: Simulations of the deflagration stage and their implications," *Science*, vol. 299, no. 5603, pp. 77–81, 2003.

[43] Gates, S. D., McCartt, A. D., Jeffries, J. B., Hanson, R. K., Hokama, L. A., and Mortelmans, K. E., "Extension of Bacillus endospore gas dynamic heating studies to multiple species and test conditions," *Journal of Applied Microbiology*, vol. 111, pp. 925–931, 2011.

[44] Gates, S. D., McCartt, A. D., Lappas, P., Jeffries, J. B., Hanson, R. K., Hokama, L. A., and Mortelmans, K. E., "Bacillus endospore resistance to gas dynamic heating," *Journal of Applied Microbiology*, vol. 109, pp. 1591–1598, 2010.

[45] Génin, F. and Menon, S., "Studies of shock / turbulent shear layer interaction using large-eddy simulation," *Computers & Fluids*, vol. 39, pp. 800–819, 2010.

[46] Gidsapow, D., *Multiphase Flow and Fluidization*. Academic Press, 1994.

[47] Gilbert, J. S. and Sparks, R. S. J., *The Physics of Explosive Volcanic Eruptions*. Bath, UK: The Geological Society, 2002.

[48] Gottiparthi, K. C., Génin, F., Srinivasan, S., and Menon, S., "Simulation of cellular detonation structures in ethylene-oxygen mixtures," *AIAA Paper 2009-0437*, 2009.

[49] Gottiparthi, K. C. and Menon, S., "Study of deflagration-to-detonation transition in gas-particle mixtures," *AIAA Paper 2010-0801*, 2011.

[50] Gottiparthi, K. C. and Menon, S., "Multi-scale simulation of deflagration-to-detonation transition in turbulent dense two-phase reactive mixtures," *Proceedings of 22nd User Group Conference, DoD High Performance Computing Modernization Program*, 2012.

[51] Gottiparthi, K. C. and Menon, S., "Simulations of heterogeneous detonations and post detonation turbulent mixing and afterburning," *AIP Conference Proceedings*, vol. 1426, pp. 1639–1642, 2012.

[52] Gottiparthi, K. C. and Menon, S., "A study of interaction of clouds of inert particles with detonation in gases," *Combustion Science and Technology*, vol. 184, no. 3, pp. 406–433, 2012.

[53] Gottiparthi, K. C., Schulz, J. C., and Menon, S., "On the neutralization of bacterial spores in post-detonation flows," *Shock Waves*, vol. 24, pp. 455–466, 2014.

[54] Gowardhan, A. A. and Grinstein, F. F., "Numerical simulation of Richtmyer-Meshkov instabilities in shocked gas curtains," *Journal of Turbulence*, vol. 12, no. 43, pp. 1–24, 2011.

[55] Herrmann, M., "A parallel Eulerian interface tracking/Lagrangian point particle multi-scale coupling procedure," *Journal of Computational Physics*, vol. 229, no. 3, pp. 745–759, 2010.

[56] Hill, D. J., Pantano, C., and Pullin, D. I., "Large-eddy simulation and multiscale modeling of Richtmyer-Meshkov instability with reshock," *Journal of Fluid Mechanics*, vol. 557, pp. 29–61, 2006.

[57] Houim, R. W. and Oran, E. S., "A technique for computing dense granular compressible flows with shock waves," *arXiv:1312.1290[physics.comp-ph]*, 2014.

[58] Igra, O. and Takayama, K., "Shock tube study of the drag coefficient of a sphere in a non-stationary flow," *Proceedings Mathematical and Physical Sciences*, vol. 442, pp. 231–247, 1993.

[59] Kauffmann, C. W., Wolanski, P., Arisoy, A., Adams, P. R., Maker, B. N., and Nicholls, J. A., "Dust, hybrid and dusty detonations," *AIAA Progress in Aeronautics and Astronautics*, vol. 94, pp. 221–239, 1984.

[60] Kellenberger, M., Johansen, C., Ciccarelli, G., and Zhang, F., "Dense particle cloud dispersion by a shock wave," *Shock waves*, vol. 23, pp. 415–430, 2013.

[61] Kuhl, A. L., *Dynamics of Exothermicity*, ch. Spherical Mixing Layers in Explosions. Amsterdam, The Netherlands: Gordon and Breach Science Publishers SA, 1996.

[62] Kuhl, A. L. and Balakrishnan, K., "Gasdynamic model of dilute two-phase combustion fields," *Combustion, Explosion, and Shock Waves*, vol. 48, pp. 544–560, 2012.

[63] Kuhl, A. L., Bell, J. B., Beckner, V. E., Balakrishnan, K., and Aspden, A. J., "Spherical combustion clouds in explosions," *Shock Waves*, vol. 23, pp. 233–249, 2013.

[64] Kuhl, A. L., Bell, J. B., Beckner, V. E., and Reichenbach, H., "Gasdynamic model of turbulent combustion in TNT explosions," *Proceedings of the Combustion Institute*, vol. 33, pp. 2177–2185, 2011.

[65] Kuhl, A., Ferguson, R., and Oppenheim, A., "Gasdynamic model of turbulent exothermic fields in explosions," *Progress in Astronautics and Aeronautics*, vol. 173, pp. 251–261, 1997.

[66] Kuhl, A., Forbes, J., Chaudler, J., Oppenheim, A. K., Spektor, R., and Ferguson, R. E., "Confined combustion of TNT explosion products in air," *UCRL-JC-131748, Lawrence Livermore National Laboratory, Livermore*, 1998.

[67] Kumar, R., Saurav, S., Titov, E. V., Levin, D. A., Long, R. F., Neely, W. C., and Setlow, P., "Thermo-structural studies of spores subjected to high temperature gas environments," *International Journal of Heat and Mass Transfer*, vol. 54, pp. 755–765, 2011.

[68] Lebel, L. S., Brousseau, P., Erhardt, L., and Andrews, W. S., "Thermochemistry of the combustion of gas phase and condensed phase detonation products in an explosive fireball," *Combustion and Flame*, vol. 161, pp. 1038–1047, 2014.

[69] Lee, J. H. S., *The Detonation Phenomenon*. New York: Cambridge university press, 2008.

[70] Leinov, E., Malamud, G., Elbaz, Y., Levin, L. A., Ben-Dor, G., Shvarts, D., and O., S., "Experimental and numerical investigation of the RichtmyerâĂŞMeshkov instability under re-shock conditions," *Journal of Fluid Mechanics*, vol. 626, pp. 449–475, 2009.

[71] Ling, Y., Haselbacher, A., and Balachandar, S., "Importance of unsteady contributions to force and heating for particles in compressible flows, part 1: Modeling and analysis for shock-particle interaction," *International Journal of Multiphase Flow*, vol. 37, pp. 1026–1044, 2011.

[72] Ling, Y., Haselbacher, A., Balachandar, S., Najjar, F. M., and Stewart, D. S., "Shock interaction with a deformable particle: Direct numerical simulation adn point-particle modeling," *Journal of Applied Physics*, vol. 113, no. 013504, 2013.

[73] Ling, Y., Wagner, J. L., Beresh, S. J., Kearney, S. P., and Balachandar, S., "Interaction of a planar shock wave with a dense particel curtain: Modeling and experiments," *Physics of Fluids*, vol. 24, no. 11301, 2012.

[74] Liou, M. S., "A sequel to AUSM, part II: AUSM$^+$," *Journal of Computational Physics*, vol. 214, pp. 137–170, 2006.

[75] Liu, H., Guo, Y., and Lin, W., "Simulation of shock-powder interaction using kinetic theory of granular flow," *Powder Technology*, 2015.

[76] Mankbadi, M. R. and Balachandar, S., "Compressible inviscid instability of rapidly expanding spherical material interfaces," *Physics of Fluids*, vol. 24, p. 034106, 2012.

[77] Massot, M., *Multiphase Reacting Flows: Modelling and Simulation*, vol. 492, ch. Eulerian multi-fluid models for polydisperse evaporating sprays, pp. 79–123. Vienna: Springer, 2007.

[78] Maxey, M. R. and Riley, J. J., "Equation of motion for a small rigid sphere in a nonuniform flow," *Physics of Fluids*, vol. 26, p. 883, 1983.

[79] McBride, B. J., Gordon, S., and Reno, M. A., "Coefficients for calculating thermodynamic and transport properties of individual species," *NASA Technical Memorandum*, vol. 4513, 1993.

[80] McCartt, A. D., Gates, S., Lappas, P., Jeffries, J. B., and Hanson, R. K., "In situ optical measurments of bacterial endospore breakdown in a shock tube," *Applied Physics B*, vol. 106, pp. 769–774, 2012.

[81] McGraw, R., "Description of aerosol dynamics by the quadrature method of moments," *Aerosol Science and Technology*, vol. 27, pp. 255âĂŞ–265, 1997.

[82] Mei, R., Adrian, R. J., and Hanratty, T. J., "Particle dispersion in isotropic turbulence under stokes drag and basset force with gravitational settling," *Journal of Fluid Mechanics*, vol. 225, pp. 481–495, 1991.

[83] Menon, S. and Patel, N., "Subgrid modeling for simulation of spray combustion in large-scale combustors," *AIAA Journal*, vol. 44, pp. 709–723, 2006.

[84] Miles, A. R., "Bubble merger model for the nonlinear Rayleigh-Taylor instability driven by a strong blast wave," *Physics of Plasmas*, vol. 11, p. 5140, 2004.

[85] Miles, A. R., Blue, B., Edwards, M. J., Greenough, J. A., Hansen, J. F., Robey, H. F., Drake, R. P., Kuranz, C., and Leibrandt, D. R., "Transition to turbulence and effect of initial conditions on three-dimensional compressible mixing in planar blast-wave-driven systems," *Physics of Plasmas*, vol. 12, p. 056317, 2005.

[86] Needham, C. E., *Blast Waves*. Heidelberg: Springer, 2010.

[87] Nicholson, W. L., Munakata, N., Horneck, G., Melosh, H. J., and Setlow, P., "Resistance of Bacillus endospores to extreme terrestrial and extraterrestrial environments," *Microbiology and Molecular Biology Reviews*, vol. 64, pp. 548–572, 2000.

[88] Oefelein, J. C., "Large eddy simulation of turbulent combustion processes in propulsion and power systems," *Progress in Aerospace Sciences*, vol. 42, pp. 2–37, 2006.

[89] Oran, E. S. and Gamezo, V. N., "Origins of the deflagration-to-detonation transition in gas-phase combustion," *Combustion and Flame*, vol. 148, pp. 4–47, 2007.

[90] Oran, E. S., Gamezo, V. N., and Zipf Jr., R. K., "Large-scale experiments and absolute detonability of methane/air mixtures," *Combustion Science and Technology*, vol. 187, pp. 324–341, 2014.

[91] Papalexandris, M. V., "Numerical simulation of detonations in mixtures of gases and solid particles," *Journal of Fluid Mechanics*, vol. 507, pp. 95–142, 2004.

[92] Parmar, M., Haselbacher, A., and Balachandar, S., "Improved drag correlation for spheres application to shock-tube experiments," *AIAA Journal*, vol. 48, no. 6, pp. 1273–1276, 2010.

[93] Patankar, N. A. and Joseph, D. D., "Modeling and numerical simulation of particulate flows by the Eulerian-Lagrangian approach," *International Journal of Multiphase Flow*, vol. 27, pp. 1659–1684, 2001.

[94] Patel, N., *Simulation of Hydrodynamic Fragmentation from a Fundamental and an Engineering Perspective*. PhD thesis, Georgia Institute of Technology, Atlanta, Georgia, U.S.A, 2007.

[95] Pope, S. B., "PDF methods for turbulent reactive flows," *Progress in Energy and Combustion Science*, vol. 11, pp. 119–192, 1985.

[96] Putnam, A., "Integrable form of droplet drag coefficient," *American Rocket Society Journal*, vol. 31, pp. 1467–1468, 1961.

[97] Ranjan, D., Oakley, J., and Bonazza, R., "Shock-bubble interactions," *Annual Review of Fluid Mechanics*, vol. 43, pp. 117–140, 2011.

[98] Regele, J. D., Rabinovitch, J., Colonius, T., and Blanquart, G., "Unsteady effects in dense, high speed, particle laden flows," *International Jounral of Multiphase Flow*, vol. 61, pp. 1–13, 2014.

[99] Richtmyer, R. D., "Taylor instability in shock acceleration of compressible fluids," *Communications in Pure and Applied Mathematics*, vol. 13, no. 297, 1960.

[100] Rodriguez, V., Saurel, R., Jourdan, G., and Houas, L., "Solid-particle jet formation under shock-wave acceleration," *Physical Review E*, vol. 88, no. 063011, 2013.

[101] Rouge, X., Rodriguez, G., Haas, J. F., and Saurel, R., "Experimental and numerical investigation of the shock-induced fluidization of a particle bed," *Shock Waves*, vol. 8, pp. 29–45, 1998.

[102] Rudinger, G., "Effective drag coefficient for gas-particle flow in shock tubes," *ASME Transactions*, vol. 920, pp. 165–172, 1970.

[103] Sankaran, V. and Menon, S., "LES of spray combustion in swirling flows," *Journal of Turbulence*, vol. 3, no. 11, 2001.

[104] Saurel, R. and Lemetayer, O., "A multiphase model for compressible flows with interfaces, shocks, detonation waves and cavitation," *Journal of Fluid Mechanics*, vol. 431, pp. 239–271, 2001.

[105] Schulz, J. C., Gottiparthi, K. C., and Menon, S., "Ionization in gaseous detonation waves," *Shock Waves*, vol. 22, pp. 579–590, 2012.

[106] Schulz, J. C., Gottiparthi, K. C., and Menon, S., "Uncertainty quantification of bacterial aerosol neutralization in shock heated gases," *Shock Waves*, vol. 25, no. 1, pp. 77–90, 2015.

[107] Setlow, P., "Spores of Bacillus subtilis: their resistance to and killing by radiation, heat and chemicals," *Journal of Applied Microbiology*, vol. 101, pp. 514–525, 2006.

[108] Shankar, S. K., Kawai, S., and Lele, S. K., "Two-dimensional viscous flow simulation of a shock accelerated heavy gas cylinder," *Physics of Fluids*, vol. 23, no. 024102, 2011.

[109] Sharpe, G. J., "Transverse waves in numerical simulations of cellular detonations," *Journal of Fluid Mechanics*, vol. 447, pp. 31–51, 2001.

[110] Sislian, P. R., Rau, J., Zhang, X., Pham, D., Li, M., Madler, L., and Christofides, P. D., "Bacterial aerosol neutralization by aerodynamic shocks using an impactor system: experimental results for b. atropheus spores," *Chemical Engineering Science*, vol. 65, pp. 4803–4815, 2010.

[111] Taylor, G. I., "The instability of liquid surfaces when accelerated in a direction perpendicular to their planes," *Proceedings of Royal Society of London. Series A, Mathematical and Physical Sciences*, vol. 201, pp. 192–196, 1950.

[112] Togashi, F., Baum, J. D., Mestreau, E., Lohner, R., and Sunshine, D., "numerical simulation of long-duration blast wave evolution in confined facilities," *Shock Waves*, vol. 20, pp. 409–424, 2010.

[113] Toro, E. F., *Riemann Solvers and Numerical Methods for Fluid Dynamics - A Practical Introduction*. Addison-Wesley Publishing Company, inc., 1999.

[114] Tritschler, V. K., Hu, X. Y., Hickel, S., and Adams, N. A., "Numerical simulation of a RichtmyerâĂŞMeshkov instability with an adaptive central-upwind sixth-order WENO scheme," *Physica Scripta*, vol. 2013, p. 014016, 2013.

[115] Ukai, S., Balakrishnan, K., and Menon, S., "On Richtmyer-Meshkov instability in dilute gas-particle mixtures," *Physics of Fluids*, vol. 22, no. 104103, 2010.

[116] Ukai, S., Balakrishnan, K., and Menon, S., "Growth rate predictions of single- and multi-mode Richtmyer-Meshkov instability with reshock," *Shock Waves*, vol. 21, pp. 533–546, 2011.

[117] Verlet, L., "Computer experiments on classical fluids. I. Thermodynamical properties of Lennard-Jones molecules," *Physical Review*, vol. 159, pp. 98–103, 1967.

[118] Vetter, M. and Sturtevant, B., "Experiments on the Richtmyer-Meshkov instability," *Shock Waves*, vol. 4, pp. 247–252, 1995.

[119] Vorobieff, P., Anderson, M., Conroy, J., White, R., and Truman, C. R., "Vortex formation in a shock-accelerated gas induced by particle-seeding," *Physical Review Letters*, vol. 106, no. 184503, 2011.

[120] White, F. M., *Viscous Fluid Flow*. McGraw-Hill, Third Edition, 2006.

[121] Whitney, E. A. S., Beatty, M. E., Jr., T. H. T., Weyant, R., Sobel, J., Arduino, M. J., and Ashford, D. A., "Inactivation of Bacillus anthracis spores," *Emerging Infectious Diseases*, vol. 9, no. 6, 2003.

[122] Wolanski, P., Gut, Z., Trzcinski, W. A., Szymanczyk, L., and Paszula, J., "Visualization of turbulent combustion in TNT detonation products in a steel vessel," *Shock Waves*, vol. 10, pp. 127–136, 2000.

[123] Xu, S., Aslam, T., and Stewart, D. S., "High resolution numerical simulation of ideal and non-ideal compressible reacting flows with embedded internal boundaries," *Combustion Theory and Modelling*, vol. 1, pp. 113–142, 1997.

[124] Xu, T., Lien, F.-S., Ji, H., and Zhang, F., "Formation of particle jetting in a cylindrical shock tube," *Shock Waves*, vol. 23, pp. 619–634, 2013.

[125] Yuen, M. C. and Chen, L. W., "Heat-transfer measurements of evaporating liquid droplets," *International Journal of Heat and Mass Transfer*, vol. 21, pp. 537–542, 1978.

[126] Zhang, F., "Detonation in reactive solid particle-gas flow," *Journal of Propulsion and Power*, vol. 22, no. 6, pp. 1289–1309, 2006.

[127] Zhang, F., *Heterogeneous Detonation*. Berlin Heidelberg: Springer, 2009.

[128] Zhang, F., Anderson, J., and Yoshinaka, A., *Shock Compression of Condensed Matter-2007*, ch. Post detonation energy release from TNT-aluminum explosives, pp. 885–888. Melville: American Institute of Physics, 2007.

[129] Zhang, F., Frost, F. D., Thibault, P. A., and Murray, S. B., "Explosive dispersal of solid particles," *Shock Waves*, vol. 10, pp. 431–443, 2001.

[130] Zhang, F., Gerrard, K., and Ripley, R. C., "Reaction mechanism of aluminum-particle-air detonation," *Journal of Propulsion and Power*, vol. 25, no. 4, pp. 845–858, 2009.

[131] Zhang, F., Murray, S. B., and Gerrard, K. B., "Aluminum particles-air detonation at elevated pressures," *Shock Waves*, vol. 15, pp. 313–324, 2006.

[132] Zhang, F., Ripley, R. C., Yoshinaka, A., Findlay, C. R., Anderson, J., and von Rosen, B., "Large-scale spray detonation and related particle jetting instability phenomenon," *Shock Waves*, vol. 25, pp. 239–254, 2014.

[133] Zukas, J. A. and Walters, W. P., *Explosive Effects and Applications*. New York: Springer, 1998.

[134] Zuzio, D., Estivalezes, J.-L., Villedieu, P., and Blanchard, G., "Numerical simulation of primary and secondary atomization," *Competes Rendus Mecanique*, vol. 341, pp. 15–25, 2013.

VITA

Kalyana Chakravarthi Gottiparthi is from Hyderabad, India, where he attended high school before joining Indian Institute of Technology, Kharagpur, India for his undergraduate studies in 2003. He obtained Bachelor of Technology (Hon's) in Aerospace Engineering in 2007 and joined Georgia Institute of Technology, Atlanta, for his doctoral studies. At Georgia Tech, he investigated dense gas-particle flows in post-shock and post-detonation environments. The research conducted resulted in more than 6 peer-reviewed articles and 10 conference proceedings. Kalyan is a member of AIAA and a full member of Sigma Xi. He is the recipient of the Institute silver medal (2007) and J. C. Ghosh memorial prize (2006) from Indian Institute of Technology, Kharagpur. He also received Pratibha award and National Merit Scholarship certificate of merit from Government of Andhra Pradesh and Government of India, respectively.